UNIVERSITÀ DI PARMA

UNIVERSITÀ DEGLI STUDI DI PARMA

PhD Programme in Civil Engineering and Architecture

36th cycle

Mechanical Behavior of Human Skin: Testing, Modeling and Simulations

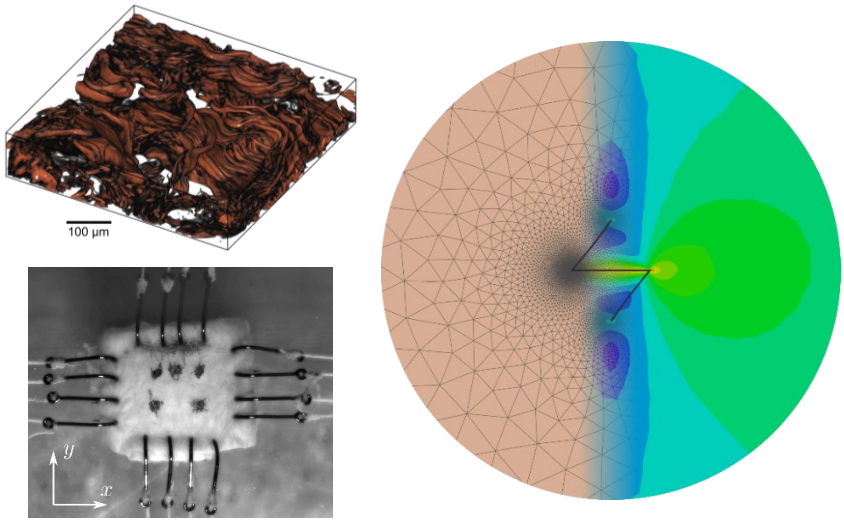

Coordinator:
Prof. Andrea Spagnoli

Tutor:
Prof. Andrea Spagnoli

Co-tutor:
Prof. Bjørn H. Skallerud, NTNU Trondheim, Norway

Candidate: Riccardo Alberini

Years 2020/2024

Alle persone a me care.
Alla mia famiglia.
Ai miei genitori Stefania e Giuseppe.

Acknowledgments

The doctoral programme has been for me a journey full of formative experiences that allowed me to grow both professionally and personally in the fascinating world of research. Along this path, I had the fortune to meet wonderful people who helped, guided, and supported me in achieving this goal.

Above all, I must thank Prof. Andrea Spagnoli, my tutor, for giving me the opportunity to embark on this journey, allowing me to work on the exciting topic of the biomechanics. Over these three years, he always gave me a lot of freedom to test and realize the ideas I had in mind, which ultimately turned into scientific works that I am proud of. I would also like to thank him for his incredible patience despite the various challenges that led to the completion of this thesis. This allowed me to work comfortably and productively.

A special thank goes to Michele Terzano, friend and colleague, who sustained and helped me face the first work challenges during the initial stages of the doctorate. I owe to him part of the passion towards the research topics I worked on, and which today drives me to continue on this path.

I must also thank all the people I met during my stay in Trondheim. In particular, I want to express my gratitude to Prof. Bjørn Skallerud for hosting me at the Norwegian University of Science and Technology (NTNU), and to my esteemed colleague Javad Sadeghinia for introducing me to the fascinating world of the biomechanical experimentation. Without them, part of this thesis would not have been possible. I am also grateful to Prof. Gerhard Holzapfel for his valuable contribution in outlining the research conducted in Trondheim. I owe an important part of this thesis to them.

I also want to thank my fellow doctoral students who stood by me and with whom I have formed important bonds of friendship. Together we supported each other through difficulties to reach the significant milestone that is the doctorate.

Finally, I want to express my heartfelt thank to Enrica for her precious emotional support. She always encouraged me during these three years and helped me to go ahead on my journey.

Abstract

Skin is the largest and one of the most complex organs of the human body, representing the first interface between the inner physiology and the external environment. It is not merely a protective envelope but a dynamic and multifaceted structure that plays a crucial role in various physiological functions, including temperature regulation, D vitamin synthesis, and haptic sensation. Its microstructure, mainly composed of elastin and collagen fibers, confers the tissue its characteristic non-linear anisotropic mechanical response, which guarantee the integrity of the membrane while allowing for the mobility of the body. Understanding the mechanical properties of skin is fundamental for enhancing surgical outcomes, improving wound healing, aiding in the design of prosthetics and wearable devices, and advancing dermatological treatments. This knowledge is crucial for both medical innovation and patient care.

In this thesis the complex mechanical behavior of skin is modeled by means of advanced constitutive models which can account for the non-uniform dispersion of the collagen fibers. Experimental tests on human skin samples were conducted to determine the parameters required to inform such models. In particular, microstructural parameters related to the collagen fiber dispersion are obtained from Second Harmonic Generation (SHG) images of the collagen fibers using a novel algorithm capable of measuring the the three-dimensional orientation distribution of the fibers.

Based on the experimental mechanical and microstructural data, the constitutive models implemented in the commercial Finite Element (FE) software ABAQUS are used to simulate skin corrective surgeries, specifically focusing on the *Z-plasty*, the *triple Z-plasty*, and the *rhombic flap transposition*. These simulations provide mechanical insights into the expected outcomes of surgical interventions, allowing us to define optimized configurations that minimizes deformations and stresses, thus contributing to improved surgical planning and outcomes.

The results achieved, beside confirming the effectiveness of mechanical simu-

lations in biomedical applications, represent a step forward in the pursuit of more effective and tailored approaches to skin corrective surgeries. Moreover, the developed algorithms, as well as the experimental results of human skin, are not limited to the scope of the present thesis, but can be exploited in further biomechanical analyses.

Sommario

La pelle è il più esteso e uno dei più complessi organi del corpo umano e rappresenta la prima interfaccia tra la fisiologia interna al corpo umano e l'ambiente esterno. Essa non costituisce solamente una semplice barriera protettiva, ma una struttura dinamica e multifunzionale che svolge un ruolo cruciale in varie funzioni fisiologiche, tra cui la regolazione della temperatura, la sintesi della vitamina D e la sensazione tattile. La sua microstruttura, composta principalmente da fibre di elastina e collagene, conferisce al tessuto la sua caratteristica risposta meccanica non lineare e anisotropa, garantendo l'integrità della membrana pur consentendo la mobilità del corpo. La comprensione delle proprietà meccaniche della pelle è fondamentale per migliorare i risultati chirurgici, accelerare la guarigione delle ferite, aiutare nella progettazione di protesi e dispositivi indossabili, e progredire nei trattamenti dermatologici.

Nella presente tesi, il complesso comportamento meccanico della pelle è modellato attraverso modelli costitutivi avanzati che possono tenere conto della dispersione non uniforme delle fibre di collagene. Per determinare i parametri necessari a caratterizzare tali modelli sono state condotte prove sperimentali su campioni di pelle umana. In particolare, i parametri microstrutturali legati alla dispersione delle fibre di collagene sono ottenuti dalle immagini SHG, Second Harmonic Generation, delle fibre di collagene utilizzando un nuovo algoritmo capace di misurare la distribuzione dell'orientamento tridimensionale delle fibre.

Sulla base dei dati meccanici e microstrutturali sperimentali, i modelli costitutivi implementati nel software commerciale a elementi finiti ABAQUS sono poi stati utilizzati per simulare interventi chirurgici correttivi della pelle. In particolare sono state analizzate la *Z-plasty*, la tripla *Z-plasty* e la *rhombic flap transposition*. Queste simulazioni forniscono utili informazioni meccaniche circa i risultati attesi degli interventi chirurgici, consentendo di definire configurazioni ottimizzate che minimizzano deformazioni e stress, contribuendo così a migliorare la pianificazione e i risultati chirurgici.

I risultati ottenuti, oltre a confermare l'efficacia delle simulazioni meccaniche nelle applicazioni biomediche, rappresentano un passo avanti nella ricerca di approcci più efficaci e personalizzati per le chirurgie correttive della pelle. Inoltre, gli algoritmi sviluppati, così come i risultati sperimentali della pelle umana, non sono limitati all'ambito della presente tesi, ma possono essere efficacemente utilizzati in ulteriori analisi biomeccaniche.

Contents

Acknowledgments . . . . . **v**
Abstract . . . . . **vii**
Sommario . . . . . **ix**
Contents . . . . . **xi**
Figures . . . . . **xv**
Tables . . . . . **xix**
Acronyms . . . . . **xxi**
1 Introduction **1**
1.1 Thesis outline 12
2 Anatomy and Biomechanics of Human Skin **15**
2.1 Skin Anatomy 15
2.2 Wound Healing and Potential Issues 21
2.3 Skin Lines 24
2.4 Skin Mechanics 28
2.5 Skin Corrective Surgeries 31
2.5.1 History of Z-Plasty 31
2.5.2 Modern Z-Plasty 33
2.5.3 Other Types of Scar Relaxation Surgeries 36
2.5.4 Defect Closure Surgeries 38
3 Mechanical Modeling for Soft Fibrous Tissues **41**
3.1 Finite Strain Continuum Mechanics 42
3.1.1 Kinematics 42
3.1.2 Stress Definitions 48
3.1.3 Hyperelastic Constitutive Modeling 50
3.1.4 Linearization of the Mechanical Problem 54
3.1.5 Stiffness Tensors Derivation 56
3.1.6 Plane Stress Formulation 58
3.2 Implemented Constitutive Models 60

3.2.1 Ogden Wrinkling Model 60
3.2.2 Description of General Fiber Distributions 69
3.2.3 GST Model for Non-Symmetrical Fiber Dispersions 71
3.2.4 Discrete Fiber Dispersion Model 73
4 Measurement of the Collagen Fiber Orientation Distribution 83
4.1 Description of the Algorithm 84
4.1.1 Computation of the Raw dFOD 85
4.1.2 Deconvolution of the Raw dFOD 88
4.1.3 Estimation of the Distribution Parameters 89
4.2 Algorithm Calibration and Validation 91
4.2.1 Artificial Fiber Dispersion Volume 91
4.2.2 Statistical analysis 91
4.2.3 Calibration 92
4.2.4 Robustness Assessment 92
4.2.5 Precision Assessment 97
4.3 Application to Skin Tomography 100
4.3.1 Collagen Fiber Tomography 100
4.3.2 Human skin 101
4.3.3 Mouse skin 103
4.4 Discussion 105
5 Mechanical and Microstructural Parameters of Human Skin 109
5.1 Experiments and Data Acquisition 111
5.1.1 Tissue Acquisition and Storage 111
5.1.2 Planar Tensile Tests 111
5.1.3 Tomographic Reconstruction of Fibers 113
5.1.4 Identification of the Microstructural Parameters 116
5.1.5 Constitutive Model Fitting 116
5.1.6 Statistical analysis 117
5.2 Results 118
5.2.1 Healthy skin 118
5.2.2 Scarred skin 129
5.3 Discussion 132
6 Finite Element Modeling of Skin Surgeries 137
6.1 Internal Boundaries with Prescribed Dislocations 138
6.2 FE Model Geometry of Skin Surgeries 141
6.2.1 Boundaries Topology 141
6.2.2 Meshing 143
6.2.3 Disposition of Internal Boundary Nodes 145

6.3 Representative Examples 146
7 Numerical Simulations of Skin Corrective Surgeries 151
7.1 Isotropic Analysis of the Z-plasty and the Triple Z-plasty 153
7.2 Anisotropic Analysis of the Z-plasty 163
7.3 Isotropic Analysis of the Rhombic Flap Transposition 171
8 Conclusions 177
Bibliography 181

Figures

2.1 Anatomy of the skin 16
2.2 Anatomy of the epidermis 17
2.3 Anatomy of the dermis 19
2.4 Collagen structure hierarchy 20
2.5 Wound healing phases 23
2.6 Collagen organization in normal skin and scar tissue 24
2.7 Representation of the Langer's lines 25
2.8 Langer's circular cuts 26
2.9 RSTL vs Langer's lines on the face 27
2.10 Skin mechanical behavior 29
2.11 Skin anisotropic response 30
2.12 Denonvilliers operation 31
2.13 Berger operation 32
2.14 Traditional Z-plasty procedure 34
2.15 Unequal Z-plasty procedure 34
2.16 Scar realignment 35
2.17 Four-flaps plasty and square flap plasty 37
2.18 Traditional Z-plasty vs Planimetric Z-plasty 38
2.19 Alternative surgical techniques 39
2.20 Defect closure plasties 40

3.1 Configurations of the continuum body in the Euclidean space 43
3.2 Traction vectors acting on infinitesimal surfaces elements in the reference and current configurations 48
3.3 Configurations of a unit membrane element under different loading conditions 62

3.4 Normalized stress-stretch responses on a single plane stress element analyzed with the standard Ogden model and the Ogden wrinkling model 63
3.5 Comparison of the strain domains maps plotted onto the deformed configuration of a rectangular membrane beam analyzed with the Ogden wrinkling model and the standard Ogden model 65
3.6 Normalized force-displacement curves of the rectangular beam under bending 66
3.7 Comparison of the strain domains maps plotted onto the deformed configuration of a notched rectangular membrane analyzed with the Ogden wrinkling model and the standard Ogden model 67
3.8 Normalized force-displacement curves of the notched sheet under tension 68
3.9 Schematic representation of the unit vector **N** in the global frame and in the principal fiber family frame 70
3.10 Plots of the in-plane and out-of-plane dispersion parameters κ_{ip} and κ_{op} versus the von Mises concentration parameters a and b . . 72
3.11 Lebedev integration points distribution 76
3.12 Contour plot of the von Mises stress of the annular disk solved employing $n = 50, 74, 86, 110, 146, 170, 194$ representative fiber directions 77
3.13 Plots of the von Mises stress versus the angle ξ from $\mathbf{E}_1$ along the inner boundary for $n = 50, 86, 146, 194, 266$ and for the reference solution $n = 974$ 78
3.14 Mean Squared Error (MSE) of the von Mises stress along the inner boundary versus n 79
3.15 Uniaxial test on a unit square element in plane stress condition . . . 80
3.16 Shear test on a unit square element in plane stress condition 81

4.1 Illustration of the 3D discrete Fourier transform algorithm 86
4.2 Application of the 3D discrete Fourier transform algorithm 90
4.3 Algorithm calibration 93
4.4 Algorithm robustness assessment in relation to the number of fibers 95
4.5 Algorithm robustness assessment in relation to the fibers diameter . 96
4.6 Algorithm precision assessment for in-plane parameters 98
4.7 Algorithm precision assessment for out-of-plane parameters 98
4.8 Application of the algorithm to human skin collagen fiber SHG tomography 102

4.9 Application of the algorithm to mouse skin collagen fiber SHG tomography 104

5.1 Location of samples and views of a representative sample 112
5.2 SHG acquisition for tomographic reconstruction of collagen fibers . 115
5.3 Measured fiber orientation distributions $d'(\theta, \phi)$ computed from the SHG tomographies 119
5.3 Figure continued 120
5.3 Figure continued 121
5.4 Average collagen fiber orientation in azimuthal direction 122
5.5 Representative experimental mechanical response of sample ABR2-p3 in horizontal and vertical directions for two different biaxial tests 125
5.6 Box-and-whiskers plots of GST and DFD parameters 126
5.7 Significant correlation between the parameters 127
5.8 Average mechanical responses of the uniaxial tests performed along the horizontal and vertical directions 128
5.9 Fiber architecture in healthy and scarred skin 130

6.1 Schematics of joining dislocations kinematic constraint applied to paired subsets $\partial\Omega^{+}_{\mathrm{I},i}$ and $\partial\Omega^{-}_{\mathrm{I},i}$ of the internal boundary $\partial\Omega_{\mathrm{I}}$ 141
6.2 Offset scheme of the internal boundary vertices $\mathbf{V}_{\mathrm{I},k}$ 144
6.3 Application of the algorithm to a Z-plasty model 147
6.4 Representative FE model geometries generated with the developed algorithm in the reference configuration Ω (left figures) and in the final configuration $\omega(t_f)$ 148
6.4 Figure continued 149
6.4 Figure continued 150

7.1 General scheme of the single Z-plasty 154
7.2 General scheme of the triple Z-plasty 155
7.3 Vertical elongation and horizontal shortening strains in relation to the angle ϑ for the single and triple Z-plasty models 157
7.4 Normal Cauchy stress along the suture of the single Z-plasty 158
7.5 Normal Cauchy stress along the suture of the triple Z-plasty 158
7.6 Strain domains for the single Z-plasty 159
7.7 Strain domains for the triple Z-plasty 159
7.8 Diagrams of the mechanical metrics for the single and triple Z-plasty 160
7.9 Elongation efficiency coefficients of the single and triple Z-plasty . . 162

7.10 Vertical elongation and horizontal shortening strains in relation to the angle ϑ and the mean in-plane fiber orientation α for the single Z-plasty models 165
7.11 Maps of the von Mises stress field of the single Z-plasty with $\vartheta = 60°$ for different mean in-plane fiber orientations α 166
7.12 Strain domains maps of the single Z-plasty with $\vartheta = 60°$ for different mean in-plane fiber orientations α 167
7.13 Normal Cauchy stress along the suture of the single Z-plasty for the mean in-plane fiber orientation $\alpha = 90°$ 168
7.14 Diagrams of the mechanical metrics for the single for all the considered in-plane fiber orientation α 169
7.15 Elongation efficiency coefficients of the single Z-plasty for different mean in-plane fiber orientations α 170
7.16 General scheme of the rhombic flap transposition 172
7.17 Strain domains for the rhombic flap transposition 174
7.18 Diagrams of the mechanical metrics for the rhombic flap transposition175

Tables

5.1 Overall collagen fiber data determined from the SHG tomographies 118
5.2 Microstructural parameters of the fitted distributions in Figure 5.3 and goodness of fit (R^2). 123
5.3 Estimated mechanical parameters of the GST and DFD models from the biaxial tests and the relative mechanical fitting residual in terms of wMAPE error. The sample thickness is given in the first column. . 124
5.4 Microstructural parameters of the scarred skin samples and relative control samples of healthy skin. The last column indicates the goodness of fit (R^2). 131
5.5 Estimated mechanical parameters and fitting residual wMAPE error of the scarred skin samples and the healthy control skin samples. The sample thickness is given in the first column. 131

Acronyms

AI Angular Integration. 7, 8, 74

BVP boundary-value problem. 54, 55

DFD Discrete Fiber Dispersion. xvii, xix, 8, 11, 12, 42, 74, 75, 80–83, 110, 116, 117, 123–126, 131–133, 152, 163, 178, 179

dFOD discrete Fiber Orientation Distribution. 84–93, 95–97, 100–107, 116

DFT Discrete Fourier Transform. 12

DIC Digital Image Correlation. 9, 67, 112, 113, 116, 125, 134

ECM extracellular matrix. 15, 18, 19, 21, 22, 28, 56

FE Finite Element. vii, xvii, 11–13, 42, 56, 59, 61, 138, 139, 141, 146–150, 152, 154, 155, 177, 179

FEM Finite Element Method. 5, 7–9, 11, 12, 42, 55, 137, 151, 180

FOD Fiber Orientation Distribution. 83, 84

GAGs glycosaminoglycans. 18

GOH Gasser-Ogden-Holzapfel. 8, 10

GST Generalized Structure Tensor. xvii, xix, 8, 11, 12, 42, 71, 73, 74, 83, 110, 116, 117, 123–126, 131–133, 178

MSE Mean Squared Error. xvi, 79

PDF Probability Density Function. 7, 8, 69, 70, 83, 91

PGs proteoglycans. 18, 29, 56

ROI Region of Interest. 84, 88, 101–103

RSTL Relaxed Skin Tension Lines. 27, 28, 35, 36, 38, 164

SEF strain-energy function. 50, 51, 53, 54, 56, 60, 61, 71, 72, 75, 178

SEM Scanning Electron Microscope. 28

SHG Second Harmonic Generation. vii, ix, xvi, xvii, xix, 83, 84, 100–104, 107, 109, 110, 113–121, 129, 130, 132, 134, 178

wMAPE weighted Mean Absolute Percentage Error. xix, 117, 123–126, 131

Chapter 1

Introduction

Preliminaries

The skin, the largest and one of the most complex organ of the human body, is a dynamic and multifaceted structure that plays a crucial role in various physiological functions, including temperature regulation, D vitamin synthesis, and haptic sensation [1]. At the same time, the skin serves as a remarkable barrier between the inner physiology and the external environment, protecting the body against pathogens and physical harm, ensuring water resistance, providing UV protection, and more [2]. However, this protective armor is constantly exposed to irritants and potential threats, making it susceptible to injury. When the skin does get injured, it initiates a complex series of events known as wound healing. This process involves inflammation and the creation and remodeling of new tissue, all of which require coordinated regulation among different cell types [3]. In contrast to the fetal wounds that heal without scarring [4], in adult mammals this process is imperfect and less regenerative, leading to the formation of scar tissue [5, 6].

Scars and Wounds

The appearance of a healed wound is influenced by an intricate mix of biological, environmental, lifestyle, and treatment-related factors. Each plays a crucial role in determining how a wound heals and how the resulting scar looks. Biologically, age is a significant factor. In elderly individuals the overall healing process is slower and delayed compared to young ones, but the scarring is reduced and, in general, of higher quality [7]. The type and color of the skin also matter, as different skin types respond differently to injury. For instance, keloid scars are more prevalent in darker skin [8]. Moreover, overall health and existing medical

conditions, like e.g. diabetes, obesity and anemia, can impede the healing process [4]. Lifestyle choices, as well, contribute to how a wound heals. Smoking, for instance, can impair blood flow to the wound area, slowing down the healing process and potentially worsening the scar appearance [9]. Similarly, alcohol and drug abuse have a detrimental effect on wound healing as skin becomes prone to ulcers [10]. Environmental aspects also play a role. Wounds can heal differently based on exposure to infections, sunlight, and the surrounding temperature and humidity [2]. Under moist conditions the healing is accelerated and produces better scars [11]. In contrast, infections can delay healing and turn into ulcers, while UV radiation from sunlight can lead to scar discoloration [12]. Treatment-related factors are equally influential. Post-operative wound care, involving cleaning and dressing the wound properly, is pivotal for optimal healing [13]. Additionally, the use of specific topical treatments, like silicone-based creams or vitamin E can significantly influence the final appearance of the scar [14].

Beside all of these factors, mechanical stress and tension at the wound site are pivotal in determining how a wound heals. Continuous pressure, whether from bandaging or prolonged hospitalization in bed, can impede blood flow and tissue regeneration leading to pressure ulcers [15]. Similarly, shear forces in the substrates, which occur when layers of skin slide against each other [16], can slow the healing process or even cause wounds to reopen [17, 18]. High tension across the wound often leads to wider and more noticeable scars. While some wounds heal with minimal scarring, others may develop hypertrophic scars, which are raised, red, and confined to the wound area, particularly in high-tension regions [8, 19]. This type of scar is also common in burn scar and might develop spontaneously during the healing, especially when the injury is extended over a big body surface [20]. Hypertrophic scars occur soon after the trauma or inflammation, remain restricted to the original wound and regress in months to years [2]. They are not to be confused with keloids, which are influenced by genetic factors and extend beyond the original wound, rarely showing regressions [2, 21].

Impact of Scars and Wounds

The impact of these healing outcomes drastically affect the patient quality of life under various points of view. From an aesthetic and emotional standpoint, visible scars, especially on exposed areas like the face, can significantly affect a patient self-esteem and body image, potentially leading to emotional and psychological distress [22]. Furthermore, the visible and functional impacts of scarring can pose social and occupational challenges, affecting a patient social interactions and ca-

reer opportunities [23]. Scarring also can lead to reduced mobility, especially if it occurs over a joint or a frequently moving area. This physical limitation can be accompanied by discomfort or pain [20], affecting the daily activities and the overall quality of life. Furthermore, the treatment of scars has a non negligible economical impact on the public health and society [24].

Surgery

Surgical intervention is then essential to relief, fully or partially, contracted hypertrophic scars, offering improved functionality to patients affected by these debilitating conditions. In less severe cases, the scar can be surgically removed (excised) and the wound edges closed primarily. This approach is suitable when there is enough laxity in the surrounding skin to allow for tension-free closure [25]. When these conditions are not met this method is not practical, and skin grafting is a possible solution. Skin is taken from a donor site, possibly from nearby regions with similar pigmentation, and used to cover the area where the scar has been excised. This method is particularly useful for larger scars or when there is limited skin elasticity. However, full-thickness skin grafts have a reduced blood supply due to the complete excision from the donor site, which increases the risk of complications, such as infections and necrosis [26]. Therefore, tissue rearrangement using skin flaps without full excision is a preferable choice when possible, which preserves the vascularity of the tissue, thus increasing the success rate of the intervention [27, 28]. A simple technique called Z-plasty is frequently employed to relieve tension and improve the functional and aesthetic outcome of the contracted scars. Z-plasty involves making angled incisions on either side of the scar, creating small flaps of skin that are then transposed. This rearrangement changes the direction of the scar, making it less constrictive and improving skin flexibility [29].

The invention of this technique dates back to 1837 by a surgeon of the Philadelphia hospital, who used it to correct a facial defect of the lower eyelid [30]. His work remained unknown for decades, but similar procedures were later discovered and developed independently by other surgeons [31]. However, it was only by the beginning of the XX century, after its detailed descriptions operated by McCurdy [32], and later by Limberg [33] and Davis [34], that the Z-plasty became a popular practice to treat contracted scar. Nowadays, this technique is still effectively used, and multiple variants have been developed to achieve similar or higher elongations effects depending on the scar location on the body, its severity, and the surrounding skin availability. For instance, multiple concatenated Z-plasties

are used for relaxing particularly long scar without using excessively wide skin flaps [35]. Alternatively, the two triangular flaps of the Z-plasty can be split into four flaps and transposed alternately, forming the so called four-flaps plasty [36]. To treat extensive burn scars in upper elbows Koyama and Fujimori [37] developed a VW-shaped incision that also removes part of the scarred tissue while relieving the contracture. Similarly, Karacaoglan and Uysal [38] proposed a seven-flaps plasty to treat scars across elbows and fingers on the volar side of the hand. Exploiting the concept of tissue rearrangement, various surgical archetypes have also been proposed to close large defects resulting from the removal of skin cancers, nevi or other kind of skin flaws. Some of the most common are the rhombic transposition flap [39], the bilobe flap [40], and the V-Y advancement [41], to mention a few.

Issues Related to Scars Configurations

These techniques are powerful and versatile, but require high levels of expertise in order to select the most suitable one depending on the specific needs and expectations of the patient. If not correctly executed these surgeries could potentially worsen the existing conditions, with the consequent need of further and more risky interventions. Therefore, a preoperative inspection is extremely important, and surgeons must assess key factors such as skin quality, underlying bone structure, vascular supply, the extension of the defect, and the direction of the natural skin tension. By combining these information the surgeon can determine the appropriate technique and plan the operation, as well as informing the patient about the risks and the possible outcomes [16]. To this end, several guidelines can be found in literature [16, 42–44], some of which providing an algorithmic approach to determine the most suitable technique depending on factors such as the defect length, the skin availability or the skin tension [45]. This should direct doctors toward the best option, especially during the early stages of their training. Nonetheless, these guidelines mostly rely on their authors experience, and are the result of decades of trial and error. On the one hand, this empirical optimization process provides direct and physical evidences of which technique does work and which does not, but on the other hand, this has led to many dissimilar strategies, and even to this date new flap designs continue to be proposed [46]. Seen the paramount relevance of the biomechanics involved in the skin surgeries, the lack of quantitative information about the mechanical factors influencing the surgery result makes difficult, if not impossible, to demonstrate which technique works best under equal conditions. New strategies, indeed, are always seen with skepti-

cism by surgeons in common clinical applications, who prefer to stick with known and proved techniques, even though the new ones could potentially give better results.

Quantitative Studies on Skin Scars

Early analytical studies on the Z-plasty were carried by Davis and Kitlowski [47] and McGregor [48], who computed the theoretical scar elongation, about 73% for the standard configuration, using simple trigonometrical considerations. Later, Furnas [49] generalized the previous studies to the three-dimensional case for applications on curved surfaces. However, the mechanics of the material was not taken into account and the flaps were assumed to be undeformable. The first study providing an extensive mechanical insights was conducted by Furnas and Fischer [50], who quantified the actual scar elongation performances of the Z-plasty and its combinations, as well as the force required to close the flaps, by means of testing on anesthetized dogs. Their results represent a cornerstone in the field of the skin surgery mechanical analysis, and were used by Danielson and Natarajan [51] to formulate and validate the tension field theory for membranes in large deformations applied to the skin. The theory can take into account the geometrical and material nonlinearity to solve the stress field inside triangular skin flaps. Despite this impressive achievement, such analytical tools can only describe simple problems, and offer limited room for the generalization to more complex cases.

Computational Studies

In recent decades, the advancement of the computational capabilities offered by computer technologies, opened new vistas in the field of biomechanics, offering insights that were previously unattainable through traditional analytical tools [52]. Indeed, numerical tools like the Finite Element Method (FEM) are more versatile and can be used to solve mechanical problems of whatever geometry and material behavior. Pioneering simulations using the FEM have been performed by DeHoff and Key [53], who compared the stresses resulting from the numerical model of the Z-plasty with those obtained from the experiments performed by Furnas and Fischer [50]. Later, other researcher used the same approach to analyze simple wound closures [18, 54] and skin flaps advancement surgeries [55]. Recent advancements in the field, as exemplified by the works of Topp *et al.* [56] and Rajabi *et al.* [57], have identified an optimized configuration for the rhombic transposition flap that differs from the established medical literature. These results, in particular, demonstrated the great potential of the FEM simulations for

exploring new surgical techniques, allowing to analyze multiple cases without the need of *in vivo* tests. Stowers *et al.* [58] made notable progress by analyzing the rhombic flap transpositions with an anisotropic model and optimizing their orientation relative to the mean direction of collagen fibers. However, this study made some simplifications about the material, and the geometry of the rhombic flap was constrained to a single configuration. For a more comprehensive understanding of the effects of aging and defect size on skin stress conditions in reconstructive surgeries, Lee *et al.* [59] provided valuable insights.

Material Response

While these developments represent significant progress, it is worth noting that all the simulations mentioned made simplifying assumptions, and omitted one or more fundamental biomechanical aspect of the skin in living conditions. In fact, as demonstrated by the historical study of Lanir and Fung [60], the skin can be regarded as an anisotropic viscoelastic material. Moreover, it consistently exists under an initial tension field that varies across different regions of the human body [2]. Among the three layers comprising the skin, the dermis, located between the epidermis and the hypodermis, plays a dominant role in conferring mechanical strength. This layer is composed of a complex network of crimped collagen and elastin fibers [61, 62], which exhibit a highly non-linear response under tensile loading, characterized by a distinctive J-shaped stress–strain loading curve [63, 64]. This curve exhibits three distinct phases. In the initial linear phase (toe region), the tissue response is primarily isotropic, influenced by the elastin network and the unstructured ground substance matrix. During this phase, the collagen fibers are still undulated and interwoven, and do not take part to the global response [65]. In the second phase (heel region), falling within the typical physiological range, the collagen fibers gradually begin to uncrimp and align with the force, thus, starting to carry part of the load [66]. This represents a transitional zone between the first and third phases, and it is characterized by high non-linearity. Finally, once all the fibers are recruited and straightened along the load direction, the material enters in the third phase (linear region) characterized by a stiff and almost linear response [66]. Then, upon the cessation of loading, the collagen primarily recoils due to the elastin component, bringing the material to its original state. However the unloading path is not the same as the loading one, and during the full cycle some energy is dissipated mainly due to the viscous nature of the ground matrix [67]. Furthermore, it is important to note that only the tensile stress is considered, since thin membranes as skin are prone to instability

under compressive stresses, often forming wrinkles and ripples [68]. Accordingly, FEM models represent an excellent tool to predict the mechanics of skin surgeries, provided the underlying constitutive models and the aforementioned biomechanical aspects are appropriately considered.

Since the early work of Lanir and Fung [60] a great variety of constitutive models have been proposed to capture the complex behavior of the skin and other soft fiber-reinforced biological tissues. Initially, models developed for rubber materials were adapted to approximate elastic and highly non-linear response. Some of the most popular are the Mooney-Rivlin [69], the Yeoh [70], and the Ogden [71] models. The latter, in particular, saw widespread utilization thanks to its ability to model a wide spectrum of materials using a simple formulation, and it is still used nowadays for simulating skin behavior [57, 72–74]. Nonetheless, since these models are designed for rubber-like materials, whose loading curve typically follows an S-shape, alternative models have been introduced to capture the extreme stiffening of soft tissues in the linear region. Based on the observation of the experimental evidences, Fung [75] introduced an exponential model as the natural approach to capture the typical J-shaped loading curve of soft tissues un uniaxial tension regime, paving the way for the development of the so called Fung-type models. This purely phenomenological model was then generalized into an anisotropic model by Tong and Fung [76], and used to reproduce the tests of Lanir and Fung [60]. Even though it can describe fairly different tissue responses it lacks of explanatory power, being the material treated as a whole without considerations about its structural components. In addition, it requires twelve (non-physical) material coefficients, making it impractical for real applications.

Unlike phenomenological models, structure-based models consider the mechanical contributions of the material structural constituents, like the ground substance matrix, and the networks of collagen and elastin fibers. The first of this kind was formulated by Lanir [77], who included the contribution of the collagen fiber through two Probability Density Function (PDF), one accounting for the non-uniform fiber dispersion and the other for the distribution of the fiber waviness. Moreover, he also assumed that fibers under compressive stresses have a negligible mechanical contribution. Basically, the overall strain-energy of a material point is computed by integrating the single fiber strain-energy along every direction of the unit sphere angular domain, weighted with the PDFs. For this reason, this kind of models are often referred to as Angular Integration (AI) models. Despite their excellent predictive power, they are also computationally expensive as the integral has to be recomputed every time the material deformation changes.

By exploiting a similar concept, Gasser *et al.* [78] formulated a different model based on a modified strain measure obtained by averaging the axial fiber strain over the unit sphere angular domain using the PDF. Explicit calculation of such strain, assuming an axially symmetric fiber distributions, leads to a simple expression dependent on the state of deformation and on a Generalized Structure Tensor (GST) representative of the fiber distribution. Hence, once the GST is obtained from the integral over the unit sphere, the overall strain-energy becomes dependent on the state of deformation only. This significantly improves the computational efficiency, as only a single integration is required to fully describe the fiber dispersion. Consequently, as long as the predictive power is the same, this model, best known as Gasser-Ogden-Holzapfel (GOH) model, is computationally more convenient than the AI one [79]. Based on the same method, Holzapfel *et al.* [80] also generalized the GOH model to the case of non-symmetrical fiber dispersion. The ability to account for a complex microstructure with a simple and efficient formulation made GST-based models extremely popular in the field of biomechanics, and some of them have been also implemented in commercial FEM software [81]. In some circumstances, however, it is desirable to exclude the contribute of the compressed fibers to obtain a more realistic simulation. This is the case of modeling the membrane wrinkling by means of planar simulations [82, 83], for instance. This operation can be easily handled during the integration by excluding the directions in a compression state from the computation. Nonetheless, this makes the GST deformation dependent, and requiring to be integrated each time the state of deformation changes. This vanishes the computational advantage of GST-based models [84], and some authors modified the formulation trying to include an efficient criterion for excluding compressed fibers while preserving a pre-integrated scheme [85]. However, Latorre and Montáns [86], in a work comparing different approaches, have shown that some choices for the compressed fiber exclusion criterion may produce nonphysical discontinuities in the stress–strain behavior. A different approach to address the compression problem has been advanced by Li *et al.* [87], who formulated a model which approximates the AI model by computing the integral using a finite number of representative fiber directions. The directions are obtained by discretizing the unit sphere surface in area elements and taking their centroids. Accordingly, if the discretization is fine enough to assume the integrand function to be constant within the area elements, it becomes straightforward to exclude the directions displaying a compressed state. This method, called Discrete Fiber Dispersion (DFD) model, represents a compromise between the computational efficiency of GST models and the versatility of AI ones. Recently, Rolf-Pissarczyk *et al.* [88] also improved the

computational efficiency by implementing an adaptive meshing to discretize the unit sphere surface.

Materials Parameters

Setting aside their advantages and shortcomings, each of these constitutive models can yield good approximations of the material response, as long as the material parameters are accurately determined through experimental tests. These tests are broadly classified into *in vivo* and *ex vivo* experiments, each offering unique insights and advantages. Experiments *in vivo* provide data on tissue in its natural state on the body and in living conditions. Among the mostly diffused techniques there are indentation [89, 90], suction [91, 92], and wave propagation [93, 94]. Another interesting technique has been developed by Evans and Holt [72] who computed the parameters for the Ogden model of the volar aspect of the elbow. He first applied a force on the surface of the skin using a glued thread, and measured the resulting displacement field with a Digital Image Correlation (DIC) system. Then, he replicated the experiment in a FEM model and obtained the material parameters by optimizing the displacement field onto that measured from the DIC system. Similar experiments have been conducted by Kvistedal and Nielsen [95] and Flynn *et al.* [96], but they used computer-driven actuators to apply the force along multiple directions. These methods represents an interesting approach for computing mechanical parameters, but suffers of a number uncertainties about skin *in vivo*, including pre-stress, boundary conditions, and the variability of the skin properties across the observed area [97]. In addition, regardless the used technique, other uncertainties arise from the interconnection of the skin with the other subcutaneous tissues. In fact, even though the global mechanical response is mainly attributed to the dermis, muscles and fat might play a significant contribute, which is difficult to isolate from that of skin [98]. However, the main limitation of *in vivo* tests is that they must be non-invasive and, mostly, non-destructive. Accordingly, the range of investigated deformation must be restricted to the that of the physiological strains to avoid damage to the tissue, thus limiting the information required for an accurate constitutive modeling. In contrast, *ex vivo* experiments on excised skin can characterize the mechanical response over the full range of deformations, from the toe region to the rupture. One widely used method is the uniaxial tensile testing. The setup usually involves clamping the skin sample of few centimeters size at both ends and gradually applying force, while recording the force-elongation relationship. Usually, the sample is submerged in a saline solution at 36°C in order to recreate the physiological conditions [99].

These tests are particularly useful for comparing the properties of healthy skin versus scarred or aged skin. Specifically, the tangent stiffness modules of the toe and linear regions are usually computed [100]. However, these parameters are useful only for comparison purposes, and cannot be used for a thorough nonlinear mechanical characterization. In fact, uniaxial tests cannot capture the anisotropic response of the material, unless multiple tests are performed along different directions. The current standard for investigating soft tissues properties is by biaxial tensile testing. Unlike uniaxial testing, this technique loads skin samples along two perpendicular directions simultaneously. Since the applied deformation can be controlled independently for the two directions, different loading protocols can be performed, providing the mechanical data required to define the material parameters for anisotropic models [101, 102]. Biaxial test have been extensively used to find the properties of the GOH model for various tissues like aortic walls [103] and mitral valve leaflets [104, 105], but despite its relevance few studies did the same for the skin. A noticeable work on mouse skin was conducted by Meador *et al.* [106], who also investigated the influence of the physiological prestrain on the computed parameters. However, a study of this kind is still missing for the human skin.

For structure-based models, in addition to the mechanical parameters, it is also fundamental to quantify the microstructural parameters of the fiber network governing the anisotropy, such as the mean orientation and the concentration. These parameters can be deduced from the orientation distribution of the fiber network, which is obtained by analyzing microscopy images of the collagen fibers. Current methods to quantify the fiber orientation distribution are based on texture analysis [107], pixelwise gradients and directional variance [108, 109], Gabor filter [110], and Fourier transform [111, 112]. The latter in particular gained prominence thanks to its characteristics of insensitivity to image complexity, computation speed, and reduced sensitivity to image noise [113]. All of these methods are developed to analyze two-dimensional (2D) images, and therefore cannot give a comprehensive overview of the 3D fiber organization. This limits the information that can be extracted to the microstructural parameters of a 2D fiber dispersion solely, thus posing limitations for a precise constitutive modeling. Some authors tried to extend the 2D methods to the 3D case [114, 115], but they all display technical limitations that makes their measured fiber orientation distribution not suitable for practical uses in constitutive models [116].

Summary

In summary, the skin is an extraordinary material featuring a complex mechanical behavior which has evolved in order to protect the body from various external hazards, while accomplishing several biological functions. To maintain its integrity, it has evolved self-repair strategies to restore the continuity of the membrane after injuries, but the process is not perfect, and the result always leads to the formation of a scar, which in some cases can be contracted or disfiguring. Treatment for severe conditions is possible only by surgical operation, which involves rearrangement of skin flaps. The problem is strictly governed by the skin mechanics, but current guidelines for such operations rely on decades of clinical experience, and lack of strong mechanical foundations. Numerical simulations through the FEM can provide quantitative information about the mechanics behind the skin surgeries, being useful not only for validating and optimizing current surgical procedures, but also for planning patient-specific operations, developing new healthcare devices, and improving wound healing strategies. However, the state of the art of FEM simulations of skin biomechanics still presents some technical limitations that prevent this method from being a sufficiently reliable tool for use in the applications mentioned above. Developments are needed on various fronts in order to obtain realistic results, including the constitutive modeling of the skin, the evaluation of precise mechanical and microstructural parameters from experiments, and the automation of accurate FEM problem geometry of skin surgeries.

In this thesis all these aspects are addressed, with the twice objective of increasing the accuracy and the precision of mechanical simulations, and then using these simulations for providing quantitative and precise mechanical insights on the skin corrective surgeries. Specifically, three constitutive models have been considered: the isotropic Ogden model accounting for the no-compression behavior of thin membranes, the Generalized Structure Tensor (GST) model of Holzapfel *et al.* [80], and the DFD model of Li *et al.* [87]. The Ogden and DFD models have been further implemented in the commercial FE software ABAQUS. Then, a campaign of experimental test on excised human skin was conducted to determine the material parameters for structure-based constitutive models. In particular, to determine the microstructural parameters, a new algorithm capable of quantifying the 3D fiber orientation distribution from tomographic reconstruction of the collagen fibers has been developed. Finally, three surgical techniques, namely the Z-plasty, the triple Z-plasty, and the rhombic flap transposition, have been analyzed and optimized by employing the implemented constitutive models. This process was carried out by simulating multiple geometrical configurations, and comparing them in terms of key mechanical data, such as the maximum stress and the

global strain energy. To facilitate this operation, an algorithm dedicated to the generation of multiple FEM geometries of skin surgeries has been developed.

1.1 Thesis outline

The thesis is structured as follows:

- Chapter 2: the physiology and the biomechanics of the layers composing the human skin is introduced. Particular focus is set on the dermis, explaining the mechanical role of its embedded fibers, elastin and collagen, in regard to the hyperelastic, anisotropic and viscous behavior of the skin. The variability of the mechanical properties of the human skin are illustrated by means of the Langer lines, showing also their relation with the process of wound healing. Finally, the history of the Z-plasty is delineated, showing its practical use and the other modern techniques derived from it.
- Chapter 3: the continuum approach to the finite strain mechanics is introduced, with particular focus on the aspect regarding the formulation of constitutive models for incompressible materials in plane stress state. The models under consideration are the Ogden model, appropriately modified to account for the no-compression behavior of thin membranes, the GST model for nonsymmetrical fiber dispersion, and the DFD model based on the Lebedev quadrature rule. The Ogden model and the DFD model are then the implemented in the commercial FE software ABAQUS, and are validated with single elements uniaxial/biaxial/shear tests, and with benchmark tests from the literature.
- Chapter 4: a novel algorithm based on the 3D Discrete Fourier Transform (DFT) developed for quantifying the orientations distribution of fiber networks is presented. The algorithm is validated and calibrated with artificial 3D fiber dispersion images, and allows for an accurate identification of the microstructural parameters from tomographic reconstructions of the collagen fibers distribution in the skin.
- Chapter 5: the identification of the material parameters from experiments on human abdominal skin is addressed. The microstructural parameters are obtained employing the algorithm described in Chapter 4, while the mechanical parameters for the GST and DFD models are computed from biaxial tensile tests. The results are also analyzed in statistical terms, highlighting the differences and the similarities between the two models.
- Chapter 6: the FEM modeling of reconstructive skin surgeries is shown, ex-

plaining in details the choices adopted to achieve reliable simulations. An algorithm has been developed to automate the creation process of FE models geometries for different skin surgical techniques.

- Chapter 7: the analysis of the Z-plasty, the triple Z-plasty, and the rhombic flap transposition is addressed. Several mechanical aspects have been studied in order to understand the properties and the optimal conditions to achieve the best surgical performances of such techniques. The simulations have been performed in the commercial FE software ABAQUS using the implemented constitutive models.
- Chapter 8: the conclusions about the developed algorithms and the results achieved are discussed.

Chapter 2

Anatomy and Biomechanics of Human Skin

2.1 Skin Anatomy

The skin is the largest organ in the human body, accounting for about $15-20\%$ our total body weight, and has a surface area of approximately 1.5 to 2 square meters [117]. As a protective barrier, it safeguards internal organs against external aggressions like mechanical friction, UV radiation, bacteria, and harmful chemicals. The skin is also a sensory organ, equipped with a network of nerve endings that relay information about pressure, heat, stretching, and pain to the brain. Moreover, it plays an integral role in several vital bodily functions, such as regulating body temperature, synthesizing Vitamin D, and storing nutrients [1].

These diverse functions are performed within a skin layer about 1.5 to 4 millimeters thick, divided into three layers: ***epidermis***, ***dermis***, and ***hypodermis*** (Figure 2.1) [2]. All of these layers consist of different cells and other layer-specific apparatus, like blood vessels, glands, nerves, and hair follicles, embedded in an extracellular matrix (ECM). The structure of the skin is not uniform throughout the body, and it varies depending on factors such as age, gender, race, and health conditions [2]. The ECM occupies a significantly larger volume than the cells themselves, and makes up about 75% of the skin weight, thus playing a crucial role in conferring structure and strength.

The epidermis is the outermost and thinnest layer, protecting from mechanical friction and forming a barrier against microorganisms. Its thickness varies across different body parts, being thicker on the palms and soles (approximately 0.5 mm) and thinner elsewhere (about 0.08 mm) [1]. The epidermis mainly con-

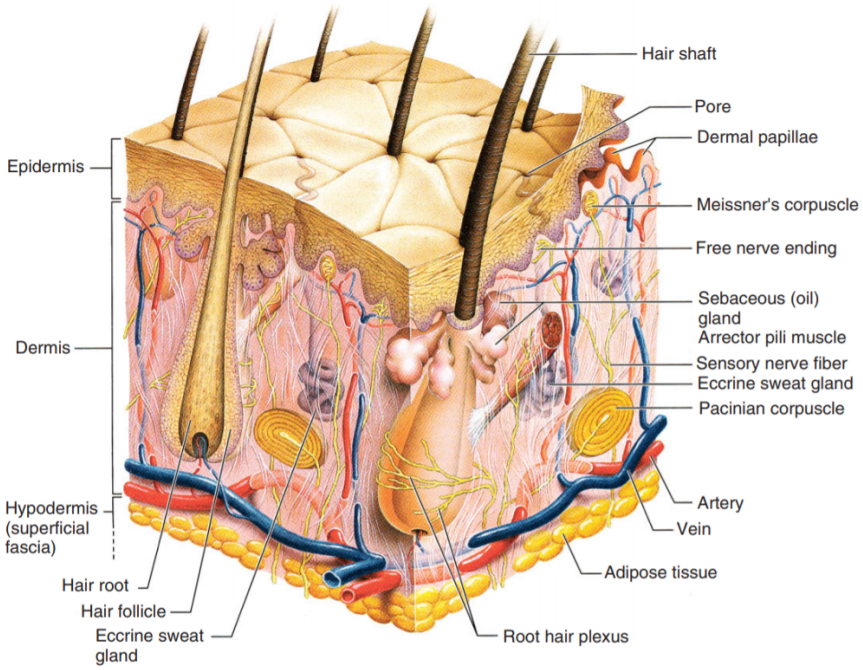

Figure 2.1: Schematic section of the skin including the three layers, epidermis, dermis, and hypodermis, with their internal apparatus. Figure from Marieb and Hoehn [118].

sists of keratinocytes, which produce keratin and keratohyalin, two proteins that provide structural strength to hair, nails, and skin [117]. The epidermis itself is subdivided into several layers: the *stratum germinativum* (contacting the dermis), followed by the *stratum spinosum*, *granulosum*, *lucidum* (present only in palms and soles), and the outermost *stratum corneum* (Figure 2.2). The epidermis does not contain blood vessels, so its cells receive nutrients through capillary diffusion from the vascularized dermis. This arrangement ensures that the layers with higher metabolic needs are closer to the dermis, where capillary diffusion is more effective [1]. The stratum germinativum, the deepest layer of the epidermis, is attached to the basal membrane separating the epidermis from the dermis. It contains stem cells that continuously produce new cells, pushing the older ones upwards. This layer also houses Merkel cells responsible for touch sensitivity and melanocytes, which produce melanin, providing skin color and protecting lower layers from harmful sun exposure. The unique fingerprints on our fingertips are

maintained by the structure of this layer and are genetically determined [118]. Above the stratum germinativum is the stratum spinosum, comprising 8 to 10 layers of mature keratinocytes. This layer gets its name from the spiny aspect of the cell-to-cell adherent bridge proteins called desmosomes which join cells attaching to cytoskeletal keratin. It also contains Langerhans cells, playing a role in immune response against microorganisms and skin surface cancers. In this layer, cells continue to divide, contributing to the skin thickness [1, 2]. Next is the stratum granulosum, where keratinocytes stop dividing and start producing large amounts of keratin, keratohyalin, and lipids, forming a hydrophobic barrier. As keratin fibers grow, cells flatten and their membranes become harder and less permeable. The cells eventually die due to the granulation of the keratohyalin inside the cytoplasm, creating a tough layer of dehydrated cells interconnected by keratin fibers and surrounded by keratohyalin [1]. The stratum lucidum, present only in palms and soles, is a layer of flattened cells located between the stratum granulosum and the stratum corneum. The stratum corneum is the thickest epidermal layer, consisting of 15-30 layers of keratinized cells. These cells are so tightly bound by the desmosomes proteins that they shed in scales rather than individually. The whole life-cycles of the cells from the stratum germinativum to the stratum corneum occurs in 28-50 days [1]. The outer surface of the skin is generally dry, inhibiting bacterial growth, and is further protected by sebaceous glands, placed in the dermis, that produce a lipid layer enhancing the antibacterial effect.

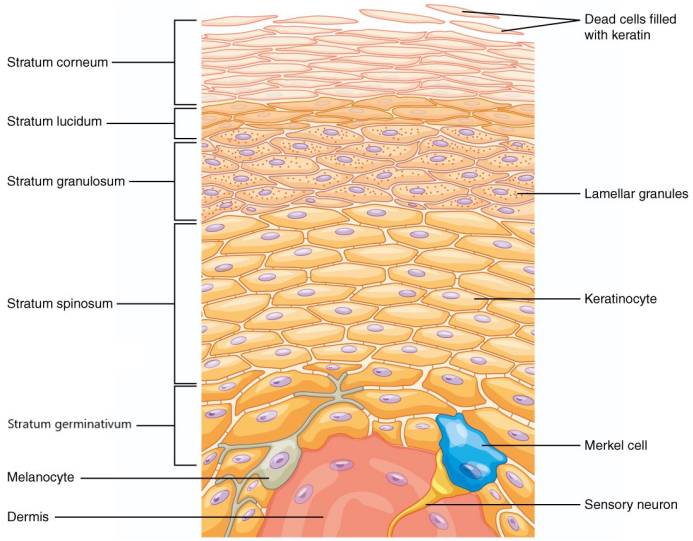

Figure 2.2: Anatomy of the epidermis. Figure from Betts *et al.* [119].

Beneath the epidermis lies the dermis, a dense layer that provides structural support and flexibility to the skin. It varies in thickness from about 0.6 mm in the eyelids to 3 mm in the back, palms, and soles, accounting about 90% of its total thickness [2]. The dermis is divided into two distinct parts, the superficial *papillary dermis* and the deeper *reticular dermis*, each with different fiber organization, cellular density, and patterns of nerves and blood vessels. The papillary dermis, right below the basal membrane of the epidermis, contains capillary blood vessels and sensory nerve endings [2]. It is named for its unique structure of papillae, small, undulated extensions that interlock with the crests of the epidermis, enhancing the bond between these two layers (Figure 2.3). The reticular dermis contains a variety of specialized cells and corpuscles, including nerve endings, sweat glands, sebaceous glands, hair follicles and their arrector pili muscles (see Figure 2.1). The nerve endings in the dermis are responsible for conveying sensations such as touch, pressure, pain, and temperature, making the skin a key sensory organ. Sweat glands play an essential role in thermoregulation, helping to control body temperature through the evaporation of sweat. Sebaceous glands secrete sebum, an oily substance that helps to keep the skin moisturized and provides a layer of protection against microbial invaders [1]. The dermis is also home to fibroblasts, the most prevalent cell lineage in the human dermis, responsible for continuously creating the macromolecules that form the ECM of the dermis [120]. The ECM has a fundamental role in human physiology not only for connecting cells to form tissues but also for cell-to-cell signals transfer, wounds healing, and mechanical strength [6, 121, 122].

The molecules of the dermis ECM can be divided into two major classes: proteoglycans (PGs), complex proteins formed by multiple glycosaminoglycans (GAGs) polysaccharides linked to a hyaluronate core chain, and fibrous proteins [121]. The PGs form an unstructured protein mass, frequently called ground substance or ground matrix, which accounts for 20% of the dry weight of the skin and 80% of the volume [123]. The PGs attract and retain water, thus making the ground substance the main responsible for the mechanical behavior in volumetric compression and at the onset of loading in tension. Running through this matrix are various protein fibers, including collagen, which provides great tensile strength, elastin for elasticity, and other microfibrillar components as fibronectin and laminins [121].

Collagen is the predominant component, representing 75% of the dry weight and $18-30$% of the volume of the dermis [2]. The basic structure of collagen is the tropocollagen, a triple helix tread composed of three amino acid α-chains (Figure 2.4(a)i). Each type of collagen is then identified by a Roman numeral, along

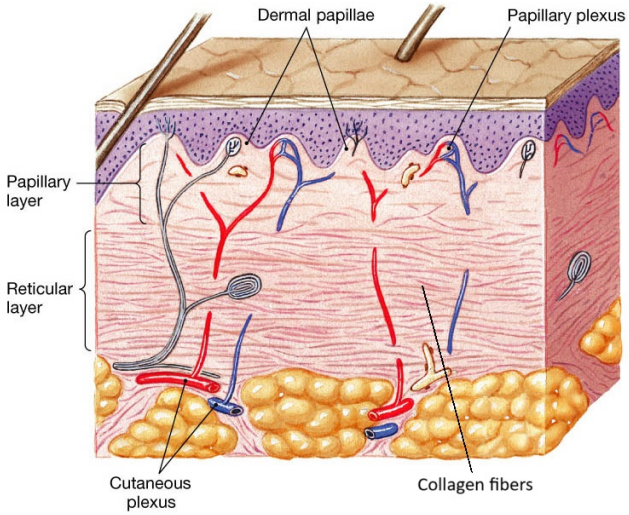

Figure 2.3: Anatomy of the dermis. Figure from Martini and Nath [1].

with the three classes of the helix, $\alpha 1$, $\alpha 2$, $\alpha 3$ [121]. For instance, the triple helix of collagen type I is formed by two $\alpha 1$(I) and one $\alpha 2$(I) chains, while the triple helix of collagen type III has three $\alpha 1$(III) chains [124]. In the human body, there are 28 different types of these helices found across various ECMs [122]. Within the dermis six different types of collagen are present: types I, III, IV, V, VI, and VII [124]. Of these, type I is the most prevalent, constituting 90% of the total collagen. In contrast, types III and V make up only 10% and 2%, respectively [122]. Despite being less abundant, other collagen types play significant roles, especially considering skin disorders related to genetic mutations in types IV and VII [122]. Tropocollagen has a period of 8.6 nm, a thickness of 1.6 nm and a total length of 300 nm. Tropocollagen threads are reciprocally cross-linked, combining in fibrils of roughly 50 nm diameter (Figure 2.4(a)iii). The threads are evenly spaced forming an overlapping region of about 67 nm, producing a striated effect visible with the electron microscope (Figure 2.4(b)). Again, fibrils combine themselves in the final configuration of undulated collagen fibers lamellae (Figure 2.4(a)v) [125].

In the papillary dermis, collagen fibers are generally thinner ($3-30$ μm) and are less densely packed and spatially organized. In contrast, the reticular dermis features a quasi-planar, dense distribution of larger collagen fibers ($10-40$ μm), becoming less dense in the deeper zones. Collagen fibers runs mainly parallel to the skin surface, with some statistical preference in direction within that plane and some deviations out of plane [123]. As it will be later discussed, the preferential

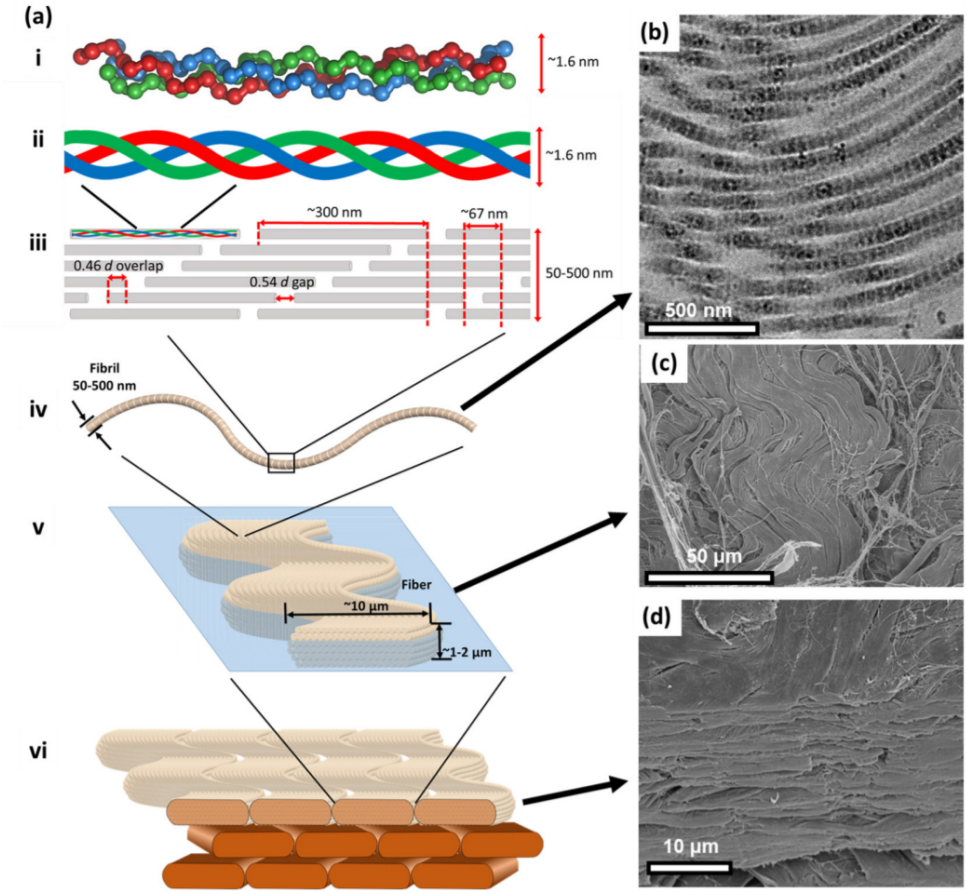

Figure 2.4: The full hierarchy of collagen in the dermis. (a) Collagen packing order: (i) and (ii) collagen triple helix, (iii) and (iv) collagen fibril, (v) collagen fiber and (vi) stacks of collagen fibers. (b) Curved collagen fibrils forming a fiber. (c) Parallel fibers in a single lamella of the skin (d) Cross-section of skin with multiple lamellae. Figure from Sherman *et al.* [125].

direction of the fibers over the human body is described by the Langer's lines. Due to this spatial arrangement the skin is often modeled as an in-plane reinforced material [123].

The other relevant fiber in the dermis ECM is the elastin, accounting for 4% of the skin dry weight [97], made of highly stretchable spring-like tropoelastin molecules combined in quadruplet by desmosine cross-links. Elastin interacts with collagen making a matrix that wraps and joints fibers together. Collagen and elastin are cross-linked to hyaluronic acid embedded in the ground substance amorphous material, a highly viscous, thixotropic semi-fluid [123].

The final skin layer is the hypodermis, which mainly consists of adipose tissue. It is composed of adipocytes, or fat cells, which primarily serves as an energy reserve, but also acts as shock absorber, protecting underlying muscles and bones from impacts. The fat in the subcutaneous layer helps to insulate the body, retaining heat in cold conditions and aiding in temperature regulation. The hypodermis is also rich in blood vessels, making it an effective route for drug delivery [1]. In babies, who require more protection against physical shocks, the subcutaneous fat layer is more pronounced than in adults. Starting from puberty, hormonal changes lead to different patterns of fat deposition in men and women. Men typically accumulate fat in the neck, arms, back, and buttocks, while women tend to accumulate it in the breasts, hips, and thighs. In adulthood, both genders are prone to increased fat accumulation in the abdominal region [1]. The hypodermis is significant in the mechanics of skin, anchoring it to underlying tissues like muscles and bones, yet allowing considerable movement at the joints [16]. That floating-like behavior allows the skin, under a mechanical point of view, to be treated as a free membrane for planar displacements.

2.2 Wound Healing and Potential Issues

Skin exhibits significant autonomous functional capabilities, responding directly and independently to injuries without the need for nervous or endocrine system intervention. This is especially evident in its response to extensive injuries, where it can initiate self-repair due to a high density of stem cells present in both the dermis and epidermis layers. The efficacy of healing is influenced by the size and nature of the injury and the risk of bacterial infection. Typically, thin, clean cuts heal more rapidly than abrasions, as they expose a smaller and more protected area to the environment.

The healing process of the skin is a complex phenomenon divided into four slightly overlapping successive stages: *hemostasis*, *inflammation*, *proliferation*, and

remodeling [1]. When a cut penetrates the dermis bleeding occurs, flushing out antigens and bacteria from the injury, and filling the gap between wound edges with blood. This represent the beginning of the hemostasis (Figure 2.5(a)), which takes place during the first hours after the injury [120]. Following hemostasis is the inflammation phase (Figure 2.5(b)), where blood coagulation partially restores the superficial integrity of the skin, forming a scab and a protective clot primarily composed of fibrin, a key protein in blood coagulation. This provisional scaffold allows the migration of cells to the injured site, such as macrophages, promoting the immune response against infiltrated pathogens [120].

The proliferation phase begins 24-48 hours after injury (Figure 2.5(c)). This phase is marked by the arrival of the first fibroblasts at the injury site, attracted by the macrophages present in the fibrin clot. Once in the clot, fibroblasts begin to proliferate and produce various components of the ECM, including collagen type III, hyaluronic acid, and fibronectin [120]. This activity transforms the fibrin clot into a new matrix of connective tissue. After about a week into the proliferation stage, several critical processes unfold simultaneously. One key process is re-epithelialization, which involves the formation of a new epidermal layer. During this phase, keratinocytes and fibroblasts are stimulated to migrate from the edge of the wound and proliferate within the newly formed ECM [5]. This regeneration is further aided by stem cells from the hair follicle bulge, which differentiate into epidermal progenitor cells, contributing significantly to the repair of the epidermis [120]. In parallel with re-epithelialization, two other essential processes occur: neovascularization, involving the formation of new blood vessels, and the formation of granulation tissue [120]. These processes are integral to re-establishing the vascular network, essential for restoring blood flow, and creating the necessary tissue for effectively closing the wound. While these processes collectively facilitate the reconstruction of the basement membrane and various epidermal layers, it is important to note that certain structures, such as hair follicles and other skin appendages, typically do not regenerate [120].

As the healing progresses, the clot gradually resolves, and by the end of the proliferation phase, the surface scab detaches. The final stage, remodeling (Figure 2.5(d)), begins about 2–3 weeks after injury and can lasts for more than two years [120]. It involves the contraction and reorganization of granulation tissue and fiber structure, leading to the development of a mature scar. Fibroblasts differentiate into myofibroblasts, which, thanks to their high contractile capacity, cause wound contraction [2]. Also, collagen type III is replaced by collagen type I, which has a much higher tensile strength, producing a more cross-linked matrix [7, 120, 122]. The scar, which can be depressed, gradually elevates to the

level of surrounding skin, sometimes resulting in a raised scar [1]. Although skin continuity is restored, the scar tissue has not the same properties of the healthy skin. Indeed, wound strength increase during the healing process, but it restores only about 80% the original skin strength within 2 years [5, 126].

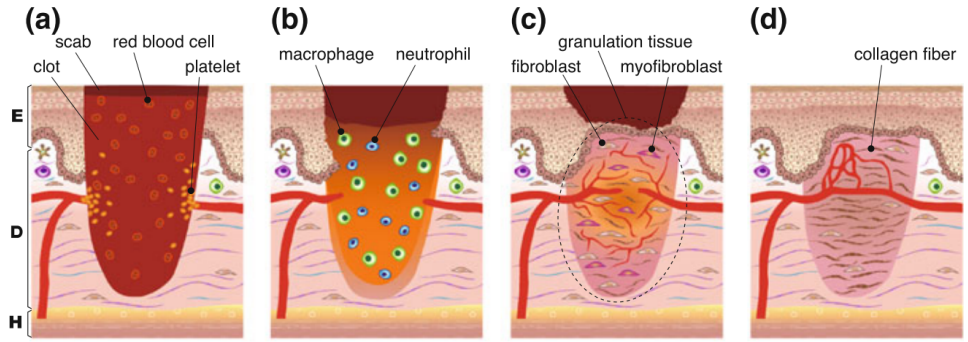

Figure 2.5: Wound healing phases. (a) hemostasis, (b) inflammation, (c) proliferation and (d) remodeling. Figure from Kawasumi *et al.* [5].

This multiphase process can be affected by various biological factors, including age, nutrition, and overall health [4, 7, 127]. Younger individuals typically experience more efficient healing due to higher cellular activity, but in elderly ones the scarring can be of higher quality and less visible [7]. Conversely, factors like poor nutrition, smoking, and chronic diseases can significantly slow down the healing process [9, 10]. Additionally, the environment in which healing occurs, including humidity and temperature, can impact the rate and efficacy of the process [11], underlining the importance of appropriate wound care.

Beside, mechanical factors also have a significant impact on the wound healing process and, consequently, on the appearance of the resulting scar. Reduced blood flow from either constant pressure or tension within the skin dermis lead to complications like pressure ulcers [15] or distal necrosis in skin flaps [18, 20, 128]. High tension across wounds often results in wider and more noticeable scars [19], that might develop into an hypertrophic scar if the stress is excessive. This deviation initiates between 3 and 5 weeks after injury during the development of the granulation tissue. Whereas in normal scars the collagen network is well organized and aligned across the line of the wound (Figure 2.6(b)), in hypertrophic scars it is randomly arranged and produced in excess (Figure 2.6(c)-(d)), causing the scar to bulge [4]. This type of scar is also common in large burns scars [20], which in addition tend to contract and impede body movements [127]. Therefore, proper stress management across the wound, using devices like stress

shields [129] for instance, is of primary importance to foster wound healing, and to promoting good quality scarring.

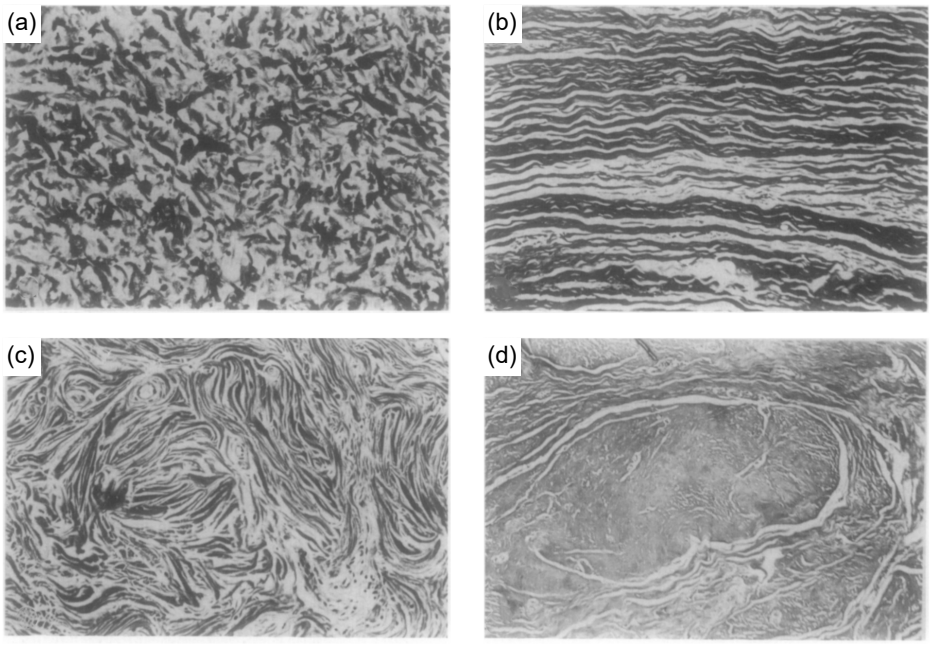

Figure 2.6: Collagen organization in normal skin and scar tissue. Histological sections of the reticular dermis of (a) healthy skin, (b) normal scar, and (c)-(d) hypertrophic scar. In (c) and (d) are shown a whorl-like arrangement and a nodular pattern, respectively. Figure from Linares [4]

2.3 Skin Lines

Due to the great variability of the human body topology, the skin has not uniform properties, but changes from point to point in both natural tension and collagen fiber organization. Understanding these properties is of paramount importance in the surgical field in order to select the best incisions that minimize the tension across the wound and reduce healing complications. To this end, various authors tried to define a map of ideal incision lines over the human body [130].

The first analysis was conducted by the Viennese professor Karl Langer in 1861. Upon the earlier observation of the doctor Guillaume Dupuytren in 1834,

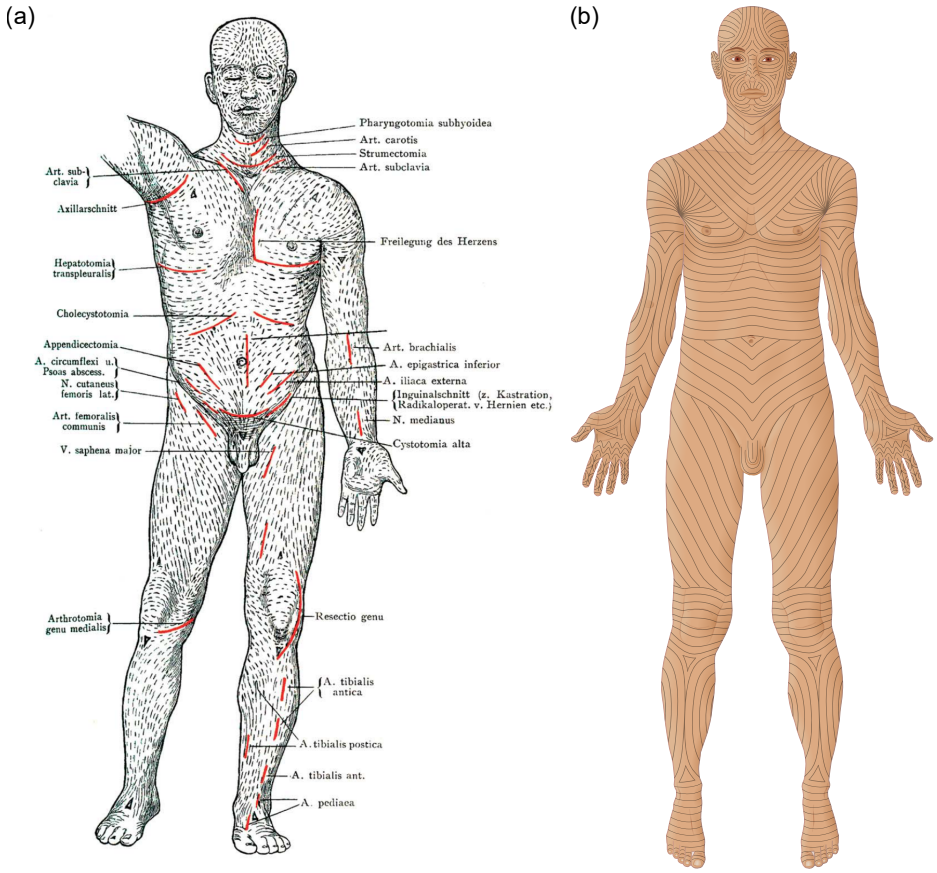

Figure 2.7: Representation of the Langer's lines. (a) Clefts over the human body generated by stabbing the skin with a round awl (Figure from Carmichael [130]), and (b) Langer's lines following the direction of the clefts (Figure adapted from Goran [131]).

who discovered that puncturing skin with a round stilet produces linear clefts [130], Langer systematically repeated the process on human cadavers, observing that the orientation of the clefts varies across different locations on the body (Figure 2.7(a)). He also noted that the overall pattern of the clefts is the same among all the cadavers he studied. Further analyzing the clefts under the microscope he discovered that their orientation follows the direction of what we now know to be that of the collagen fibers of the dermis [132]. Thus, sketching lines that follows the orientation of the clefts produces a map of the average collagen fiber orientation on the human body (Figure 2.7(b)). These lines are best known as *Langer's lines* or *cleavage lines* [133].

In an effort to better understand skin tensions, Langer conducted further investigations on cadavers by cutting circular skin flaps of 3 cm diameter to observe deformation of both the central circular portion and the external wound. In areas where skin tension is uniform the outer wound would open axisymmetrically while the central skin flap shrinks remaining round (Figure 2.8(b)). Conversely, in areas where skin tensions are not evenly distributed, the central round flap becomes elliptical, with its major axis perpendicular to the direction of minor tension (Figure 2.8(c)). Using this procedure, Langer was able to consistently describe the direction of skin tension on cadavers in a natural posture. Nonetheless, it is important to note that Langer's work, though significant, described skin tension in *rigor mortis*. As a result, these findings were not directly applicable to surgical practices on living patients. The skin tension during *rigor mortis* bears no relation to the optimal lines for making incisions in living patients to achieve the best possible surgical outcomes [134].

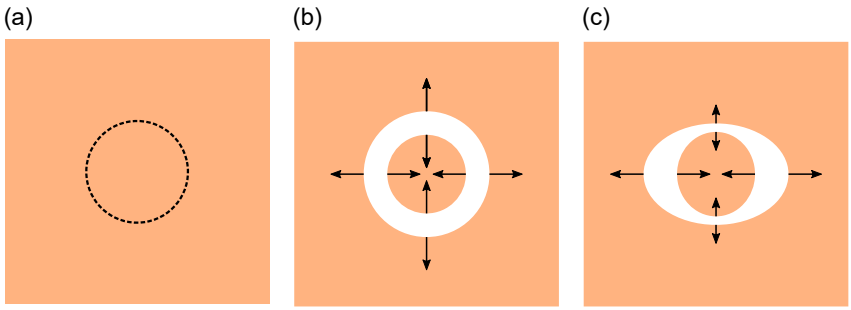

Figure 2.8: Langer's circular cuts. (a) Edge of the circular cut (dashed line), and deformations of the external wound and central round flap in presence of a uniform tension (b), and a mainly horizontal tension (c).

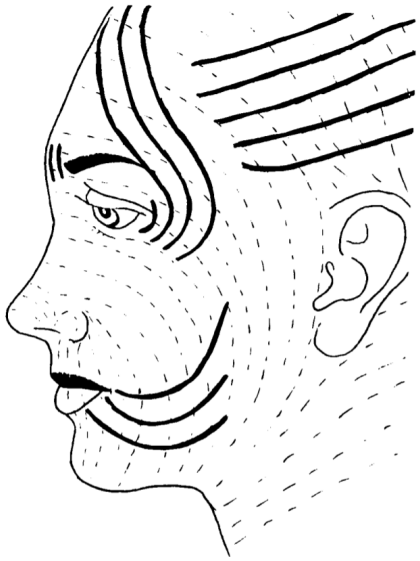

Figure 2.9: Facial Relaxed Skin Tension Lines (RSTL) (dotted lines) and Langer's lines (solid lines). Figure from Borges and Alexander [29].

An extensive analysis on skin tension in living conditions was later conducted by Borges in 1962, who first introduced the concept of Relaxed Skin Tension Lines (RSTL) as the optimal lines to follow for surgical incisions [29]. The RSTL describe the direction of the maximum tension of the skin in a relaxed and natural position. Indeed, skin tension can be temporarily modified by movements of the underlying muscles and joints, but when the body stands still in a relaxed position the RSTL are always the same and constant among individuals, unless some pathological distortions are present [29]. Therefore they can be used as elective lines to make decisions about surgical incisions [133]. When cuts are made parallel to the RSTL, they tend to remain narrow and spindle-shaped, requiring minimal force to close and resulting in a shorter wound healing process and more aesthetically pleasing scar. In contrast, incisions made obliquely to the RSTL assume an undulated shape that aligns with the direction of maximum tension, leading to non-optimal results. The least favorable scenario occurs when incisions are made at right angles to the RSTL, as the wound edges tend to open up widely, resulting in more visible scars. The primary method to identify RSTL is by pinching the skin and observing the direction of the furrows formed. Pinching at right angles to the RSTL creates linear and extended ridges, whereas inclined pinches result in distorted furrows. These lines are significantly different from the Langer lines, underlining the uncoupling

of the orientation of the collagen fibers from the direction of the skin tension. This is particularly evident on the face, in which in some regions the RSTL run perpendicular to the Langer lines (Figure 2.9).

2.4 Skin Mechanics

Since the early 60s, thanks to the development and diffusion of new technologies such as the Scanning Electron Microscope (SEM), various researchers performed uniaxial tensile tests on excised skin while capturing images of the microstructure. The scope was to understand the mechanical role of the constituents of the dermis ECM: ground substance or ground matrix, elastin and collagen. The experiments highlighted a highly viscoelastic nonlinear behavior that can be divided into three distinct phases (Figure 2.10(a)).

In the first phase, called *toe region*, the tissue undergoes large deformations at low stresses. The response is mainly isotropic with low stiffness ($\sim$ 5 kPa) [135, 136], and it is influenced by the ground matrix and the elastin. The collagen fiber network, interwoven with the elastin, is still crimped and does not participate significantly to the global response [65, 136]. As the deformation increases, the collagen fibers begin to uncrimp and align with the direction of the applied force, starting to bear part of the load [66]. This phase, called *heel region*, falls within the typical physiological range, is highly nonlinear, and it is characterized by a rapid increase in stiffness. This behavior allows the tissue to accommodate wide body movements, but remaining in a elastic regime. Then, once all the fibers are fully recruited and straightened toward the load, the tissue enters in the third phase, the *linear region*, in which the mechanical response is almost linear and governed by the collagen fibers [65, 66, 136]. As the the material approaches its ultimate strength, collagen fibrils start to delaminate, and they eventually break leading to the failure of the tissue [64]. However, if the load is reversed before the fiber rupture, the tissue primarily returns to its original state due to the recoil of the elastin component [20, 137], but following an unloading path less stiff than the loading one. During the complete cycle, some energy is dissipated, mainly due to the viscosity of the ground matrix [67]. If the loading-unloading cycle is repeated multiple times, the path softens, until a steady mechanical response is reached, leaving still some hysteretic damping typical of viscoelasticity [75] (Figure 2.10(b)). This procedure, called *preconditioning* [60], requires 3 to 10 cycles, and it is essential to guarantee the repeatability of the mechanical tests. This behavior is attributed to several factors, such as the stabilization of the collagen fibers orientation, the extrusion of water, and the break of collagen fibrils and

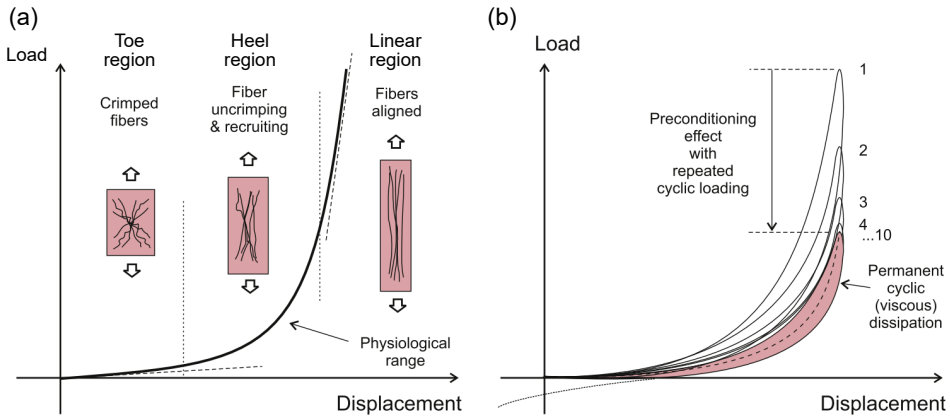

Figure 2.10: Skin mechanical behavior. (a) The response under uniaxial tension characterized by the three distinct regions: toe, heel, and linear. (b) Effect of the viscosity on the cyclic uniaxial loading behavior. After few preconditioning cycles the cycles stabilizes to a constant hysteretic damping cycle. Figure from Benítez and Montáns [123]

proteoglycans [138, 139]. Due to the viscosity, the rate of deformation also influences the mechanical response, which produces stiffer stress-strain curves for higher strain rates [140, 141]. Typically, tensile tests are performed at strain rates of $\sim 1\%\ s^{-1}$ to replicate a quasi-static loading condition [125, 141].

Uniaxial tests were extensively used to analyze the variability of the mechanical properties of the skin in relation to biological factors like, for instance, sex, age, and anatomical region [142, 143]. Common mechanical properties computed from the stress-strain curve are the tangent Young modules of the toe and linear regions, the ultimate tensile stress, and the failure stretch [98, 142, 144]. It is also important to note that the skin mechanical behavior is largely determined by the orientation of the collagen fibers, and that the non-uniform distribution of the fibers translates in an anisotropic tissue response. Accordingly, the direction of the uniaxial test relative to the Langer lines is the main factor influencing the uniaxial mechanical response. When tests are performed parallel to the Langer lines, the aligned collagen fibers efficiently bear the load, exhibiting a stiffer stress-strain curve. On the other hand, when the skin is stretched perpendicular to the Langer lines, the collagen fibers are not optimally aligned to bear the load, resulting in a softer response [63, 145, 146] (Figure 2.11).

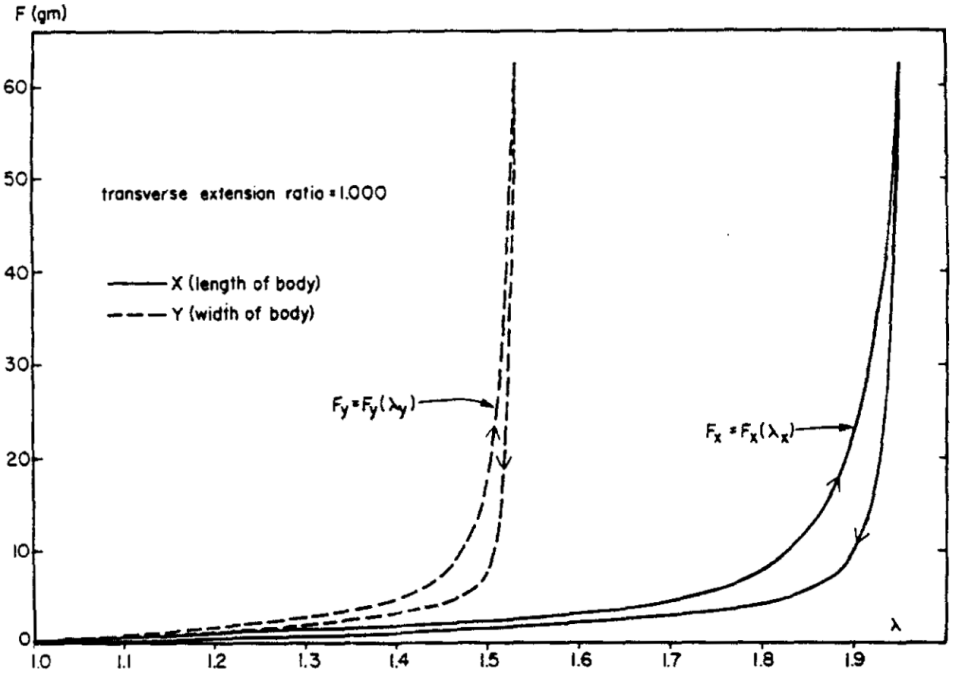

Figure 2.11: Different uniaxial tensile response of rabbit skin along two perpendicular directions. Horizontal axis refers to the uniaxial specimen stretch in the direction of the load, while the vertical axis indicates the force in grams. Figure from Lanir and Fung [60].

2.5 Skin Corrective Surgeries

2.5.1 History of Z-Plasty

In 1837, William E. Horner, a surgeon at the Philadelphia Hospital, Blockley, and Professor of Anatomy at the University of Pennsylvania, documented a clinical case of a 42-year-old laborer who suffered from ectropion of the lower right eyelid induced by the contraction of a burn scar [30]. This condition led to the exposure and inflammation of the conjunctiva, characterized by the formation of scabs and thickening, causing both pain and discomfort. His condition was also worsened by the dusty environment of his working place, hindering his ability to work effectively. Horner addressed this issue with a minor surgical procedure near the affected eye. Essentially, the technique involved transposing a triangular skin flap from the cheek below the eye to elevate the sagging eyelid. This surgical intervention was effective and yielded almost immediate improvement in the patient's condition.

Later in 1854 Denonvilliers, an European surgeon from Paris, unaware of the Horner's report, operated the same disease using a similar surgical procedure. He performed two incisions on the external side of the eye above and below the lids, forming a V-shaped flap including the lateral canthus. Afterward, he performed a third incision below the eyebrow, meeting with the upper eyelid incision, so as to form a second triangular flap opposed to the first one (Figure 2.12(a)). Then, after cutaneous delamination, he transposed the two triangular flaps, thus raising the the lateral canthus and correcting the ectropion (Figure 2.12(b)). This procedure is similar to that proposed by Horner, but in Denonvilliers' case the lower eyelid is raised instead of being pushed from below. Such surgical procedure remained

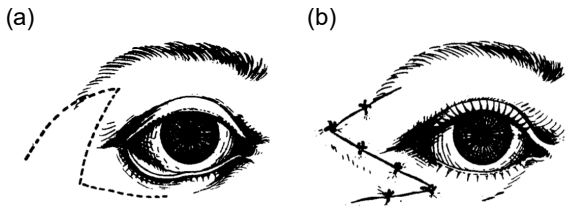

Figure 2.12: Denonvilliers operation. (a) Incision lines forming two opposite triangular skin flaps, one including the lateral canthus, and the other including part of the skin below the eyebrow. (b) Appearance of the operation after flaps transposition. Figure from Borges and Gibson [31].

quite unchanged for several decades, until Berger in 1904 exploited its properties for a different application. Berger envisioned the transposition of triangular flaps as a method for rearranging the tissue in order to achieve a distension along a specific line. Then, he innovatively applied the procedure to extend a constricted axilla resulting from a burn scar [147], as depicted in Figure 2.13. Around the same time, McCurdy, a surgeon from Pittsburgh, Pennsylvania, independently discovered a similar use for the transposed triangular flaps, arriving at the same conclusion as Berger [32]. He gradually developed the idea of triangular flaps starting from simple skin rearrangement sketches, suggesting that he was likely unaware of the works of previous authors on this subject [31]. However, McCurdy was the first to coin the term "*Z-plasty*" for this procedure [32], a name that is still used in medical practice. However, this nomenclature was not universally accepted. Notably, Limberg, a renowned surgeon in this field, preferred the term "*transposed triangular flaps*" in his publications [35]. Limberg argued that the term Z-plasty was technically incorrect, as the central limb in the letter "Z" is typically longer than the side arms, whereas in the surgery, all three limbs should be of equal length. Despite his correct observation, the term "*Z-plasty*" has remained popular due to its conciseness and clear depiction of the surgical technique, avoiding any confusion. To date, it is widely used in medical practice and encompasses a broad spectrum of geometrical variations [31].

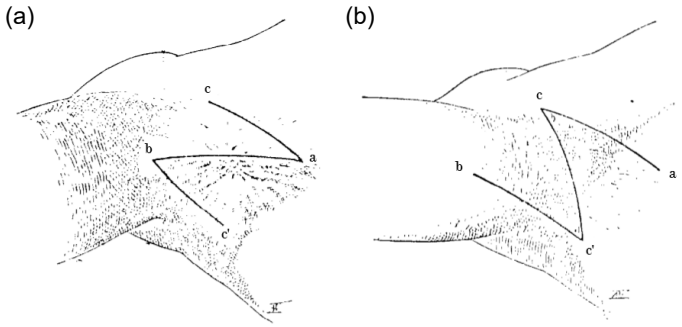

Figure 2.13: Berger operation. Incision lines before (a) and after (b) skin flaps transposition. Note that points *a* and *b* after the transposition are spaced apart, providing release to the contracture. Figure adapted from Borges and Gibson [31].

In the works of McCurdy [32] and Berger [147] several clinical cases are reported, showing the extreme effectiveness of the Z-plasty. Nonetheless, these works lack of extensive description of the procedure and its principles. Specifically, no clear guidelines were established for determining when Z-plasty was appropriate, nor was provided a geometric theory for achieving optimal results. This lack of detailed guidance led to considerable confusion within the medical community, especially as the popularity of Z-plasty grew. To address this ambiguity, Davis [148] made a significant contribution by elucidating the fundamental principles of Z-plasty with a focus on geometric planning. He not only imparted a more scientific aspect to the technique but also delved into practical medical aspects such as anesthesia, skin preparation, and post-operative care. Borges also considerably contributed to this topic [29]. His comprehensive description enabled surgeons to gain a better understanding of Z-plasty, thereby improving their ability to apply the technique effectively and appropriately in their surgical practices.

2.5.2 Modern Z-Plasty

The Z-plasty technique, despite its historical roots, remains widely used today due to its versatility and simplicity. It has not undergone significant changes since its initial description by Berger, and the basic method is now well-established, with detailed descriptions available in most surgical handbooks [16].

The traditional Z-plasty consists of three incisions of equal length. The central incision is aligned along the axis of the contracted scar, which could be a linear scar or an extended burn scar (Figure 2.14(a)). Alternatively, a linear scar may be completely excised, with the resulting fusiform defect serving as the central incision (Figure 2.14(b)). Two additional incisions start from either end of the central line, extending in opposite directions at equal angles of 60° to the central line. This configuration forms two triangular flaps. When these flaps are delaminated from the subcutaneous tissues, they can be raised and transposed to create a new configuration resembling an inverted Z, where the central line becomes perpendicular to the original incision. This procedure increases the distance between the two ends of the initial scar, providing immediate relief in cases where the scar is significantly contracted [36]. Adjusting the angles of the lateral limbs, which can vary between 20° and 60°, allows for different levels of elongation [50, 148]. Generally, larger angles result in greater elongation, offering surgeons a range of geometric options to address specific needs.

The technique can be adapted for areas with varying skin elasticity by creating unequal triangular flaps. This is particularly useful for lengthening extended burn

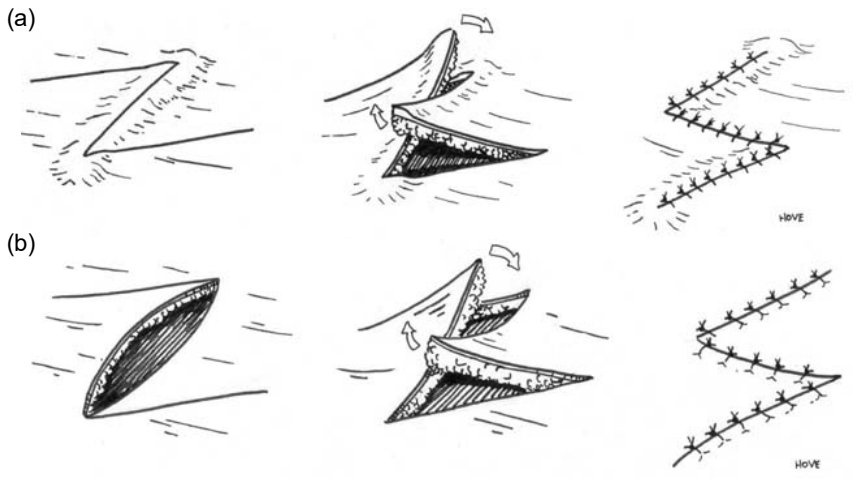

Figure 2.14: Traditional Z-plasty procedure. (a) Z-plasty steps applied on a contracted scar and, (b) same procedure applied after removal of the undesired scar tissue. Figures from Hove *et al.* [36].

scars. By borrowing a smaller flap from normal skin and inserting it into a larger incision on the scar side, the altered tissue can be elongated, also camouflaging the edge of the scar (Figure 2.15). The length gained on the scar side is directly proportional to the width of the triangular flap on the normal side [36], allowing for precise adjustments in response to specific surgical requirements.

Figure 2.15: Unequal Z-plasty procedure applied on an extended burn scar. The smaller healthy skin flap inserted in the burn scar tissue homogenizes the mechanical performances of the interested skin region. Figures from Hove *et al.* [36].

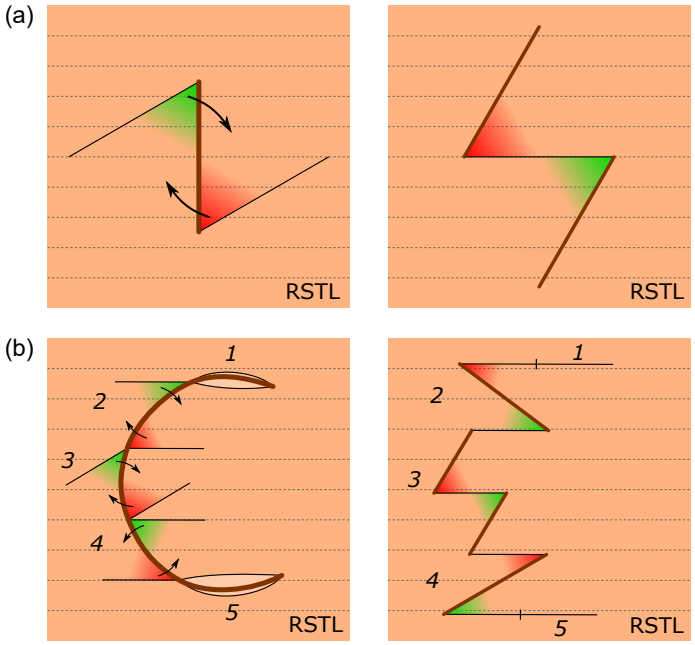

Figure 2.16: Realignment of scar (thick brown line) to the RSTL. (a) Realignment of a scar perpendicular to the RSTL using a 60° Z-plasty. (b) Realignment of a circular scar by segments: *1* and *5* fusiform excisions and direct closure, *2* and *4* low angle Z-plasties, and *3* classical 60° Z-plasty [29].

The Z-plasty can also be used to realign scars with the relaxed skin tension lines RSTL. This application was proposed by Borges and Alexander [29], who greatly contributed to the development of this topic through his work in defining RSTL. As previously discussed in Section 2.2, tension across a wound is a major factor leading to hypertrophic scarring. Incisions that lie at various angles to the RSTL, which follow the direction of maximum skin tension, tend to become wider and more unaesthetic. Therefore, Z-plasties are effectively used to realign old and hypertrophic scars with the RSTL, thereby improving the overall aesthetic outcome [29]. The choice of angle for the lateral limbs of the Z-plasty is critical and should be based on the orientation of the scar relative to the RSTL. For scars perpendicular to the RSTL, the classic configuration of equal 60° angles is ideal, aligning the central limb horizontally (Figure 2.16(a)). This procedure is counterintuitive, as a longer wound is generated, including two limbs slanted to the RSTL. However, since most of the force to keep the wound closed is concentrate

in the central limb, the final arrangement generally yields a better cosmetic result than the original vertical scar [29]. In cases where a scar is not perpendicular but lies at a generic angle to the RSTL, employing two or more Z-plasties is advantageous. Moreover, multiple Z-plasties can be concatenated to realign any scar shape to the RSTL, as demonstrated with a circular scar in Figure 2.16(b) [29]. The main benefit of using multiple Z-plasties is that they break up one long scar into two smaller segments less inclined to the RSTL. Additionally, these segments are separated by healthy tissues and connected only by scars that follow the RSTL, leading to an improved overall cosmetic result [29].

2.5.3 Other Types of Scar Relaxation Surgeries

Surgeons have explored various modifications and combinations of Z-plasty to expand its potential to a wider spectrum of contracted scar types. This led to the invention of new surgeries based on the concept of transposing skin flaps.

One of the simplest yet effective modifications is the series of Z-plasties linked along the central limb, first introduced by Limberg [33]. This approach is particularly useful for large scars where a single Z-plasty would result in excessively large flaps. Additionally, as each lengthening along the central limb results in contraction in the transverse direction, employing multiple Z-plasties distributes the shortening across different transverse axes.

While this configuration increases the versatility of the Z-plasty, it does not fundamentally alter its configuration. To further evolve the technique, Limberg [149] introduced a *four-flaps plasty* (Figure 2.17(a)), which involves adding two extra limbs to the classic Z-plasty. This method is particularly effective for releasing severe scar contractures in areas like the anterior and lateral neck. The technique can be further expanded by adding more limbs, creating a *six-flaps plasty* or more [36].

Additionally, Limberg [35] developed a different approach called the *three-flaps plasty* or *square flap method*, which is distinct from Z-plasty. It consists of one square flap and two triangular flaps, each made from segments of equal length (Figure 2.17(b)). This method was designed to achieve greater scar lengthening than what is possible with a Z-plasty. Theoretically, based on simple trigonometrical calculations, the three-flaps plasty can attain a theoretical length gain of 180% compared to the 73% of a standard 60° Z-plasty [150]. However, increased lengthening also means more lateral shortening, leading Hyakusoku and Fumiiri [150] to propose a variation that facilitates the advancement of the square flap.

Every surgical operation involving flap rotation can lead to out-of-plane dis-

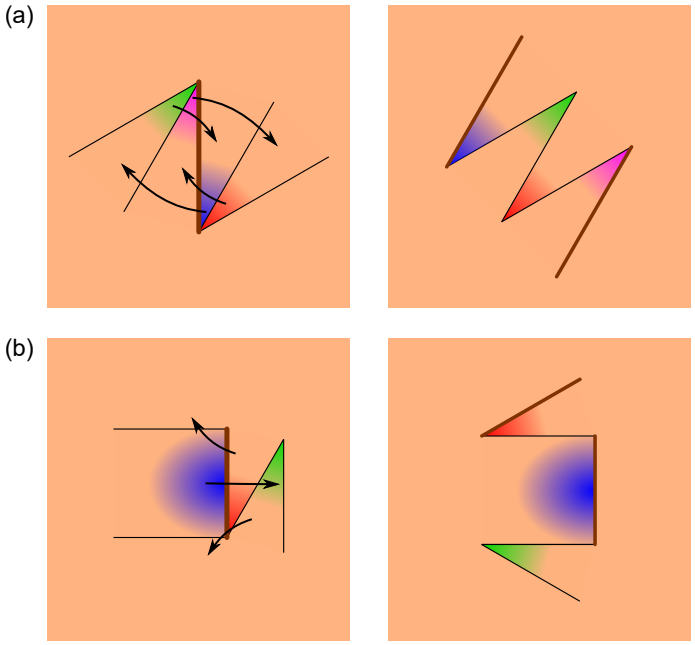

Figure 2.17: Surgical techniques inspired from the Z-plasty. (a) The four-flaps plasty, and (b) the three-flaps plasty or square flap method. Thick brown line represents the scar.

placements, resulting in the formation of bumps in region under considerable compression stresses due to the membrane buckling of the skin. This phenomenon is well known in the medical society as "dog ear" formation [43, 45, 151]. A study by Roggendorf [152] demonstrated that a Z-plasty performed on pig skin does not lie flat. Instead, it forms dog ears close to the two ends of the suture, as illustrated in Figure 2.18(a). Roggendorf noted that the skin excess extending beyond the Z-plasty, manifesting as an elevation, does not contribute to the planimetric elongation effect and could be removed. Based on this observation, he developed a variation of the Z-plasty, called *planimetric Z-plasty*, where the excess skin is excised before suturing. The resulting shape is an inverted Z with the horizontal limb being about half the length of the lateral ones (Figure 2.18(b)).

Over the years, additional techniques have been developed as alternatives to Z-plasty, particularly for achieving better outcomes in severe contracture releases. Some of these techniques can achieve extreme elongations, and have been specifically developed for treating scars in elbows, axillae and neck. Some of the most

common are the *V-Y plasty* [153], the *V-W plasty* [37], and the *seven-flap plasty* [38] (Figure 2.19).

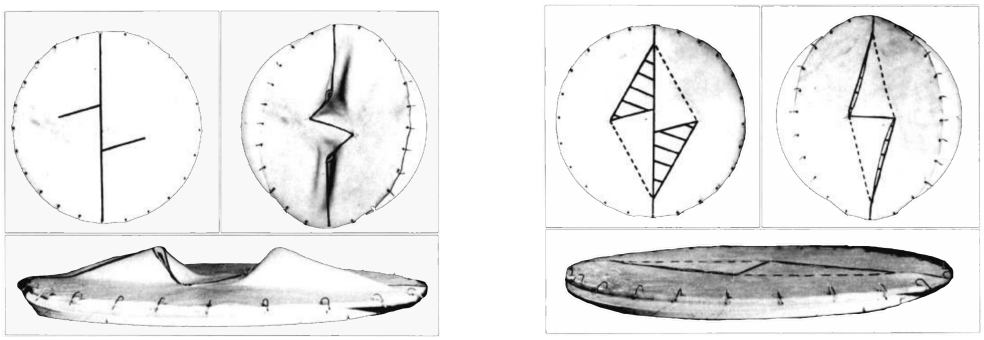

(a) **(b)**

Figure 2.18: Roggendorf's Z-plasties tests on pig skin. (a) Traditional Z-plasty, and (b) planimetric Z-plasty. In (a) are clearly visible the so called "dog ears" close to the tips of the suture. Figures adapted from Roggendorf [152]

2.5.4 Defect Closure Surgeries

Other useful application of skin flaps rearrangement concerns the closure of large skin defects. These operations are applied when a direct closure of the primary defect would lead to excessive tension across the sutured wound. In such cases skin flaps transpositions help in redistributing the deformation over a wider skin area, thus reducing the average stress across the wound. Common techniques are the *rhombic flap transposition* and the *rotation flap* [16] (Figure 2.20). As for the Z-plasty and its derivative surgeries, these techniques offer some room for geometrical adaptation, in order to achieve better cosmetic results. In the rhombic flap transposition, for instance, the two angles defining the rhombic flap (shown in red and green in Figure 2.20(a)) can be increased or reduced depending on the surround skin availability and the local direction of the RSTL [154]. Although any geometrically admissible configuration of the flap can be chosen, specific combinations of angles have been studied and documented in the surgical literature, each with its advantages and disadvantages [16]. The two most famous are the Limberg flap [149] and the Dufourmentel flap [155], shown in Figure 2.20(a).

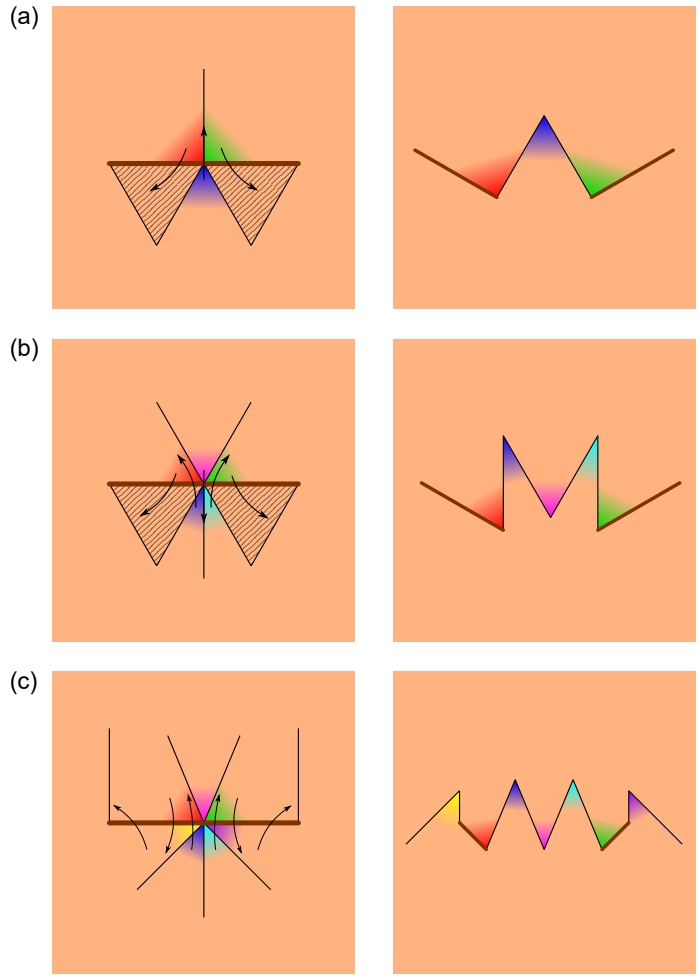

Figure 2.19: Alternative surgical techniques developed for treating contracted scars on body joints. (a) The V-Y plasty [153], (b) the V-W plasty [37], and (c) the seven-flap plasty [38]. Thick brown line represents the scar. Dashed areas represent the tissue to be discarded.

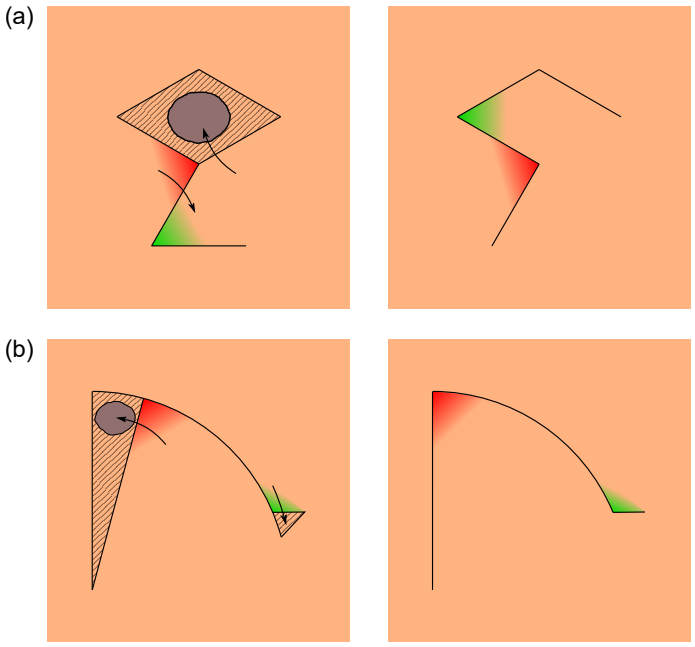

Figure 2.20: Defect closure plasties. (a) The rhombic flap transposition according to the Dufourmentel design [155], and (b) the rotation flap. Dashed areas represent the tissue to be discarded.

Chapter 3

Mechanical Modeling for Soft Fibrous Tissues

Physical solids are composed of atoms and molecules, which themselves are made up of subatomic particles. Ideally, to thoroughly analyze the global mechanical behavior of these objects, one should consider the microscopic interactions between their constituent particles. However, such a microscopic approach is exceedingly complex and impractical for engineering applications. Instead, continuum mechanics offers a successful way to describe the physical phenomena of solid objects without accounting for their individual microstructural components. This approach essentially replaces the overwhelming number of individual particles with a few average quantities, simplifying the model from a physical standpoint [156].

Applying this approach, the mechanical behavior of soft biological fibrous tissues, including the skin, can be precisely analyzed by deducing a few material parameters from experimental tests on small representative material samples, circumventing the need to understand the intricate interactions between individual elastin and collagen fibers composing the microstructure. The material is then treated as a homogeneous continuum body with uniform properties across its domain. To capture the highly nonlinear behavior, the problem is addressed by means of the theory of continuum mechanics at finite strain. Unlike small strain theory, which assumes deformations are infinitesimal and linear, finite strain theory accounts for large, nonlinear deformations, providing a more accurate and comprehensive understanding of the behavior of soft materials under real-world conditions. This theory is largely used to simulate complex biomechanical problems.

In this chapter the finite strain continuum mechanics is first addressed. First,

the fundamentals of kinematics are introduced, which lay the groundwork for understanding how material points move, deform, and interact under the influence of external forces. This includes a thorough description of strain measures, deformation gradients, and the concept of stress in the context of finite deformations. Particular focus is posed on the formulation of planar problems as a simplified approach to analyze skin mechanics.

Subsequently, the chapter moves into the formulation of constitutive models for hyperelastic materials. These models describe the stress-strain relationships for materials undergoing large deformations and form the backbone of finite strain analysis. The models therein discussed include the Ogden model accounting for the no-compression response typical of soft membranes undergoing wrinkling, the Generalized Structure Tensor (GST) model accounting for non-symmetrical fiber dispersions, and the Discrete Fiber Dispersion (DFD) model. These models have been implemented into the commercial Finite Element software ABAQUS, and have been validated with analytical solutions and benchmark FEM analyses.

3.1 Finite Strain Continuum Mechanics

3.1.1 Kinematics

A material object can be represented by a body $\mathcal{B}$ having a continuous distribution of matter in space and time. The body $\mathcal{B}$ moves in the Euclidean space, defined by the orthonormal basis vectors $\{\mathbf{E}_1, \mathbf{E}_2, \mathbf{E}_3\}$, occupying a continuous sequence of geometrical regions, called **configurations**, during time. We define the **reference** (or **undeformed**) **configuration** the region Ω occupied by $\mathcal{B}$ at the initial time t_0. The other regions ω occupied by $\mathcal{B}$ at time t are named **current** (or **deformed**) **configurations**. Accordingly, a material particle $\mathsf{P} \in \mathcal{B}$ occupying the point X at the time t_0 is identified by the **referential position** vector $\mathbf{X} \in \Omega$ relative to the origin point O. During the motion, the particle moves to the point x at time t, represented by the **current position** vector $\mathbf{x} \in \omega$, according to a biunivocal vector field function

$$\mathbf{x} = \chi(\mathbf{X}, t), \quad \forall \mathbf{X} \in \Omega, \tag{3.1}$$

called **motion** of the body $\mathcal{B}$ (Figure 3.1). The function $\chi(\mathbf{X}, t)$ is assumed to be continuous and differentiable with respect to both the position $\mathbf{X}$ and time t. The succession of the positions $\mathbf{x}$ during time represents the trajectory of the particle P in the Euclidean space. Since the motion function is bijective it admits the inverse relation $\mathbf{X} = \chi^{-1}(\mathbf{x}, t)$. From the motion χ we can obtain the field

$$\mathbf{U}(\mathbf{X}, t) = \mathbf{x} - \mathbf{X} = \chi(\mathbf{X}, t) - \mathbf{X}, \tag{3.2}$$

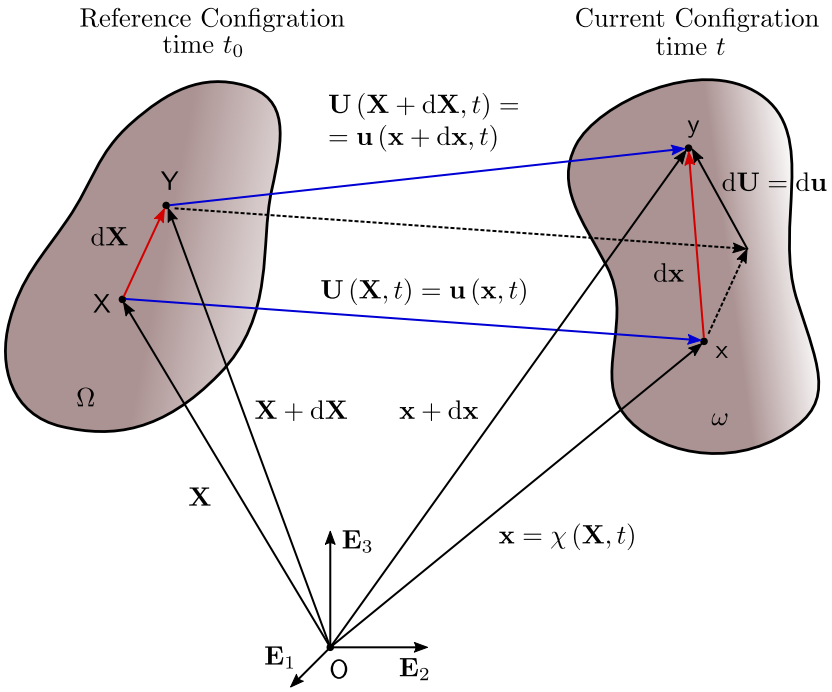

Figure 3.1: Configurations of the continuum body in the Euclidean space.

representing the displacement field in **material** (or **Lagrangian**) **description**, i.e. with respect to the material point **X**. Alternatively, the displacement field can be expressed in **spatial** (or **Eulerian**) **description**, referred to the spatial point **x**, using

$$\mathbf{u}(\mathbf{x},t)=\mathbf{x}-\mathbf{X}=\mathbf{x}-\chi^{-1}(\mathbf{x},t)\ . \tag{3.3}$$

Being the two displacement fields related to χ, the relation $\mathbf{U}(\mathbf{X},t)=\mathbf{u}(\mathbf{x},t)$ holds.

Now, to understand the distortion occurring close to P during the motion, we introduce a second material particle Q in the neighborhood of P. The particle moves from the point Y in the reference configuration to the point y in the current configuration. These points are identified by the position vectors $\mathbf{X}+\mathrm{d}\mathbf{X}\in\Omega$ and $\mathbf{x}+\mathrm{d}\mathbf{x}\in\omega$, where $\mathrm{d}\mathbf{X}$ and $\mathrm{d}\mathbf{x}$ denote the incremental positions relative to the points X and x, respectively. According to the motion function in Equation (3.1), the position of y can be expressed as $\mathbf{x}+\mathrm{d}\mathbf{x}=\chi(\mathbf{X}+\mathrm{d}\mathbf{X},t)$. By using the Taylor's

expansion around $\mathbf{X}$, we can then approximate the position of y as

$$\mathbf{x} + \mathrm{d}\mathbf{x} = \chi(\mathbf{X} + \mathrm{d}\mathbf{X}, t) = \chi(\mathbf{X}, t) + \frac{\partial \chi(\mathbf{X}, t)}{\partial \mathbf{X}} \mathrm{d}\mathbf{X} + o(\mathrm{d}\mathbf{X}) , \tag{3.4}$$

where the Landau order symbol $o(\mathrm{d}\mathbf{X})$ refers to a small error that tends to zero faster than $\mathrm{d}\mathbf{X}$ does. Hence, neglecting the higher-order terms, and substituting (3.1) into (3.4), we can express $\mathrm{d}\mathbf{x}$ for infinitesimal $\mathrm{d}\mathbf{X}$ as

$$\mathrm{d}\mathbf{x} = \frac{\partial \chi(\mathbf{X}, t)}{\partial \mathbf{X}} \mathrm{d}\mathbf{X} = \mathbf{F}(\mathbf{X}, t)\, \mathrm{d}\mathbf{X} , \tag{3.5}$$

where the second-order tensor quantity

$$\mathbf{F}(\mathbf{X}, t) = \frac{\partial \chi(\mathbf{X}, t)}{\partial \mathbf{X}} = \mathrm{Grad}\, \mathbf{x}(\mathbf{X}, t) , \tag{3.6}$$

is called **deformation gradient**. Equation (3.5) shows that $\mathbf{F}(\mathbf{X}, t)$ is responsible for linearly transforming a material line element $\mathrm{d}\mathbf{X}$ originating from $\mathbf{X}$ in the reference configuration to the deformed line $\mathrm{d}\mathbf{x}$ in the current configuration. For this reason, $\mathbf{F}$ is a **two-point tensor** involving points in two distinct configurations. The tensor $\mathbf{F}$ has in general 9 components for every t, and it characterizes the motion in the neighborhood of the position $\mathbf{X}$. The continuity and the differentiability of the motion $\chi(\mathbf{X}, t)$ implies that during the deformation process no cracks and voids are formed. Combing Equations (3.2) and (3.6), the deformation gradient can be computed in terms of displacement field gradient as

$$\mathbf{F}(\mathbf{X}, t) = \mathrm{Grad}\, \mathbf{X} + \mathrm{Grad}\, \mathbf{U}(\mathbf{X}, t) = \mathbf{I} + \mathrm{Grad}\, \mathbf{U}(\mathbf{X}, t) , \tag{3.7}$$

with $\mathbf{I}$ denoting the second-order identity tensor. The existence of the inverse motion relation $\mathbf{X} = \chi^{-1}(\mathbf{x}, t)$ also guarantees the invertibility of the deformation gradient

$$\mathbf{F}^{-1}(\mathbf{x}, t) = \frac{\partial \chi^{-1}(\mathbf{x}, t)}{\partial \mathbf{x}} = \mathrm{grad}\, \mathbf{X}(\mathbf{x}, t) . \tag{3.8}$$

Recalling (3.5), the **inverse deformation gradient** (3.8) allows us to transform back $\mathrm{d}\mathbf{x}$ into the original material line element $\mathrm{d}\mathbf{X}$ in the reference configuration

$$\mathrm{d}\mathbf{X} = \mathbf{F}^{-1}(\mathbf{x}, t)\, \mathrm{d}\mathbf{x} . \tag{3.9}$$

During the motion, the infinitesimal volume $\mathrm{d}V$ in the neighborhood of the position $\mathbf{X}$ changes to the volume $\mathrm{d}v$ around $\mathbf{x}$ in the current configuration according to

$$\mathrm{d}v = J(\mathbf{X}, t)\, \mathrm{d}V = \det \mathbf{F}(\mathbf{X}, t)\, \mathrm{d}V , \tag{3.10}$$

in which J is the determinant of the deformation gradient $\mathbf{F}$, and represents the **volume ratio**. Since $\mathbf{F}$ is invertible we have $J \neq 0$. In addition, since matter in the real-world cannot self-penetrate, negative values of the volume ratio are not admissible, although mathematically possible. Therefore, the volume ratio must be $J(\mathbf{X}, t) = \det \mathbf{F}(\mathbf{X}, t) > 0$, $\forall \mathbf{X} \in \Omega$. As a consequence, also the inverse volume ratio must be greater than zero, $J^{-1}(\mathbf{x}, t) = \det \mathbf{F}^{-1}(\mathbf{x}, t) > 0$. By introducing the infinitesimal area element vectors $\mathrm{d}\mathbf{A}$ and $\mathrm{d}\mathbf{a}$ in the neighborhood of $\mathbf{X}$ and $\mathbf{x}$, respectively, and adopting the relation (3.9), we may rewrite Equation (3.10) as

$$\begin{aligned} \mathrm{d}v &= \mathrm{d}\mathbf{x} \cdot \mathrm{d}\mathbf{a} = J\mathrm{d}V = \\ &= J\mathrm{d}\mathbf{X} \cdot \mathrm{d}\mathbf{A} = J\mathbf{F}^{-1}\mathrm{d}\mathbf{x} \cdot \mathrm{d}\mathbf{A} = J\mathrm{d}\mathbf{x} \cdot \mathbf{F}^{-\mathrm{T}}\mathrm{d}\mathbf{A}\,, \end{aligned}$$

from which we can deduce the important area element vector transformation

$$\mathrm{d}\mathbf{a} = J\mathbf{F}^{-\mathrm{T}}\mathrm{d}\mathbf{A}\,, \tag{3.11}$$

also known as **Nanson's formula**.

We now focus on the kinematics of a material line, represented by $\mathrm{d}\mathbf{X}$, around the position $\mathbf{X}$. Let the material line element in the reference configuration to be expressed as $\mathrm{d}\mathbf{X} = \mathrm{d}\epsilon\mathbf{N}$, where $\mathrm{d}\epsilon$ is the infinitesimal line length, and $\mathbf{N}$ is a unit vector ($|\mathbf{N}| = 1$) in the direction of the line. In the most general case, the linear transformation (3.5) causes the material line $\mathrm{d}\mathbf{X}$ to change in both length and direction, such that in the current configuration it can be written as $\mathrm{d}\mathbf{x} = \lambda\mathrm{d}\epsilon\mathbf{n}$, where the unit vector $\mathbf{n}$ denotes the new direction, and the quantity $\lambda\mathrm{d}\epsilon$ represents the new length obtained by scaling the original length $\mathrm{d}\epsilon$ by a factor λ called **stretch ratio**, or just **stretch**. If the line is extended during the motion then $\lambda > 1$, otherwise it is compressed and we have $\lambda < 1$. Only when the line is unstretched $\lambda = 1$. Therefore, this quantity describes the length deformation of a material line in the neighborhood of the position $\mathbf{X}$. By eliminating $\mathrm{d}\epsilon$, it follows from Equation (3.5) that

$$\lambda\mathbf{n} = \mathbf{F}\mathbf{N}\,, \tag{3.12}$$

allowing us to understand the deformation effects of $\mathbf{F}$ along a generic direction $\mathbf{N}$ around $\mathbf{X}$ regardless the length of the material line. We can then derive the square of the stretch from Equation (3.12) according to

$$\begin{aligned} \lambda^2 = \lambda\mathbf{n} \cdot \lambda\mathbf{n} = \mathbf{F}\mathbf{N} \cdot \mathbf{F}\mathbf{N} = \mathbf{N} \cdot \mathbf{F}^{\mathrm{T}}\mathbf{F}\mathbf{N} = \\ = \mathbf{N} \cdot \mathbf{C}\mathbf{N} = \mathbf{C} : \mathbf{N} \otimes \mathbf{N}\,, \end{aligned} \tag{3.13}$$

$$\mathbf{C} = \mathbf{F}^{\mathrm{T}}\mathbf{F}\,, \tag{3.14}$$

where the symbols : and $\otimes$ denote the double dot product (or double contraction) and the tensor product (or dyadic product), respectively. In Equation (3.13) it has been introduced the **right Cauchy-Green** tensor $\mathbf{C}$ (3.14), which is symmetric, $\mathbf{C}^{\mathrm{T}} = \left(\mathbf{F}^{\mathrm{T}}\mathbf{F}\right)^{\mathrm{T}} = \mathbf{F}^{\mathrm{T}}\mathbf{F} = \mathbf{C}$, and positive definite, $\mathbf{a}\cdot\mathbf{Ca} > 0$, $\forall \mathbf{a} \neq \mathbf{0}$, for each $\mathbf{X} \in \Omega$. Such tensor represents a fundamental deformation measure in terms of material description. Similarly to Equation (3.13) we can compute the reciprocal of the squared stretch in terms of inverse deformation gradient $\mathbf{F}^{-1}$ by exploiting (3.9) and the inverse relation of (3.12) as follows

$$\begin{aligned}\lambda^{-2} = \lambda^{-1}\mathbf{N}\cdot\lambda^{-1}\mathbf{N} = \mathbf{F}^{-1}\mathbf{n}\cdot\mathbf{F}^{-1}\mathbf{n} = \mathbf{n}\cdot\mathbf{F}^{-\mathrm{T}}\mathbf{F}^{-1}\mathbf{n} = \\ = \mathbf{n}\cdot\mathbf{b}^{-1}\mathbf{n} = \mathbf{b}^{-1} : \mathbf{n}\otimes\mathbf{n}\,,\end{aligned} \tag{3.15}$$

$$\mathbf{b} = \mathbf{F}\mathbf{F}^{\mathrm{T}}\,, \tag{3.16}$$

where $\mathbf{b}$ is the **left Cauchy-Green** tensor, and represents an important deformation measure in terms of spatial description. The tensor is symmetric, $\mathbf{b}^{\mathrm{T}} = \left(\mathbf{F}\mathbf{F}^{\mathrm{T}}\right)^{\mathrm{T}} = \mathbf{F}\mathbf{F}^{\mathrm{T}} = \mathbf{b}$, and positive definite, $\mathbf{a}\cdot\mathbf{ba} > 0$, $\forall \mathbf{a} \neq \mathbf{0}$, for each $\mathbf{x} \in \omega$.

The deformation gradient $\mathbf{F}$, as for all invertible second-order tensors, admits a unique factorization, called **polar decomposition**, of the form

$$\mathbf{F} = \mathbf{RU} = \mathbf{vR}\,, \tag{3.17}$$

where $\mathbf{R}$ is the unique proper orthogonal **rotation tensor** representing a pure rotation, while $\mathbf{U}$ and $\mathbf{v}$ define the unique, positive definite, and symmetric **right** (or **material**) **stretch tensor** and **left** (or **spatial**) **stretch tensor**, representing a pure deformation in the material and spatial descriptions, respectively. Note that $\mathbf{U}$ in Equation (3.17) must not to be confused with the displacement field in Equation (3.2). The rotation tensor has the properties $\mathbf{R}^{-1} = \mathbf{R}^{\mathrm{T}}$, and $\det\mathbf{R} = 1$. Accordingly, it follows from Equations (3.14), (3.16) and (3.17) that $\mathbf{C} = \mathbf{U}^{\mathrm{T}}\mathbf{U} = \mathbf{U}^2$, and $\mathbf{b} = \mathbf{v}\mathbf{v}^{\mathrm{T}} = \mathbf{v}^2$. From Equations (3.10), (3.14) and (3.16) we also deduce that $\det\mathbf{C} = \det\mathbf{b} = (\det\mathbf{F})^2 = J^2$, implying that $\det\mathbf{U} = \det\mathbf{v} = J$.

The material deformation tensor $\mathbf{U}$ can now be represented in spectral form, i.e. in terms of mutually orthogonal **eigenvectors** $\hat{\mathbf{N}}_a$, and **eigenvalues** λ_a, which satisfy the condition

$$\mathbf{U}\hat{\mathbf{N}}_a = \lambda_a\hat{\mathbf{N}}_a, \quad \text{with} \quad |\hat{\mathbf{N}}_a| = 1, \quad a = 1,2,3\,. \tag{3.18}$$

Eigenvectors and eigenvalues are obtained by solving for λ the **characteristic polynomial** written as

$$\lambda^3 - I_1\lambda^2 + I_2\lambda - I_3 = 0, \tag{3.19}$$

where the scalar quantities I_a, $a = 1,2,3$, are the **invariants** of $\mathbf{U}$ given by

$$\begin{aligned} I_1(\mathbf{U}) &= \mathbf{U} : \mathbf{I} = \lambda_1 + \lambda_2 + \lambda_3 \,, \\ I_2(\mathbf{U}) &= \frac{1}{2}\left[(\mathbf{U} : \mathbf{I})^2 - \mathbf{U}^2 : \mathbf{I}\right] = \lambda_1\lambda_2 + \lambda_2\lambda_3 + \lambda_3\lambda_1 \,, \\ I_3(\mathbf{U}) &= \det \mathbf{U} = \lambda_1\lambda_2\lambda_3 \,. \end{aligned} \tag{3.20}$$

Thus, for the **spectral theorem**, the tensor $\mathbf{U}$ reads

$$\mathbf{U} = \sum_{a=1}^{3} \lambda_a \hat{\mathbf{N}}_a \otimes \hat{\mathbf{N}}_a \,. \tag{3.21}$$

The set $\left\{\hat{\mathbf{N}}_a\right\}_{a=1,2,3}$ of mutually orthonormal vectors defines the **principal referential directions** basis, while the eigenvalues λ_a, $a = 1,2,3$, represent the **principal stretches** along their respective principal direction $\hat{\mathbf{N}}_a$. Exploiting Equations (3.17) and (3.21) and the properties of $\mathbf{R}$ it is possible to write

$$\mathbf{v} = \mathbf{R}\mathbf{U}\mathbf{R}^{\mathrm{T}} = \sum_{a=1}^{3} \lambda_a \left(\mathbf{R}\hat{\mathbf{N}}_a\right) \otimes \left(\mathbf{R}\hat{\mathbf{N}}_a\right) = \sum_{a=1}^{3} \lambda_a \hat{\mathbf{n}}_a \otimes \hat{\mathbf{n}}_a \,, \tag{3.22}$$

where the set $\{\hat{\mathbf{n}}_a\}_{a=1,2,3}$ of mutually orthonormal vectors defines the **principal spatial directions** basis, related to the principal material vectors through

$$\hat{\mathbf{n}}_a = \mathbf{R}\hat{\mathbf{N}}_a, \quad \text{with} \quad |\hat{\mathbf{n}}_a| = 1, \quad a = 1,2,3 \,. \tag{3.23}$$

By left multiplying Equation (3.18) by $\mathbf{R}$, and adopting Equations (3.17) and (3.23), we find the useful relation

$$\mathbf{F}\hat{\mathbf{N}}_a = \lambda_a \hat{\mathbf{n}}_a \,. \tag{3.24}$$

Finally, recalling Equation (3.17) and using Equations (3.21) and (3.23), the deformation gradient in spectral form may be written as

$$\mathbf{F} = \sum_{a=1}^{3} \lambda_a \hat{\mathbf{n}}_a \otimes \hat{\mathbf{N}}_a \,, \tag{3.25}$$

in which the presence of both the principal referential and spatial directions emphasizes the two-point nature of $\mathbf{F}$. Accordingly, following from Equations (3.14) and (3.16) the left and right Cauchy-Green tensors in spectral form are written as

$$\mathbf{C} = \sum_{a=1}^{3} \lambda_a^2 \hat{\mathbf{N}}_a \otimes \hat{\mathbf{N}}_a \,, \tag{3.26}$$

$$\mathbf{b} = \sum_{a=1}^{3} \lambda_a^2 \hat{\mathbf{n}}_a \otimes \hat{\mathbf{n}}_a \,. \tag{3.27}$$

3.1.2 Stress Definitions

Stress is the result of forces acting on particles within a material and their interactions with neighboring particles. It is quantitatively described as the force exerted per unit area within the material. As shown in Nanson's formula of Equation (3.11), area elements are not constant and change during the motion. Therefore, the concept of stress is not unique, and different stress definitions can be postulated for both the reference and current configurations.

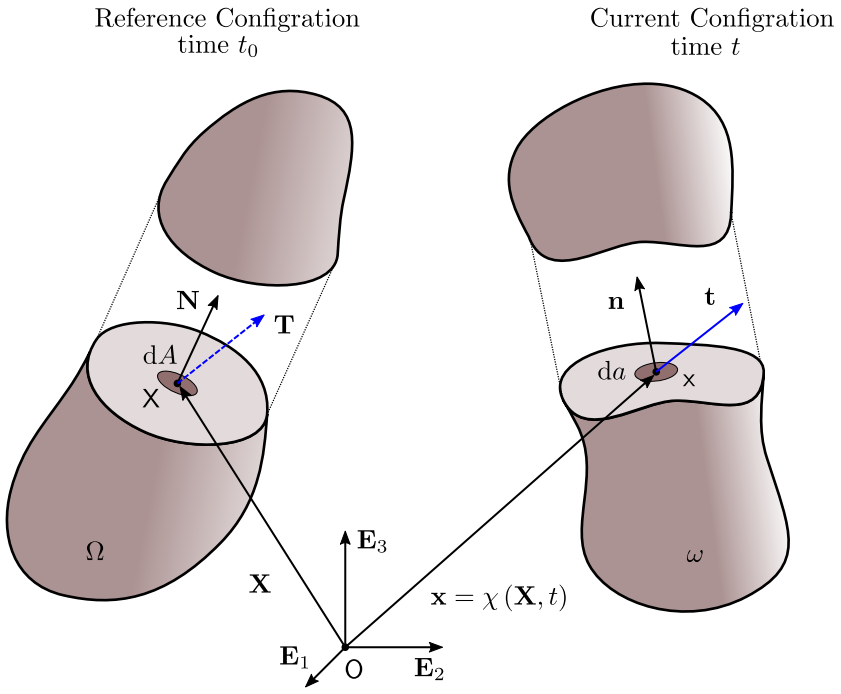

Figure 3.2: Traction vectors **t**, **T** acting on infinitesimal surfaces elements dA, da with outward normal vectors **N** and **n** = **RN** in the reference and current configurations, respectively.

We consider the continuum body $\mathcal{B}$ in the current configuration, occupying the region ω and delimited by the surface boundary $\partial\omega$ at time t (Figure 3.2). External forces acting on the surface boundary $\partial\omega$ generate external stresses. Likewise, internal forces acting on the ideal plane internally cutting the body generate internal stresses. Different cutting planes passing through the same given point are

associated to different internal stresses. With reference to Figure 3.2, for every surface element dA and da with normal $\mathbf{N}$ and $\mathbf{n} = \mathbf{RN}$ in the position $\mathbf{X}$ and $\mathbf{x}$, respectively, the infinitesimal acting force can be expressed as

$$\mathrm{d}\mathbf{f} = \mathbf{t}\mathrm{d}a = \mathbf{T}\mathrm{d}A\,, \tag{3.28}$$

in which $\mathbf{t}$ denotes the **Cauchy** (or **true**) **traction vector** defined in the current configuration, whereas $\mathbf{T}$ identifies the **first Piola-Kirchhoff** (or **nominal**) **traction vector**, defined in the reference configuration and pointing in the same direction of $\mathbf{t}$.

For the Cauchy theorem, these vectors are defined for every cutting plane, represented by normals $\mathbf{N}$ and $\mathbf{n}$ in reference and current configuration, and for every position $\mathbf{X} \in \Omega$ and $\mathbf{x} \in \omega$, by two unique second-order tensor fields, given by

$$\mathbf{t}(\mathbf{x}, t, \mathbf{n}) = \boldsymbol{\sigma}(\mathbf{x}, t)\,\mathbf{n}\,, \tag{3.29}$$

$$\mathbf{T}(\mathbf{X}, t, \mathbf{N}) = \mathbf{P}(\mathbf{X}, t)\,\mathbf{N}\,, \tag{3.30}$$

where $\boldsymbol{\sigma}$ denotes the symmetric spatial **Cauchy** (or **true**) stress tensor, while $\mathbf{P}$ characterizes the **first Piola-Kirchhoff** (or **nominal**) stress tensor.

Following from Equations (3.28) to (3.30) and recalling the Nanson's formula (3.11), the relation between $\boldsymbol{\sigma}$ and $\mathbf{P}$ can be expressed as

$$\begin{aligned}
\mathbf{P}\mathbf{N}\mathrm{d}A &= \boldsymbol{\sigma}\mathbf{n}\mathrm{d}a\,,\\
\mathbf{P}\mathrm{d}\mathbf{A} &= \boldsymbol{\sigma}\mathrm{d}\mathbf{a}\,,\\
\mathbf{P}\mathrm{d}\mathbf{A} &= \boldsymbol{\sigma}J\mathbf{F}^{-T}\mathrm{d}\mathbf{A}\,,
\end{aligned}$$

thus

$$\mathbf{P} = J\boldsymbol{\sigma}\mathbf{F}^{-\mathrm{T}}\,. \tag{3.31}$$

Another important stress measure in finite strain continuum mechanics is the **second Piola-Kirchhoff stress tensor S**. Defined the **Kirchhoff stress tensor** as

$$\boldsymbol{\tau} = J\boldsymbol{\sigma}\,, \tag{3.32}$$

the second Piola-Kirchhoff stress tensor is obtained, by definition, through the pull-back operation $\chi_*^{-1}(\bullet)$ by the motion χ on $\boldsymbol{\tau}$, i.e.

$$\mathbf{S} = \chi_*^{-1}(\boldsymbol{\tau}) = \mathbf{F}^{-1}\boldsymbol{\tau}\mathbf{F}^{-\mathrm{T}} = J\mathbf{F}^{-1}\boldsymbol{\sigma}\mathbf{F}^{-\mathrm{T}}\,. \tag{3.33}$$

Since the tensor $\boldsymbol{\sigma}$ is symmetric, the tensor $\mathbf{S}$ is symmetric as well. The inverse of Equation (3.33) provides the useful relation

$$\boldsymbol{\sigma} = J^{-1}\mathbf{F}\mathbf{S}\mathbf{F}^{\mathrm{T}} . \tag{3.34}$$

Finally, by substituting Equation (3.31) into (3.33), the relation between the first and second Piola-Kirchhoff tensors is derived

$$\mathbf{P} = \mathbf{F}\mathbf{S} . \tag{3.35}$$

3.1.3 Hyperelastic Constitutive Modeling

Equations introduced in the previous sections are defined for a generic continuum body in the Euclidean space. They do not establish any relationship between stresses and strains, hence, they hold for any kind of material behavior. Therefore, in order to describe the mechanical response of real materials it is fundamental to establish such relationship, called **constitutive law** [157].

In the context of skin, the stress-strain relationship, as for instance determined from experimental tensile tests, demonstrates a highly nonlinear behavior (refer to Section 2.4). This behavior can be approximated as hyperelastic. A **hyperelastic material** is characterized by the existence of a **Helmholtz free-energy function** Ψ, defined per unit reference volume. In general, for a **heterogeneous** material whose properties change point-to-point, this function depends on both strains and position. For a **homogeneous** material, instead, this function depends solely on strains, $\Psi = \Psi(\mathbf{F})$, and it is referred to as **strain-energy function (SEF)**. Although skin is a heterogeneous material, the size of its microstructural constituents is typically so small compared to the scale of the analyzed problems that it can be regarded as homogeneous. This approximation is generally effective and significantly simplifies the analysis.

The constitutive relationship for a hyperelastic material can be defined as

$$\mathbf{P} = \frac{\partial \Psi(\mathbf{F})}{\partial \mathbf{F}} , \tag{3.36}$$

and (by recalling Equation (3.31))

$$\boldsymbol{\sigma} = J^{-1}\frac{\partial \Psi(\mathbf{F})}{\partial \mathbf{F}}\mathbf{F}^{\mathrm{T}} = J^{-1}\mathbf{F}\left(\frac{\partial \Psi(\mathbf{F})}{\partial \mathbf{F}}\right)^{\mathrm{T}} . \tag{3.37}$$

Any particular function Ψ can be chosen, provided that it satisfies the requirements $\Psi(\mathbf{F}) \geq 0$, and $\Psi(\mathbf{I}) = 0$, which means that energy increases with deformations, and that only the unreformed configuration ($\mathbf{F} = \mathbf{I}$) is associated to the

zero energy. The function, also, must tend to $+\infty$ whenever the body is infinitely expanded or compressed in a vanishing volume. To ensure the existence and the unique solution of boundary-value problems Ψ must satisfy the further fundamental requirement of **polyconvexity** [158].

A crucial aspect in the continuum mechanics concerns the concept of **objectivity**, i.e. the invariance of the physical processes upon the change of observer. Considering a continuum body in the deformed configuration, the objectivity requires that its strain-energy function is the same for any observer, or equivalently, for any rigid body rotation in the current configuration by an orthogonal tensor $\mathbf{Q}$, such that $\Psi(\mathbf{F}) = \Psi(\mathbf{QF})$. Without loss of generality, and exploiting the polar decomposition (3.17), we can choose $\mathbf{Q} = \mathbf{R}^{\mathrm{T}}$, in order to obtain the formulation

$$\Psi(\mathbf{F}) = \Psi(\mathbf{QF}) = \Psi\left(\mathbf{R}^{\mathrm{T}}\mathbf{RU}\right) = \Psi(\mathbf{U}) \,, \tag{3.38}$$

which holds true for any $\mathbf{F}$. Equation (3.38) clearly shows that the strain-energy function must be dependent on the stretching part of $\mathbf{F}$ only. This allows to define the strain-energy function in terms of principal stretches λ_a, or invariants I_a, $a = 1,2,3$, of $\mathbf{U}$. Knowing from Equation (3.14) that $\mathbf{C} = \mathbf{F}^{\mathrm{T}}\mathbf{F} = \mathbf{U}^2$ it is also possible to express Ψ as a function of the right Cauchy-Green tensor, $\Psi(\mathbf{F}) = \Psi(\mathbf{C})$. Hence, Equation (3.36) may be rewritten as

$$\mathbf{P} = 2\mathbf{F}\frac{\partial \Psi(\mathbf{C})}{\partial \mathbf{C}} \,, \tag{3.39}$$

and Equation (3.37) as

$$\boldsymbol{\sigma} = 2J^{-1}\mathbf{F}\frac{\partial \Psi(\mathbf{C})}{\partial \mathbf{C}}\mathbf{F}^{\mathrm{T}} \,. \tag{3.40}$$

Following from Equations (3.34) and (3.40) the constitutive relation for the second Piola-Kirchhoff tensor is obtained

$$\mathbf{S} = 2\frac{\partial \Psi(\mathbf{C})}{\partial \mathbf{C}} \,. \tag{3.41}$$

If the mechanical response of a material point at $\mathbf{X}$ is invariant under any rigid body transformation by an orthogonal tensor $\mathbf{Q}$ in the reference configuration, such that

$$\Psi(\mathbf{F}) = \Psi\left(\mathbf{FQ}^{\mathrm{T}}\right) \,, \tag{3.42}$$

the material point is said to be **isotropic**. From Equation (3.42) it can be demonstrated that explicit forms of the general constitutive equation in Equations (3.40)

and (3.41) for an isotropic elastic material can be expressed as

$$\boldsymbol{\sigma} = f_1\mathbf{I} + f_2\mathbf{b} + f_3\mathbf{b}^2\,, \tag{3.43}$$

$$\mathbf{S} = g_1\mathbf{I} + g_2\mathbf{C} + g_3\mathbf{C}^{-1}\,, \tag{3.44}$$

where $f_i(\mathbf{b})$, and $g_i(\mathbf{C})$, $i = 1,2,3$, are scalar invariant functions of the left and right Cauchy-Green tensors [159].

A direct consequence of Equations (3.43) and (3.44), following from the Cayley-Hamilton equation, is that in isotropic materials the principal directions $\hat{\mathbf{N}}_a$, $\hat{\mathbf{n}}_a$ of stretch in the deformed state are also a principal directions of stress [159].

Isotropic Formulation Using Principal Stretches

By formulating Ψ in terms of principal stretches, $\Psi = \Psi(\lambda_1, \lambda_2, \lambda_3)$, and using the chain rule for the derivative, Equation (3.41) becomes

$$\begin{aligned}\mathbf{S} &= 2\sum_{a=1}^{3}\frac{\partial\Psi}{\partial\lambda_a^2}\frac{\partial\lambda_a^2}{\partial\mathbf{C}} = \sum_{a=1}^{3}\frac{1}{\lambda_a}\frac{\partial\Psi}{\partial\lambda_a}\hat{\mathbf{N}}_a\otimes\hat{\mathbf{N}}_a = \\ &= \sum_{a=1}^{3} S_a\hat{\mathbf{N}}_a\otimes\hat{\mathbf{N}}_a\,,\end{aligned} \tag{3.45}$$

where S_a, $a = 1,2,3$, are the principal second Piola-Kirchhoff stresses. Substituting Equation (3.45) in (3.35) and using the relation (3.24), $\mathbf{F}\hat{\mathbf{N}}_a = \lambda_a\hat{\mathbf{n}}_a$, the first Piola-Kirchhoff tensor reads

$$\begin{aligned}\mathbf{P} = \mathbf{F}\mathbf{S} &= \sum_{a=1}^{3}\frac{1}{\lambda_a}\frac{\partial\Psi}{\partial\lambda_a}\left(\mathbf{F}\hat{\mathbf{N}}_a\right)\otimes\hat{\mathbf{N}}_a = \sum_{a=1}^{3}\frac{\partial\Psi}{\partial\lambda_a}\hat{\mathbf{n}}_a\otimes\hat{\mathbf{N}}_a = \\ &= \sum_{a=1}^{3} P_a\hat{\mathbf{n}}_a\otimes\hat{\mathbf{N}}_a\,,\end{aligned} \tag{3.46}$$

which includes both the principal referential and spatial directions emphasizing the two-point nature of the tensor. Analogously, the Cauchy stress tensor $\boldsymbol{\sigma}$ is obtained by substituting Equation (3.46) in the inverse relation of Equation (3.31), i.e.

$$\begin{aligned}\boldsymbol{\sigma} = J^{-1}\mathbf{P}\mathbf{F}^T &= \sum_{a=1}^{3}J^{-1}\frac{\partial\Psi}{\partial\lambda_a}\hat{\mathbf{n}}_a\otimes\left(\hat{\mathbf{N}}_a\mathbf{F}^{\mathrm{T}}\right) = \sum_{a=1}^{3}J^{-1}\lambda_a\frac{\partial\Psi}{\partial\lambda_a}\hat{\mathbf{n}}_a\otimes\hat{\mathbf{n}}_a = \\ &= \sum_{a=1}^{3}\sigma_a\hat{\mathbf{n}}_a\otimes\hat{\mathbf{n}}_a\,,\end{aligned} \tag{3.47}$$

in which σ_a, $a = 1,2,3$, are the Cauchy principal stresses. Summarizing, the principal stresses are given by

$$S_a = \frac{1}{\lambda_a}\frac{\partial \Psi}{\partial \lambda_a}, \quad P_a = \frac{\partial \Psi}{\partial \lambda_a}, \quad \sigma_a = J^{-1}\lambda_a \frac{\partial \Psi}{\partial \lambda_a}, \quad a = 1,2,3\,. \tag{3.48}$$

Note that all the stress tensors in Equations (3.45) to (3.47) share the same principal direction of the deformation tensors $\mathbf{C}$ and $\mathbf{b}$ (see Equations (3.26) and (3.27)), implying that they represent constitutive equations for an isotropic material.

Anisotropic Formulation Using Invariants

The strain-energy function can be also formulated in terms of invariants of $\mathbf{C}$, $I_i(\mathbf{C})$, $i = 1,2,3$, (see Equation (3.20)). This type of formulation is particularly useful for modeling **anisotropic materials** because it allows to use additional scalar values, called **pseudo-invariants**, which account for the anisotropy along arbitrary directions $\mathbf{M}_i$, $|\mathbf{M}_i| = 1$, $i = 1,\ldots,m$. In fiber-reinforced materials, for instance, such anisotropy arises from the non-uniform fiber distribution. Indeed, along the **preferential fiber directions** $\mathbf{M}_i$, or mean **fiber family directions**, the stiffness is much greater than in the direction orthogonal to the fibers. The simplest pseudo-invariant definition is the square of the stretch in the direction of $\mathbf{M}_i$. Thus, recalling (3.13), we may define

$$I_{4,i} = \lambda_i^2 = \mathbf{C} : \mathbf{M}_i \otimes \mathbf{M}_i\,, \tag{3.49}$$

in which the second-order tensor $\mathbf{M}_i \otimes \mathbf{M}_i$ is called **structure tensor**. Hence the strain-energy function formulated in terms of invariants reads

$$\Psi = \Psi\left(I_1(\mathbf{C}), I_2(\mathbf{C}), I_3(\mathbf{C}), I_{4,1}(\mathbf{C}, \mathbf{M}_1 \otimes \mathbf{M}_1), \ldots, I_{4,m}(\mathbf{C}, \mathbf{M}_m \otimes \mathbf{M}_m)\right)\,. \tag{3.50}$$

Such formulation depends on vectors $\mathbf{M}_i$ referred to the reference configuration. Therefore the objectivity requirement for Ψ is trivially satisfied [156]. By introducing the derivatives of the invariants with respect to $\mathbf{C}$ as follows

$$\frac{\partial I_1}{\partial \mathbf{C}} = \frac{\partial}{\partial \mathbf{C}}[\mathbf{C} : \mathbf{I}] = \mathbf{I}\,, \tag{3.51}$$

$$\frac{\partial I_2}{\partial \mathbf{C}} = \frac{\partial}{\partial \mathbf{C}}\left[\frac{1}{2}\left[(\mathbf{C} : \mathbf{I})^2 - \mathbf{C}^2 : \mathbf{I}\right]\right] = I_1\mathbf{I} - \mathbf{C}\,, \tag{3.52}$$

$$\frac{\partial I_3}{\partial \mathbf{C}} = \frac{\partial}{\partial \mathbf{C}}[\det \mathbf{C}] = \det \mathbf{C}\mathbf{C}^{-1} = I_3\mathbf{C}^{-1}\,, \tag{3.53}$$

$$\frac{\partial I_{4,i}}{\partial \mathbf{C}} = \frac{\partial}{\partial \mathbf{C}}[\mathbf{C} : \mathbf{M}_i \otimes \mathbf{M}_i] = \mathbf{M}_i \otimes \mathbf{M}_i\,, \tag{3.54}$$

and using the chain rule for the derivative, the second Piola-Kirchhoff tensor in Equation (3.41) can be expressed as

$$\begin{aligned}\mathbf{S} &= 2\left[\frac{\partial\Psi}{\partial I_1}\frac{\partial I_1}{\partial \mathbf{C}} + \frac{\partial\Psi}{\partial I_2}\frac{\partial I_2}{\partial \mathbf{C}} + \frac{\partial\Psi}{\partial I_3}\frac{\partial I_3}{\partial \mathbf{C}} + \sum_{i=1}^{m}\frac{\partial\Psi}{\partial I_{4,i}}\frac{\partial I_{4,i}}{\partial \mathbf{C}}\right] = \\ &= 2\left[\left(\frac{\partial\Psi}{\partial I_1} + I_1\frac{\partial\Psi}{\partial I_2}\right)\mathbf{I} + \frac{\partial\Psi}{\partial I_2}\mathbf{C} + I_3\frac{\partial\Psi}{\partial I_3}\mathbf{C}^{-1} + \sum_{i=1}^{m}\frac{\partial\Psi}{\partial I_{4,i}}\mathbf{M}_i\otimes\mathbf{M}_i\right].\end{aligned} \tag{3.55}$$

Accordingly, following from Equation (3.34), and using Equation (3.49), we may write the Cauchy stress tensor from $\mathbf{S}$ as

$$\boldsymbol{\sigma} = 2J^{-1}\left[\left(\frac{\partial\Psi}{\partial I_1} + I_1\frac{\partial\Psi}{\partial I_2}\right)\mathbf{b} + \frac{\partial\Psi}{\partial I_2}\mathbf{b}^2 + I_3\frac{\partial\Psi}{\partial I_3}\mathbf{I} + \sum_{i=1}^{m} I_{4,i}\frac{\partial\Psi}{\partial I_{4,i}}\mathbf{m}_i\otimes\mathbf{m}_i\right], \tag{3.56}$$

where $\mathbf{F}\mathbf{M}_i = \lambda_i\mathbf{m}_i$. Note that the first terms in Equations (3.55) and (3.56) are expressed in the forms in Equations (3.43) and (3.44), thus representing the isotropic contribution of the strain-energy function.

3.1.4 Linearization of the Mechanical Problem

We now focus on the causes of the motion described in Section 3.1.1. A continuum body $\mathcal{B}$ in the Euclidean space, subjected to the external constraint $\bar{\mathbf{u}}$ on the boundary $\partial\omega_{\mathbf{u}} \subset \partial\omega$, deforms under the effects of body forces $\mathbf{f}(\mathbf{x},t)$ acting on ω, and prescribed external forces $\bar{\mathbf{t}}(\mathbf{x},t)$ acting on the boundary $\partial\omega_{\boldsymbol{\sigma}} \subset \partial\omega$, $\partial\omega_{\mathbf{u}} \cap \partial\omega_{\boldsymbol{\sigma}} = \emptyset$. The boundary-value problem (BVP) can be stated combining the equilibrium equation of the continuum body, derived from the momentum balance principle, with the boundary conditions on $\partial\omega$ and the initial conditions of the body $\mathcal{B}$ in the reference configuration at t_0, i.e.

$$\begin{cases} \operatorname{div}\boldsymbol{\sigma}(\mathbf{x},t) + \mathbf{f}(\mathbf{x},t) = \rho(\mathbf{x},t)\,\ddot{\mathbf{u}}(\mathbf{x},t) & \\ \mathbf{u}(\mathbf{x},t) = \bar{\mathbf{u}}(\mathbf{x},t) & \text{on} \quad \partial\omega_{\mathbf{u}} \\ \boldsymbol{\sigma}(\mathbf{x},t)\,\mathbf{n}(\mathbf{x},t) = \bar{\mathbf{t}}(\mathbf{x},t) & \text{on} \quad \partial\omega_{\boldsymbol{\sigma}} \\ \mathbf{u}(\mathbf{x},t) = \mathbf{U}_0(\mathbf{X}) & \text{at} \quad t = t_0 \\ \dot{\mathbf{u}}(\mathbf{x},t) = \dot{\mathbf{U}}_0(\mathbf{X}) & \text{at} \quad t = t_0 \end{cases} \tag{3.57}$$

where ρ is the density field, $\mathbf{n}$ is the outward normal vector to the boundary surface $\partial\omega_{\boldsymbol{\sigma}}$ at $\mathbf{x}$, and $\dot{\mathbf{u}}$ and $\ddot{\mathbf{u}}$ are the velocity and acceleration fields, respectively. The operator $\operatorname{div}(\bullet)$ denotes the divergence of $(\bullet)$. Given the constitutive equation

for stress $\boldsymbol{\sigma}$, Equation (3.57), representing the problem in the so called **strong form**, must be solved for the unknown displacement field $\mathbf{u}(\mathbf{x}, t)$. If the quantities are independent on the time the problem is referred to as **static**, whereas if the accelerations are negligible, $\ddot{\mathbf{u}} \approx 0$, it is referred to as **quasi-static**.

In numerical approaches, like the Finite Element Method (FEM), the boundary-value problem (BVP) is formulated in the equivalent **weak form**, written as (neglecting the accelerations)

$$\begin{aligned}
\delta\Pi(\mathbf{u}, \delta\mathbf{u}) &= \int_{\omega} (-\operatorname{div}\boldsymbol{\sigma} - \mathbf{f}) \cdot \delta\mathbf{u} \mathrm{d}v = \\
&= \int_{\omega} (\boldsymbol{\sigma} : \operatorname{grad}\delta\mathbf{u} - \mathbf{f} \cdot \delta\mathbf{u}) \mathrm{d}v - \int_{\partial\omega_{\sigma}} \bar{\mathbf{t}} \cdot \delta\mathbf{u} \mathrm{d}a = \\
&= \left(\int_{\omega} \boldsymbol{\sigma} : \operatorname{grad}\delta\mathbf{u} \mathrm{d}v \right) - \left(\int_{\omega} \mathbf{f} \cdot \delta\mathbf{u} \mathrm{d}v + \int_{\partial\omega_{\sigma}} \bar{\mathbf{t}} \cdot \delta\mathbf{u} \mathrm{d}a \right) = \\
&= \delta W_{\mathrm{int}}(\mathbf{u}, \delta\mathbf{u}) - \delta W_{\mathrm{ext}}(\mathbf{u}, \delta\mathbf{u}) = 0 \,,
\end{aligned} \tag{3.58}$$

where the divergence theorem has been applied on the quantity $\operatorname{div}\boldsymbol{\sigma} \cdot \delta\mathbf{u}$. Thereby, $\delta\Pi(\mathbf{u}, \delta\mathbf{u})$ is the virtual variation of the global potential energy $\Pi(\mathbf{u})$ by the arbitrary virtual variation $\delta\mathbf{u}$ of the displacement field. Basically, Equation (3.58) states that whether the deformed body is in equilibrium, then the virtual variation of the internal work δW_{int} must be equal of the virtual variation of the external work δW_{ext} for any virtual displacement field $\delta\mathbf{u}$.

The quantity δW_{int} is generally nonlinear in the unknown displacement vector field $\mathbf{u}$ due to the kinematics of the body (**geometrical nonlinearity**) and the constitutive equations of the material (**material nonlinearity**). Therefore, to solve Equation (3.58) for $\mathbf{u}$, the problem must be treated in spatial description stepwise by linear increments. To this end, the virtual internal work is linearized by computing the directional derivative (or Gâteaux derivative) of δW_{int} in the direction of the incremental displacement field $\Delta\mathbf{u}$, i.e.

$$D_{\Delta\mathbf{u}} \delta W_{\mathrm{int}}(\mathbf{u}, \delta\mathbf{u}) = \int_{\omega} (\operatorname{grad}\delta\mathbf{u} : \operatorname{grad}\Delta\mathbf{u}\ \boldsymbol{\sigma} + \operatorname{grad}\delta\mathbf{u} : \mathbb{C} : \operatorname{grad}\Delta\mathbf{u}) \mathrm{d}v \,. \tag{3.59}$$

Equation (3.59) is linear with respect to both $\delta\mathbf{u}$ and $\Delta\mathbf{u}$ depending on the position $\mathbf{X}$. The quantity $\mathbb{C}$ is the **fourth-order stiffness** (or **elasticity**) **tensor** in spatial

description, and it is obtained by the standard push-forward operation $\chi_*(\bullet)$ by the motion χ on the **fourth-order stiffness tensor** $\mathbb{C}$ in material description

$$\mathbb{c} = J^{-1}\chi_*(\mathbb{C}), \qquad \mathbb{C} = 2\frac{\partial \mathbf{S}(\mathbf{C})}{\partial \mathbf{C}} = 4\frac{\partial^2 \Psi(\mathbf{C})}{\partial \mathbf{C}\partial \mathbf{C}}. \tag{3.60}$$

Being obtained by derivatives with respect to the symmetric right Cauchy-Green tensor **C**, the material stiffness tensor, as well as the spatial stiffness tensor, has the minor symmetries $(\mathbb{C})_{IJKL} = (\mathbb{C})_{JIKL} = (\mathbb{C})_{IJLK}$, and the major symmetry $(\mathbb{C})_{IJKL} = (\mathbb{C})_{KLIJ}$. Therefore, they have only 21 independent components. In FE software, for computation reasons, the stiffness tensors must be implemented as a symmetric 6×6 matrix $[\mathbb{C}]$, or $[\mathbb{c}]$, in which the components are reorganized according to the Voigt's notation.

3.1.5 Stiffness Tensors Derivation

As discussed in Section 2.1, the ECM of the skin dermis is primarily a composite of elastin and collagen fibers embedded in a protein ground matrix largely constituted of proteoglycans. This substance is almost incompressible [123], and for many problems of interest its movement induced by stresses in and out of the ECM can be neglected. Therefore, it is a common approach, which also simplifies analytical derivations, to assume skin as perfectly incompressible. The incompressibility constraint, $J = \det \mathbf{F} = 1$, can be enforced in the strain-energy function by postulating it as

$$\Psi = \Psi(\mathbf{C}) - p\,(J-1)\,, \tag{3.61}$$

where the scalar p, denoting an unknown Lagrange multiplier, has the physical meaning of a hydrostatic pressure. Plugging Equation (3.61) into $(3.60)_2$, we can now derive the material stiffness tensor for perfectly incompressible materials.

Using the formulation in terms of principal stretches we obtain

$$\begin{aligned}\mathbb{C} = &\sum_{a,b=1}^{3} \frac{1}{\lambda_b}\frac{\partial S_a}{\partial \lambda_b}\hat{\mathbf{N}}_a \otimes \hat{\mathbf{N}}_a \otimes \hat{\mathbf{N}}_b \otimes \hat{\mathbf{N}}_b \\ &+ \sum_{a,b=1;a\neq b}^{3} \frac{S_b - S_a}{\lambda_b^2 - \lambda_a^2}\left(\hat{\mathbf{N}}_a \otimes \hat{\mathbf{N}}_b \otimes \hat{\mathbf{N}}_a \otimes \hat{\mathbf{N}}_b + \hat{\mathbf{N}}_a \otimes \hat{\mathbf{N}}_b \otimes \hat{\mathbf{N}}_b \otimes \hat{\mathbf{N}}_a\right),\end{aligned} \tag{3.62}$$

where S_a calculated from Equation $(3.48)_1$ and Equation (3.61) reads

$$S_a = \frac{1}{\lambda_a}\frac{\partial \Psi}{\partial \lambda_a} - pJ\frac{1}{\lambda_a^2}, \quad \Psi = \Psi(\lambda_1, \lambda_2, \lambda_3)\,. \tag{3.63}$$

In case two principal stretches are equal, it follows from the isotropy that also the principal stresses are equal. Hence the fraction $(S_b - S_a)/\left(\lambda_b^2 - \lambda_a^2\right)$ becomes an indeterminate form of type 0/0. In this case the rule of De l'Hôpital can be used to solve the indeterminate form for λ_b approaching λ_a as [160]

$$\lim_{\lambda_b \to \lambda_a} \frac{S_b - S_a}{\lambda_b^2 - \lambda_a^2} = \frac{\partial S_b}{\partial \lambda_b^2} - \frac{\partial S_a}{\partial \lambda_b^2}\,. \tag{3.64}$$

By applying the push-forward operation $(3.60)_1$ the spatial stiffness tensor in terms of principal stretches becomes

$$\begin{aligned}\mathbb{c} = &\sum_{a,b=1}^{3} J^{-1}\lambda_a^2\lambda_b \frac{\partial S_a}{\partial \lambda_b}\hat{\mathbf{n}}_a \otimes \hat{\mathbf{n}}_a \otimes \hat{\mathbf{n}}_b \otimes \hat{\mathbf{n}}_b \\ &+ \sum_{a,b=1;a\neq b}^{3} \frac{\sigma_b\lambda_a^2 - \sigma_a\lambda_b^2}{\lambda_b^2 - \lambda_a^2}\left(\hat{\mathbf{n}}_a \otimes \hat{\mathbf{n}}_b \otimes \hat{\mathbf{n}}_a \otimes \hat{\mathbf{n}}_b + \hat{\mathbf{n}}_a \otimes \hat{\mathbf{n}}_b \otimes \hat{\mathbf{n}}_b \otimes \hat{\mathbf{n}}_a\right),\end{aligned} \tag{3.65}$$

with the principal Cauchy stresses $\sigma_a = J^{-1}\lambda_a^2 S_a$ (see Equation (3.48)), in which S_a has the form of Equation (3.63). As described for the stress tensors, the presence of the principal directions $\hat{\mathbf{N}}_a$ and $\hat{\mathbf{n}}_a$ in (3.62) and (3.65) emphasizes the **isotropic** nature of the stiffness tensors formulated with the principal stretches.

To derive the stiffness tensor in terms of invariants, we first need to derive again the second Piola-Kirchhoff tensor $\mathbf{S}$ including the incompressibility constraint. Hence, Equation (3.55) becomes

$$\begin{aligned}\mathbf{S} = &2\left[\left(\frac{\partial \Psi}{\partial I_1} + I_1\frac{\partial \Psi}{\partial I_2}\right)\mathbf{I} + \frac{\partial \Psi}{\partial I_2}\mathbf{C} + I_3\frac{\partial \Psi}{\partial I_3}\mathbf{C}^{-1} + \sum_{i=1}^{m}\frac{\partial \Psi}{\partial I_{4,i}}\mathbf{M}_i \otimes \mathbf{M}_i\right] \\ &- 2\frac{\partial p}{\partial \mathbf{C}}(J-1) - pJ\mathbf{C}^{-1}\,.\end{aligned} \tag{3.66}$$

Even though the term including $(J-1)$ would vanish for $J = 1$, we keep it during the derivations as it is essential to obtain the complete stiffness tensor. Since $I_3(\mathbf{C}) = J^2 = \lambda_1^2\lambda_2^2\lambda_3^2 = 1$ for the incompressibility constraint, Ψ is independent of I_3. Moreover, since soft biological tissue predominantly operate in a tensile regime, I_2 is frequently omitted in constitutive models [123, 161]. In fact, from $J = \lambda_1\lambda_2\lambda_3 = 1$, the second invariant (see Equation $(3.20)_2$) can be written as $I_2(\mathbf{C}) = \lambda_1^{-2} + \lambda_2^{-2} + \lambda_3^{-2}$, and it mainly characterizes the behavior in compression. Thus, substituting Equation (3.66) into $(3.60)_2$, and assuming Ψ to be an function of the first and fourth invariants I_1, $I_{4,i}$, with $\frac{\partial^2 \Psi}{\partial I_1 \partial I_{4,i}} = 0$, the tensor $\mathbb{C}$ is derived

as [162]

$$\begin{aligned}\mathbb{C} = 2\frac{\partial \mathbf{S}}{\partial \mathbf{C}} =& 4\left[\frac{\partial^2\Psi}{\partial I_1^2}\mathbf{I}\otimes\mathbf{I} + \sum_{i=1}^{m}\frac{\partial^2\Psi}{\partial I_{4,i}^2}\mathbf{M}_i\otimes\mathbf{M}_i\otimes\mathbf{M}_i\otimes\mathbf{M}_i\right] \\ & - 4\frac{\partial^2 p}{\partial\mathbf{C}\partial\mathbf{C}}(J-1) - 2J\left(\frac{\partial p}{\partial\mathbf{C}}\otimes\mathbf{C}^{-1} + \mathbf{C}^{-1}\otimes\frac{\partial p}{\partial\mathbf{C}}\right) \\ & + 2pJ\mathbf{C}^{-1}\odot\mathbf{C}^{-1} - pJ\mathbf{C}^{-1}\otimes\mathbf{C}^{-1}\,,\end{aligned} \tag{3.67}$$

where the operator $\odot$ defines the symmetric dyadic product between two second order tensors, $(\circ\odot\bullet)_{ijkl} = 1/2\big((\circ)_{ik}(\bullet)_{jl} + (\circ)_{il}(\bullet)_{jk}\big)$. Finally, applying the push-forward operation we obtain the stiffness tensor in spatial description, i.e.

$$\begin{aligned}\mathbb{c} = J^{-1}\chi_*(\mathbb{C}) =& 4J^{-1}\left[\frac{\partial^2\Psi}{\partial I_1^2}\mathbf{b}\otimes\mathbf{b} + \sum_{i=1}^{m} I_{4,i}^2\frac{\partial^2\Psi}{\partial I_{4,i}^2}\mathbf{m}_i\otimes\mathbf{m}_i\otimes\mathbf{m}_i\otimes\mathbf{m}_i\right] \\ & - 4J^{-1}\mathbf{b}\frac{\partial^2 p}{\partial\mathbf{b}\partial\mathbf{b}}\mathbf{b}(J-1) - 2\left(\mathbf{b}\frac{\partial p}{\partial\mathbf{b}}\otimes\mathbf{I} + \mathbf{I}\otimes\frac{\partial p}{\partial\mathbf{b}}\mathbf{b}\right) \\ & + 2p\mathbf{I}\odot\mathbf{I} - p\mathbf{I}\otimes\mathbf{I}\,.\end{aligned} \tag{3.68}$$

These stiffness tensors, containing the preferential material directions $\mathbf{M}_i$ and $\mathbf{m}_i$, are **anisotropic**.

3.1.6 Plane Stress Formulation

From a mechanical standpoint, the skin can be regarded as a thin membrane. For this reason, in mechanical problems, it is convenient to approximate the skin as a bi-dimensional structure subjected solely to forces within its mean plane. This condition is called **plane stress** state, and it requires the out-of-plane stress component to be zero. This assumption is also useful to find an explicit expression of the unknown hydrostatic pressure p. We then assume the mean plane in the reference configuration to be co-planar with the global plane $\{\mathbf{E}_1, \mathbf{E}_2\}$, such that the plane stress constraint is defined by $S_{33} = P_{33} = \sigma_{33} = 0$. Accordingly, with the principal stretches formulation, p can be expressed from Equation (3.63) as

$$p = \lambda_3\frac{\partial\Psi}{\partial\lambda_3}, \quad \Psi = \Psi(\lambda_1,\lambda_2,\lambda_3)\,. \tag{3.69}$$

This expression for p is sufficient for determining the isotropic stiffness tensors $\mathbb{C}$ and $\mathbb{c}$ in Equations (3.62) and (3.65). On the other hand, using the formulation with invariants, the explicit expression of p is not sufficient alone, as some terms

in Equations (3.67) and (3.68) depend on the derivative of p with respect to $\mathbf{C}$ and $\mathbf{b}$. Obtained p from Equation (3.66) by assuming $\Psi = \Psi\left(I_1, I_{4,1}, \ldots, I_{4,m}\right)$,

$$p = 2J^{-1}\left[\frac{\partial \Psi}{\partial I_1}(\mathbf{b})_{33} + \sum_{i=1}^{m} I_{4,i}\frac{\partial \Psi}{\partial I_{4,i}}(\mathbf{m}_i \otimes \mathbf{m}_i)_{33}\right], \tag{3.70}$$

the only non-vanishing derivative of p with respect to $\mathbf{b}$, after some tensor calculus, reads

$$\mathbf{b}\frac{\partial p}{\partial \mathbf{b}} = \frac{\partial p}{\partial \mathbf{b}}\mathbf{b} = -\frac{1}{2}p\mathbf{I} + p\mathbf{E}_3 \otimes \mathbf{E}_3 + J^{-1}\sum_{i=1}^{m} 2I_{4,i}^2 \frac{\partial^2 \Psi}{\partial I_{4,i}^2}(\mathbf{m}_i \otimes \mathbf{m}_i)_{33}\,\mathbf{m}_i \otimes \mathbf{m}_i\,. \tag{3.71}$$

With both the incompressibility and the plane stress constraints applied, the three-dimensional problem reduces to a two-dimensional problem in the subspace $\{\mathbf{E}_1, \mathbf{E}_2\}$, in which the out-of-plane component of the right Cauchy-green tensor C_{33} depends solely on the planar components. Thus, we have

$$[\mathbf{C}] = \begin{bmatrix} C_{11} & C_{12} & 0 \\ C_{21} & C_{22} & 0 \\ 0 & 0 & (C_{11}C_{22} - C_{12}C_{21})^{-1} \end{bmatrix}, \tag{3.72}$$

where $C_{12} = C_{21}$ follows from the symmetry. Alternatively the the out-of-plane deformation can be expressed in terms of principals stretches, $\lambda_3 = (\lambda_1\lambda_2)^{-1}$. As a consequence, the component related to C_{33} in the stiffness tensor $\mathbb{C}$ can be eliminated by static condensation [162], leading to

$$(\check{\mathbb{C}})_{ijkl} = (\mathbb{C})_{ijkl} - \frac{(\mathbb{C})_{ij33}\,(\mathbb{C})_{33kl}}{(\mathbb{C})_{3333}}\,. \tag{3.73}$$

Directly eliminating the stiffness components related to the unused out-of-plane shear deformations, the tensor is further reduced to only 6 independent components, and it can be implemented in FE software as a 3×3 matrix $[\check{\mathbb{C}}]$.

3.2 Implemented Constitutive Models

3.2.1 Ogden Wrinkling Model

Thin membranes, like skin, buckles under in-plane compressive forces resulting in out-of-plane displacements [163]. This instability phenomenon is known as **wrinkling**. In general, in order to determine the exact out-of-plane deflection of the membrane, the flexural buckling and post-buckling behavior should be analyzed [164–166]. However, if no specific information about wrinkle wavelength and amplitude is needed, a properly modified plane stress constitutive model can be adopted in numerical analysis, in which the geometrical nonlinearity induced by finite out-of-plane displacements is treated as a material nonlinearity [82, 83, 167–169]. This represents a computationally efficient approach suitable to determine the in-plane tension field of the membrane, and precisely identify the distribution of wrinkled regions.

In general, the instability occurs in the direction of the principal compressive stress, which is perpendicular to the direction of the principal tensile stress. As described in Section 3.1.3, if the mechanical behavior is isotropic stresses and strains share the same principal directions. Therefore, the wrinkling behavior can be conveniently defined in terms of the principal stretches. Taking λ_1 as the reference stretch, there are three possible strain configurations for the membrane, depending on λ_2. A modified strain-energy function $\Psi = \Psi_{\mathrm{w}}$ can be defined, depending on the configuration. This procedure, which somehow treats the out-of-plane deflection as a constitutive material nonlinearity, is known as quasi-convexification of Ψ [170].

In the following, the material behavior is assumed to be described by the Ogden model [71], defined as

$$\Psi_{\mathrm{o}} = \sum_{i=1}^{N} \frac{\mu_i}{\alpha_i} \left(\lambda_1^{\alpha_i} + \lambda_2^{\alpha_i} + \lambda_3^{\alpha_i} - 3 \right), \tag{3.74}$$

where N is the order of the series, μ_i are shear moduli and α_i are dimensionless constants governing the stiffening, which must satisfy $\mu_i \alpha_i > 0$. When $\lambda_1 \geq 1$ and $\lambda_2 \geq \lambda_1^{-1/2}$, the lateral deformation λ_2 is greater than that due to Poisson contraction. In this case, no wrinkling occurs as lateral stretches greater than $\lambda_1^{-1/2}$ provide positive stresses. This is the so-called **taut** condition (Figure 3.3(a)), and the relative strain-energy function Ψ_{w} is given by Equation (3.74), substituting λ_3 obtained from the incompressibility constraint, $\lambda_3 = (\lambda_1 \lambda_2)^{-1}$. If $\lambda_1 \geq 1$ and $\lambda_2 < \lambda_1^{-1/2}$, the membrane is actually compressed in the lateral direction, re-

sulting in a **wrinkling** condition (Figure 3.3(b)). Wrinkles parallel to λ_1 direction develop, carrying no loads along their orthogonal direction. Keeping fixed λ_1, further reductions of λ_2 do not increase the strain-energy, which remains equal to the minimum reached in the uniaxial stress state. Following the works of Evans [168] and Massabò and Gambarotta [68], Ψ_w depends only on λ_1, and can be obtained substituting $\lambda_3 = \lambda_2 = \lambda_1^{-1/2}$ into Equation (3.74). Thus, we find

$$\Psi_w = \sum_{i=1}^{N} \frac{\mu_i}{\alpha_i} \left(\lambda_1^{\alpha_i} + 2\lambda_1^{-\frac{\alpha_i}{2}} - 3 \right). \tag{3.75}$$

Finally, if $\lambda_2 < \lambda_1 < 1$ the membrane is **slack** (Figure 3.3(c)) and does not carry any load. No energy is stored within the material under loading, and hence the associated strain-energy function is set to zero. The full function Ψ_w for both cases of $\lambda_1 > \lambda_2$ and $\lambda_2 > \lambda_1$ is called the relaxed strain-energy function, and it is summarized as

$$\Psi_w = \begin{cases} \sum_{i=1}^{N} \frac{\mu_i}{\alpha_i} \left(\lambda_1^{\alpha_i} + \lambda_2^{\alpha_i} + (\lambda_1\lambda_2)^{-\alpha_i} - 3 \right) & \lambda_1 \geq 1,\ \lambda_2 \geq \lambda_1^{-1/2} \text{ or} \\ & \lambda_2 \geq 1,\ \lambda_1 \geq \lambda_2^{-1/2}, \\ \sum_{i=1}^{N} \frac{\mu_i}{\alpha_i} \left(\lambda_1^{\alpha_i} + 2\lambda_1^{-\frac{\alpha_i}{2}} - 3 \right) & \lambda_1 \geq 1,\ \lambda_2 < \lambda_1^{-1/2}, \\ \sum_{i=1}^{N} \frac{\mu_i}{\alpha_i} \left(\lambda_2^{\alpha_i} + 2\lambda_2^{-\frac{\alpha_i}{2}} - 3 \right) & \lambda_2 \geq 1,\ \lambda_1 < \lambda_2^{-1/2}, \\ 0 & \lambda_1 < 1,\ \lambda_2 < 1\,. \end{cases} \tag{3.76}$$

This function is quasi-convex and does not satisfies the polyconvexity requirement. If implemented as is in Equation (3.65) it would give rise to zero stiffness in the direction of the principal compressive stress, ill-conditioning the problem and causing numerical instabilities in FE software. To circumvent this issue, an additional non-wrinkling term is added to the strain-energy function, such that the total function Ψ is written as

$$\Psi = \Psi_w + \nu\Psi_o\,, \tag{3.77}$$

where Ψ_o is the standard Ogden model in Equation (3.74) in which the parameters are taken the same as of Ψ_w, and ν is a weight factor assumed to be $\nu = 10^{-2}$ in order to have a negligible influence on the overall strain-energy.

The **Ogden wrinkling model** (3.77) has been implemented in the commercial FE code ABAQUS, through the user-defined material subroutine UMAT. A preliminary verification have been performed by comparing the Ogden wrinkling model

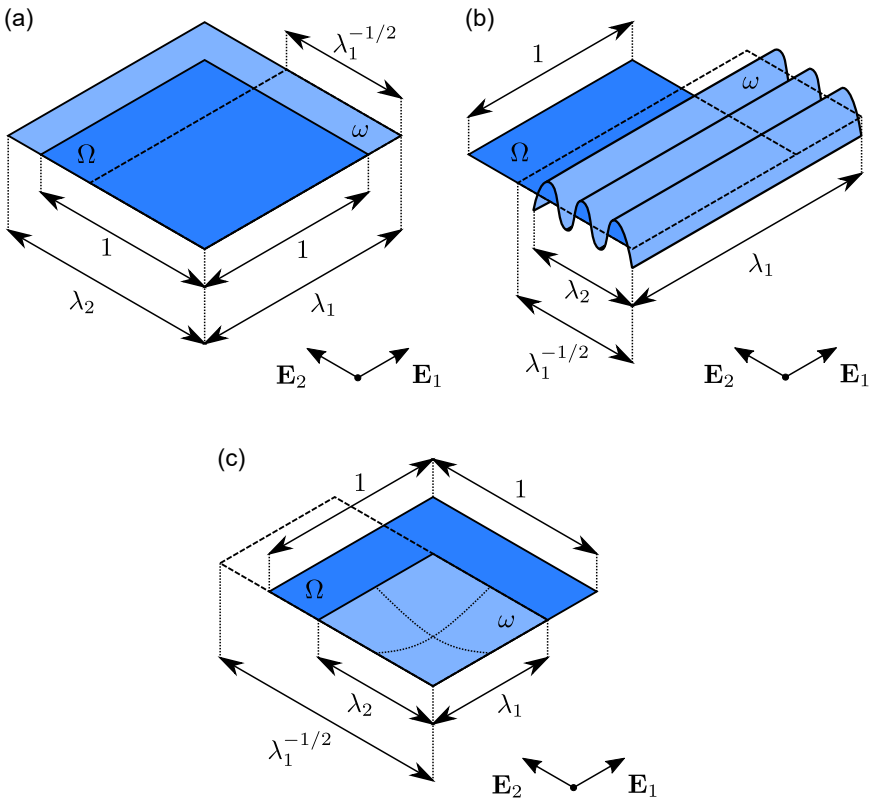

Figure 3.3: Reference Ω and deformed ω configurations of a unit membrane element. (a) Taut, (b) wrinkled and (c) slack configurations.

to the standard Ogden model of the ABAQUS library, under uniaxial tension and uniaxial and equibiaxial compression. As expected, the stress-strain response in uniaxial tension is not influenced by wrinkling (Figure 3.4(a)), while the uniaxial and biaxial compression cases highlight a significant reduction of the compressive stresses due to wrinkling, by one and two orders of magnitude, respectively (Figure 3.4(b)-(c)).

In order to explore the capabilities of the implemented Ogden wrinkling model in predicting the non-linear response of hyperelastic membranes, two relevant illustrative examples have been analyzed. The first one is related to a rectangular polyethylene membrane beam under bending, which was introduced by Barsotti *et al.* [171] and later employed by Massabò and Gambarotta [68] to test their

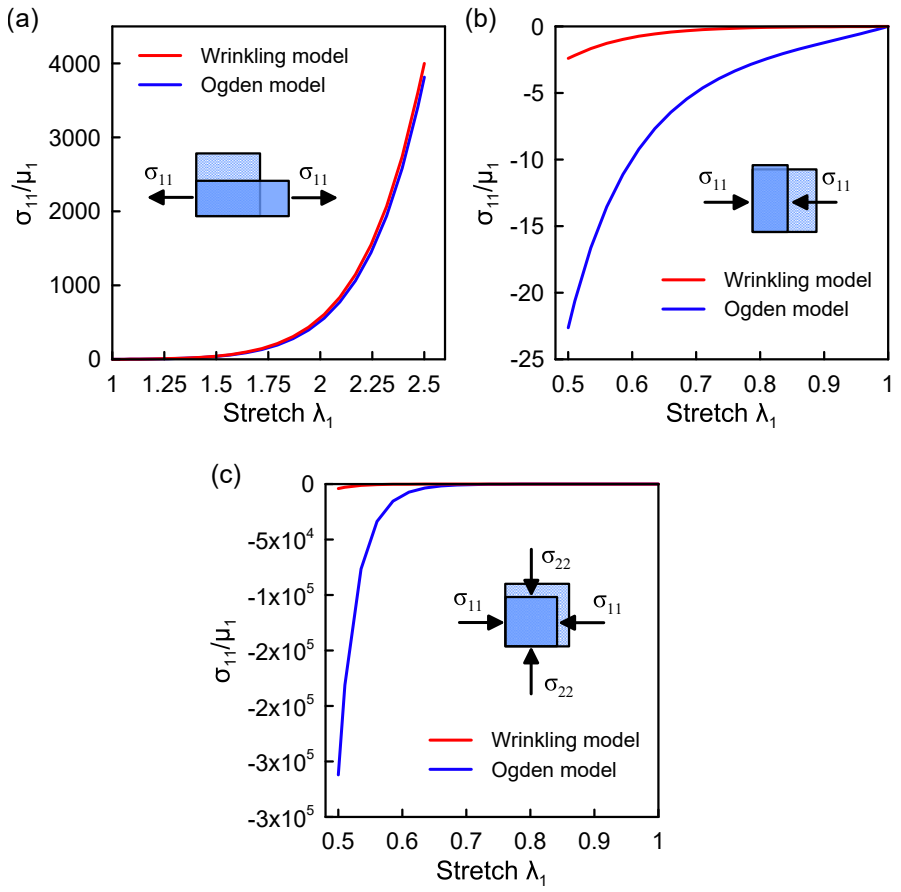

Figure 3.4: Normalized stress-stretch responses on a single plane stress element analyzed with the standard Ogden function Ψ_o in Equation (3.74) (solid blue line) and the Ogden wrinkling model based on the relaxed function Ψ_w in Equation (3.77) (solid red lines). Material parameters: $\mu_1 = 200\,\text{Pa}$, $\alpha_1 = 9$. (a) Uniaxial tension, (b) uniaxial compression, and (c) equibiaxial compression. The slightly stiffer response in (a), as well as the non-zero response under compression in (b) and (c), is due to the introduction of the non-wrinkling term (weighted with $\nu = 10^{-2}$) to prevent ill-conditioning during slackness and wrinkling.

wrinkling model. The second example refers to a rectangular silicone membrane containing an elliptical hole under tension, which was tested experimentally by Spagnoli *et al.* [172].

Example 1: Rectangular Beam Under Bending

The geometry of the first example consists of a rectangular elastomeric beam with span $l = 75$ mm, height $h = 25$ mm and thickness $t = 1$ mm, laterally constrained along the shorter edge, with imposed displacements $u_2 = -6$ mm applied to the central fifth of the lower edge [171]. The model has been discretized with a uniform mesh of 1700 3-nodes plane stress isoparametric elements (CPS3), with an average size $h_{avg} = 1.5$ mm. The mechanical behavior of the material was described by Massabò and Gambarotta [68] using an exponential isotropic Fung model. The equivalent first-order Ogden constants, fitted under uniaxial tension, are $\mu_1 = 749.18$ Pa and $\alpha_1 = 17.14$.

Figure 3.5 shows the resulting stretch domains, obtained by comparing the Ogden wrinkling model with the standard Ogden one. Taut regions, characterized by two positive principal stress components, are highlighted in red, while wrinkled regions, with only one positive principal stress, have been colored in green. Slack regions where both the principal stresses are negative are blue marked. Note that, using the standard Ogden function, regions are simply identified through the value of the principal stretches, see Figure 3.3. The main differences between the two models can be found in the central portion of the membrane. With the standard Ogden model (Figure 3.5(a)), a wide central taut region exists, which is separated from the top slack domain by a small strip of wrinkled membrane. Along the lateral edges, the membrane is taut at top and slack at bottom with a triangular shape. In the case with the Ogden wrinkling model (Figure 3.5(b)), the top slack domain extends downward to the taut region, which is here narrower. Furthermore, taut zones near the lateral edges disappear. The domains in Figure 3.5(b) compare qualitatively good with those observed in experiments, see Figure 3.5(c). In Figure 3.6, the total vertical reaction force F along the constrained lower edge is shown against the imposed displacement, showing a relaxation in the situation where the Ogden wrinkling model is used.

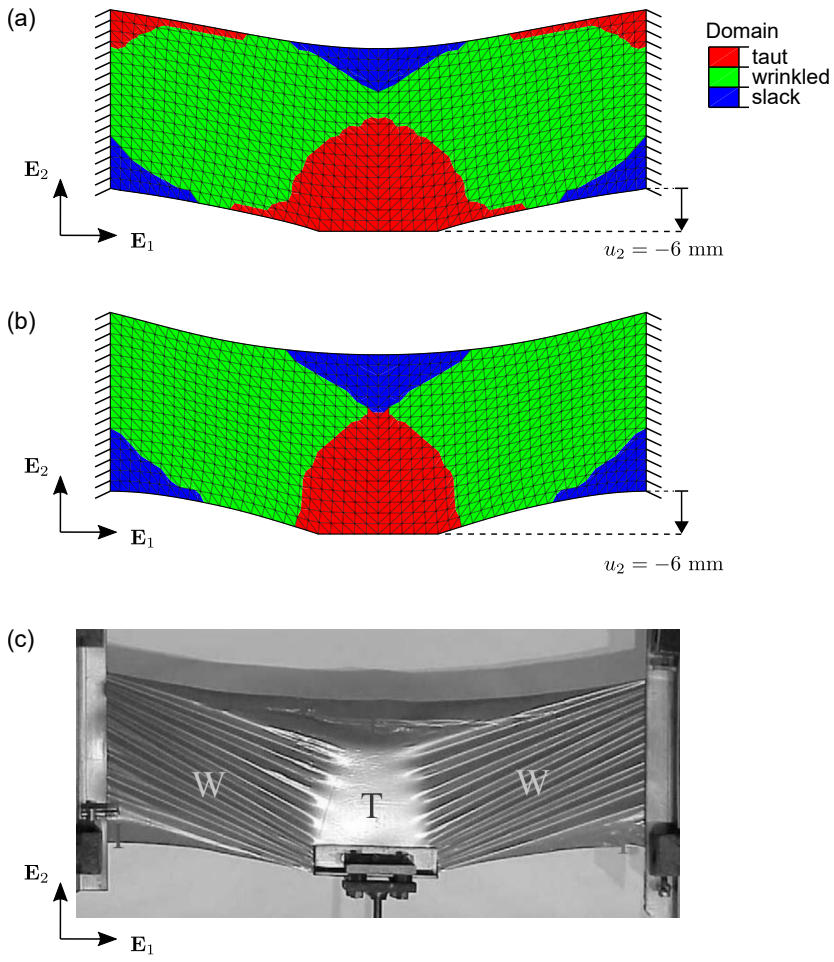

Figure 3.5: Comparison of the strain domains maps (taut: red, wrinkled: green, and slack: blue) plotted onto the deformed configuration of a rectangular membrane beam analyzed with the Ogden wrinkling model and the standard Ogden model. (a) Rectangular membrane beam analyzed with standard Ogden model and (b) the Ogden wrinkling model. (c) Experimental test on a clamped rectangular polyethylene membrane conducted by Barsotti *et al.* [171].

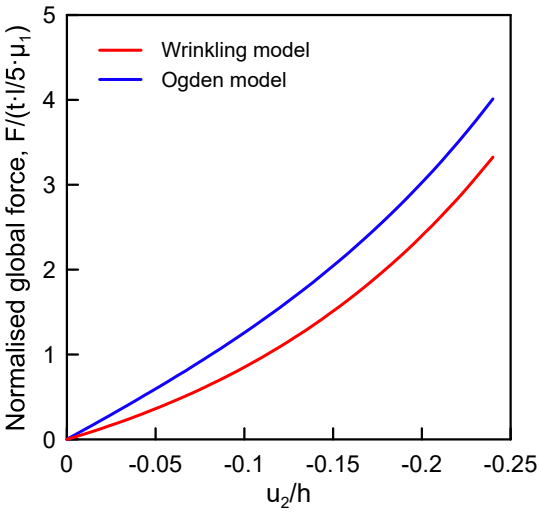

Figure 3.6: Normalized force-displacement curves of the rectangular beam under bending. The global force F has been divided by the loaded area $l/5 \cdot t$ and normalized with respect to μ_1.

Example 2: Notched Sheet Under Tension

The geometry of the second example consists of a rectangular silicone polymer sheet with width $l = 117$ mm, height $h = 234$ mm and thickness $t = 2$ mm, containing a centered elliptical notch, with semi-axes $r_1 = 20$ mm and $r_2 = 5$ mm aligned with $\mathbf{E}_1$ and $\mathbf{E}_1$, respectively. The material constants are $\mu_1 = 0.461$ MPa and $\alpha_1 = 2$ [172]. The membrane is clamped on top and bottom edges and is stretched by applying a vertical displacement $u_2 = 60$ mm, corresponding to a remotely applied stretch of $\lambda_0 \approx 1.25$. The model has been discretized with 3-nodes plane stress isoparametric elements (CPS3), with a minimum size $h_{min} = 0.6$ mm near the notch, and a maximum size $h_{max} = 5$ mm at the constrained edges.

A comparison of the analyses, conducted using the standard Ogden model and the Ogden wrinkling model, is shown in Figure 3.7. Both models show a characteristic X-shaped wrinkling region, which seems to extend larger for the membrane analyzed with the Ogden wrinkling model (Figure 3.7(b)). Slack regions are small and localized near the top and bottom edges of the ellipse. Interestingly, a rele-

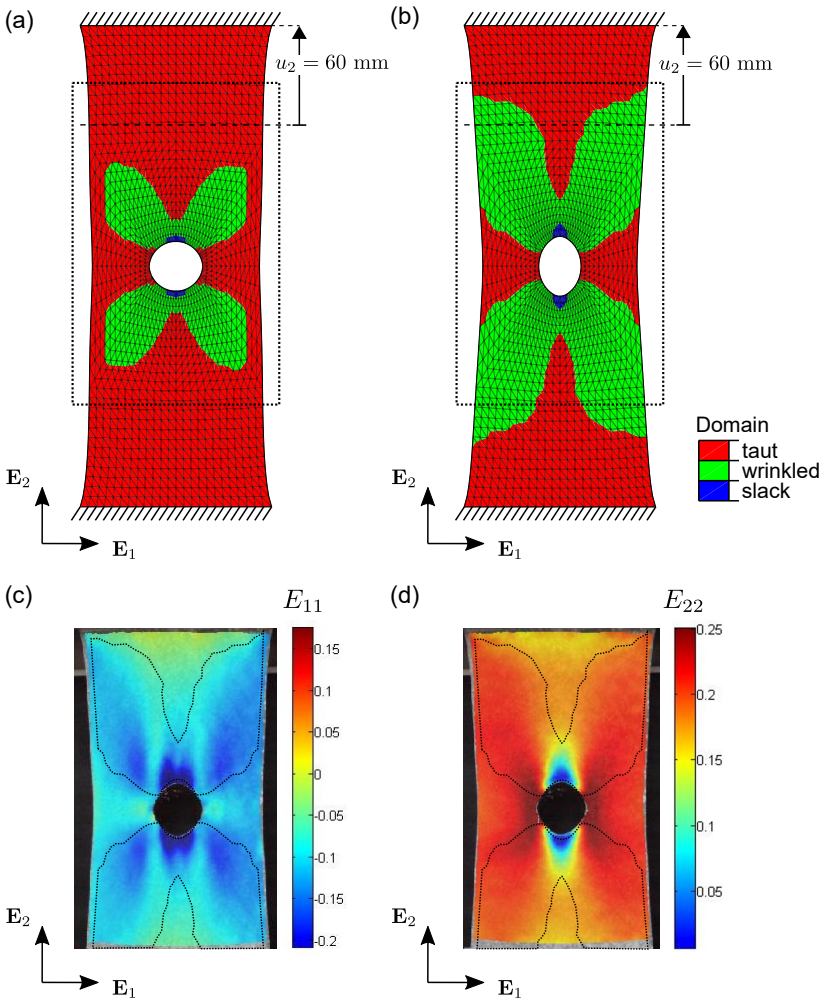

Figure 3.7: Comparison of the strain domains maps (taut: red, wrinkled: green, and slack: blue) plotted onto the deformed configuration of a notched rectangular membrane analyzed with the Ogden wrinkling model and the standard Ogden model. (a) Notched rectangular membrane analyzed with standard Ogden model and (b) the Ogden wrinkling model. Dotted boxes in (a) and (b) highlight the same area shown in the experimental full-field maps in (c)-(d) showing, respectively, the components E_{11} and E_{22} of the Green-Lagrange strain tensor $\mathbf{E} = \frac{1}{2}(\mathbf{C} - \mathbf{I})$, measured with a DIC system [172]. Regions by dotted lines in (c)-(d) represent the winkling area predicted by the Ogden wrinkling model in (b).

vant difference in the shape of the deformed elliptical notch can be appreciated. Initially wider in the horizontal direction, the inner ellipse transforms into a circle upon deformation in the first case (Figure 3.7(a)), and in a vertically extended ellipse in the second (Figure 3.7(b)). This behavior highlights the effective reduction of the stiffness in compression with the Ogden wrinkling model, allowing higher compressive stretches in the transversal direction to develop. From a qualitative point of view, the Ogden wrinkling model shows an improved prediction of the experimental X-shaped wrinkling area, which in Figure 3.7(c) is represented by the blue butterfly-like region. In fact, since the vertical component E_{22} of the Green-Lagrange strain tensor $\mathbf{E} = \frac{1}{2}(\mathbf{C}-\mathbf{I})$ is mostly positive across the domain (Figure 3.7(d)), larger negative E_{11} strains represents wrinkling areas. Similarly to the previous example, the total vertical reaction force on the clamped top edge illustrated in Figure 3.8 confirms a slight relaxation obtained with the Ogden wrinkling model.

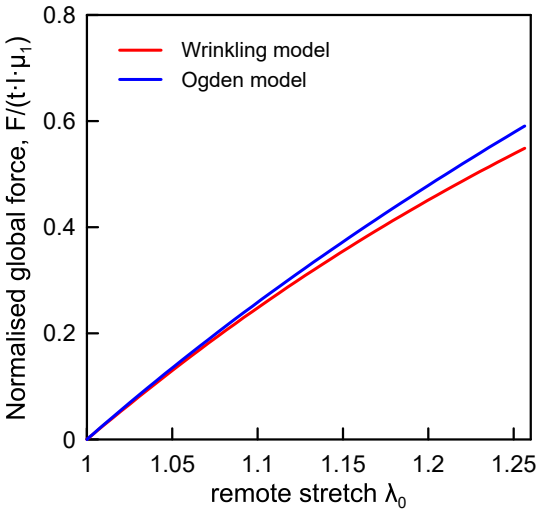

Figure 3.8: Normalized force-displacement curves of the notched sheet under tension. The global force F has been divided by the section area $l \cdot t$ and normalized with respect to μ_1.

3.2.2 Description of General Fiber Distributions

As described in Section 3.1.3, fiber-reinforced materials with a non-uniform fiber dispersion display a stiffer response along the preferential fiber directions $\mathbf{M}_i$. Based on experimental evidences, collagen fibers in soft biological tissues, like skin and aortic walls, have one or more fiber families laying almost parallel to the mean tissue plane [103, 173]. To account for general fiber distributions in the mechanical models, we assume each fiber family to be described by a Probability Density Function (PDF) $\rho_i(\mathbf{N}) = \rho_i(\theta, \phi)$ providing the normalized angular density of the fibers in the direction of the unit vector

$$\mathbf{N}(\theta, \phi) = \cos\phi \cos\theta \mathbf{E}_1 + \cos\phi \sin\theta \mathbf{E}_2 + \sin\phi \mathbf{E}_3 \,, \tag{3.78}$$

defined in the Cartesian basis $\{\mathbf{E}_1, \mathbf{E}_2, \mathbf{E}_3\}$ (Figure 3.9(a)) by the azimuth angle θ and the elevation angle ϕ. Hence, the global fiber distribution can be written as

$$\rho(\mathbf{N}) = \sum_{i=1}^{m} \nu_i \rho_i(\mathbf{N}) \,, \tag{3.79}$$

where ν_i represents the volume fraction ($\Sigma \nu_i = 1$) of the fiber family, and m is the total number of fiber families. Each distribution must satisfy the normalization condition over the unit sphere $\mathbb{S}^2$

$$\frac{1}{4\pi} \int_{\mathbb{S}^2} \rho_i(\mathbf{N}) \mathrm{d}S = \int_{\theta=-\pi}^{\pi} \int_{\phi=-\pi/2}^{\pi/2} \rho_i(\theta, \phi) \cos\phi \, \mathrm{d}\theta \mathrm{d}\phi = 1 \,. \tag{3.80}$$

To precisely describe the non-symmetrical distribution of the fiber family about its preferential direction $\mathbf{M}_i$, the PDF is assumed to be a bivariate distribution decoupled in the form

$$\rho_i(\mathbf{N}) = \rho_{\mathrm{ip},i}(\mathbf{N}) \, \rho_{\mathrm{op},i}(\mathbf{N}) \,, \tag{3.81}$$

in which $\rho_{\mathrm{ip},i}(\mathbf{N})$ and $\rho_{\mathrm{op},i}(\mathbf{N})$ are two independent univariate PDFs defined in the principal orthonormal basis $\{\mathbf{M}_i, \mathbf{M}_{\mathrm{ip},i}, \mathbf{M}_{\mathrm{op},i}\}$ of the i-th fiber family (Figure 3.9(b)). Specifically, $\{\mathbf{M}_i, \mathbf{M}_{\mathrm{ip},i}\}$ defines the mean plane of the fiber family, and $\mathbf{M}_{\mathrm{op},i}$ is the out-of-plane normal. The rotation of this basis relative to the global basis $\{\mathbf{E}_i\}_{i=1,2,3}$ is described by the triplet of angles α_i, β_i, γ_i, where the first two denote the azimuthal and elevation angle of the mean fiber direction, $\mathbf{M}_i = \mathbf{N}(\alpha_i, \beta_i)$, while the last is the rotation of the frame about $\mathbf{M}_i$ (Figure 3.9(c)). Since a fiber orientation is identified independently of the direction of $\mathbf{N}$, we require ρ_i to be symmetric such that $\rho_i(\mathbf{N}) = \rho_i(-\mathbf{N})$, or equivalently $\rho_i(\theta, \phi) = \rho_i(\theta + \pi, -\phi)$.

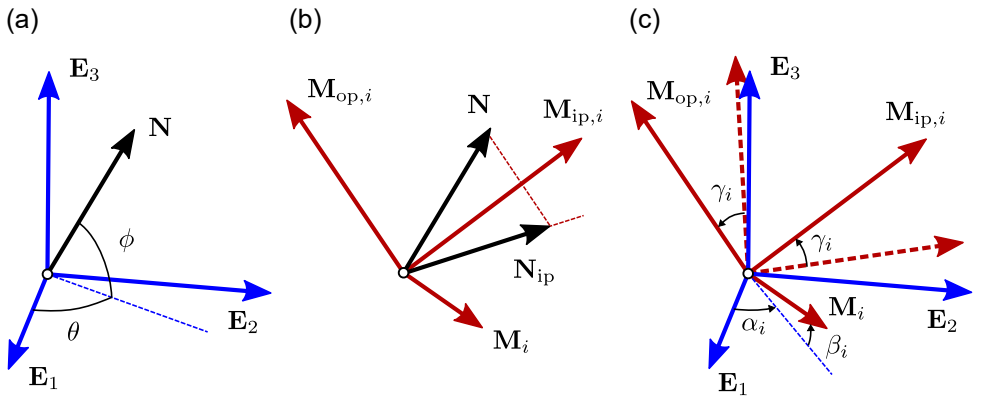

Figure 3.9: Schematic representation of the orientation of the unit vector $\mathbf{N}$ (in black), the global Cartesian basis $\{\mathbf{E}_1, \mathbf{E}_2, \mathbf{E}_3\}$ (in blue) and the principal fiber family basis $\{\mathbf{M}_i, \mathbf{M}_{\mathrm{ip},i}, \mathbf{M}_{\mathrm{op},i}\}$ (in red). (a) Unit vector $\mathbf{N}$ in the global frame; (b) unit vector $\mathbf{N}$ in the principal fiber family basis and its projection $\mathbf{N}_{\mathrm{ip}}$ onto the mean fiber plane $\{\mathbf{M}_i, \mathbf{M}_{\mathrm{ip},i}\}$; (c) rotation of the principal basis with respect to the global basis using the angles α_i, β_i, γ_i. Dashed vectors represent $\mathbf{M}_{\mathrm{ip},i}$ and $\mathbf{M}_{\mathrm{op},i}$ before the rotation about $\mathbf{M}_i$.

Thus, we specialize the in-plane and out-of-plane PDFs employing two von Mises distributions of the form

$$\rho_{\mathrm{ip},i}(\mathbf{N}) = \frac{\exp[a_i(2(\mathbf{N}\cdot\mathbf{M}_i/|\mathbf{N}_{\mathrm{ip}}|)^2 - 1)]}{I_0(a_i)}, \tag{3.82}$$

$$\rho_{\mathrm{op},i}(\mathbf{N}) = 2\sqrt{\frac{2b_i}{\pi}}\frac{\exp[-2b_i(\mathbf{N}\cdot\mathbf{M}_{\mathrm{op},i})^2]}{\mathrm{erf}(\sqrt{2b_i})}, \tag{3.83}$$

where the vector $\mathbf{N}_{\mathrm{ip}}$ represent the projection of $\mathbf{N}$ onto the plane $\{\mathbf{M}_i, \mathbf{M}_{\mathrm{ip},i}\}$. The functions $I_0(\bullet)$ and $\mathrm{erf}(\bullet)$ are the zero-order Bessel function of type I, and the error function of $(\bullet)$, respectively, which ensure the normalization condition (3.80). The constants a_i and b_i are parameters that define the in-plane and out-of-plane concentrations, respectively. The limit case of a_i, $b_i \to \infty$ corresponds to perfect fiber alignment along the mean fiber direction $\mathbf{M}_i$, while for a_i, $b_i \to 0$ an isotropic distribution is obtained. Negative values are also admissible, but describe a fiber distribution no longer concentrated in the direction $\mathbf{M}_i$. For instance, $a_i = 0$ and $b_i < 0$ represent an axially symmetric fiber distribution with preferential direction along $\mathbf{M}_{\mathrm{op},i}$.

The particular choice for the distributions in Equations (3.82) and (3.83) ver-

ifies the above-mentioned symmetry requirement $\rho_i(\mathbf{N}) = \rho_i(-\mathbf{N})$, and has the additional symmetries about $\mathbf{M}_i$ in-plane and out-of-plane. Then, each fiber family is fully described by the parameters set $\{a_i,\ b_i,\ \alpha_i,\ \beta_i,\ \gamma_i,\ \nu_i\}$.

3.2.3 GST Model for Non-Symmetrical Fiber Dispersions

Within the framework defined in Section 3.2.2, it is possible to define a strain-energy function based on a generalized fourth invariant $I^*_{4,i}$, which accounts for the non-uniform fiber dispersion through the distribution in Equation (3.81). Following [80], and recalling Equation (3.49), this invariant is defined as

$$I^*_{4,i} = \frac{1}{4\pi}\int_{\mathbb{S}^2} \rho_i(\mathbf{N})\, I_{4,i}\mathrm{d}S = \frac{1}{4\pi}\int_{\mathbb{S}^2} \rho_i(\mathbf{N})\, \mathbf{C}:\mathbf{N}\otimes\mathbf{N}\mathrm{d}S\,. \tag{3.84}$$

Since the tensor $\mathbf{C}$ does not depend on $\mathbf{N}$ it can be taken outside the integral, such that Equation (3.84) can be rewritten as

$$I^*_{4,i} = \mathbf{C}:\mathbf{H}_i, \quad \text{with} \quad \mathbf{H}_i = \frac{1}{4\pi}\int_{\mathbb{S}^2} \rho_i(\mathbf{N})\,\mathbf{N}\otimes\mathbf{N}\mathrm{d}S\,, \tag{3.85}$$

where $\mathbf{H}_i$ is the so called Generalized Structure Tensor (GST). The normalization condition (3.80) ensures that for a uniform distribution $\rho_i(\mathbf{N})$ an isotropic structure tensor $\mathbf{H}_i = \mathbf{I}$ is obtained. Explicit calculation of $\mathbf{H}_i$ leads to the following expression in closed form

$$\begin{aligned}\mathbf{H}_i =& 2\kappa_{\mathrm{ip},i}\kappa_{\mathrm{op},i}\mathbf{I} + 2\kappa_{\mathrm{op},i}\left(1-2\kappa_{\mathrm{ip},i}\right)\mathbf{M}_i\otimes\mathbf{M}_i \\ &+ \left(1-2\kappa_{\mathrm{op},i}-2\kappa_{\mathrm{ip},i}\kappa_{\mathrm{op},i}\right)\mathbf{M}_{\mathrm{op},i}\otimes\mathbf{M}_{\mathrm{op},i}\,,\end{aligned} \tag{3.86}$$

in which $\kappa_{\mathrm{ip},i}$ and $\kappa_{\mathrm{op},i}$ are the in-plane and out-of-plane dispersion parameters, respectively, computed as

$$\kappa_{\mathrm{ip},i} = \frac{1}{2}\left(1 - \frac{I_1(a_i)}{I_0(a_i)}\right), \tag{3.87}$$

$$\kappa_{\mathrm{op},i} = \frac{1}{2} - \frac{1}{8b_i} + \frac{1}{4}\sqrt{\frac{2}{\pi b_i}}\frac{\exp(-2b_i)}{\mathrm{erf}(\sqrt{2b_i})}, \tag{3.88}$$

with $I_0(\bullet)$ and $I_1(\bullet)$ denoting the Bessel function of type I of order zero and one, respectively. From Equations (3.85) and (3.86) the generalized fourth invariant

can be also directly computed in terms of invariants I_1, $I_{4,i}$, $I_{\mathrm{op},i}$, i.e.

$$\begin{aligned} I^*_{4,i} =& 2\kappa_{\mathrm{ip},i}\kappa_{\mathrm{op},i} I_1 + 2\kappa_{\mathrm{op},i}\left(1-2\kappa_{\mathrm{ip},i}\right) I_{4,i} \\ &+ \left(1-2\kappa_{\mathrm{op},i}-2\kappa_{\mathrm{ip},i}\kappa_{\mathrm{op},i}\right) I_{\mathrm{op},i}\,. \end{aligned} \tag{3.89}$$

Plots of the dispersion parameters are shown in Figure 3.10. Note that $0 \leq \kappa_{\mathrm{ip},i} \leq 1$ and $0 \leq \kappa_{\mathrm{op},i} \leq 0.5$. The isotropic fiber dispersion is achieved for $a_i,\ b_i = 0$ which are associated to $\kappa_{\mathrm{ip},i} = 1/2$ and $\kappa_{\mathrm{op},i} = 1/3$. In this case, the generalized fourth invariant from Equation (3.89) reduces to $I^*_{4,i} = 1/3 I_1$, clearly representing an isotropic invariant. An axially symmetric distribution about $\mathbf{M}_{\mathrm{op},i}$ can be obtained by setting $a_i = 0$ and $b_i < 0$, for which $I^*_{4,i} = \kappa_{\mathrm{op},i} I_1 + \left(1-3\kappa_{\mathrm{op},i}\right) I_{\mathrm{op},i}$. Lastly, for $a_i,\ b_i \to \infty$ the dispersion parameters become $\kappa_{\mathrm{ip},i} = 0$ and $\kappa_{\mathrm{op},i} = 1/2$, representing a perfect fiber alignment with a generalized fourth invariant dependent solely on the deformation along $\mathbf{M}_i$, $I^*_{4,i} = I_{4,i}$.

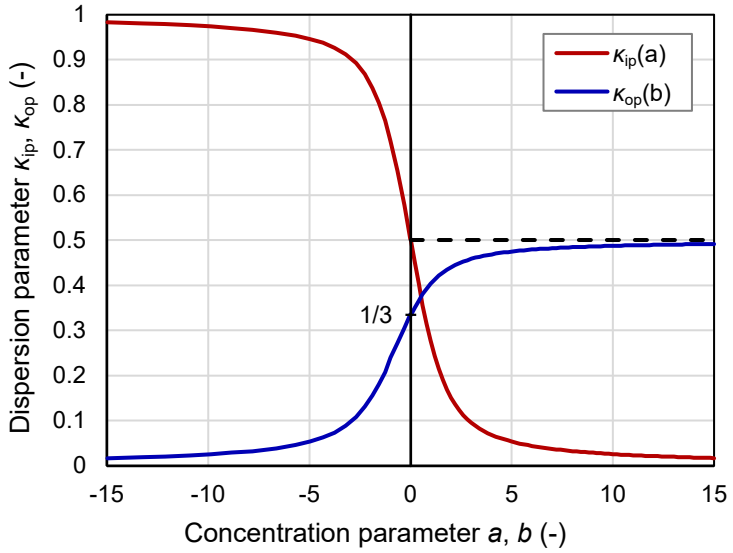

Figure 3.10: Plots of the in-plane and out-of-plane dispersion parameters κ_{ip} and κ_{op} versus the von Mises concentration parameters a and b, respectively, according to Equations (3.87) and (3.88).

Now the generalized fourth invariant $I^*_{4,i}$ can be used to formulate a strain-energy function accounting for the non-uniform fiber dispersion. Following the work of Holzapfel *et al.* [80], the total strain-energy function for soft collagenous materials is obtained by superposition of the strain-energies contributions of the

ground matrix Ψ_{g}, and the fiber families $\Psi_{\mathrm{f},i}$, given by

$$\Psi = \Psi_{\mathrm{g}} + \sum_{i=1}^{m} \nu_i \Psi_{\mathrm{f},i} \,, \tag{3.90}$$

in which the energy contribution of each family is weighted with its volume fraction ν_i. The isotropic ground matrix is modeled as a neo-Hookean material [161], whose function reads

$$\Psi_g = \frac{\mu}{2} (I_1 - 3) \,. \tag{3.91}$$

Note that Equation (3.91) represents a special case of the Ogden model (3.74) assuming a single order of parameters, $N = 1$, with $\alpha_1 = 2$. To capture the highly non-linear behavior of the collagen fibers in tension, the function is assumed to be of exponential type [78, 80], i.e.

$$\Psi_{\mathrm{f},i} = \frac{k_1}{2k_2} \left\{ \exp\left[k_2 \left(I^*_{4,i} - 1 \right)^2 \right] - 1 \right\} \,, \tag{3.92}$$

where k_1 is a stiffness-like parameter and k_2 a dimensionless parameter controlling the hardening.

Being the generalized fourth invariant $I^*_{4,i}$ herein presented defined for a general orientation of the i-th fiber family in the Euclidean space $\{\mathbf{E}_1, \mathbf{E}_2, \mathbf{E}_3\}$, the formulation (3.92) represents a generalization of the model introduced by Holzapfel *et al.* [80], in which the fiber families were assumed to be all co-planar, such that $\mathbf{M}_{\mathrm{op},i} \equiv \mathbf{E}_3$, $i = 1, \ldots, m$.

The model (3.90) has been implemented in a custom MATLAB script (v. R2023a; The MathWorks Inc., Natick, MA, USA).

3.2.4 Discrete Fiber Dispersion Model

According to the hypothesis of Lanir [77], collagen fibers can be approximated as slender uniaxial entities which buckle in compression with almost zero stress. They bear loads only when positively stretched, $\lambda > 1$, and therefore their contribution in compression should be neglected.

In the GST model described in Section 3.2.3 the fiber strain-energy $\Psi_{\mathrm{f},i}$ is a function of a generalized structure tensor $\mathbf{H}_i$ which accounts for all the fibers in the unit sphere domain $\mathbb{S}^2$. The main advantage of this approach is that $\mathbf{H}_i$ can be easily computed employing the explicit expression in Equation (3.86) independent of the state of deformation. This guarantees a low computational cost, as the structure tensor needs to be computed only a single time before the analysis [78,

80]. However, all the fibers are included *a priori* into the model, and, as proposed in recent studies [84, 174], the introduction of a compression switch that excludes compressed fibers requires repeated numerical integrations of $\mathbf{H}_i$, vanishing the advantages of the GST approach.

In Angular Integration (AI) models the probability distribution is used to weight the single fiber strain-energy $\Psi\left(I_4\right)$ along all the directions $\mathbf{N}$, such that the total fiber strain energy $\Psi_{\mathrm{f},i}$ is given by

$$\Psi_{\mathrm{f},i} = \frac{1}{4\pi} \int_{\mathbb{S}^2} \rho_i\left(\mathbf{N}\right) \Psi\left(I_4\right) \mathrm{d}S \,, \tag{3.93}$$

where $I_4 = \mathbf{C} : \mathbf{N} \otimes \mathbf{N}$. The main disadvantage of AI models is that, except for simple cases, it requires multiple integration during the analysis, with consequent low computational efficiency.

Following the method proposed by Li *et al.* [87], the computation efficiency of AI models can be increased by discretizing the integration of $\Psi_{\mathrm{f},i}$ using a finite number of representative fiber directions $\mathbf{N}_j$, hence, turning the AI model into a Discrete Fiber Dispersion (DFD) model. Accordingly, the integral (3.93) is approximated as

$$\Psi_{\mathrm{f},i} \approx \sum_{j=1}^{n} \rho_i\left(\mathbf{N}_j\right) \Psi\left(I_{4,j}\right) w_j = \sum_{j=1}^{n} \rho_{i,j} \Psi\left(I_{4,j}\right) \,, \tag{3.94}$$

where n is the number of representative fiber directions, w_j is the weight defined by the particular integration scheme over the unit sphere, and $\rho_{i,j} = \rho_i\left(\mathbf{N}_j\right) w_j$ is the discrete fiber density. Recalling Equation (3.80), the normalization condition is now defined as

$$\sum_{j=1}^{n} \rho_{i,j} = 1 \,. \tag{3.95}$$

Hence, employing the approximation in Equation (3.94) the energy of the compressed fibers can be efficiently neglected by defining a criterion based on $I_{4,j}$. Accordingly, the single fiber strain-energy is specialized as

$$\Psi\left(I_{4,j}\right) = \begin{cases} \dfrac{c_1}{2c_2} \left\{ \exp\left[c_2 \left(I_{4,j} - 1\right)^2 \right] - 1 \right\}, & I_{4,j} \geq 1 \,, \\ 0, & I_{4,j} < 1 \,, \end{cases} \tag{3.96}$$

with c_1 and c_2 denoting the two material parameters, analogue to k_1 and k_2 in Equation (3.92), respectively.

Li *et al.* [87] proposed to compute the discrete fiber densities $\rho_{i,j}$ using

$$\rho_{i,j} = \frac{1}{4\pi} \int_{\Delta\mathbb{S}^2_j} \rho_i\left(\mathbf{N}_j\right) \mathrm{d}S \,, \tag{3.97}$$

in which $\Delta\mathbb{S}^2_j$ is the unit sphere subdomain associated to the representative fiber direction $\mathbf{N}_j$. In our case, instead of using Equation (3.97), we adopt the Lebedev quadrature rule, which can exactly integrate polynomials of degree up to 131 [175]. Representative directions $\mathbf{N}_j$ and relative weights w_j of this technique are predefined and specific for a determined basis $\{\mathbf{L}_i\}_{i=1,2,3}$. Indeed, this technique exploits octahedral rotation and inversion symmetries to build a uniform integration points grid on the unit sphere (see Figure 3.11), with the advantage of having same and non-negative weights for all the points that are equivalent under a specific rotational and inversion group. In general, quadrature schemes give the same result under any rigid rotation of the integration points relative to the integrand function. With reference to Equation (3.94), this means that any rotation of the representative directions $\mathbf{N}_j$ relative to the principal fiber basis $\{\mathbf{M}_i, \mathbf{M}_{\mathrm{ip},i}, \mathbf{M}_{\mathrm{op},i}\}$ associated to $\rho_i(\mathbf{N})$ produces the same result. Therefore, without loss of generality, we can choose $\{\mathbf{L}_i\}_{i=1,2,3}$ to be coincident with the basis $\{\mathbf{M}_i, \mathbf{M}_{\mathrm{ip},i}, \mathbf{M}_{\mathrm{op},i}\}$. In this way, we make coincide both the symmetries of $\rho_i(\mathbf{N})$ - as defined in Equation (3.81) - and the representative directions $\mathbf{N}_j$. This translates in a symmetric mechanical response for deformations symmetric about the principal fiber directions. This also allows us to reduce the computational cost by restricting the integration to only on one half of the sphere domain $\mathbb{S}^2$, since each fiber family distribution is independent of the verse of $\mathbf{N}$, $\rho_i(\mathbf{N}) = \rho_i(-\mathbf{N})$.

Once defined the $\Psi_{\mathrm{f},i}$ using Equation (3.94), the total strain-energy function is obtained by adding the isotropic contribution of the ground matrix as defined in Equation (3.90), i.e.

$$\Psi = \Psi_g + \sum_{i=1}^{m} \nu_i \Psi_{\mathrm{f},i} \,. \tag{3.98}$$

The DFD model (3.98) has been implemented in the commercial FE code ABAQUS, through the user-defined material subroutine UMAT, and in a custom MATLAB script (v. R2023a; The MathWorks Inc., Natick, MA, USA). To define the minimum number of representative fiber direction for the integration, a calibration has been performed by analyzing an annular disk with an isotropic fiber dispersion. Then, to illustrate the numerical performances of the implemented model, two examples in uniaxial and pure shear deformation with one element have been analyzed, and

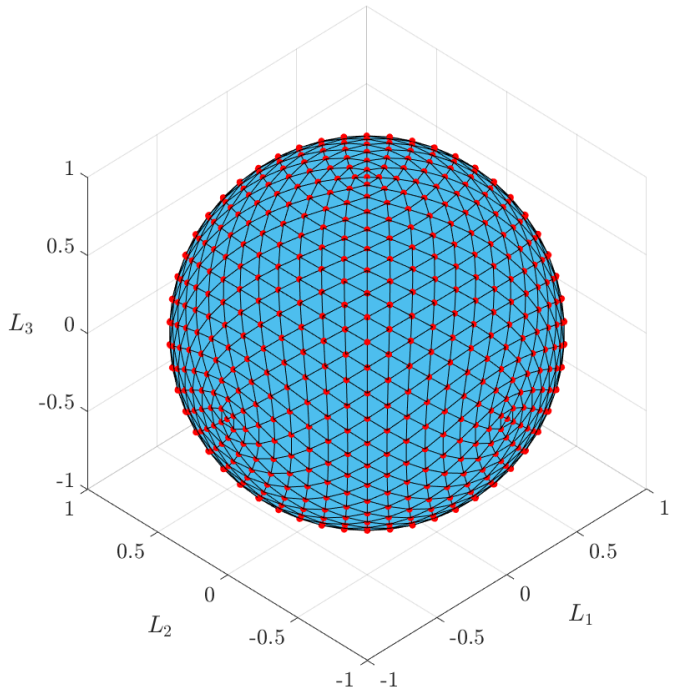

Figure 3.11: Distribution of 974 Lebedev integration points (red dots) on the unit sphere in the basis $\{\mathbf{L}_i\}_{i=1,2,3}$. A triangular mesh is shown for visualization purposes, and does not represent any influence area related to the points.

the results compared with the analytical solution provided by exactly integrating Equation (3.93) [176].

Model Calibration

The number n of representative fiber direction must be carefully selected. A poor number of integration points produces inaccurate mechanical predictions, but, on the other hand, an excessive number increases the computational cost. To select the proper n we then analyze a problem with an isotropic fiber distribution. By definition, a material is isotropic if the mechanical response is independent of the direction of the applied deformation, i.e. if the strain-energy is the same for any rigid body rotation in the reference configuration, $\Psi(\mathbf{F}) = \Psi\left(\mathbf{F}\mathbf{Q}^{\mathrm{T}}\right)$, for any orthogonal tensor $\mathbf{Q}$ [156]. If n is sufficiently high, an isotropic fiber distribution verifies such isotropy requirement. Otherwise, possible integration-induced

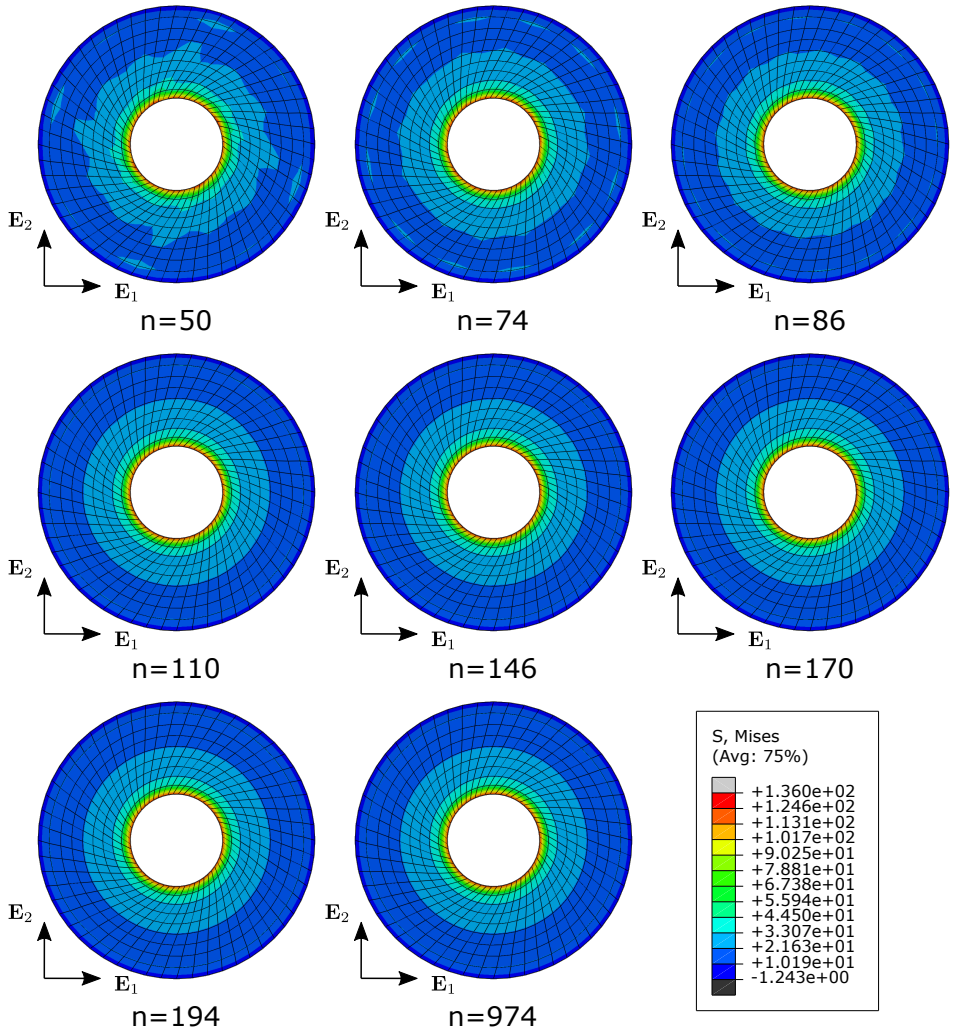

Figure 3.12: Contour plot of the von Mises stress of the annular disk solved employing $n = 50, 74, 86, 110, 146, 170, 194$ representative fiber directions (solutions for $n = 230, 266, 302$ not shown) compared to the reference model solved with $n = 974$.

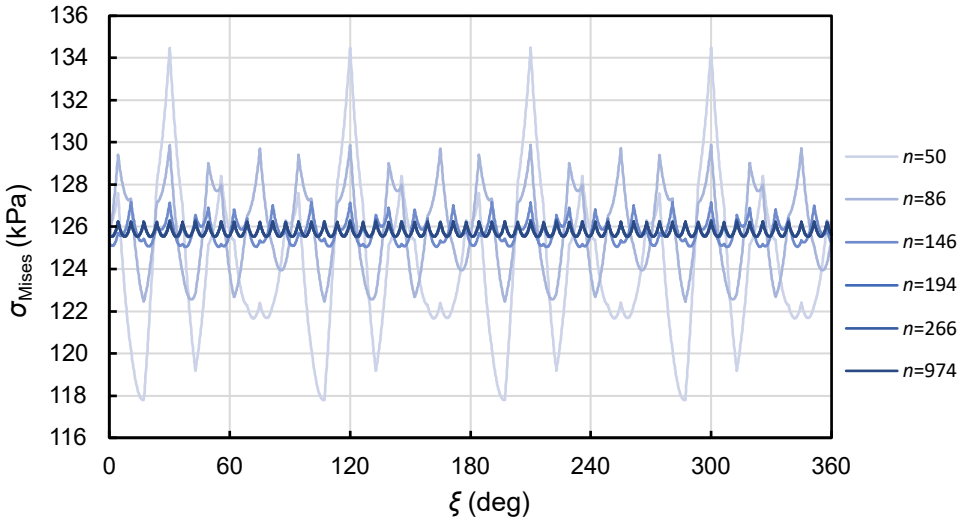

Figure 3.13: Plots of the von Mises stress versus the angle ξ from $\mathbf{E}_1$ along the inner boundary for $n = 50$, 86, 146, 194, 266 and for the reference solution $n = 974$.

anisotropy may arise [177, 178]. To find the number n that produces an isotropic mechanical response for an isotropic fiber distribution, we analyze an annular disk in which the basis $\{\mathbf{L}_i\}_{i=1,2,3}$ of the discrete fiber directions $\mathbf{N}_j$ is aligned with the global Cartesian basis$\{\mathbf{E}_i\}_{i=1,2,3}$ for every point $\mathbf{X}$ in the reference configuration Ω. The annular disk has outer radius $R_{\text{out}} = 150$ mm and inner radius $R_{\text{in}} = 50$ mm, with thickness $t = 5$ mm, and it has been discretized with 504 8-node 3D hybrid elements (C3D8H). The outer boundary is constrained in radial and tangential direction, and a counter-clockwise rotation of 30° has been applied to the inner boundary while keeping radial displacement fixed. Mechanical parameters, taken from Li *et al.* [176], are $\mu = 1.64$ kPa, $c_1 = 5.63$ kPa, $c_2 = 14.25$, with in-plane and out-of-plane fiber concentrations a, $b = 0$. Since the exact solution of the problem is clearly characterized by axial symmetry, any non-symmetric deviation is due to poor integration. The integration orders considered are $n = 50$, 74, 86, 110, 146, 170, 194, 230, 266, 302, while $n = 974$ is used as reference [177].

As shown in Figure 3.12, for low n, the solution is anisotropic, as the distribution of the von Mises stress across the domain is not axially symmetric. For a quantitative comparison we considered the distribution of the von Mises stress along the inner boundary. From Figure 3.13 is clear that high stress peaks, appearing for low n, are related to the poor quality of the integration, while, as the

number of representative directions increases, the solution converges to the reference solution ($n = 974$). Even though the exact solution should be a constant stress at ~ 126 kPa small stress fluctuations remain, arising from the interpolation within the element. In Figure 3.14 is shown the Mean Squared Error (MSE) of the von Mises stress plots in Figure 3.13 computed with respect to that of the reference solution ($n = 974$). We then select $n = 194$ as the ideal integration order, being the first value of the number n reaching a MSE lower than 10^{-2}.

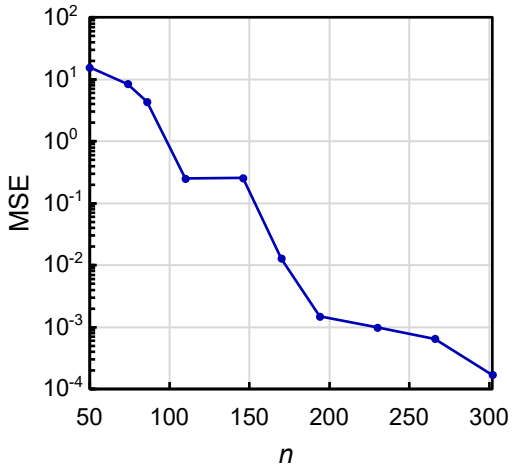

Figure 3.14: Mean Squared Error (MSE) of the von Mises stress plot versus n, computed with respect to the reference solution ($n = 974$).

Uniaxial Stretch

In this case, we consider two different transversely isotropic fiber distributions ($a = 0$) with out-of-plane concentration parameters $b = -0.01$ and $b = -5$, respectively, and fiber orientation $\alpha = \beta = \gamma = 0°$. A stretch of $\lambda = 1.2$ is applied in $\mathbf{E}_3$ direction, such that fibers are stretched along the direction $\mathbf{M}_{\text{op}}$, in plane stress condition within the $\{\mathbf{E}_1, \mathbf{E}_3\}$ plane (see Figure 3.15(a)). The analysis has been performed with a unit square element in plane stress formulation, integrated with $n = 974$ representative fiber directions. Plots of σ_{33} versus λ_3, for material parameters $\mu = 1.64$ kPa, $c_1 = 5.63$ kPa, $c_2 = 14.25$, are reported in Figure 3.15(b), and compared to the analytical solution related to Equation (3.93), given by [176].

$$\sigma_{33} = (\mu + Y_1)\,\lambda_3^2 - (\mu + Y_2)\,\lambda_3^{-1}\,, \tag{3.99}$$

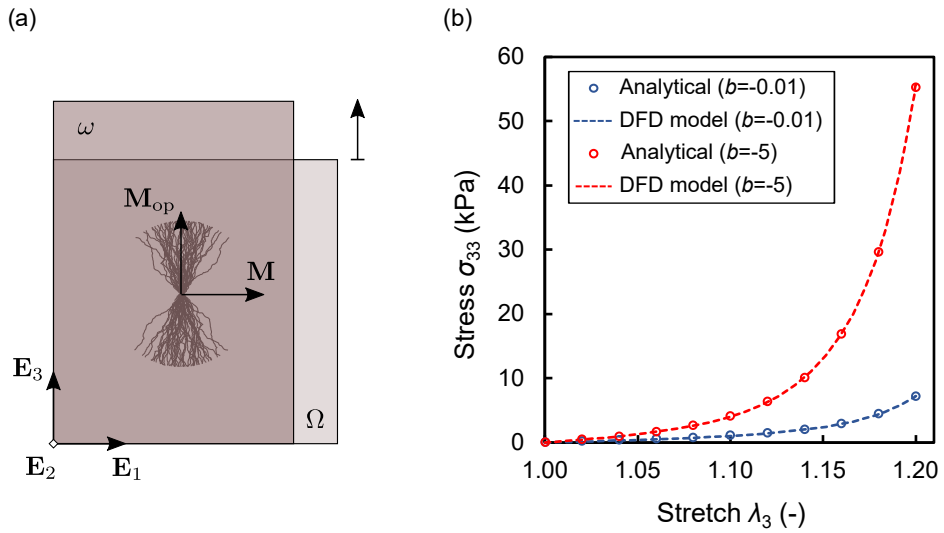

Figure 3.15: Uniaxial test on a unit square element in plane stress condition within the plane $\{\mathbf{E}_1, \mathbf{E}_3\}$. (a) Scheme of the uniaxial test, with axially symmetric fibers dispersion along $\mathbf{M}_{\text{op}}$. (b) Stress σ_{33} versus stretch λ_3 response for concentration parameters $b = -0.01$ and $b = -5$, computed from the analytical solution (circles) and the DFD model (dashed line) employing $n = 974$.

with

$$Y_1 = 2c_1 \int_{\Sigma} \rho_{\text{op}}(\mathbf{N}(\phi)) \exp\left[c_2 \left(I_4 - 1\right)^2\right] \left(I_4 - 1\right) \cos\phi \sin^2\phi \, \mathrm{d}\phi \,, \tag{3.100}$$

$$Y_2 = c_1 \int_{\Sigma} \rho_{\text{op}}(\mathbf{N}(\phi)) \exp\left[c_2 \left(I_4 - 1\right)^2\right] \left(I_4 - 1\right) \cos^3\phi \, \mathrm{d}\phi \,, \tag{3.101}$$

where $\Sigma = \left\{\phi \in [0, \pi/2] \,|\, I_4(\theta, \phi) > 1\right\}$. Equations (3.100) and (3.101) are solved numerically using a MATLAB script. As shown in Figure 3.15(b), results of the DFD model are in agreement with the analytical solution.

Simple Shear

In this case, a pure shear deformation $\gamma = 0.5$ is applied on the top element face in $\mathbf{E}_1$ direction. Two different transversely isotropic fiber distributions ($a = 0$) with out-of-plane concentration parameters $b = -1.08$ and $b = -2$, respectively, have been considered. To test the performances of the implemented model in compression, the fiber dispersion has been rotated about $\mathbf{E}_2$, using the principal fiber

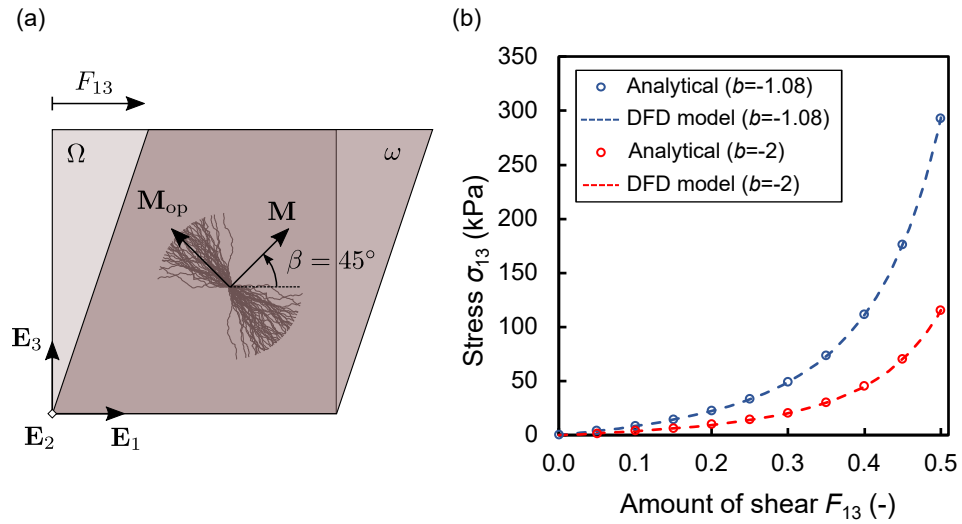

Figure 3.16: Shear test on a unit square element in plane stress condition within the plane $\{\mathbf{E}_1, \mathbf{E}_3\}$. (a) Scheme of the uniaxial test, with axially symmetric fibers dispersion along $\mathbf{M}_{op}$, left-rotated by $\beta = 45°$ about $\mathbf{E}_2$. (b) Stress σ_{13} versus F_{13} response for concentration parameters $b = -1.08$ and $b = -2$, computed from the analytical solution (circles) and the DFD model (dashed line) employing $n = 974$.

basis angles $\alpha = \gamma = 0°$, $\beta = 45°$, such that the fiber direction $\mathbf{M}_{op}$ is mainly under compression (see Figure 3.16(a)). The problem is treated in plane stress condition within the $\{\mathbf{E}_1, \mathbf{E}_3\}$ plane. The analysis has been performed with a unit square element in plane stress formulation, integrated with $n = 974$ representative fiber directions. Plots of σ_{13} versus F_{13}, for material parameters $\mu = 7.64$ kPa, $c_1 = 996.6$ kPa, $c_2 = 5.249$, are reported in Figure 3.16(b), and compared to the analytical solution related to Equation (3.93), given by [176]

$$\sigma_{13} = (\mu + Y_3) F_{13} - Y_4 \,, \tag{3.102}$$

with

$$Y_3 = \frac{c_1}{\pi} \int_\Sigma \rho(\theta, \phi) \exp\left[c_2 \left(I_4 - 1\right)^2\right] \left(I_4 - 1\right) \cos\phi \sin^2\phi \, \mathrm{d}\phi \, \mathrm{d}\theta \,, \tag{3.103}$$

$$Y_4 = \frac{c_1}{\pi} \int_\Sigma \rho(\theta, \phi) \exp\left[c_2 \left(I_4 - 1\right)^2\right] \left(I_4 - 1\right) \cos^2\phi \sin\phi \cos\theta \, \mathrm{d}\phi \, \mathrm{d}\theta \,, \tag{3.104}$$

where $\Sigma = \left\{(\theta, \phi) | I_4(\theta, \phi) > 1\right\}$. Again, Equations (3.103) and (3.104) are solved numerically using a MATLAB script. As in the previous example, results of the DFD model are in agreement with the analytical solution (Figure 3.16(b)).

Concluding Remarks

Considering the results of the examples reported, the Lebedev quadrature rule is more computationally efficient compared to the integration scheme proposed by Li *et al.* [87]. Indeed 194 integrand evaluations are sufficient to provide an accurate result compared to the reference solution (974), with further densities of the representative fiber directions providing approximately the same level of accuracy. This number is considerably lower to the 2571 to 4000 points used by Li *et al.* [87].

Chapter 4

Measurement of the Collagen Fiber Orientation Distribution

The GST and DFD constitutive models presented in Chapter 3 rely on a Probability Density Function $\rho(\mathbf{N})$, as defined in Equation (3.79), describing the normalized amount of fibers along every direction $\mathbf{N}$ in the Euclidean space. To precisely model soft collagenous materials, the function $\rho(\mathbf{N})$ must be a close approximation of the actual Fiber Orientation Distribution (FOD), which is commonly obtained experimentally by analyzing microscopic images of real tissues microstructure. In the specific case of collagen fibers, several techniques are used to acquire such images, including histological staining [110, 145], polarized light microscopy [179, 180], optical coherence microscopy [113, 181], and Second Harmonic Generation (SHG) microscopy [103, 105, 182]. Among others, SHG microscopy has become increasingly popular for its capacity to produce three - dimensional (3D), high-resolution images of collagen fibers deep within tissues without staining.

However, current methods to quantify the FOD are mainly designed for two-dimensional (2D) image analysis, yielding only planar distributions. These methods include texture analysis [107, 183], fiber segmentation and tracking (such as the CT-FIRE algorithm) [184, 185], pixel-based gradient analysis [108, 186], directional variance techniques [109, 187], Gabor filter approaches [110], and Fourier transform techniques [111–113, 188]. Notably, Fourier transform methods, including wavelet transforms, are advantageous in computational efficiency, adaptability to complex images, computational speed, and reduced sensitivity to noise and fiber crimping [113].

Two-dimensional analyses, while useful, face technical challenges that limit

the amount of information that can be extrapolated from images. One issue is that fibers at a steep angle to the image plane often get undetected, as their cross-section appears nearly circular and their direction becomes indiscernible [115]. Furthermore, existing 2D algorithms typically focus on either in-plane or out-of-plane measurements, limiting a full description of fiber dispersion. Attempting to combine in-plane and out-of-plane fiber distributions from separate 2D analyses into a 3D distribution is problematic, as reconstructing a 3D distribution from two perpendicular directions is unfeasible without covariance data.

There are only a few algorithms specifically designed for comprehensive 3D measurements, creating a notable gap in the research field [116]. For instance, Liu *et al.* [114] employed a pixel-by-pixel method to spatially describe collagen fibers and then used 3D directional variance as an average metric to evaluate fiber concentration levels. Their approach resulted in separate in-plane and out-of-plane fiber distributions. Lau *et al.* [115] developed a 3D Fourier transform method, but this technique involves the division of the 3D image into regions of interest (ROIs) and the determination of the predominant fiber orientation in each region. This approach does not account for the fiber distribution within each region, potentially overlooking critical information in regions containing multiple fiber families. Additionally, the number of obtainable measurements is limited to the number of ROIs. Rauff *et al.* [189] made a significant step forward using the 3D Fourier transform method, but their algorithm is not well optimized for large 3D images.

In this chapter, a novel 3D Fourier transform-based method for quantifying the FOD is presented [190]. This new approach offers a comprehensive 3D view of fiber dispersion in an image, enabling the identification of distinct fiber families. The algorithm features rapid computation times, even for large-sized images, making it highly suitable for both research and clinical settings. To test the efficacy and accuracy of this algorithm, 3D images with artificial fibers were created to evaluate its capability in determining in-plane and out-of-plane distribution parameters. Furthermore, the performance of the algorithm is verified for mouse and human skin collagen fibers obtained from SHG images.

4.1 Description of the Algorithm

The algorithm consists of two fundamental steps. First, the raw distribution is computed along a discrete number of fiber directions $\mathbf{N}(\theta, \phi)$ (see definition in Equation (3.78)) yielding to a discretely evaluated function $d(\theta, \phi)$, called discrete Fiber Orientation Distribution (dFOD). Then, the raw dFOD undergoes a de-

convolution process to refine $d(\theta,\phi)$ from the measurements of self-interferences occurring during the first step, thereby obtaining the final dFOD $d'(\theta,\phi)$. The algorithm is described below in details, and it is implemented in a custom MATLAB application (v. R2023a; The MathWorks Inc., Natick, MA, USA).

4.1.1 Computation of the Raw dFOD

Let $g(x,y,z)$, $g:\mathbb{N}^3\to\mathbb{R}$, be the signal in the discrete spatial domain representing a $M\times M\times M$ image (voxel volume). We assume that the x, y, z axes are aligned with the global basis vectors $\mathbf{E}_1$, $\mathbf{E}_2$, $\mathbf{E}_3$, respectively, so that the definition of the azimuthal and elevation angles θ and ϕ, as illustrated in Figure 3.9, is the same in both frames. If $g(x,y,z)$ depicts a bundle of straight fibers all oriented along a certain direction $\mathbf{N}(\theta,\phi)$ (Figure 4.1(a)), then its spectrum $\hat{g}(u,v,w)$, $\hat{g}:\mathbb{N}^3\to\mathbb{C}$, is defined by the 3D discrete Fourier transform

$$\hat{g}(u,v,w)=\sum_{x=0}^{M-1}\sum_{y=0}^{M-1}\sum_{z=0}^{M-1} g(x,y,z)e^{-i2\pi\left(\frac{ux}{M}+\frac{vy}{M}+\frac{wz}{M}\right)}, \tag{4.1}$$

where the dominant magnitudes $|\hat{g}(u,v,w)|$ (yellow voxels in Figure 4.1(b)) are scattered in a plane that pass through the center of the frequency domain, $(u,v,w)=1/2(M,M,M)$, and perpendicular to the frequency direction $\mathbf{f}(\theta,\phi)$, $[\mathbf{f}(\theta,\phi)]=[\cos\phi\cos\theta\ \ \cos\phi\sin\theta\ \ \sin\phi]^{\mathrm{T}}$. Note that the values of the spectrum are shifted such that the lower frequencies occupy the central position, with frequency $\mathrm{f}=0$ located at $(u,v,w)=1/2(M,M,M)$. Gibbs artifacts characterized by high magnitudes distributed along the u, v, w axes are removed by tapering $g(x,y,z)$ with a 3D Tukey window with 40% cosine before the transform. Note that the orientation of the plane in the frequency domain is invariant with changes in fiber position in the spatial domain. Therefore, the sum of the moduli $|\hat{g}(u,v,w)|$ filtered from this plane is a measure of the amount of straight fibers oriented towards $\mathbf{N}(\theta,\phi)$. Due to the aliasing filter plane, however, this measure reacts sensitively to small variations in the sampled direction $\mathbf{N}(\theta,\phi)$. To reduce this sensitivity, we perform the computation over a finite solid angle rather than the exact direction, so that the filter corresponds to a volume obtained by enveloping all planes of all directions within the solid angle. The volume is still aliased along its boundary, as shown in Figure 4.1(c), but it represents only a lower fraction of the total number of frequencies filtered. Therefore, it is less sensitive to small changes in the sampled direction. To exclude the part of the spectrum that does not contain relevant fiber information the filter is reduced to include magnitudes only between minimum and maximum cut-off frequencies $\mathrm{f}_{\mathrm{min}}$ and $\mathrm{f}_{\mathrm{max}}$. Assuming a conical solid angle

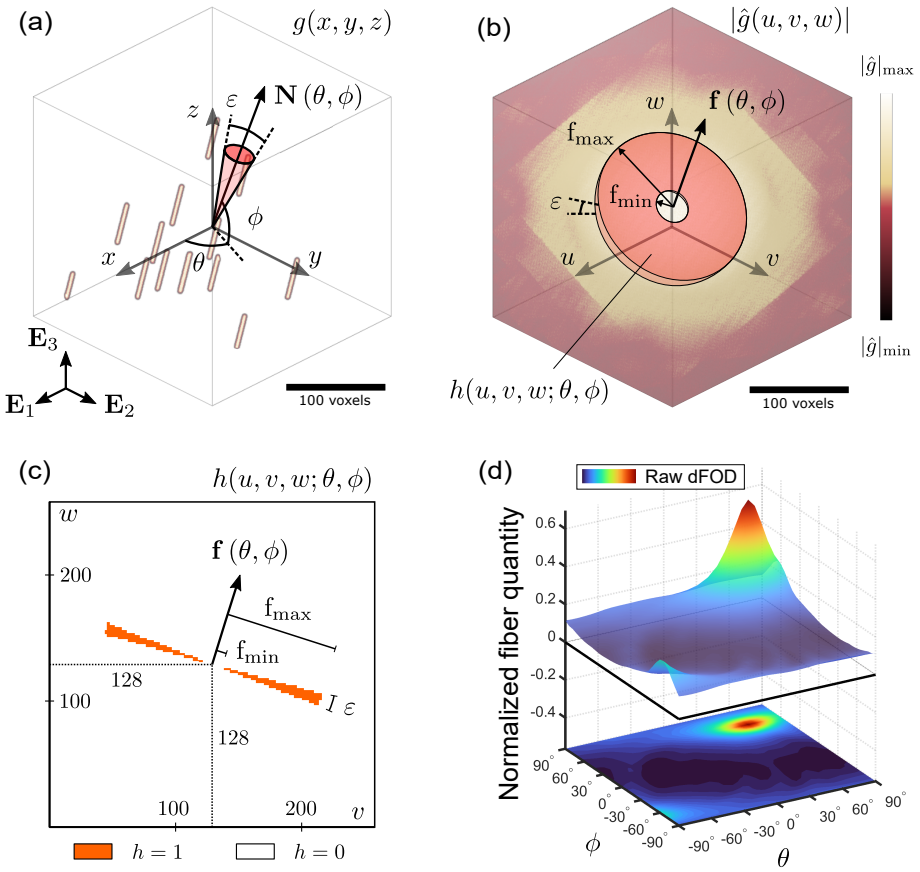

Figure 4.1: Illustration of the 3D discrete Fourier transform algorithm: (a) signal $g(x,y,z)$ of a $256\times256\times256$ representative image in the discrete spatial domain with $N=13$ fibers aligned to $\mathbf{N}(\theta,\phi)=\mathbf{N}(60^\circ,60^\circ)$; (b) center-shifted spectrum $|\hat{g}(u,v,w)|$ in the frequency domain, with a sketch of the overlapping funnel filter sampling the frequencies associated with the fibers with orientations within the cone, shown in (a), with mean frequency direction $\mathbf{f}(\theta,\phi)=\mathbf{f}(60^\circ,60^\circ)$, $|\mathbf{f}|=1$, and opening ε; (c) cross section of the filter in the local v-w plane at $u=128$. The filter is axisymmetric about the frequency direction $\mathbf{f}(\theta,\phi)$ (note that the symmetry axis shown is slightly skewed with respect to the v-w plane); (d) raw dFOD of the representative fiber dispersion shown in (a) using $q=2.4$, and $D=31$, corresponding to an angular resolution of $\Delta\theta=\Delta\phi=5.8^\circ$ (ε is taken to be equal to $\Delta\theta=\Delta\phi$).

with mean direction $\mathbf{N}(\theta,\phi)$ and amplitude ε, as exemplified in Figure 4.1(a), its associated funnel-shaped filter in the frequency direction $\mathbf{f}(\theta,\phi)$ is defined by the function $h:\mathbb{N}^3\times\mathbb{R}^2\rightarrow\{0;1\}$, namely

$$h(u,v,w;\mathbf{f}(\theta,\phi))=\begin{cases}1 & \text{if} \quad \tilde{u}^2-\tan(\varepsilon/2)^2\left(\tilde{v}^2+\tilde{w}^2\right)\leq 0 \quad \text{and} \\ & \mathrm{f}_{\min}\leq\sqrt{\tilde{u}^2+\tilde{v}^2+\tilde{w}^2}\leq\mathrm{f}_{\max}\,,\\ 0 & \text{else}\,,\end{cases} \tag{4.2}$$

where $[\tilde{u}\ \tilde{v}\ \tilde{w}]^{\mathrm{T}}=\mathbf{R}_w^{-1}(\theta)\mathbf{R}_v^{-1}(-\phi)\left([u\ v\ w]^{\mathrm{T}}-1/2[M\ M\ M]^{\mathrm{T}}\right)$, $\mathbf{R}_w$ and $\mathbf{R}_v$ are the rotation matrices around the w and v axes, respectively (Figure 4.1(b)). We can then define the raw discrete Fiber Orientation Distribution (dFOD) as a function $d:\mathcal{O}\rightarrow\mathbb{R}$,

$$d(\theta,\phi)=\sum_{u=0}^{M-1}\sum_{v=0}^{M-1}\sum_{w=0}^{M-1}|\hat{g}(u,v,w)|^q\,h(u,v,w;\theta,\phi)\,, \tag{4.3}$$

computed along all the couples (θ,ϕ) of the discrete angular domain

$$\mathcal{O}=\left\{\left(-90^\circ+\frac{2i-1}{2}\Delta\theta,-90^\circ+\frac{2j-1}{2}\Delta\phi\right)|i,j=1,\cdots,D\right\}\,, \tag{4.4}$$

where $\Delta\theta=\Delta\phi=180^\circ/D$ defines the angular resolution in terms of D evenly spaced angles (Figure 4.1(d)). In Equation (4.3) we introduced an exponent q to correct the distribution. Usually, in 2D discrete Fourier transform-based algorithms [173, 191, 192], the exponent is set to $q=2$, but other values can be used to achieve better results [188]. To identify the optimal value for q a calibration analysis is performed in the following Section 4.2.3 using artificially generated 3D images with prescribed fiber distribution. To ensure a thorough measurement of all fibers in the discrete angle set, we assume that the cone opening corresponds to the angular resolution $\varepsilon=\Delta\theta=\Delta\phi$. Assuming an image size of $M=256$ voxels, which is suitable for most biological applications, and without assumptions about the investigated fiber diameter, we set the cut-off frequencies to $\mathrm{f}_{\min}=4$ and $\mathrm{f}_{\max}=43$ to exclude high frequencies related to noise and low frequencies associated with exposition variations within the image [192]. Given the relationship $\mathrm{f}=M/(2t)$, this frequency range corresponds to fiber diameters between $t=32$ and $t=3$ voxels. However, this does not necessarily mean that fibers larger than 32 voxels and smaller than 3 voxels will not be detected, as the information conveyed by the discrete Fourier transform about a specific fiber diameter t' is spread in a band of about $\mathrm{f}'\pm 0.1\mathrm{f}'$ [191].

An essential aspect of the proposed method is that the signal g and accordingly the spectrum $\hat{g}$ correspond to cubes with size $M \times M \times M$. Different sizes along the three dimensions of g and $\hat{g}$ would result in an inaccurate dFOD since the higher number of frequencies along the dominant direction would make a larger contribution with respect to other directions in Equation (4.3).

Another aspect to consider is computational efficiency. For computational reasons, all filters are computed before the analysis, which requires free memory proportional to the product between the number of directions D^2 and the number of voxels in the filter M^3. This might become too demanding when analyzing high-resolution 3D images ($M \approx 1024$). To limit the amount of memory required for the computations while maintaining a cubic shape for $\hat{g}$, the 3D image is divided into ROIs of $256 \times 256 \times 256$ voxels. Then the raw dFOD $d(\theta, \phi)$ is computed as the sum of the raw dFODs of each individual ROI. The sum does not require any weighting, since $\hat{g}$ already takes into account the luminance, i.e. the overall amount of fibers within the ROI. If the dimensions are not a multiple of 256, the 3D image can be divided into cubic ROIs of different size (possibly close to 256), which can be scaled up or down to $M = 256$ by volumetric interpolation before the 3D discrete Fourier transform.

4.1.2 Deconvolution of the Raw dFOD

The distribution $d(\theta, \phi)$ needs to be deconvoluted to obtain the actual dFOD $d'(\theta, \phi)$. Because the filters intersect in the frequency domain, the measured amount of fibers for a generic direction $\mathbf{N}_I = \mathbf{N}\left(\theta_i, \phi_j\right)$ contains a percentage of the actual amount of fibers from all other directions $\mathbf{N}_J = \mathbf{N}(\theta_k, \phi_l)$ that is proportional to the number of shared magnitudes between filters along the frequency directions $\mathbf{f}_I = \mathbf{f}\left(\theta_i, \phi_j\right)$ and $\mathbf{f}_J = \mathbf{f}(\theta_k, \phi_l)$. Mathematically, we can write the raw dFOD in vector form by the linear relationship $\mathbf{d} = \mathbf{K}\mathbf{d}'$, where $\mathbf{d}'$ denotes the unknown deconvoluted dFOD in vector form. The symmetric convolution kernel matrix K_{IJ} represents the normalized number of common magnitudes between Ith and Jth filters, computed as

$$K_{IJ} = \frac{1}{M^3} \sum_{u=0}^{M-1} \sum_{v=0}^{M-1} \sum_{w=0}^{M-1} h(u, v, w; \mathbf{f}_I)\, h(u, v, w; \mathbf{f}_J)\,, \tag{4.5}$$

Since the discrete functions d and d' can be arbitrarily rearranged from matrix to vector, we use the index rule $I = (j-1)D + i$. We obtain the deconvoluted vector $\mathbf{d}'$ using the iteratively constrained Tikhonov–Miller algorithm, which gives the

optimal non-negative solution to

$$\arg\min_{\mathbf{d}'} \left(\|\mathbf{K}\mathbf{d}' - \mathbf{d}\|^2 + \lambda \|\mathbf{J}\mathbf{d}'\|_2^2 \right) . \tag{4.6}$$

Here the second term depends on the discrete Jacobian operator matrix $\mathbf{J}$ and the regularization parameter $\lambda \in [0,1]$ which is introduced to avoid noise amplification in the solution [193]. This method is required because direct matrix inversion would provide noisy and possibly non-physical (negative values) results. A step-size of 0.1 and $\lambda = 10^{-3}$ is used for the iterations. Once the solution is found, the deconvoluted vector $\mathbf{d}'$ is rearranged again as a matrix using the aforementioned reordering rule, providing the sought dFOD $d'(\theta, \phi)$. An example of application of the algorithm to an artificially generated 3D image (see Section 4.2.1) is shown in Figure 4.2. Therein, it is evident that the raw dFOD illustrated in Figure 4.2(c) is refined by the deconvolution process. As a result, it more closely approximates the prescribed distribution $\overline{\rho}(\theta, \phi)$ (see Equation (4.7) below) as shown in Figure 4.2(d).

4.1.3 Estimation of the Distribution Parameters

To estimate the parameters of the fiber orientation distribution from the dFOD, required for the mechanical modeling of soft tissues, the function

$$\overline{\rho}(\theta, \phi) = \rho(\theta, \phi) \cos(\phi) , \tag{4.7}$$

is fitted to the distribution $d'(\theta, \phi)$, where $\rho(\theta, \phi)$ is a combination of elementary bivariate von Mises distributions as defined in Equation (3.79). The cosine of the elevation angle ϕ accounts for the surface area $\mathrm{d}S$ on the unit sphere, $\mathrm{d}S = \cos\phi \, \mathrm{d}\theta \mathrm{d}\phi$, to ensure that the normalization condition in Equation (3.80) is satisfied over the rectangular domain $\mathcal{O}$ in Equation (4.4). This factor is necessary since $d'(\theta, \phi)$, being defined and normalized over $\mathcal{O}$, is implicitly multiplied by $\cos\phi$. The operation is performed in MATLAB using the integrated nonlinear least squares function `lsqnonlin`. The quality of the fit is assessed with the coefficient of determination R^2.

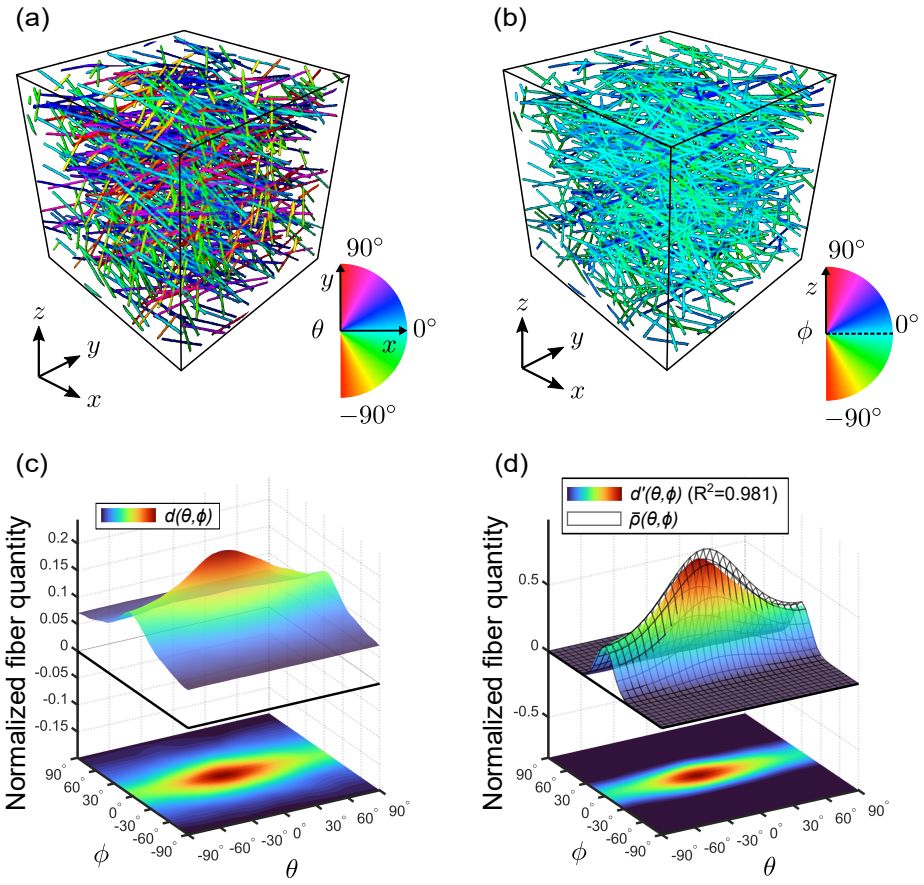

Figure 4.2: Application of the 3D discrete Fourier transform algorithm: (a),(b) maps of the azimuthal and elevation angles θ and ϕ of a representative artificial fiber dispersion with $N = 1\,000$ fibers of $t = 3$ voxel diameter. The prescribed von Mises distribution parameters are $\alpha = \beta = \gamma = 0°$, $a = 0.5$, $b = 5$ (single fiber family, $m = 1$); (c) corresponding raw dFOD $d(\theta, \phi)$ discretized with $D = 31$ angular intervals (5.8° angular resolution) and spectrum parameter $q = 2.4$; (d) deconvoluted dFOD $d'(\theta, \phi)$, with overlapping prescribed von Mises distribution $\overline{\rho}(\theta, \phi)$ (wire-frame plot).

4.2 Algorithm Calibration and Validation

4.2.1 Artificial Fiber Dispersion Volume

To calibrate and validate the algorithm artificial grayscale 3D images are created using a custom MATLAB code (v. R2023a; The MathWorks Inc., Natick, MA, USA). These images are generated placing N straight fibers oriented according to a prescribed distribution $\rho(\theta,\phi)$ within a $M \times M \times M$ voxels volume. The midpoint $(x,y,z)_k$ of each fiber, $k = 1,\dots,N$, is determined using a three-dimensional uniform distribution. The orientations $(\theta,\phi)_k$ of the fibers are sampled from the PDF outlined in Equation (3.79) through a rejection method. This involves generating random points uniformly distributed within the domain

$$\mathcal{D} = \{(\theta,\phi,r) | -90^\circ \leq \theta \leq 90^\circ, -90^\circ \leq \phi \leq 90^\circ, 0 \leq r \leq \max(\overline{\rho})\} \ , \qquad (4.8)$$

and selecting points that lie under the function $\overline{\rho}(\theta,\phi)$. Since sampling is performed over a rectangular angular domain, $\overline{\rho}(\theta,\phi)$ is taken in the form defined in Equation (4.7).

After establishing the positions $(x,y,z)_k$ and orientations $(\theta,\phi)_k$ of the fibers, a 3D binary image is formed with dimensions of $M \times M \times M$ voxels. In this image, voxels belonging to a fiber are assigned an intensity $Y = 1$, while others are set to $Y = 0$. All fibers share a similar aspect ratio, greater than 10, to facilitate a meaningful analysis of the dFOD through discrete Fourier transform methods [191, 192]. The image is subsequently smoothed with a Gaussian kernel, having a standard deviation of 0.7 voxel, to mitigate the sharpness of the fibers that could otherwise cause artifacts in the spectrum $|\hat{g}|$. This smoothing process transforms the image from binary to grayscale (8 bit). Since the smoothing operation diminishes the peak intensity $Y_{\max}$, all voxel intensities are scaled by the factor $Y_{\max}^{-1}$ to readjust the maximum intensity back to 1.

4.2.2 Statistical analysis

A two-way ANOVA analysis is used to calibrate the algorithm and to analyze the precision of the estimated parameters of the in-plane and out-of-plane fiber orientation distribution. Instead, a one-way ANOVA is used to evaluate the robustness of the algorithm. For all analyses, a post-hoc Tukey HSD (honestly significant difference) test is used to assess pairwise differences between groups. The results are considered significant at the 5% level. Due to the high number of pairwise comparisons, we use the compact letter display with uppercase letters to report

the results. The data analysis is carried out employing the Real Statistics Resource Pack software [194].

4.2.3 Calibration

The form of the deconvoluted dFOD $d'(\theta, \phi)$ is modulated by the power parameter q, which is applied to the spectrum $|\hat{g}|$ of the 3D image g prior to the filtering process, (Equation (4.3)). To understand how the spectrum power parameter influences the standard deviations of $d'(\theta, \phi)$, the relative errors $\Delta\sigma_{\theta\theta}$ and $\Delta\sigma_{\phi\phi}$ between the standard deviations of both the prescribed and the computed distributions is examined. For this analysis, four distinct single-fiber family distributions ($m = 1$) are generated to represent different scenarios of high/low in-plane and out-of-plane fiber concentrations: **Case 1** with low concentration in both planes ($a = 0.5$, $b = 0.5$); **Case 2** with high out-of-plane concentration ($a = 0.5$, $b = 5$); **Case 3** featuring high in-plane concentration ($a = 5$, $b = 0.5$); and **Case 4** displaying high concentrations in both planes ($a = 5$, $b = 5$). We assumed $\alpha = \beta = \gamma = 0^\circ$ and generated 10 three-dimensional $256 \times 256 \times 256$ voxels images for each case, containing $N = 6\,000$ fibers of diameter $t = 3$ voxels.

Figure 4.3(a) presents contour plots of the prescribed von Mises distributions. The relative error $\Delta\sigma_{\theta\theta}$ is depicted in Figure 4.3(b). In Cases 1 and 2, the error is minimal and shows a slight increase with q, remaining under 6%. However, in Case 3, the error significantly reduces from 50% to below 10%, with little variation between $q = 2.4$ and $q = 2.8$. In Case 4, the error significantly decreases as q increases, reaching its lowest at $q = 2.8$. As for the relative error $\Delta\sigma_{\phi\phi}$ concerning the elevation angle, the findings are illustrated in Figure 4.3(c). In Cases 1 and 3, the error grows with q, consistently staying below 5%. For Case 2, the errors are notably high, except when $q = 2.4$, similar to Case 4, where a decreasing trend is observed with increasing q. Thus, the best compromise to minimize both errors $\Delta\sigma_{\theta\theta}$ and $\Delta\sigma_{\phi\phi}$ at the same time and for the majority of the cases analyzed is to use $q = 2.4$. The analysis also revealed that errors are higher when concentrations along the respective directions are high. This behavior is attributed to the smaller standard deviations at higher concentrations, which makes the relative error more sensitive to small differences in the measured standard deviation as the prescribed one approaches zero.

4.2.4 Robustness Assessment

We tested the ability of the algorithm to accurately measure dFOD, independently of the fiber number N and diameter t in the 3D image. Additionally, the results

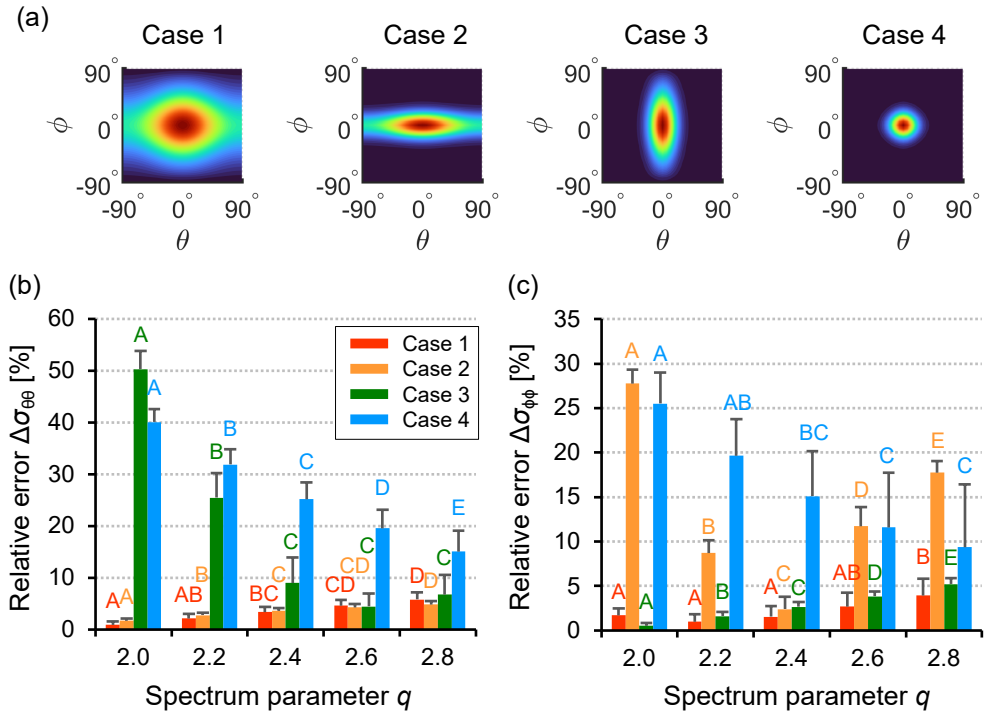

Figure 4.3: Algorithm calibration: (a) contour plots of the prescribed bivariate von Mises distributions, $\alpha = \beta = \gamma = 0°$ (one fiber family, $m = 1$). Case 1: $a = 0.5$, $b = 0.5$; Case 2: $a = 0.5$, $b = 5$; Case 3 $a = 5$, $b = 0.5$; Case 4 $a = 5$, $b = 5$. Relative errors between the standard deviation of the measured dFOD and the prescribed distribution (mean and standard deviation of 10 images); (b) error $\Delta\sigma_{\theta\theta}$ along the azimuthal direction θ for different power parameters q; (c) error $\Delta\sigma_{\phi\phi}$ along the elevation direction ϕ for different q. Means not sharing uppercase letters differ significantly by the Tukey-test at the 5% significance level. Letters must be compared among the same cases.

are analyzed in terms of fiber density δ, defined as the average voxel intensity throughout the entire 3D image volume, where 0% indicates an empty volume and 100% represents a completely bright voxel distribution.

Three-dimensional images ($256 \times 256 \times 256$ voxels) are generated with an increasing number of fibers, all maintaining a diameter of $t = 3$ voxels. Representative distributions are generated with parameters $a = 0.5$, $b = 5$, $\alpha = \beta = \gamma = 0°$ (one fiber family, $m = 1$), containing varying numbers of fibers: $N = 1\,000$, $2\,000$, $5\,000$, $10\,000$, $20\,000$, $50\,000$, $75\,000$, and $100\,000$. These different fiber counts correspond to fiber densities ranging from $\delta = 0.72\%$ to $\delta = 28.23\%$ (Figure 4.4(a)). For each case, 10 three-dimensional images are generated.

The performance of the algorithm is evaluated by calculating the relative errors in the standard deviations along azimuthal and elevation angles (Figure 4.4(b)). It was observed that the error $\Delta\sigma_{\theta\theta}$ slightly depends on the number of fibers N, typically decreasing as N increases. This trend may vary at very high N values, as for $N \to \infty$ ($\delta \to 100\%$), fibers become indistinguishable, making it impossible to measure any distribution. Nevertheless, a volume with $N = 100\,000$ fibers ($\delta = 28.23\%$) exceeds the density typically observed in real collagen fiber tomographies of skin. For example, in the following skin tissue applications, the fiber density is $\delta = 16.97\%$ for human skin and $\delta = 16.31\%$ for mouse skin (see Section 4.3). In terms of the elevation angle, the error $\Delta\sigma_{\phi\phi}$ shows little sensitivity to changes in N and remains low, except for the case with $N = 100\,000$.

To evaluate how the algorithm performs with varying fiber diameters, stacks of artificial fibers are examined, all with the same fiber count $N = 2\,000$, but with increasing diameters of $t = 3$, 5, 7, 9, 11, and 13 voxels. These diameters correspond to densities ranging from $\delta = 1.28\%$ to 64.80%. For each diameter, 10 three-dimensional images ($256 \times 256 \times 256$ voxels) are generated with consistent dispersion parameters, $a = 0.5$, $b = 5$, $\alpha = \beta = \gamma = 0°$ (one fiber family, $m = 1$). Figure 4.5(a) show representative images for each diameter.

As depicted in Figure 4.5(b), the algorithm accurately predicts the standard deviation in the azimuthal direction, with an error $\Delta\sigma_{\theta\theta}$ below 3.5% and no notable variation across diameters. However, in the elevation direction, the error remains small ($\Delta\sigma_{\phi\phi} < 8.7\%$) only for fiber diameters between 3 and 7 voxels, increasing to around 50% for diameters of $t = 13$ voxels.

Interestingly, the patterns observed in both the fiber number and fiber diameter analyses are similar and directly correlated with fiber density. By comparing the errors in Figure 4.4(b) and Figure 4.5(b) against the fiber density δ, we find that both $\Delta\sigma_{\theta\theta}$ and $\Delta\sigma_{\phi\phi}$ are associated with fiber density. The errors $\Delta\sigma_{\theta\theta}$ are consistently small and largely unaffected by the density, whereas $\Delta\sigma_{\phi\phi}$ remains

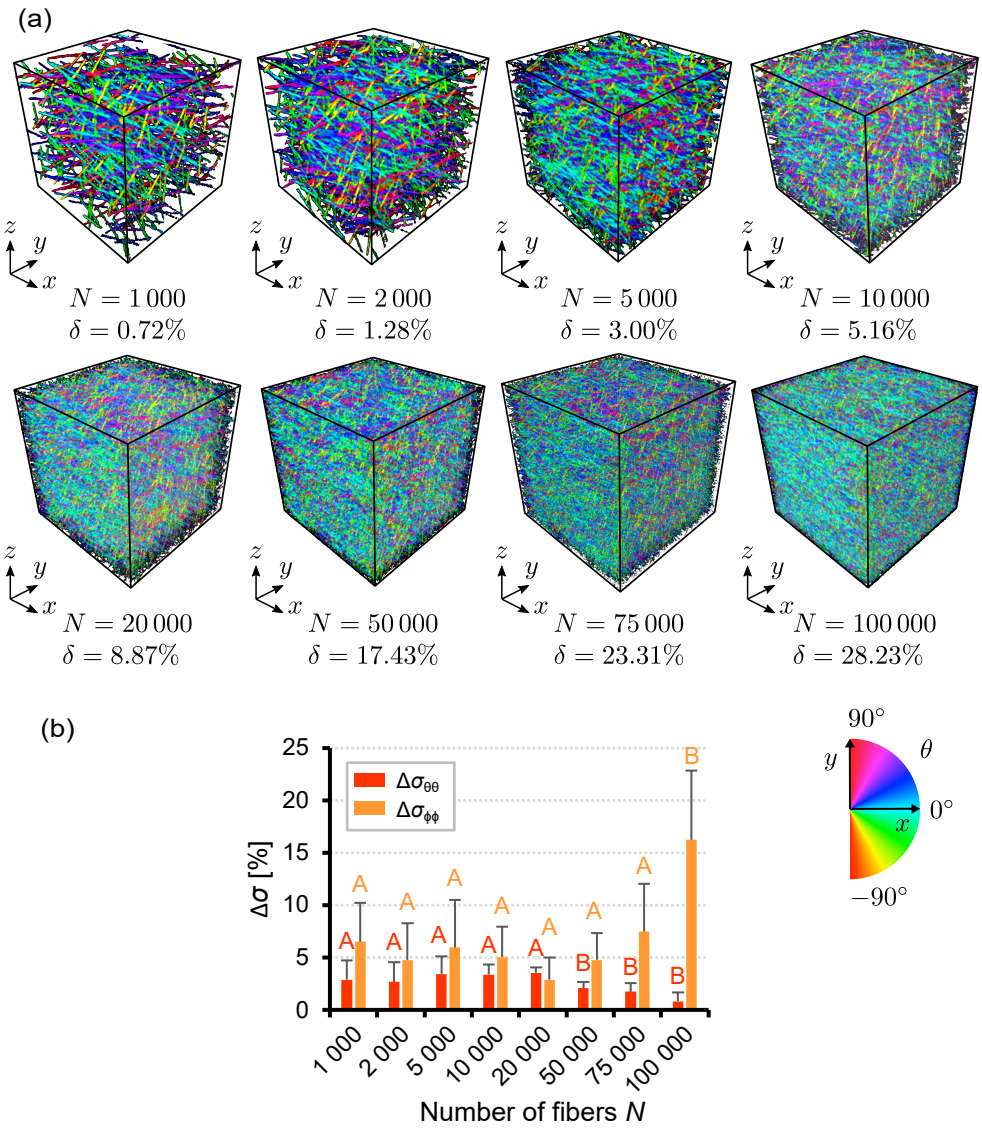

Figure 4.4: Algorithm robustness assessment in relation to the number of fibers: (a) maps of the azimuthal angle θ of 8 representative artificial 3D images ($256 \times 256 \times 256$ voxels), with $N = 1\,000$, $2\,000$, $5\,000$, $10\,000$, $20\,000$, $50\,000$, $75\,000$, $100\,000$ fibers of diameter $t = 3$ voxels, and distribution parameters $a = 0.5$, $b = 5$, $\alpha = \beta = \gamma = 0°$ (one fiber family, $m = 1$); (b) relative errors $\Delta\sigma_{\theta\theta}$ and $\Delta\sigma_{\phi\phi}$ between the standard deviations of the measured dFOD and the prescribed distribution (mean and standard deviation of 10 images). Means that do not use capital letters differ significantly by the Tukey-test at the 5% significance level. Letters must be compared in the same cases.

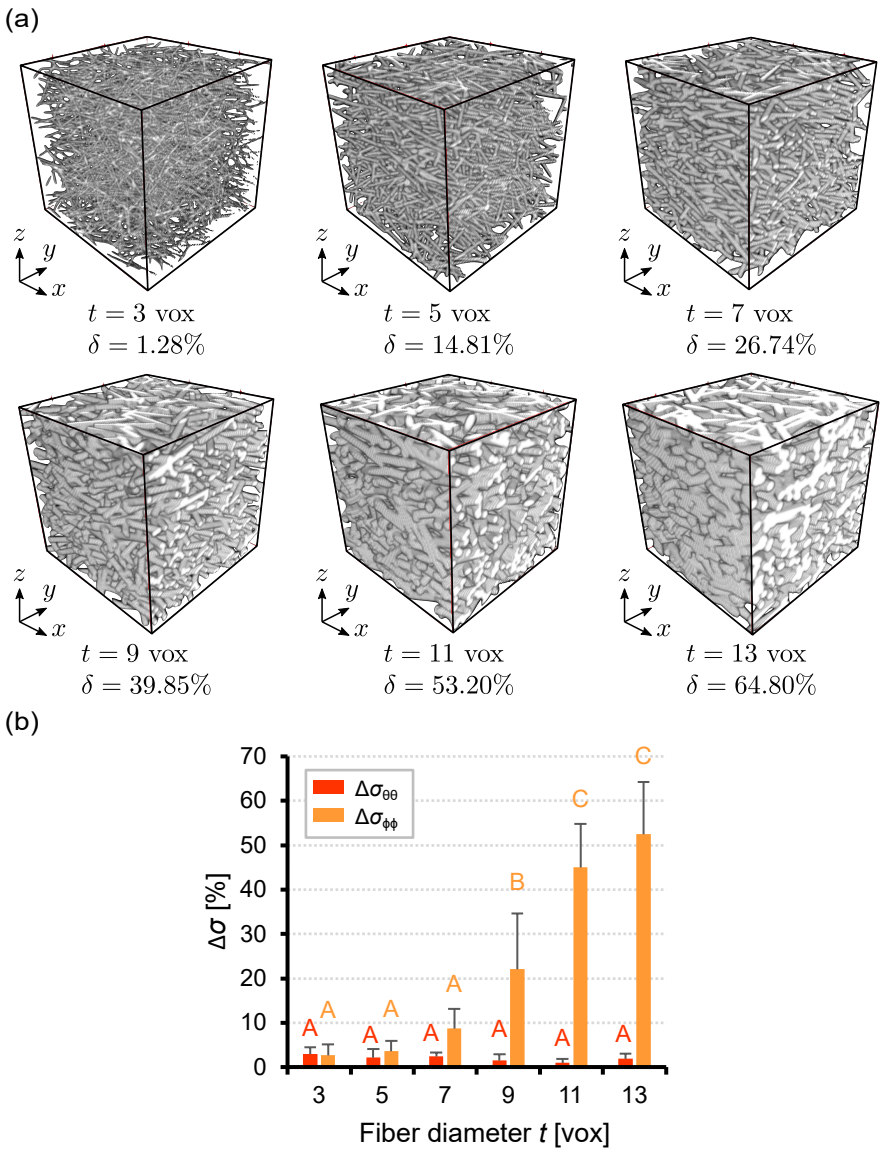

Figure 4.5: Algorithm robustness assessment in relation to the fibers diameter: (a) representative artificial fiber stacks ($256 \times 256 \times 256$ voxels), generated with $N = 2\,000$ fibers and diameters of 3, 5, 7, 9, 11 and 13 voxels. Distribution parameters: $a = 0.5$, $b = 5$, $\alpha = \beta = \gamma = 0°$ (one fiber family, $m = 1$); (b) relative errors $\Delta\sigma_{\theta\theta}$ and $\Delta\sigma_{\phi\phi}$ between the standard deviations of the measured dFOD and the prescribed distribution (mean and standard deviation of 10 images). Means not sharing uppercase letters differ significantly by the Tukey-test at the 5% significance level. Letters must be compared among the same cases.

low for densities under $\delta \approx 25\%$ ($N = 75\,000$, $t = 3$ voxels; $N = 2000$, $t = 7$ voxels) and increases significantly for densities over $\delta > 28\%$ ($N = 100\,000$, $t = 3$ voxels; $N = 2000$, $t = 9$ voxels). This indicates that the algorithm's performance is dependent on the overall fiber density rather than on the number of fibers or their individual diameters. However, the difference between $\Delta\sigma_{\theta\theta}$ and $\Delta\sigma_{\phi\phi}$ is probably due to the small prescribed standard deviation $\sigma_{\phi\phi}$ (higher concentration) along the elevation direction, increasing the relative error even though the absolute error is small.

4.2.5 Precision Assessment

The accuracy of the algorithm is measured by its effectiveness in determining the parameters of both the in-plane and out-of-plane fiber distributions. To assess this, a series of 10 three-dimensional images ($256 \times 256 \times 256$ voxels), each containing $N = 6\,000$ fibers with a diameter of $t = 3$ voxels, were created based on the parameter combinations outlined below.

For the in-plane parameters, various combinations of fiber dispersions containing a single fiber family ($m = 1$) with mean angles $\alpha = 0°$, $30°$, $60°$, $90°$ and concentrations $a = 0$, 0.5, 1, 2, 5 are examined. For all the fiber dispersions, the out-of-plane angle $\beta = 0°$ and concentration $b = 1$ is kept constant. Due to symmetry, negative angles are not considered. Errors between the estimated (subscript e) and true (subscript t) parameters are evaluated by the difference for the in-plane concentration, $\Delta a = a_e - a_t$, and the absolute difference for the mean in-plane angles, $\Delta\alpha = |\alpha_e - \alpha_t|$. The results are summarized in Figure 4.6.

It appears that the ability of the algorithm to accurately estimate the true concentration a_t is largely unaffected by the true mean fiber orientation α_t, except in cases where $a_t = 5$. In such instances, the algorithm tends to underestimate the true concentration, with an average error of -0.745 (Figure 4.6(a)). Notably, the magnitude of error generally increases with increasing a_t. In contrast, the error in estimating the mean angle (Figure 4.6(b)) behaves differently. The isotropic case $a_t = 0$ is excluded since the mean angle is irrelevant in this scenario. The precision in estimating the mean angle improves with increasing concentration a_t, since the uncertainty on the angular peak location reduces for more concentrated dFODs. These errors, independent of the true mean fiber orientation α_t, show no significant variation (except for three means) and remain relatively small across all values of a_t and α_t, with a maximum error of only 1.8°.

Concerning the assessment of the algorithm out-of-plane precision, various combinations of fiber dispersions containing a single fiber family ($m = 1$) with

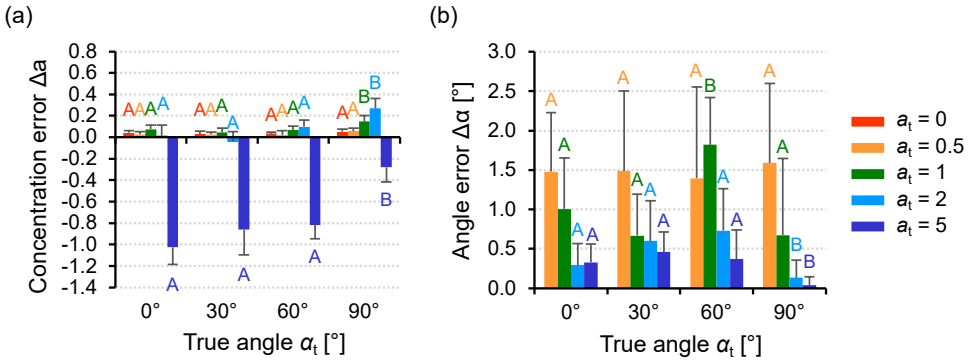

Figure 4.6: Algorithm precision assessment for in-plane parameters. Errors between the estimated (subscript e) and true (subscript t) in-plane parameters (mean and standard deviation of 10 images): (a) error in the in-plane concentration $\Delta a = a_e - a_t$; (b) error in the in-plane angle $\Delta\alpha = |\alpha_e - \alpha_t|$ (isotropic case $a_t = 0$ omitted). Means not sharing uppercase letters differ significantly by the Tukey-test at the 5% significance level. Letters must be compared within the same concentration a_t.

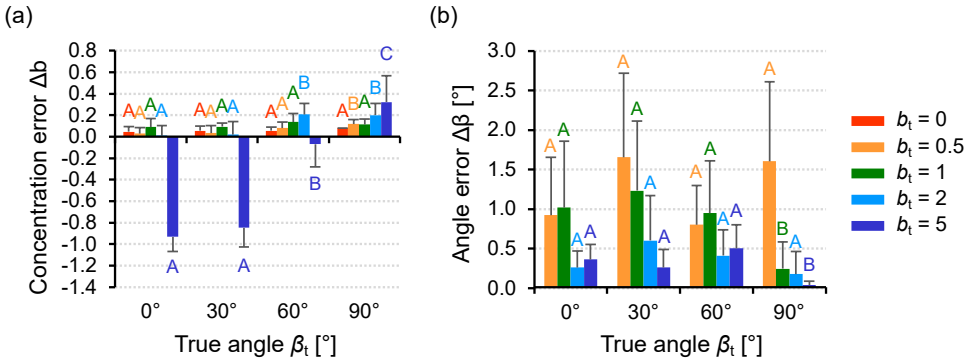

Figure 4.7: Algorithm precision assessment for out-of-plane parameters. Errors between the estimated (subscript e) and true (subscript t) out-of-plane parameters (mean and standard deviation of 10 images): (a) error in the out-of-plane concentration $\Delta b = b_e - b_t$; (b) error in the out-of-plane angle $\Delta\beta = |\beta_e - \beta_t|$ (isotropic case $b_t = 0$ omitted). Means not sharing uppercase letters differ significantly by the Tukey-test at the 5% significance level. Letters must be compared within the same concentration b_t.

mean angles $\beta = 0°$, $30°$, $60°$, $90°$ and concentrations $b = 0$, 0.5, 1, 2, 5 are examined. During these tests, the in-plane angle $\alpha = 0°$ and concentration $a = 1$ are kept constant. Negative angles are not considered due to symmetry. As for the in-plane parameters, errors between the estimated (subscript e) and true (subscript t) parameters are evaluated by the difference for the out-of-plane concentration, $\Delta b = b_e - b_t$, and the absolute difference for the mean out-of-plane angles, $\Delta\beta = |\beta_e - \beta_t|$. The results are summarized in Figure 4.7.

The estimation of the out-of-plane concentration parameter (Figure 4.7(a)) displays a moderate dependence on the angle β_t. For concentrations $b_t \leq 2$, the values are low and remain fairly consistent between $0°$ and $60°$. However, at $b_t = 5$, the algorithm tends to underestimate the concentration at lower angles, but this error decreases at $\beta_t = 60°$ and turns positive at $\beta_t = 90°$. In terms of the mean out-of-plane angle (Figure 4.7(b)), the error shows minimal dependency on β_t, with notable variations across different concentrations observed only at $\beta_t = 90°$. Similar to the in-plane assessment, the errors are generally small, peaking at $1.65°$, and tend to diminish as the concentration b_t increases.

4.3 Application to Skin Tomography

The algorithm is now applied to real SHG tomographies of human and mouse skin tissue. Performances are then qualitatively compared to standard 2D Fourier-transform based algorithms [111, 113] in terms of 2D dFOD in the mean tissue plane x-y. Tomographies were acquired at the Norwegian University of Science and Technology (NTNU), employing the confocal laser microscope at the Department of Physics.

4.3.1 Collagen Fiber Tomography

Collagen fiber images were obtained from human skin samples taken from the abdominal area during routine surgical procedures. The use of human tissue was approved from the Regional Committee for Medical and Health Research Ethics (Project ID: 474249) and adhered to the ethical standards set in the Declaration of Helsinki for human subject research. Written informed consent was obtained from all participants.

Moreover, *ex vivo* skin samples from the dorsal region of mice were analyzed. These tissues were collected from mice used in other *in vivo* studies. The mice were humanely euthanized via cervical dislocation under isoflurane anesthesia by trained professionals, and the tissue was then allocated for SHG imaging. The animal laboratory at the Department of Comparative Medicine at the Norwegian University of Science and Technology operates with approval from the Norwegian Food and Animal Safety Authority (document VSID 3506) and complies with national and EU regulations on animal care and ethics.

The samples were cleaned of adipose tissue and frozen at −28° within 2 hours of collection. For SHG imaging, the tissues were thawed at room temperature (22°) and prepared for the clearing procedure. This involved a 12-hour fixation in 4% paraformaldehyde for at least 12h to prevent tissue degradation and preserve collagen fiber structure. Then, the samples were optically cleared according to the SeeDBp protocol [195] to facilitate SHG imaging of deeper dermis layers. Clearing is carried out step by step by incubating the samples in 6 fructose solutions of increasing concentration at 25 °C. Specifically, the samples were incubated in a 20%, 40%, 60% w:v fructose:0.1×PBS (phosphate buffered saline) solution for 4h each and then in a 80%, 100% w:v fructose:0.1×PBS solution for 12h each, and finally in a 80.2% w:w fructose:distilled water solution (SeeDB solution) for 24h. This method effectively clears fibrous biological tissues without altering their morphology [196], thus preserving the collagen architecture. The cleared samples were then placed in a press-to-seal silicone isolator (CoverWell™ Imaging Cham-

bers, Grace BIO-Labs, Oregon, USA), filled with SeeDB solution, and sealed with two rectangular glass coverslips.

For SHG imaging, it was employed a Leica TCS SP8 confocal multiphoton microscope (Leica Microsystem, Germany) with a Leica HCX IRAPO 25×, NA 0.95 water objective. The second harmonic generation of collagen was induced using an 890 nm multiphoton laser (Chameleon Ultra I; Coherent Corp., Saxonburg, PA, United States), with signals emitted at 445 nm detected in both forward and backward directions. Images were acquired over a $465\,\mu$m × $465\,\mu$m area, with an x-y resolution of $0.454\,\mu$m/px and a vertical step of $0.57\,\mu$m, scanning a total thickness of approximately $116.25\,\mu$m from the epidermis side.

To mitigate blurring effects from light diffraction in the confocal microscope, particularly along the z axis, 3D images were pre-processed in Fiji [197] using the DeconvolutionLab2 plugin for deconvolution microscopy [193]. The Richardson–Lucy algorithm with total-variation regularization (regularization parameter $\lambda = 10^{-3}$, 30 iterations) and the Gibson and Lanny 3D optical model were used for the point spread function [198, 199]. The 3D images were then vertically resampled in MATLAB (v. R2023a; The MathWorks Inc., Natick, MA, USA) using the `imresize3` function, stretching by a factor of $\Delta z/\Delta x \approx 1.26$ to match the z spacing with the x-y resolution.

4.3.2 Human skin

Figure 4.8(a) displays a tomography of collagen fibers from human skin, derived from a series of SHG images acquired over a $465\,\mu$m × $465\,\mu$m × $116.25\,\mu$m volume (fiber density $\delta = 16.97\%$). Unlike the straight artificial fibers used in previous analyses, natural skin collagen fibers exhibit a wavy pattern and are compacted in bundles of various sizes and diameters [125]. These bundles are intertwined within the volume, challenging individual bundle identification. Nevertheless, the algorithm effectively measures the dFOD, recognizing fibrous structures within the designated diameter range. Moreover, wavy fibers are still captured, as they can be viewed as a continuous sequence of smaller straight fibers.

Figure 4.8(b) presents the global dFOD for the human skin sample. This was achieved by dividing the volume into 16 cubic ROIs with a size of $M = 256$ voxels ($116.25\,\mu$m), as specified in Section 4.1, and then summing the respective dFODs from these regions. The distribution, featuring an angular resolution of 5.8° ($D = 31$), is normalized such that the area under its surface equals one (with angles in radians). Consistent with experimental data [200], there is a pronounced concentration along ϕ compared to θ, indicating that fibers predominantly align

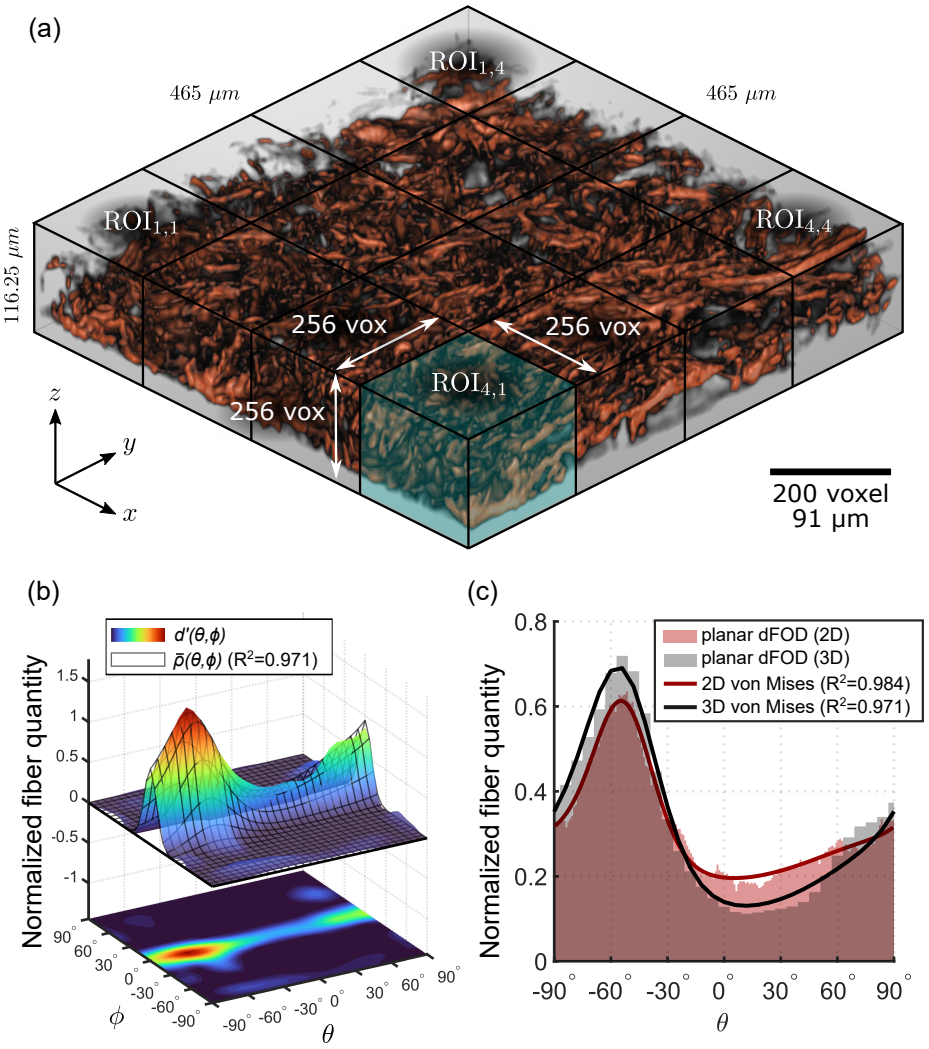

Figure 4.8: Application of the algorithm to human skin collagen fiber tomography: (a) SHG tomography of human skin collagen fibers and subdivision of the volume into cubic ROIs; (b) 3D surface plot and its projected contour on the θ-ϕ plane of the dFOD. The wire-frame plot represents the fitted distribution $\overline{\rho}$ using two bivariate von Mises functions ($a_1 = 2.34$, $b_1 = 6.15$, $\alpha_1 = -54.39°$, $\beta_1 = -4.33°$, $\gamma_1 = -8.22°$, $\nu_{f,1} = 0.44$, $a_2 = 0.38$, $b_2 = 12.45$, $\alpha_2 = 90°$, $\beta_2 = -0.35°$, $\gamma_2 = 0.84°$, $\nu_{f,2} = 0.56$). (c) Comparison of the planar dFOD derived from the 3D discrete Fourier transform and the 2D discrete Fourier transform algorithm ($a_1 = 3.46$, $\alpha_1 = -53.59°$, $\nu_{f,1} = 0.26$, $a_2 = 0.19$, $\alpha_2 = 90°$, $\nu_{f,2} = 0.74$).

within the x-y plane parallel to the skin surface. Despite the distribution reveals a single local maximum at approximately $\theta = -60°$ and $\phi = 0°$, suggesting the presence of a unique fiber family, a combination of two bivariate von Mises distributions ($m = 2$) (wireframe in Figure 4.8(b)) is adopted to improve the quality of the fit. However, the algorithm may slightly underestimate the two out-of-plane concentrations b_i, as these exceed the range tested in previous out-of-plane precision assessment.

Figure 4.8(c) compares the planar distribution derived from the 3D discrete Fourier transform-based algorithm (gray histogram) with that obtained using a conventional 2D discrete Fourier transform-based method [111, 113, 188, 201]. In our 3D method, the planar distribution is generated by summing the dFOD across the ϕ axis and re-normalizing it along the θ axis. In contrast, the 2D approach (red histogram) involves aggregating individual distributions from each in-plane x-y slice of the tomography, each computed using the 2D algorithm (angular resolution of 1°). Both distributions closely align, with peaks around $\theta = -55°$ and similar concentrations. This observation is also confirmed by the parameter set obtained from fitting the 2D von Mises distribution (red solid curve).

4.3.3 Mouse skin

Figure 4.9(a) presents a tomographic image of mouse skin collagen fibers, constructed from a series of SHG images across a 465 μm × 465 μm × 116.25 μm volume (fiber density $\delta = 16.31\%$). In comparison to human collagen fibers, mouse skin fibers are finer and tend to curve around hair follicles, appearing as cavities in the tomography.

Similar to the process used for human skin, the global dFOD for mouse skin is obtained by dividing the volume into 16 cubic ROIs with a size of $M = 256$ voxels (116.25 μm), and then aggregating the respective dFODs (the ROI schematics are not shown here). The resulting distribution, as illustrated in Figure 4.9(b), displays a more pronounced clustering along the horizontal x-y plane compared to human skin, with two distinct peaks around $\theta = -65°$ and $\theta = 60°$ ($\phi = 0°$). A combination of two bivariate von Mises PDFs ($m = 2$) is adopted for the fitting (wireframe in Figure 4.9(b))

The planar distributions derived using both 2D and 3D discrete Fourier transform-based algorithms are reported in Figure 4.9(c). The two peaks observed in the 3D dFOD distribution (Figure 4.9(b)) are also noticeable in the 2D Fourier transform-based distribution, albeit with a smoother pattern. Notably, the in-plane parameters exhibit significant differences between the two methods. This discrepancy

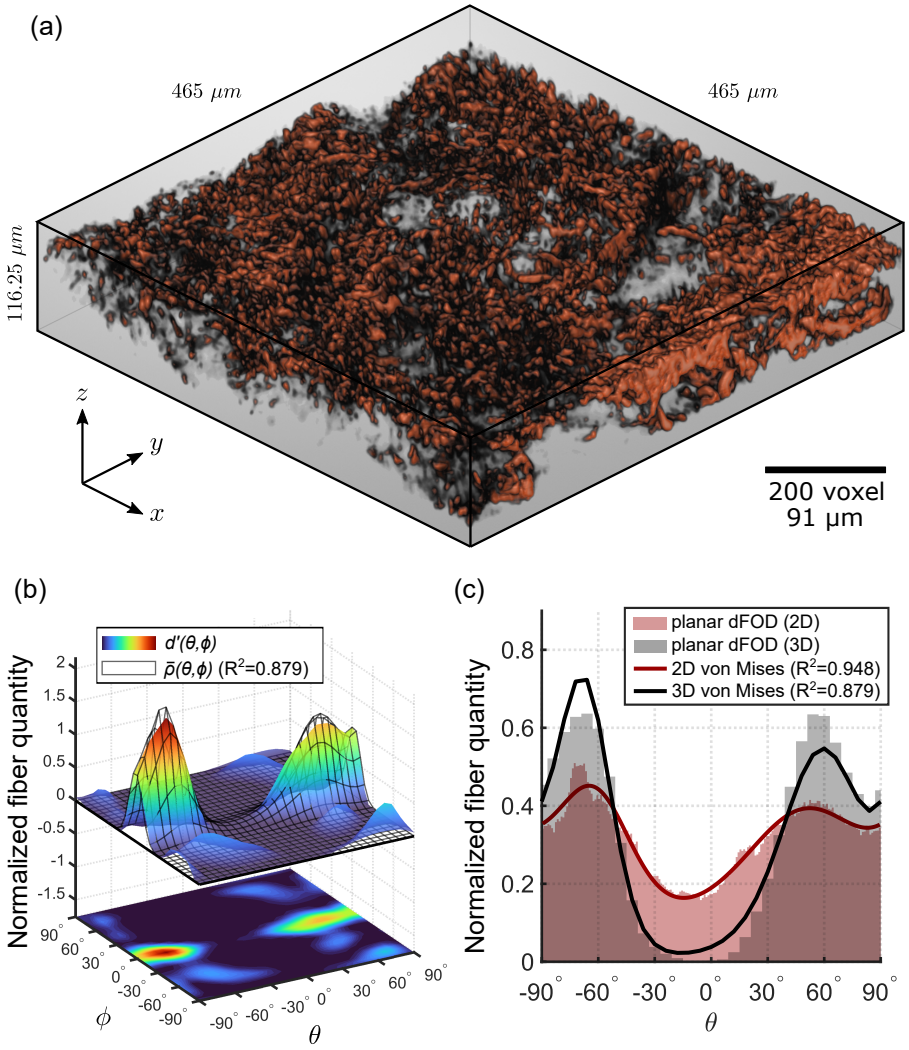

Figure 4.9: Application of the algorithm to mouse skin collagen fiber tomography: (a) collagen fiber SHG tomography of mouse skin; (b) 3D surface plot and its projected contour on the θ-ϕ plane of the dFOD. The wire-frame plot represents the fitted distribution $\overline{\rho}$ using two bivariate von Mises functions ($a_1 = 3.93$, $b_1 = 11.09$, $\alpha_1 = -67.74°$, $\beta_1 = 0.05°$, $\gamma_1 = -17.73°$, $\nu_{f,1} = 0.44$, $a_2 = 1.83$, $b_2 = 9.61$, $\alpha_2 = 58.85°$, $\beta_2 = -4.32°$, $\gamma_2 = 7.22°$, $\nu_{f,2} = 0.56$). (c) Comparison of the planar dFOD derived from the 3D discrete Fourier transform and the 2D discrete Fourier transform algorithm ($a_1 = 2.17$, $\alpha_1 = -62.05°$, $\nu_{f,1} = 0.29$, $a_2 = 0.64$, $\alpha_2 = 50.64°$, $\nu_{f,2} = 0.71$).

likely arises from the limitation of the 2D algorithm in detecting fibers at higher elevations, where quasi-circular cross-sections of fibers are interpreted as isotropically distributed in the x-y plane. With the 2D technique, the concentration parameters are lower and the volume fractions appear more uneven. Moreover, the mean in-plane fiber directions lean closer to the x axis ($\theta = 0°$). Despite these notable differences, both algorithms effectively captured the two distinct collagen families.

4.4 Discussion

In this chapter has been introduced a new algorithm based on the discrete Fourier transform which extends the concepts developed for the 2D images to 3D images [188, 191, 192, 202]. This method exploits funnel-shaped filters to quantify the amount of fibers along discrete directions in the 3D space from the spectrum of the 3D image in the frequency domain. However, in 3D, an additional deconvolution step is essential before accurately determining the actual dFOD $d'(\theta, \phi)$. This process removes the self-interferences of the measurements in the frequency domain. This issue is caused by the intersections of 3D filters pivoting around a fixed frequency point $(u, v, w) = 1/2(M, M, M)$ in the frequency domain, where M represents the size of the cubic image. Unlike 2D algorithms, where filters can be designed non to overlap, 3D filters always intersect, necessitating deconvolution to achieve a faithful representation of the actual fiber orientation distribution.

The present algorithm relies on three adjustable parameters: the cut-off frequencies $\mathrm{f_{min}}$ and $\mathrm{f_{max}}$, and a spectrum power parameter q. The frequencies are selected to exclude information not related to the fibers, while the parameter q is calibrated to match the output dFOD with the prescribed distribution in artificial fiber stacks. This parameter works similarly to the one proposed by Polzer *et al.* [188], albeit with a key distinction: here, the spectrum $|\hat{g}|$ is adjusted instead of the entire distribution d. Although this three-parameter approach yields satisfactory results, more advanced filtering techniques from 2D algorithms can also be incorporated. For instance, Witte *et al.* [112] introduced an adaptive filtering method that filters out irrelevant spectrum magnitudes, thus eliminating the need to set specific cut-off frequencies.

Given the fundamental importance of q in the proposed method, a calibration analysis was conducted to evaluate its impact on the final shape of the dFOD. Ideally, the errors $\Delta\sigma_{\theta\theta}$ and $\Delta\sigma_{\phi\phi}$ in the measured standard deviations should rely solely on q, independent of the dispersion being analyzed. In reality, however, these errors also vary with the particular fiber dispersion under consideration.

From Figure 4.3(b)-(c), it becomes evident that higher concentrations cause the algorithm to yield a dFOD that is less sharp than the prescribed one. This implies that a larger value of q may be required to enhance the precision of the measured distribution.

This tendency is also evident in Figure 4.6(a) and Figure 4.7(a), where the algorithm tends to underestimate the true concentrations at higher levels ($a_t = 5$, $b_t = 5$). Increasing the value of q could enhance precision in these instances, but it would lead to overestimations at lower concentrations. Aiming for accurate estimations across most scenarios, it is determined that $q = 2.4$ represents a suitable balance. Unlike the concentration parameters, the true mean orientation angles α_t and β_t rely solely on the distribution peaks and are not directly influenced by q. As indicated in Figure 4.6(b) and Figure 4.7(b), their precision improves with increased concentration, reducing uncertainty about peak locations in more defined distributions. Note that the precision of the parameters depends on the algorithm, while the nonlinear least squares fit ensures a reliable estimate of the dispersion parameters. The robustness analysis showed that the effectiveness of the algorithm is consistent regardless of the number of fibers N or their diameter t, though limitations may become more pronounced in out-of-plane measurements when fiber density δ is greater than about 25%.

Despite certain approximations and constraints, the algorithm effectively quantifies the spatial organization of complex fiber dispersions. Unlike 2D methods, which struggle to detect fibers significantly elevated from the x-y plane, the 3D approach encompasses fibers of all orientations. This differs from existing 3D techniques [114, 115], which offer separate θ and ϕ distributions, as the proposed algorithm provides a comprehensive spatial fiber distribution across the entire 3D angular domain. It enables identification of different fiber families and calculation of their specific parameters without ambiguity. In fact, when multiple fiber families are present, the different peaks cannot be combined together if only the separate in-plane and out-of-plane distributions are known, without information on how they co-vary in the rectangular angular domain.

In practical terms, as demonstrated in human and mouse skin analyses, scenarios with multiple fiber families are rare in biological soft tissues, where fibers predominantly align in the x-y plane (Figure 4.8(b) and Figure 4.9(b)). In such instances, in-plane parameters of fiber families can be derived from the in-plane distribution, while out-of-plane parameters are extracted from the 2D distribution of a vertical tissue section. However, this approach approximates by assigning a singular concentration b to all fiber families [80]. Another advantage of comprehensive 3D distributions is their capacity to assess the rolling angle γ (see

Figure 3.9(c)), accommodating general rotations in space and compensating for minor planar misalignments during 3D imaging.

In addition, the algorithm is fast and robust. For images sized $1024 \times 1024 \times 256$ voxels ($465\,\mu\text{m} \times 465\,\mu\text{m} \times 116.25\,\mu\text{m}$), the total processing time was 65 seconds for human skin (comprising 60.1 seconds for raw dFOD computation and 4.9 seconds for deconvolution), and 61 seconds for mouse skin (with 56.2 seconds for raw dFOD computation and 5.1 seconds for deconvolution), using a 2.20GHz CPU, 32GB RAM Desktop PC. The speed of computation is influenced by the dFOD resolution, as the number of calculations rises in proportion to the square of the angular interval D^2. Memory requirements can also be a constraint, with the necessary free memory for storing filters scaling with $D^2 \times M^3$. However, with a $D = 31$, as used in our examples, distributions of good angular resolution are attainable within a reasonable time frame.

The robustness analysis showed that the algorithm reliably predicts the same dFOD for images up to 25% fiber density. This is a significant advantage compared to pixel-by-pixel methods, which suffer from orientation uncertainties at the pixel level in dense fiber dispersions where fibers overlap [187]. Discrete Fourier transform-based methods are less affected by image complexity as they deduce fiber orientations from the frequency domain, which is not sensitive to spatial overlaps of fibers [113]. It is important to note that high-quality stacks with z resolution similar to the x-y plane are essential for this method, but acquiring such stacks is typically costly and time-intensive. The SHG stacks of human and mouse skin collagen shown in Figure 4.8(a) and Figure 4.9(a) (displayed after vertical resampling) were captured using our equipment at the highest possible z resolution ($\Delta z = 0.57\,\mu\text{m}$), each requiring around 2 hours to complete. Additionally, to mitigate blurring effects along the z direction from the confocal microscope diffraction, tomographies were pre-processed with three-dimensional deconvolution. Although this is a slow and computationally demanding step, emerging deep learning techniques offer promising prospects for deconvolution of microscope images [203] and noise reduction [204]. As the algorithm works with grayscale 3D images, various imaging technologies can be used for stack acquisition, making the method versatile for different imaging techniques, including x-ray computational tomography (xCT) [205], optical coherence tomography (OCT), and ultrasound imaging [206, 207].

In summary, the presented novel algorithm is able to precisely quantify the fiber network obtained from 3D images by determining the dispersion parameters of each individual fiber family. Thus, it will be used in the following Chapter 5 to compute the microstructure parameters required to inform the structure-based constitutive models described in Sections 3.2.3 and 3.2.4.

Chapter 5

Mechanical and Microstructural Parameters of Human Skin

Structure-based constitutive models introduced in Sections 3.2.3 and 3.2.4 account for general fiber dispersions and can potentially approximate the mechanical behavior of any kind of fiber-reinforced soft biological tissue. Therefore, accurate material-specific parameters for these models are essential to precisely simulate the characteristic mechanical properties of each material.

However, unlike many artificial materials, the mechanical properties of biological tissues are not unique, but are influenced by several biological factors and differ for each individual. These factors include age, sex, location on the body, and illnesses [142, 208–210]. Thus, multiple experiments are necessary to obtain a comprehensive view of the mechanical properties, and parameters for a specific constitutive model must be given after an accurate statistical analysis, possibly referred to a population of samples with uniform characteristics.

To calibrate these models for the skin, either *in vivo* or *ex vivo* tests can be performed. While microstructural parameters can be derived from SHG tomographies of the collagen fibers, as described in Chapter 4, mechanical parameters must be obtained through mechanical tests. Tests *in vivo* have been extensively used in the literature to characterize the mechanical behavior of the skin using techniques based on suction [91, 92], indentation [89, 90] and wave propagation [93, 94], to name just a few. These methods have the advantage of providing information about the skin in its natural state, but are affected by several uncertainties regarding pre-stress and boundary conditions [97]. Nonetheless, due to the non-invasive and non-destructive nature of *in vivo* tests, the range of investigated deformations is constrained to the range of physiological strains and is therefore limiting the

information required for accurate constitutive modeling [97]. In contrast, *ex vivo* experiments on representative skin samples can characterize the mechanical response over a full range of deformations. The current standard for investigating soft tissues properties is the biaxial tensile test [211]. Differently to uniaxial testing, skin samples are loaded in two perpendicular directions simultaneously. Since the applied deformation can be controlled independently for both directions, different loading protocols can be performed, providing the necessary mechanical data to define the material parameters for anisotropic models [101, 102]. Biaxial testing has been widely employed to determine the mechanical parameters for several tissues, such as aortic walls [103] and mitral valve leaflets [104, 105].

Despite its importance, there are relatively few studies calibrating structure-based mechanical models for the human skin using *ex vivo* tests. For example, Ní Annaidh *et al.* [146] investigated both mechanical and microstructural parameters of *ex vivo* samples using uniaxial tests along different directions relative to the Langer's lines, but provided limited mechanical data for model fitting. Other relevant studies by Tonge *et al.* [212] and Diab *et al.* [213] applied inflation tests to obtain biaxial mechanical data, but then obtained microstructural parameters through mechanical fitting rather than from images of the fiber microstructure, thereby reducing the physical significance of their results. More recently, Meador *et al.* [106] has thoroughly analyzed mouse skin, including biaxial testing and microstructural investigations, as well as considering the effects of physiological pre-strain on mechanical parameters. To date, no comparable comprehensive study has been conducted on human skin that included both biaxial tests and microstructural analysis.

To close this gap, the results of an experimental campaign on human skin samples are presented in this chapter. Fourteen healthy samples from the lower abdominal region were tested to obtain the mechanical and microstructural parameters for the GST and DFD constitutive models. Microstructural parameters describing the full three-dimensional fiber dispersion were derived using the algorithm presented in Chapter 4. Uniaxial tests were also performed to investigate the volumetric change of the skin in the uniaxial region and to demonstrate the limits of the generally accepted assumption of incompressibility stated in Equation (3.61). In addition, four samples deriving from a scar tissue were analyzed to observe the microstructural differences with healthy skin. The experiments campaign was conducted at the Norwegian University of Science and Technology (NTNU), employing the mechanical testing equipment at the Department of Structural Engineering to perform the biaxial tests, and the confocal laser microscope at the Department of Physics for the SHG imaging of the collagen fibers.

5.1 Experiments and Data Acquisition

5.1.1 Tissue Acquisition and Storage

Human skin samples were obtained from the surplus tissue of routine abdominal skin reduction surgeries at St. Olavs University Hospital, Trondheim, and at the private hospital Aleris Solsiden, Trondheim. All the patients provided written informed consent prior the surgical intervention. The study was approved by the Regional Committee for Medical and Health Research Ethics (Project ID: 474249), and all examinations were performed in accordance with the rules for the investigation of human subjects set out in the Declaration of Helsinki.

Fourteen square-shape samples of about 20 mm × 20 mm and close to the sagittal plane were obtained from the left and right sides of 3 patients as illustrated in Figure 5.1(a). Patient 1, female, 67 years old, 6 samples; Patient 2, female, 40, 4 samples; Patient 3, male, 20, 4 samples. Four additional samples were collected from an old Cesarean section scar of Patient 2, of which 2 contained healthy tissue and 2 contained scar tissue. After excision, the x and y axes were recorded on the epidermis with a permanent marker and the excess adipose tissue was removed, leaving only a layer of about 1 mm. The x axis coincided with the frontal (horizontal) axis for the fourteen healthy samples, while it was taken aligned with the scar axis in the other four samples. The samples were then stored at −28 °C prior to testing, within 2h of harvest.

5.1.2 Planar Tensile Tests

To prepare the samples for the mechanical tests, the remaining layer of adipose tissue was carefully removed while still frozen, ensuring that the dermis was not damaged during this process. Samples were then trimmed to an approximate size of 15 mm × 15 mm, and allowed to thaw at room temperature (20 °C). A schematic representation of the approximate sample location and corresponding nomenclature is shown in Figure 5.1(a). This sample size is sufficient to allow for an accurate constitutive modeling of soft tissues through biaxial tests [211]. A side view image of the samples resting on a custom 3D printed template, as shown in Figure 5.1(b), was acquired and used to measure the thickness in Fiji [197]. The samples were then attached to four hooks (Ahrex, Denmark) on each side with a distance of ∼ 3 mm. On the epidermis side, four fiducial markers were placed in the center of the samples, enclosing an approximate area of 5 mm × 5 mm (Figure 5.1(c)).

The samples were mounted on a custom-built biaxial machine [105] with

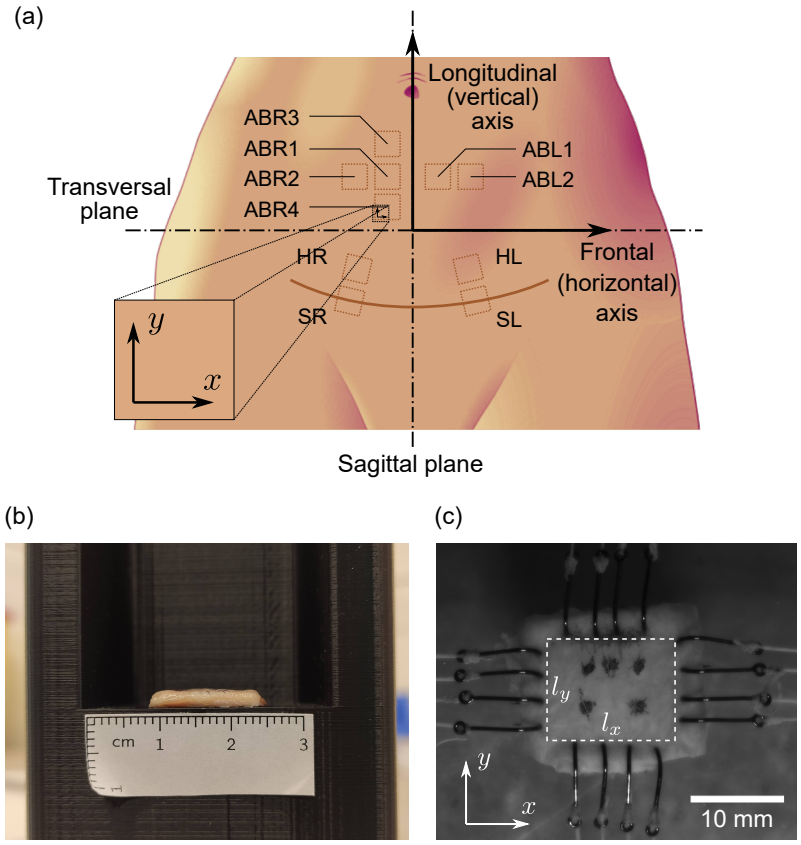

Figure 5.1: Location of samples and views of a representative sample: (a) Schematic representation of the approximate location (not to scale) and nomenclature of the samples. In the lower left corner of each sample, the corresponding x and y axes are shown (b) side view of the sample ABR3-p1 used for thickness measurement; (c) top view of the same sample mounted on the biaxial machine, with a dashed line highlighting the effectively tested sample area enclosed by the hooks with horizontal and vertical sizes l_x and l_y, respectively. The four fiducial markers at the corners are used to compute the deformations with the DIC software, while the fifth marker in the top row was used to keep track of the x axis during the preparation prior to mounting on the biaxial machine.

surgical Gore-Tex CV5 sutures (Gore Medicals, USA) attached to the hooks. The machine was equipped with rotating bars on each arm, allowing the samples to balance during loading and minimizing shear stresses. The deformations were computed based on the position of the fiducial markers tracked with a custom Digital Image Correlation (DIC) software [214], allowing us to obtain a complete description of planar deformations, including shear deformations due to material anisotropy. Data are synchronized with the measured forces at a frequency of 2 Hz. Throughout the tests, the samples were immersed in water bath filled with 0.1×PBS, phosphate buffered saline, solution at 37 °C.

After mounting, the samples were pre-loaded with 0.01 N in both the x and y directions, defining the zero-strain reference configuration, and preconditioned with 5 loading-unloading cycles with $d_x : d_y = 1 : 1$ at a rate of 0.1 mm/s, where d_x and d_y are the displacements along the x and y directions, respectively. Four loading tests were then performed, each repeated three times with different displacement protocols and a rate of 0.1 mm/s: biaxial test $1 : 1$, biaxial test with increased displacement along the less rigid direction $1 : \delta$, $0.75 \leq \delta \leq 1.25$, uniaxial test along x, and uniaxial test along y.

5.1.3 Tomographic Reconstruction of Fibers

After completing the mechanical tests and within 2h of thawing, the samples were prepared for the SHG imaging [215]. Samples were chemically fixated in 4% paraformaldehyde for at least 12h to prevent tissue degradation and preserve collagen fiber structure. The samples were then optically cleared according to the SeeDBp protocol [195], as described in Section 4.3.1. This technique allows biological tissues to be cleared while preserving their morphology [216]. In contrast, however, compared to other tissues documented in the literature [196], the treatment enhanced the clarity of the samples but complete transparency is not achieved. This is likely due to the increased density of the collagen network in the dermis layer. This makes it difficult for the solution to penetrate deep into the tissue. After the clearing process is completed, the samples were placed in a press-to-seal silicone isolator (CoverWell™ Imaging Chambers, Grace BIO-Labs, Oregon, USA) filled with SeeDB solution and sealed at the top and bottom with two rectangular glass coverslips ensuring no bubbles are placed over the acquisition site (Figure 5.2(a)). To prevent any compression of the sample against the glasses, resulting in possible alterations of the fiber arrangement, silicone isolators are stacked to match the thickness of the sample. Sealing also prevents SeeDB to evaporate and increase its concentration, thereby altering the refractive index of

the solution with negative impact on the quality of the image due to the increased light scattering.

SHG imaging was performed with a Leica TCS SP8 (Leica Microsystem, Germany) confocal multiphoton microscope using the Leica HCX IRAPO 25×, NA 0.95 water objective with a working distance of 2.4 mm. The second harmonic of collagen was induced with a multiphoton laser source tuned to 890 nm (Chameleon Ultra I; Coherent Corp., Saxonburg, PA, United States), while the signal emitted at 445 nm was detected in the forward and backward directions with standard photomultiplier tube (PMT) and highly sensitive HyD (GaAsP) detectors, respectively. No aperture was placed in front of the laser source, nor in front of the detectors. The scattering that occurred at greater depths in the tissue was compensated for by linearly increasing the laser power. Images were acquired on a 465 μm × 465 μm square target within the fiducial markers using an x-y resolution of 0.454 μm/px (Figure 5.2(b)). To enable a tomographic reconstruction of the target region, images are recorded every 0.57 μm in the z direction. This represents the lower system-optimized vertical step size in relation to image resolution, numerical aperture, refractive index, and acquisition wavelength. For the additional 4 samples from Patient 2, the 2-photon excited fluorescence (2PEF) signal was also recorded to observe the difference of elastin fiber content between the healthy and scarred samples. Due to the non-optimal transparency of the samples, only about 300 μm tissue thickness from the epidermis side could be scanned.

To compensate for the blurring artifacts in the lateral (x-y) and vertical (z) directions due to the inherent specimen-induced aberrations and light scattering, which could alter the results of the microstructural analysis, the tomographies were then deconvoluted. This procedure, applicable to SHG images [217], was performed in the open-source image processing software Fiji [197] using the DeconvolutionLab2 plugin for deconvolution microscopy [193]. In particular, the Richardson–Lucy algorithm with total variation regularization (regularization parameter $\lambda = 10^{-3}$, 25 iterations) was employed. The point spread function required for the process was derived using the Gibson and Lanny 3D optical model [198, 199] adopting the refractive index of the collagen fibers in the SeeDB solution, $n_s = 1.48$ [218]. Finally, the tomographies were resliced along the z direction to match the z spacing with the x-y resolution (Figure 5.2(c)) [190].

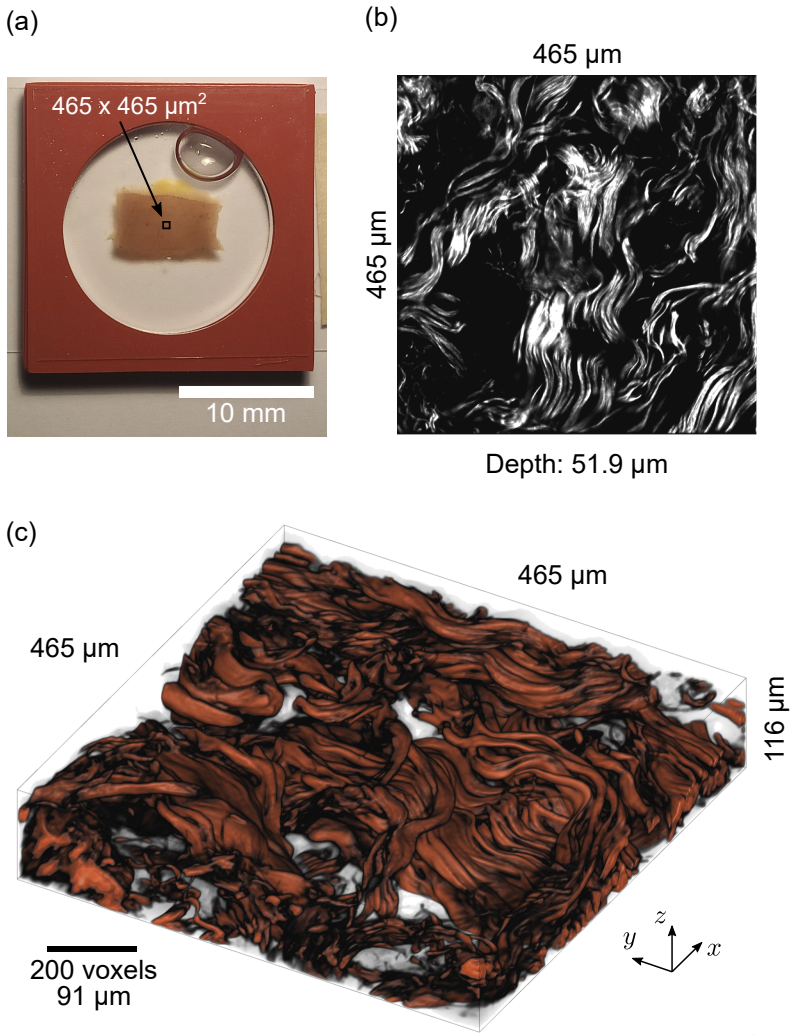

Figure 5.2: SHG acquisition for tomographic reconstruction of collagen fibers: (a) sample ABL1-p3 (cropped) in the silicone isolator filled with SeeDB solution and the representative square SHG target (at scale) ; (b) representative 465 μm × 465 μm SHG image taken at 51.9 μm below the epidermis of the sample in (a); (c) representative collagen fiber tomography of sample ABL1-p3 (first 116 μm for visualization purposes) after the deconvolution process with DeconvolutionLab2 [193].

5.1.4 Identification of the Microstructural Parameters

The sets of microstructural parameters $\{a_i,\, b_i,\, \alpha_i,\, \beta_i,\, \gamma_i,\, \nu_i\}$, $i = 1, \ldots, m$, of the collagen fiber networks were measured from the tomographies using the algorithm described in Chapter 4. To determine the number of families of each tomography, the dFOD $d'(\theta, \phi)$ was fitted stepwise with the distribution $\overline{\rho}(\theta, \phi)$ in Equation (4.7) with an increasing number of fiber families m until a quality of fit $R^2 > 0.9$ was achieved.

5.1.5 Constitutive Model Fitting

Planar tensile tests were performed before SHG imaging, thus without prior knowledge of the fiber distribution. Due to the configuration of the biaxial testing machine, the samples can deform freely during testing, allowing material anisotropy with shear deformations even when no shear stress is applied. Therefore, the experimental deformation gradient, termed $\mathbf{F}^{\mathrm{e}}$, was computed from the position of the four markers placed on the sample surface and tracked using the DIC system. Assuming that the strain field between the markers is homogeneous, the planar components of $\mathbf{F}^{\mathrm{e}}$ were computed using a bi-linear iso-parametric element with 4 nodes, where the only non-planar component F_{zz} was determined from the incompressibility assumption $J = \det \mathbf{F}^{\mathrm{e}} = 1$ [102, 219].

The nominal stress components of the experimental first Piola-Kirchhoff stress tensor $\mathbf{P}^{\mathrm{e}}$ were computed from the recorded forces f_x and f_y using [102, 219], i.e.

$$[\mathbf{P}^{\mathrm{e}}] = \mathrm{diag}\left[f_x/(t\, l_y),\, f_y/(t\, l_x),\, 0\right], \tag{5.1}$$

where t is the sample thickness, measured as described in Section 5.1.2, while l_x and l_y are the width and height of the sample relative to the area within the hooks (dashed box in Figure 5.1(c)), measured from the first DIC image of the test using Fiji [197].

Subsequently, the mechanical parameters for the GST and DFD constitutive models of each sample were determined by simultaneously minimizing all 4 objective functions Ξ_{qr}, $q, r \in \{x, y\}$, defined as

$$\Xi_{qr} = \sum_{i=1}^{K} (P^{\mathrm{e}}_{qr} - P_{qr}(\mathbf{F}^{\mathrm{e}}))^2_i\,, \tag{5.2}$$

including simultaneous mechanical data from the two biaxial tests ($d_x : d_y = 1 : 1, 1 : \delta$). In Equation (5.2), K denotes the total number of data points between the two tests, while P_{qr} is the qr component of the theoretical first Piola-Kirchhoff

stress tensor $\mathbf{P} = \mathbf{F}^{\mathrm{e}}\mathbf{S}$, where $\mathbf{S}$ is computed from Equation (3.66) by expressing the hydrostatic pressure p using the plane stress constraint $S_{zz} = 0$. From Equations (5.1) and (5.2) it follows that this method also enforces the planar shear components to zero. Note that only the parameters μ, k_1, k_2 (for the GST model) and c_1, c_2 (for the DFD model) need to be fitted since the microstructural parameters are determined from the SHG tomography (Section 5.1.4). It is also important to emphasize that despite the similarities, the two models differ substantially and agree only in the case of perfectly aligned fibers, $a_i, b_i \to \infty$. As a consequence, the two sets of mechanical parameters $\{k_1, k_2\}$ and $\{c_1, c_2\}$ are not interchangeable between the two models.

The analysis was performed using a custom MATLAB code (v. R2023a; The MathWorks Inc., Natick, MA, USA) based on the built-in nonlinear least squares function `lsqnonlin` using the trust-region-reflective algorithm. To ensure convergence to the same set of fitted parameters, the analysis was repeated several times for each sample, initiating the process from different combinations of initial parameter values [105].

5.1.6 Statistical analysis

The metrics used to assess the goodness of fit are the coefficient of determination R^2 for the fiber orientation distributions data and the weighted Mean Absolute Percentage Error (wMAPE) for the mechanical data, defined as

$$wMAPE = \sum_{q,r\in\{x,y\}} \frac{\sum_{i=1}^{K} w_i \dfrac{|P^{\mathrm{e}}_{qr} - P_{qr}|_i}{|P^{\mathrm{e}}_{qr}|_i}}{\sum_{i=1}^{K} w_i} = \sum_{q,r\in\{x,y\}} \frac{\sum_{i=1}^{K} |P^{\mathrm{e}}_{qr} - P_{qr}|_i}{\sum_{i=1}^{K} |P^{\mathrm{e}}_{qr}|_i}, \qquad (5.3)$$

in which the weights w_i were assumed to be equal to $|P^{\mathrm{e}}_{qr}|_i$. Differences between values associated with the GST and DFD models (mechanical parameters and wMAPE) were compared with paired t-tests, while significant correlations between the mechanical parameters were tested using the Pearson correlation coefficient. The analysis of the angular data was performed according to circular statistics and took into account the symmetry of the fibers, according to which the angles couples (θ, ϕ) and $(\theta + 180°, -\phi)$ represent the same fiber orientation. Specifically, the Watson-Williams high concentration F-test was used to test the difference between the average collagen fiber orientation of the samples from the left and right sides of the human body. Differences and correlations were considered significant when the P-value was less than 0.05 (95% confidence). Data analyses were carried out employing the Real Statistics Resource Pack software [194].

5.2 Results

5.2.1 Healthy skin

Figure 5.3 shows the measured distributions computed from the SHG tomographies of 14 healthy skin samples and the corresponding fitted bivariate distributions $\overline{\rho}(\theta,\phi)$. The mean fiber directions and standard deviations computed from the measured distributions are summarized in Table 5.1 together with the SHG-scanned skin thicknesses. After the clearing process with SeeDBp protocol, a thickness $311.8 \pm 50.7\,\mu$m tissue could be scanned from the epidermis side. The tomographies only included the dermis layer because the epidermis does not contain collagen fibers. However, due to sub-optimal clearing, only the backward SHG signal was suitable to obtain satisfactory collagen fiber tomographies. In particular, all samples showed a fiber distribution with low elevations and small standard deviations, $\phi_{\text{avg}} = -2.6 \pm 2.2°$ and $\sigma_{\phi\phi} = 21.4 \pm 6.5°$ for the right samples, and $\phi_{\text{avg}} = -0.8 \pm 1.7°$ and $\sigma_{\phi\phi} = 20.4 \pm 6.3°$ for the left ones, with no significant differences between the two groups. This indicates that the fiber dispersions lie

Table 5.1: Overall collagen fiber data determined from the SHG tomographies: tomography thickness t, average fiber azimuth θ_{avg} and elevation ϕ_{avg}, circular standard deviations along the azimuth $\sigma_{\theta\theta}$ and elevation $\sigma_{\phi\phi}$. Averages and standard deviations for the angular data are reported separately for the right (R) and left (L) samples.

Sample		t (μm)	θ_{avg} (°)	ϕ_{avg} (°)	$\sigma_{\theta\theta}$ (°)	$\sigma_{\phi\phi}$ (°)
ABR1-p1		301.7	–84.6	–3.8	56.1	11.8
ABR1-p2		271.9	–71.5	–1.6	54.9	14.4
ABR1-p3		381.3	–78.3	–4.9	47.2	19.4
ABR2-p1		350.6	82.4	–0.5	26.1	27.0
ABR2-p2		290.7	–41.8	–4.5	35.7	18.0
ABR2-p3		216.6	66.8	–2.5	41.3	28.8
ABR3-p1		360.8	–52.0	–4.6	16.2	23.8
ABR4-p1		322.1	57.6	1.9	33.8	27.9
ABL1-p1		238.8	–65.3	–0.6	42.7	16.6
ABL1-p2		258.8	68.9	0.2	26.4	18.9
ABL1-p3		312.9	80.8	2.0	45.0	14.7
ABL2-p1		344.9	9.4	–3.4	29.9	24.3
ABL2-p2		354.0	68.8	–2.1	23.1	31.4
ABL2-p3		360.2	–79.8	–0.7	67.1	16.5
Average	(R)	311.8	–82.8	–2.6	38.9	21.4
	(L)		82.0	–0.8	39.0	20.4
St. Dev.	(R)	50.7	27.4	2.2	13.8	6.5
	(L)		32.2	1.7	16.3	6.3

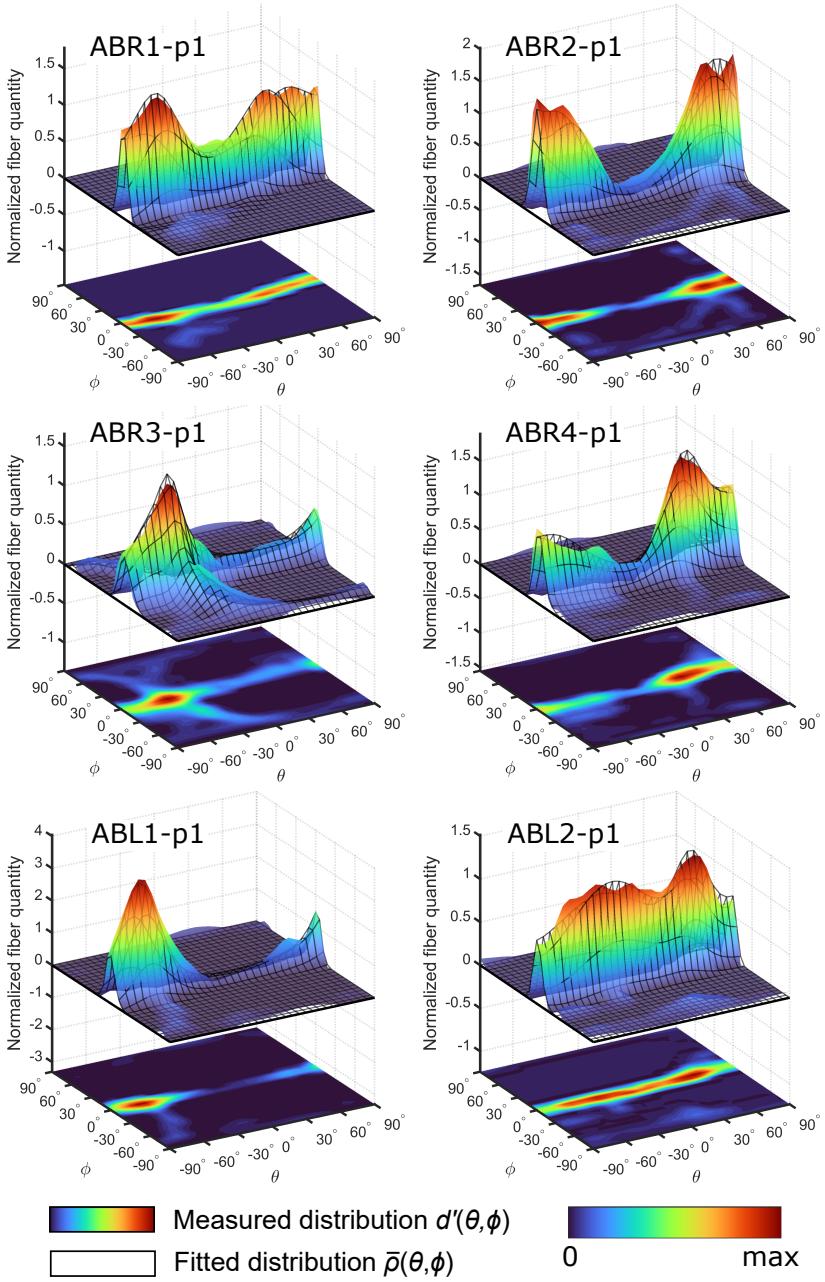

(a) Fiber orientation distributions of samples from Patient 1.

Figure 5.3: Measured fiber orientation distributions $d'(\theta,\phi)$ (colored), computed from the SHG tomographies, and the fitted von Mises distributions $\overline{\rho}(\theta,\phi)$ (wireframes) of the analyzed samples. The distributions are normalized so that the integral over the unit hemisphere is one.

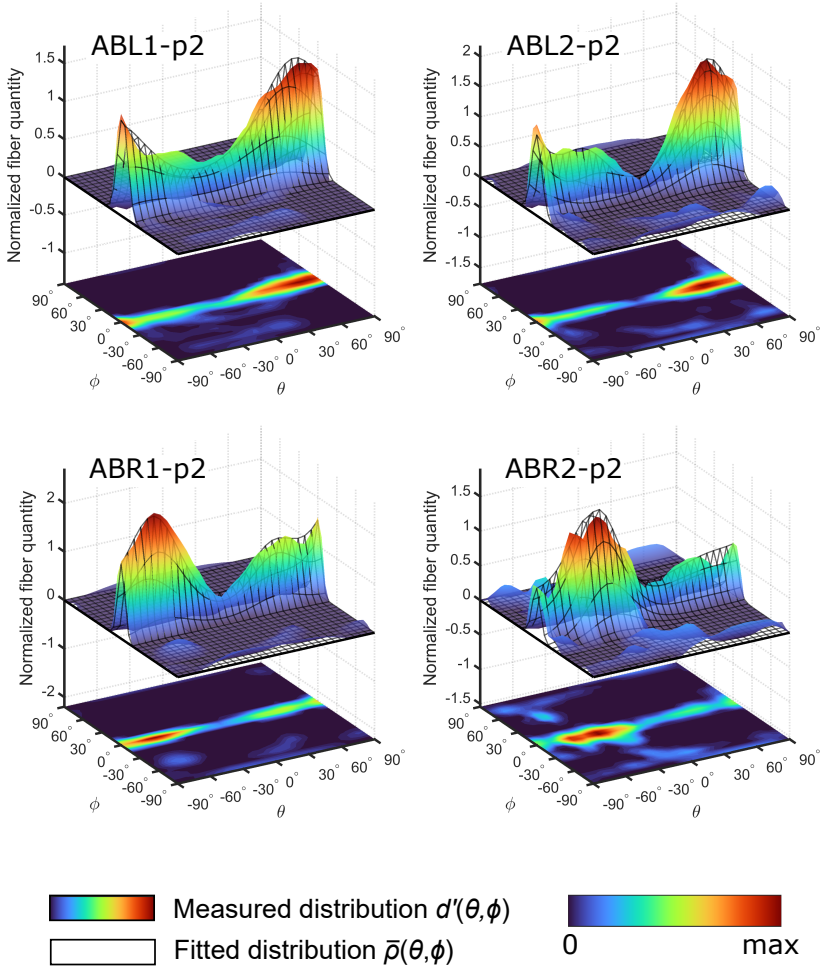

(b) Fiber orientation distributions of samples from Patient 2.

Figure 5.3: Measured fiber orientation distributions $d'(\theta,\phi)$ (colored), computed from the SHG tomographies, and the fitted von Mises distributions $\bar{\rho}(\theta,\phi)$ (wireframes) of the analyzed samples. The distributions are normalized so that the integral over the unit hemisphere is one. Continued.

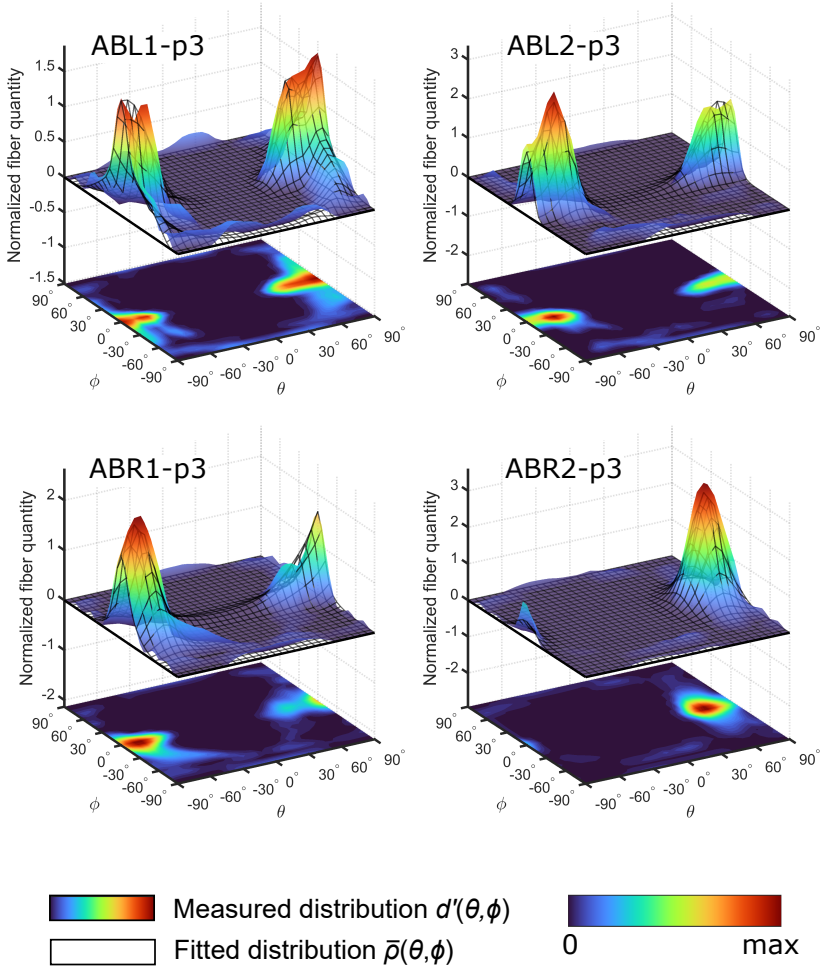

(c) Fiber orientation distributions of samples from Patient 3.

Figure 5.3: Measured fiber orientation distributions $d'(\theta,\phi)$ (colored), computed from the SHG tomographies, and the fitted von Mises distributions $\bar{\rho}(\theta,\phi)$ (wireframes) of the analyzed samples. The distributions are normalized so that the integral over the unit hemisphere is one. Continued.

mainly in the x-y plane, i.e. the skin mean plane. Looking at the azimuth quantities, there was a symmetry, but it was not significant for either the mean angles or the standard deviation. In particular, the distributions for the right samples were mainly oriented downward, $\theta_{\text{avg}} = -82.8 \pm 27.4°$, and mostly upwards for the left ones, $\theta_{\text{avg}} = 82.0 \pm 32.2°$. Furthermore, as expected, the fiber distributions were broader in the azimuthal direction with a standard deviation of $\sigma_{\theta\theta} = 38.9 \pm 13.8°$ and $\sigma_{\theta\theta} = 39.0 \pm 16.3°$ for the right and left samples, respectively. Despite the limited number of samples, these observations revealed a fiber organization consistent with the Langer's lines in the lower abdominal region, see Figure 5.4, i.e. the average direction of the collagen fibers in the human body [132, 220].

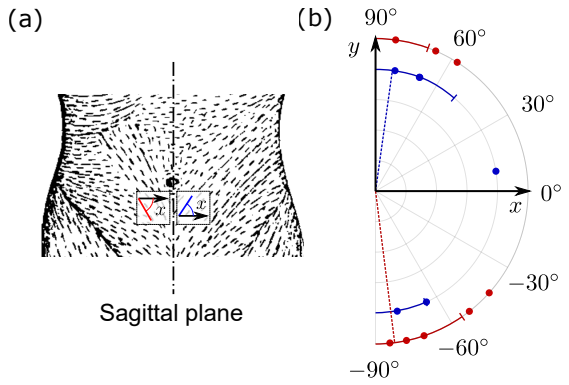

Figure 5.4: Average collagen fiber orientation in azimuthal direction: (a) Langer's lines [132], representing the average collagen fiber direction on the human body, and the highlighted directions in the abdominal region; (b) polar representation of the average fiber direction of the right (red dots) and left (blue dots) samples about the sagittal plane, computed from the measured fiber orientation distributions. Dashed lines represent the right and left averages directions at $\theta_{\text{avg}} = -82.8°$ and $\theta_{\text{avg}} = 82.0°$, respectively, while the whiskers their corresponding circular standard deviations.

Table 5.2 summarizes the microstructural parameters of the fitted von Mises distributions $\overline{\rho}(\theta, \phi)$ shown in Figure 5.3 (wireframe plots). The families are sorted in descending order by volume fraction ν_i so that the first family has the largest contribution to the overall fiber orientation distribution. The fitting made no assumptions about the number m of families, which was obtained by the lower number m, ensuring a coefficient of determination $R^2 > 0.9$. In general, the number of families is reflected in the number of distinct local maxima, which in our cases was always $m \leq 2$. However, a third isotropic family was introduced

Table 5.2: Microstructural parameters of the fitted distributions in Figure 5.3 and goodness of fit (R^2).

	Family 1						Family 2						Family 3					
Sample	a_1 (-)	b_1 (-)	α_1 (°)	β_1 (°)	γ_1 (°)	ν_1 (-)	a_2 (-)	b_2 (-)	α_2 (°)	β_2 (°)	γ_2 (°)	ν_2 (-)	a_3 (-)	b_3 (-)	α_3 (°)	β_3 (°)	γ_3 (°)	ν_3 (-)	R^2
ABR1-p1	0.5	24.8	46.3	-3.8	8.5	0.63	1.9	17.9	-60.2	-6.2	-3.0	0.33	0.0	22.5	25.0	-16.4	44.4	0.04	0.98
ABR1-p2	0.3	19.0	71.9	-0.7	2.9	0.77	2.0	25.2	-52.3	-2.7	2.9	0.23							0.97
ABR1-p3	6.9	2.4	-74.4	-10.9	10.7	0.54	1.4	11.5	90.0	-0.5	1.3	0.46							0.89
ABR2-p1	1.4	10.9	69.5	-1.8	6.2	0.77	2.4	31.2	-61.4	-2.8	-4.5	0.23							0.95
ABR2-p2	2.1	8.5	-38.0	-6.0	-7.5	0.60	0.3	21.8	70.7	-1.1	1.1	0.40							0.84
ABR2-p3	6.0	3.6	66.8	-2.5	-4.7	1.00													0.93
ABR3-p1	1.4	8.5	-58.1	-4.1	12.6	0.45	11.0	0.2	-40.0	-26.9	12.4	0.33	0.0	21.3	90.0	2.0	-0.8	0.22	0.95
ABR4-p1	0.7	17.1	-84.7	-3.5	-5.1	0.54	2.1	10.3	45.4	2.0	22.6	0.46							0.96
ABL1-p1	3.1	13.7	-64.2	-1.2	-4.5	0.76	0.5	46.5	90.0	-3.4	1.7	0.24							0.95
ABL1-p2	0.6	11.8	68.7	0.2	7.0	1.00													0.95
ABL1-p3	1.7	7.9	90.0	4.6	5.0	0.77	3.9	13.8	55.7	-5.4	5.0	0.23							0.92
ABL2-p1	0.4	20.6	-26.6	-3.9	-1.1	0.79	2.9	13.5	52.5	1.8	17.6	0.21							0.97
ABL2-p2	1.4	11.4	64.9	-2.0	5.6	0.83	1.5	44.8	-45.9	-0.6	-4.3	0.17							0.93
ABL2-p3	2.3	12.9	77.8	-1.4	10.2	0.55	11.5	6.0	-65.3	-1.8	45.0	0.45							0.93

for samples ABR1-p1 and ABR3-p1. This family, which represents the smallest volume fraction of the overall distribution with $\nu_3 = 0.04$ for ABR1-p1, and $\nu_3 = 0.22$ for ABR3-p1, does not relate to a local maximum, but rather shifts the distribution to improve the quality of the fit.

The mechanical parameters of the GST and DFD models are reported in Table 5.3 along with the sample thickness and the residual errors of the fitting expressed as wMAPE. The sample thickness, measured from the side view images taken before the mechanical tests, was $t = 2.92 \pm 0.71$ mm. The shear parameter of the neo-Hookean ground matrix, which prevails at small stretches, was relatively small, $\mu = 1.142 \pm 0.879$ kPa. The fiber parameters were instead $k_1 = 0.5914 \pm 1.3013$ kPa and $k_2 = 68.5 \pm 29.5$ for the GST model and $c_1 = 1.9074 \pm 2.4427$ kPa and $c_2 = 43.6 \pm 15.3$ for the DFD model. As reported in Figure 5.6(a), the fiber stiffness-like parameters k_1 were significantly lower than c_1 upon *log*-transformation ($P = 5.45 \times 10^{-5}$). On the other hand, the dimensionless parameter k_2, which controls the exponential stiffening of the loading curves, was significantly higher than its counterpart c_2 ($P = 7.39 \times 10^{-4}$) (Figure 5.6(b)). This suggests a stiffer behavior of the DFD model compared to the GST one. However, as shown in Figure 5.5, both constitutive models predicted the mechanical behavior of the skin with good agreement, although the DFD model proved more difficult to fit and displayed a residual wMAPE error of $38.7 \pm 5.8\%$, significantly higher

Table 5.3: Estimated mechanical parameters of the GST and DFD models from the biaxial tests and the relative mechanical fitting residual in terms of wMAPE error. The sample thickness is given in the first column.

			GST model			DFD model		
Sample	t (mm)	μ (kPa)	k_1 (kPa)	k_2 (-)	wMAPE (%)	c_1 (kPa)	c_2 (-)	wMAPE (%)
ABR1-p1	3.80	0.680	0.8736	53.7	30.0	3.3788	32.8	45.9
ABR1-p2	2.67	1.251	0.1267	52.1	28.7	1.2388	36.5	36.5
ABR1-p3	3.97	0.503	0.0300	48.5	31.5	0.7713	23.1	34.8
ABR2-p1	2.74	0.628	4.8057	66.9	50.9	8.2124	71.0	33.8
ABR2-p2	3.00	0.848	0.0497	34.4	37.1	0.5141	26.0	33.4
ABR2-p3	4.22	0.115	0.1292	63.3	24.0	4.6846	35.0	26.9
ABR3-p1	2.34	1.143	0.0166	130.0	28.0	0.5893	49.5	41.2
ABR4-p1	2.43	2.486	0.0233	102.5	20.2	0.6629	53.8	44.9
ABL1-p1	2.03	1.531	0.0205	91.5	42.8	0.0891	45.5	37.9
ABL1-p2	2.92	0.344	0.0003	51.0	37.8	0.3085	32.5	47.8
ABL1-p3	3.58	1.643	0.5251	74.9	29.0	1.3303	56.8	37.6
ABL2-p1	2.09	0.802	0.0020	38.3	38.7	0.0060	29.7	42.5
ABL2-p2	2.25	0.667	0.0215	41.0	26.3	0.1620	48.6	43.3
ABL2-p3	2.77	3.340	1.6553	110.8	34.4	4.7554	69.3	35.5
Average	2.92	1.142	0.5914	68.5	32.8	1.9074	43.6	38.7
St. Dev.	0.71	0.879	1.3013	29.5	8.1	2.4427	15.3	5.8

($P = 0.028$) than the error of the GST model, $32.8 \pm 8.1\%$ (Figure 5.6(c)).

To examine possible correlations between mechanical and microstructural parameters, a linear regression analysis was carried out. Significant correlations were found between μ and k_2, c_2, shown in Figure 5.7(a), with a Pearson coefficient of $r = 0.657$ ($P = 0.011$) and $r = 0.624$ ($P = 0.017$), respectively. Two additional correlations were found between the GST and DFD parameters. In particular, k_1 was positively correlated with c_1 in the *log*-transformation ($r = 0.773$, $P = 0.0012$)(Figure 5.7(b)), as well as k_2 with c_2 ($r = 0.627$, $P = 0.016$)(Figure 5.7(c)). Other nonlinear correlation between mechanical parameters were tested but no significant correlations were found.

In addition to the biaxial tests, we also performed uniaxial tests along the x and y directions to understand the mechanical behavior of the skin in the uniaxial tension regime. The mechanical responses along the x and y directions of all samples are shown in Figure 5.8(a) and (b), respectively, while in Figure 5.8(c) and (d), the respective principal stretches are shown. Therein, λ_1 and λ_2 were computed from the eigenvalues of the planar components of $\mathbf{F}^e$, i.e. using the position of the fiducial markers, whereas the out-of-plane stretch λ_3 was derived from the incompressibility assumption $J = \lambda_1\lambda_2\lambda_3 = 1$. Note that in Figure 5.8(c) and (d)

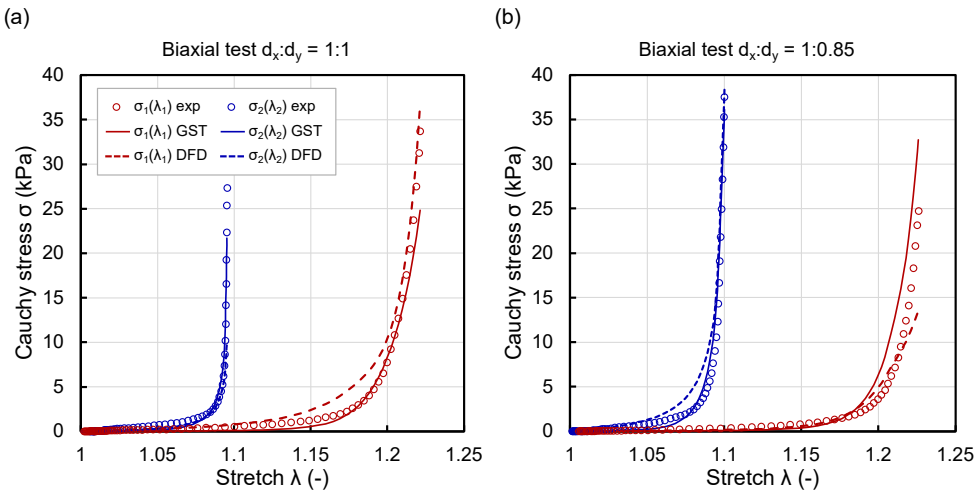

Figure 5.5: Representative experimental mechanical response of sample ABR2-p3 (circles) in horizontal (red) and vertical directions (blue) for the biaxial tests (a) $d_x : d_y = 1 : 1$, and (b) $d_x : d_y = 1 : 0.85$ (b). The mechanical models predicted the experimental data well, with a residual wMAPE error of 24% for the GST model (solid curves) and 26.85% for the DFD model (dashed curves). Note that each model used a unique set of parameters to predict both biaxial tests.

the data are truncated at axial stretches $\lambda_1 = 1.29$ and $\lambda_1 = 1.38$, respectively, to ensure a computation of the averages and standard deviations using at least 20 tests.

The transverse stretches λ_2 and λ_1, relative to the tests along the x and y directions, both decrease as the samples elongate along the loading axis, except for a small region within the standard deviation above $\lambda = 1$. This non-physical behavior, more pronounced in the tests along the x direction (Figure 5.8(c)), was caused by the movement of the samples from the bottom of the bath towards the DIC camera before reaching the stable height. During this vertical excursion (about 20 mm), the samples changed focal plane and the fiducial markers were magnified and appeared to be biaxially stretched. However, as soon as the samples reached the steady height relative to the camera, the actual movement of the markers was captured and the transverse stretches returned to a state of contraction ($\lambda < 1$). On the other hand, in both tests, the out-of-plane stretch λ_3 initially decreased to about 0.9 for axial stretches of $\lambda_1 = 1.16$ and $\lambda_2 = 1.23$. Subsequently, the trend was reversed and it expanded with increasing axial deformation. This behavior, however, seems unlikely in reality and is probably the result of the incompressibility assumption.

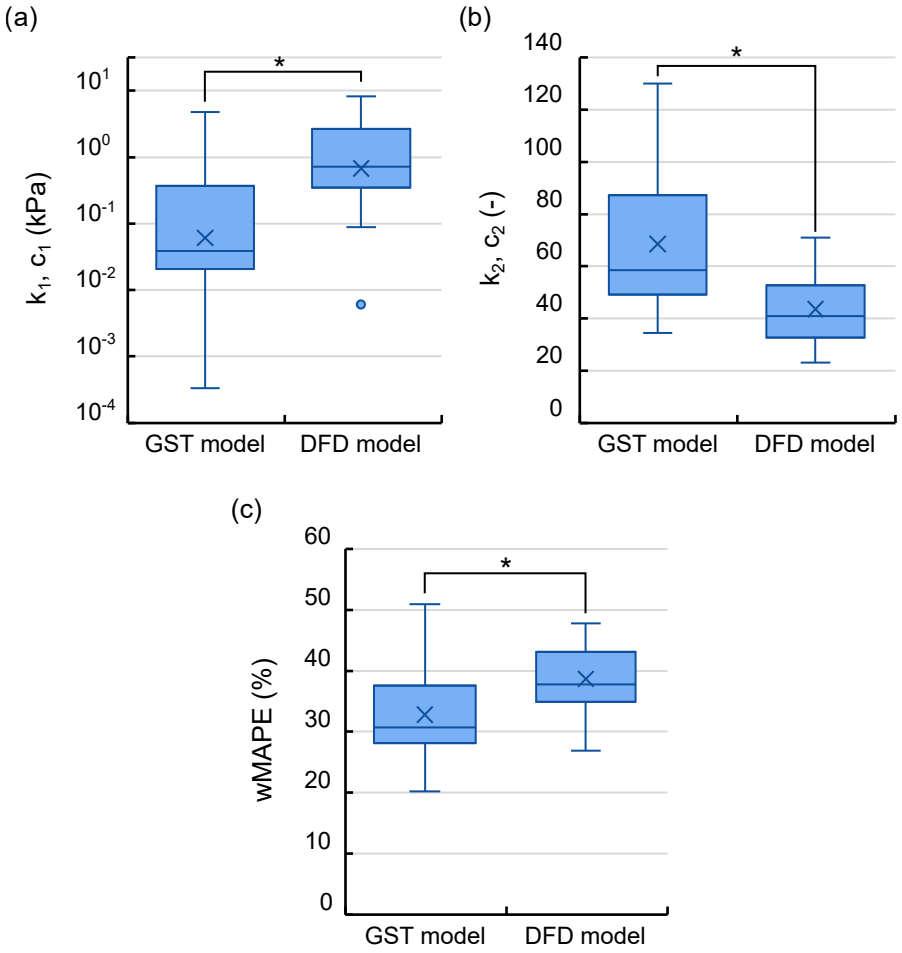

Figure 5.6: Box-and-whiskers plots of GST and DFD parameters: (a) fiber stiffness-like parameters k_1, c_1; (b) stiffening parameters k_2, c_2; (c) mechanical fitting of the residual wMAPE errors. The boxes extend from the lower to the upper quartile of the data, with a line at the median and whiskers extending to the minimum and maximum values. Crosses indicate the average values, circles the outliers ($*$: $P < 0.05$).

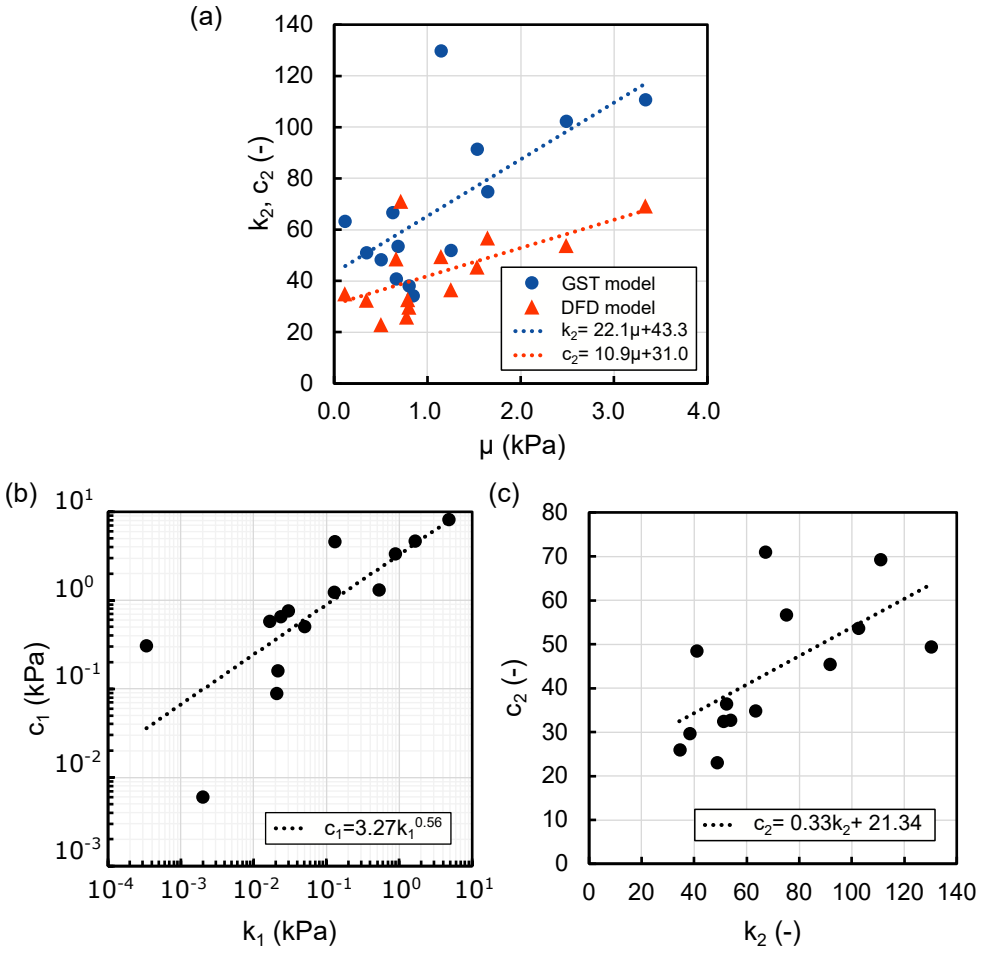

Figure 5.7: Significant correlation between the parameters: (a) isotropic neo-Hookean parameter μ for the ground matrix with stiffening parameters k_2 and c_2; (b) fiber stiffness-like parameter k_1 with c_1; (c) stiffening parameter k_2 with c_2. In (b) the exponential relationship between k_1 and c_1 is obtained from linear regression in the *log*-transformed domain.

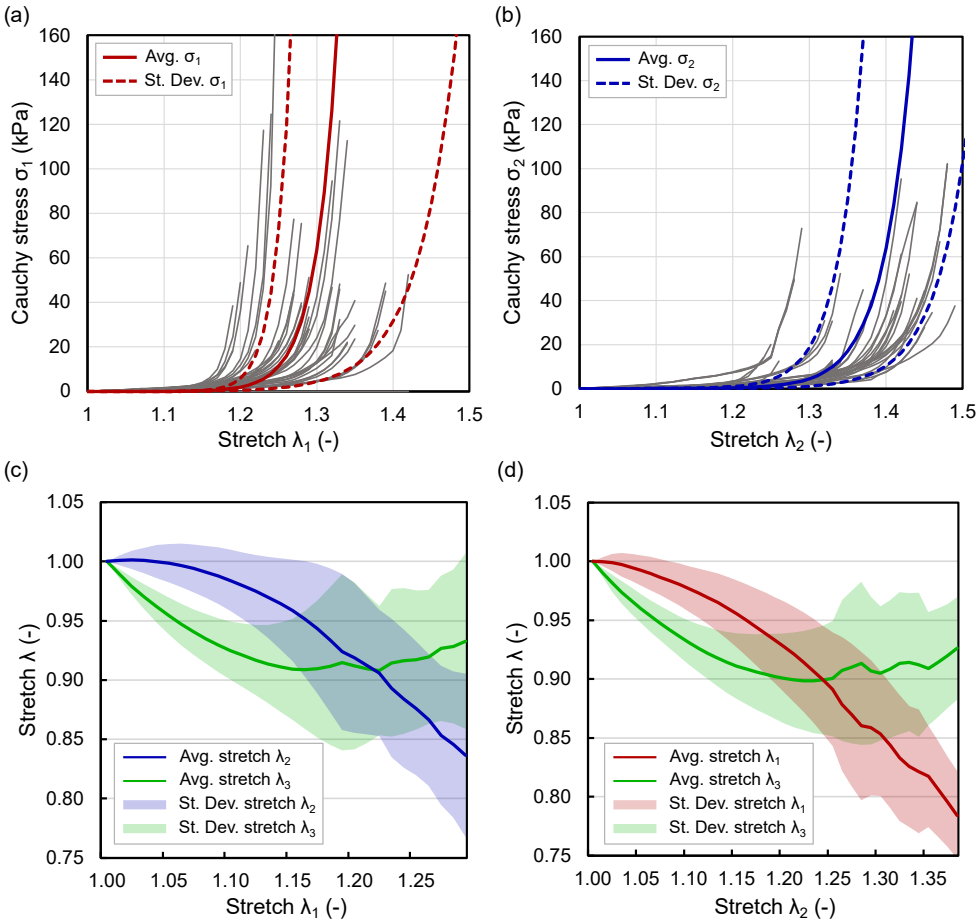

Figure 5.8: Average mechanical responses of the uniaxial tests performed along the horizontal (x-axis) and vertical (y-axis) directions: (a), (b) principal Cauchy stress σ versus principal stretch λ for uniaxial tests along x and y, respectively. Solid curves indicate the average values and dashed curves the standard deviations; (c), (d) transversal stretches λ_2, λ_1, and out-of-plane stretch λ_3 versus axial principal stretches along x and y. Averages and standard deviations computed from at least 20 tests.

5.2.2 Scarred skin

Four additional samples were analyzed from Patient 2, who reported an older C-Section scar. Two samples from the right and left sides around the sagittal plane, SR-p2 and SL-p2, were tested with the scar running along the x direction. Two additional samples of adjacent healthy skin, HR-p2 and HL-p2, taken with the same orientation parallel to the scar were tested for comparison (Figure 5.1(a)).

The SHG images revealed a consistent difference in collagen morphology between healthy and scar tissues. As shown in Figure 5.9(a) and (b), the collagen fiber bundles (in green) in scarred skin were straighter and thinner, running almost perpendicular to the scar axis and with increased concentration. This difference is also captured by the measured fiber orientation distributions shown in Figure 5.9(c) and (d). In contrast to sample HR-p2, which had two nearly symmetrical fiber families with mean orientations $\alpha_1 = -83.9^\circ$ and $\alpha_2 = 46.9^\circ$, the scarred tissue presented a single largely concentrated family at $\alpha_1 = -72.2^\circ$, along with a smaller but highly concentrated family almost parallel to the scar at $\alpha_2 = -8.1^\circ$. Similar results were observed for the other two samples (see Table 5.4). Although the focus of our study was primarily on collagen fibers, we observed a remarkable reduction in elastin fibers in the scarred skin (red fibers in Figure 5.9(a) and (b)).

The mechanical parameters obtained from biaxial tests are listed in the Table 5.5. Due to the limited number of samples and the different location on the body, these parameters are not compared to the parameters presented in the previous section.

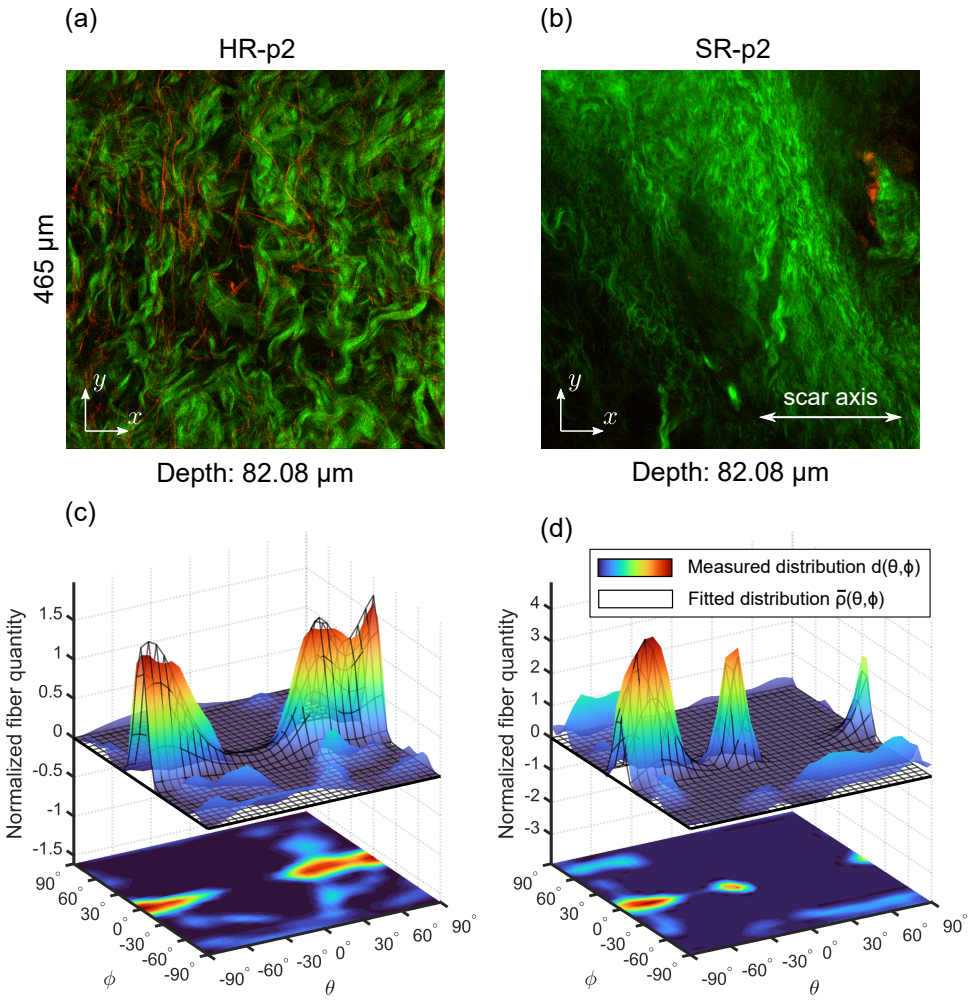

Figure 5.9: Fiber architecture in healthy and scarred skin: (a),(b) superposition of collagen (SHG signal, green) and elastin fibers (2PEF signal, red) of the right healthy and scarred skin samples HR-p2 and SR-p2, at 82.08 μm below the epidermis; (c),(d) orientation distribution of collagen fibers $d'(\theta,\phi)$ (colored) and fitted von Mises distributions $\overline{\rho}(\theta,\phi)$ (wireframes) of samples HR-p2 and SR-p2.

Table 5.4: Microstructural parameters of the scarred skin samples and relative control samples of healthy skin. The last column indicates the goodness of fit (R^2).

Sample	Family 1						Family 2						R^2
	a_1 (-)	b_1 (-)	α_1 (°)	β_1 (°)	γ_1 (°)	ν_1 (-)	a_2 (-)	b_2 (-)	α_2 (°)	β_2 (°)	γ_2 (°)	ν_2 (-)	
SR-p2	4.1	18.7	−72.2	1.0	−7.1	0.77	15.4	38.2	−8.1	−3.0	−43.6	0.23	0.90
SL-p2	6.8	16.0	58.0	13.5	−16.4	0.74	5.0	12.9	−88.5	−1.3	−1.9	0.26	0.91
HR-p2	1.5	14.2	−83.9	0.2	−2.6	0.64	3.8	9.1	46.9	3.3	24.3	0.36	0.91
HL-p2	1.1	18.0	−76.7	−0.7	−2.5	0.57	3.7	8.5	46.4	−2.0	−0.1	0.43	0.94

Table 5.5: Estimated mechanical parameters and fitting residual wMAPE error of the scarred skin samples and the healthy control skin samples. The sample thickness is given in the first column.

Sample			GST model			DFD model		
	t (mm)	μ (kPa)	k_1 (kPa)	k_2 (-)	wMAPE (%)	c_1 (kPa)	c_2 (-)	wMAPE (%)
SR-p2	2.04	1.311	0.0106	28.9	68.5	0.0148	23.2	41.9
SL-p2	2.46	0.645	0.0079	37.4	37.3	0.1185	26.1	30.8
HR-p2	1.12	3.273	0.0197	129.3	33.4	3.8832	30.6	47.6
HL-p2	2.25	0.696	0.0930	22.8	20.1	0.7592	13.8	33.9

5.3 Discussion

In this chapter, 14 human skin samples from the lower abdominal region and 4 samples, 2 healthy and 2 scarred, from an older Cesarean section scar, were analyzed (Figure 5.1). The microstructural parameters describing the organization of collagen fibers were obtained from SHG tomographies taken at a square window of $465\,\mu\text{m} \times 465\,\mu\text{m}$. By clearing the tissue with SeeDBp protocol, we were able to scan skin collagen to an average depth of $311.8\,\mu\text{m}$, whereas under normal conditions only the first $100\,\mu\text{m}$ are visible [201, 216]. Despite the improvement, this only represented about 10% of the total skin thickness ($t = 2.92 \pm 0.71\,\text{mm}$). This technique has the advantage of preserving collagen morphology as well as the 2PEF signals using a simple protocol based on a non-toxic fructose solution. On the other hand, it seems to have little effect on dense collagen tissue. SeeDB (See Deep Brain), originally developed to clear the entire brain of the mouse [195], was successfully applied to diseased human mitral valve leaflets, allowing scanning up to $1400\,\mu\text{m}$ thickness [196], but achieved similar results when applied to tendons and cartilage ($\approx 300\,\mu\text{m}$ visible thickness) [221]. But to our knowledge, this was the first time SeeDBp protocol was applied to skin tissue [222]. Other techniques such as benzylalcohol/benzylbenzoate (BABB) solutions were found to be more effective in clearing human skin [223], but showed shrinkage effects that could potentially affect the distribution of collagen fibers [224].

Collagen tomographies were analyzed after a post-processing deconvolution step using the algorithm described in Chapter 4, which provided a complete description of the fiber orientation distribution $d'(\theta, \phi)$ over the unit hemisphere for each sample. The analysis revealed that collagen architecture in most samples is characterized by a mixture of two non-symmetrical fiber families with different volume fractions although only one family was observed in samples ABR2-p3 and ABL1-p2. As in other membrane tissues, e.g., in the aortic walls [103], collagen fibers displayed an almost planar dispersion, highly concentrated in the midplane of the membrane. From a mechanical perspective, this provides the skin with the necessary tensile strength to fulfill its membrane function. Considering the azimuthal orientation, the right and left samples showed symmetrical average orientations at $\theta_{\text{avg}} = -82.0 \pm 27.4^\circ$ and $\theta_{\text{avg}} = 82.0 \pm 32.2^\circ$, respectively, although the difference was not significant. This finding is consistent with the Langer's lines of the lower abdominal region, as shown in Figure 5.4.

Specific microstructural parameters for each family were quantified by fitting a combination $\overline{\rho}(\theta, \phi)$ of bivariate von Mises distributions to the measured distribution $d'(\theta, \phi)$. These parameters were used to fit the GST and the DFD con-

stitutive models. The shear modulus μ of the neo-Hookean ground matrix, which is the same for both models, was $\mu = 1.142 \pm 0.879$ kPa. The parameters of the GST model were $k_1 = 0.5914 \pm 1.3013$ kPa and $k_2 = 68.5 \pm 29.5$. These results are of the same order of magnitude as those reported by Tonge *et al.* [212] for human dorsal skin. The authors obtained $k_1 = 1.446 \pm 2.040$ kPa and $k_2 = 76.08 \pm 71.00$ from full-field bulge test assuming planar fiber dispersion. Analogous parameters were also obtained by Wei *et al.* [90] from *in vivo* indentation tests on facial skin, $k_1 = 2.402$ kPa and $k_2 = 15.88$. Interestingly, these parameters are obviously different from each other, but are all of comparable order of magnitude when considering the differences in location on the human body and the testing technique, as well as the variability between individuals. Regarding the DFD model, the fitted parameters were $c_1 = 1.9074 \pm 2.4427$ kPa and $c_2 = 43.6 \pm 15.3$. Overall, both models predicted the mechanical behavior of the skin well, although the GST model was found to be more accurate and had significantly lower residual error.

As mentioned in Section 5.1.5, the GST and DFD models differ substantially, although the two strain-energy definitions in Equations (3.92) and (3.96) have a similar form. Then the parameter sets cannot be interchanged between the models, except in the special case of perfectly aligned fiber families [79]. This difference was demonstrated by the significant differences between k_1-c_1 ($P = 5.45 \times 10^{-5}$) and k_2-c_2 ($P = 7.39 \times 10^{-4}$). Nevertheless, the significant correlations between k_1-c_1 ($r = 0.773$, $P = 0.0012$) and k_2-c_2 ($r = 0.627$, $P = 0.016$), reported in Figure 5.7(b) and (c), could be helpful in transferring the parameters from one model to the other. Further significant correlations emerged between μ and the parameters k_2 and c_2, which could suggest a mechanical connection between the ground matrix and the embedded collagen fibers.

It is important to mention that the mechanical tests were performed assuming that the reference configuration is the state pre-loaded with 0.01 N, i.e. the smallest measurable force of the load cell, both horizontally and vertically. Therefore, the obtained parameters must be related to the pre-loaded *in vitro* configuration. Recent studies on murine skin actually analyzed the influence of different reference configurations on the final mechanical parameters and showed a significant variation between the parameters associated with the *in vitro* pre-loaded and the *in vivo* unloaded configurations [106]. Since it was not possible to measure the residual strains during the physiological pre-loading of the skin in the living state, only the *in vitro* configuration was considered as a reference.

In this study, the skin was assumed to be incompressible. This approximation, first introduced by Lanir and Fung [60], is commonly used in mechanical modeling

of several soft tissues, including aortic walls [103], mitral valve leaflets [105] and brain tissue [225]. This makes the fitting process of the mechanical models easier by allowing the explicit expression of λ_3 from the planar and measurable stretch components λ_1 and λ_2, which otherwise would be difficult to measure. However, recent studies on skin under uniaxial deformation, measuring λ_3 from side view images of the sample, showed a significant volume loss of up to 30% at uniaxial stretches $\lambda = 1.2$, which is related to dehydration depending on the osmolarity of the environment [226, 227]. To better understand the effect of the incompressibility assumption in the current analysis, uniaxial tests were performed along the x and y directions. Consistent with the observation of Wahlsten *et al.* [227], the tests showed a strong transversal contraction with an average stretch of $\lambda \approx 0.85$ at an axial stretch of $\lambda = 1.3$ (see Figure 5.8(c),(d)). In response, the stretch λ_3, computed from the incompressibility constraint $J = \lambda_1\lambda_2\lambda_3 = 1$, transitioned from a contraction phase at low axial stretches to an expansion trend beyond the axial stretch $\lambda = 1.16 \div 1.23$. Notably, this was observed in both the x and y directions. Since this behavior is unlikely, this result suggests that the volumetric changes no longer become negligible at high deformation levels. It is important to mention that our uniaxial tests are performed using square specimens and not standardized shapes, like, e.g., T-bone or dog-bone specimens. However, in uniaxial tests, we found that the rotating bars on the biaxial machine arms (see Section 5.1.2) ensure an even distribution of the forces between the hooks, thus allowing a uniaxial distribution of stresses in the specimen within the fiducial markers. Subsequently, the displacements of the fiducial markers are measured using the DIC, which allowed us to compute the stretch component in the direction of the applied uniaxial load, even though shear deformation could occur due to the anisotropic behavior of the specimens.

Finally, two scarred and two healthy samples from an old Cesarean section from Patient 2 were analyzed. The measured fiber distributions $d'(\theta, \phi)$ revealed that the collagen fibers in the scar tissue become more concentrated and are mainly located transversely to the scar axis. This finding is consistent with other SHG analyses on pathological skin tissue [228, 229]. In addition, a strong loss of elastin fibers was observed in the 2PEF signal (Figure 5.9(a),(b)). Early studied on this fiber demonstrated that it plays a role at low strains and is responsible for the recoiling mechanism of the collagen fibers after deformation [137]. During the wound healing process the regeneration of elastin fibers follow those of collagen fibers. The compact organization of collagen prevents the complete formation of an elastic fiber network in the scar tissue, causing the overall elasticity to decrease [230]. In the present analysis this stiffness difference could not be

determined due to the limited number of scar samples tested. Nonetheless, considering the relevant implications of a reduced elastin fibers content on the overall mechanical behavior as reported by Zhou *et al.* [231], this points out the importance of including elastin in the mechanical modeling.

Chapter 6

Finite Element Modeling of Skin Surgeries

The Finite Element Method (FEM) is a powerful computational technique widely used to approximate solutions to mechanical problems stated as in Equation (3.58). Basically, it simplifies a large problem by discretizing its domain Ω in the reference configuration into small subdomains, the finite elements, whose mechanical response depends on the specific constitutive model and the displacement of few reference points within the element's subdomain, called nodes. Assembling the simple equations governing each element, the boundary conditions, and the forces acting on the body, the Finite Element Method solves the problem (3.58) linearized with Equation (3.59) using numerical techniques, such as the Newton-Raphson method [52]. The result is typically the displacement of each node, from which deformations and stresses can be derived from the constitutive equations throughout the whole model domain. The FEM is especially useful for dealing with non-linear problems that have complex shapes and boundary conditions, and its versatility makes it an ideal tool for analyzing skin surgical procedures.

Skin surgeries are simple operations generally performed following three main steps. First, full thickness incisions are performed following the lines prescribed by the specific technique adopted. Then, skin is undermined from the subcutaneous tissue in a circular neighborhood of the operation, thereby releasing the skin flaps, which are finally transposed into the designated configuration and sutured in place.

In contrast to the ease of execution in the real world, these surgeries encompass several modeling challenges in FEM simulations. Due to the geometrical singularity, the regions close to the cut tips must be discretized with a finer element

mesh to capture the extreme stress gradients. Moreover, unlike common mechanical problems, the forces acting on the wound required for the suturing are unknown. Therefore, the closure must be enforced using implicit kinematic constraints on paired nodes on the two sides of the wound. These two requirements together make the generation of FE models geometries for surgical operations highly complex. Indeed, the distribution of the nodes on the wound boundary must be compliant with both the element refinement close to the geometrical singularities, and the nodal pairing required for the suture constraint. Given also the geometrical complexity of the surgical techniques illustrated in Section 2.5, the generation of these FE models with traditional user-guided tools becomes overwhelming.

To address this issue, an algorithm for skin surgeries FE models generation has been developed and implemented in a custom MATLAB code (v. R2023a; The MathWorks Inc., Natick, MA, USA), and it is linked with the open source automeshing code DistMesh developed by Persson and Strang [232]. The algorithm is capable of automatically generating FE models of surgical techniques from few geometrical input parameters like, for instance, the cuts length, the angles between cuts and the maximum and minimum elements sizes, thus requiring minimal user interaction during the process [233].

6.1 Internal Boundaries with Prescribed Dislocations

The boundary conditions applied to achieve the closure of the wound can be framed in the theory of **dislocations**. These are essentially relative displacements imposed between points on different boundaries of a discontinuity. In the specific case of skin surgeries, this involves considering cuts, with or without subtraction of material, within the membrane, and prescribing relative displacements that effectively bring the edges of these cuts and holes together. This action of joining the boundaries results in a self-balanced stress state.

Let Ω be the region occupied by the body in the reference configuration at time t_0 delimited externally by the boundary $\partial\Omega_{\mathrm{E}}$ and internally by the boundary $\partial\Omega_{\mathrm{I}}$ enclosing a simply connected space outside of Ω (Figure 6.1(a)). To account for general applications of the joining dislocation, the internal boundary is partitioned in pairs of subsets $\partial\Omega^{+}_{\mathrm{I},i}$ and $\partial\Omega^{-}_{\mathrm{I},i}$, $i = 1\ldots,N$, which are to be joined in the final configuration ω at time t_f. Therefore, if $\mathbf{X}^{+}_{i} \in \partial\Omega^{+}_{\mathrm{I},i}$ and $\mathbf{X}^{-}_{i} \in \partial\Omega^{-}_{\mathrm{I},i}$ are two paired points in the reference configuration at time t_0, their position $\mathbf{x}^{+}_{i}(t) = \mathbf{X}^{+}_{i} + \mathbf{U}(\mathbf{X}^{+}_{i}, t)$ and $\mathbf{x}^{-}_{i}(t) = \mathbf{X}^{-}_{i} + \mathbf{U}(\mathbf{X}^{-}_{i}, t)$ at time t is governed by the kinematic

constraint vector function

$$\Phi(t) = \left[\mathbf{U}\left(\mathbf{X}_i^+, t\right) - \mathbf{U}\left(\mathbf{X}_i^-, t\right)\right] - \frac{t - t_0}{t_f - t_0}\left[\mathbf{X}_i^- - \mathbf{X}_i^+\right] = \mathbf{0}\,, \quad \forall t \in [t_0, t_f]\,, \tag{6.1}$$

which states that the reciprocal displacement $\mathbf{U}\left(\mathbf{X}_i^+, t\right) - \mathbf{U}\left(\mathbf{X}_i^-, t\right)$ between the points at time t is a fraction of the initial distance $\mathbf{X}_i^- - \mathbf{X}_i^+$, increasing linearly with time, such that in the final configuration at time t_f we have

$$\Phi(t_f) = \mathbf{X}_i^+ + \mathbf{U}\left(\mathbf{X}_i^+, t_f\right) - \mathbf{X}_i^- - \mathbf{U}\left(\mathbf{X}_i^-, t_f\right) = \mathbf{x}_i^+(t_f) - \mathbf{x}_i^-(t_f) = \mathbf{0}\,, \tag{6.2}$$

which implies the joining of the points, $\mathbf{x}_i^+(t_f) = \mathbf{x}_i^-(t_f)$ (Figure 6.1(b)). The function (6.1) must be satisfied for all the points $\mathbf{X}_i^+$ and $\mathbf{X}_i^-$, which are related by a biunivocal mapping function $\Gamma : \partial\Omega_{\mathrm{I},i}^+ \rightarrow \partial\Omega_{\mathrm{I},i}^-$, with the property

$$\left|\frac{\mathrm{d}\Gamma\left(\mathbf{X}_i^+\right)}{\mathrm{d}\mathbf{X}_i^+}\right| = \text{const.}\,, \tag{6.3}$$

such that paired subdomains of different length are uniformly stretched in the final configuration. Except for trivial cases, such as the stitching of two already overlapping edges, this kind of function always generates a self-balanced stress state along the joined boundaries $\partial\omega_{\mathrm{I},i}^-(t_f) = \partial\omega_{\mathrm{I},i}^+(t_f)$, which depends on their shape in the reference configuration.

It is important to emphasize that both the partitioning of $\partial\Omega_{\mathrm{I}}$ and the particular choice for the pairing of the subsets $\partial\Omega_{\mathrm{I},i}^+$ and $\partial\Omega_{\mathrm{I},i}^-$ are arbitrary, provided that they are topologically consistent, i.e. the internal boundary in its final configuration $\partial\omega_{\mathrm{I}}(t_f)$ does not self-intersect.

The kinematic constrain function in Equation (6.1) has been implemented in the commercial FE software ABAQUS through the user-defined subroutine MPC for multi-point constraints.

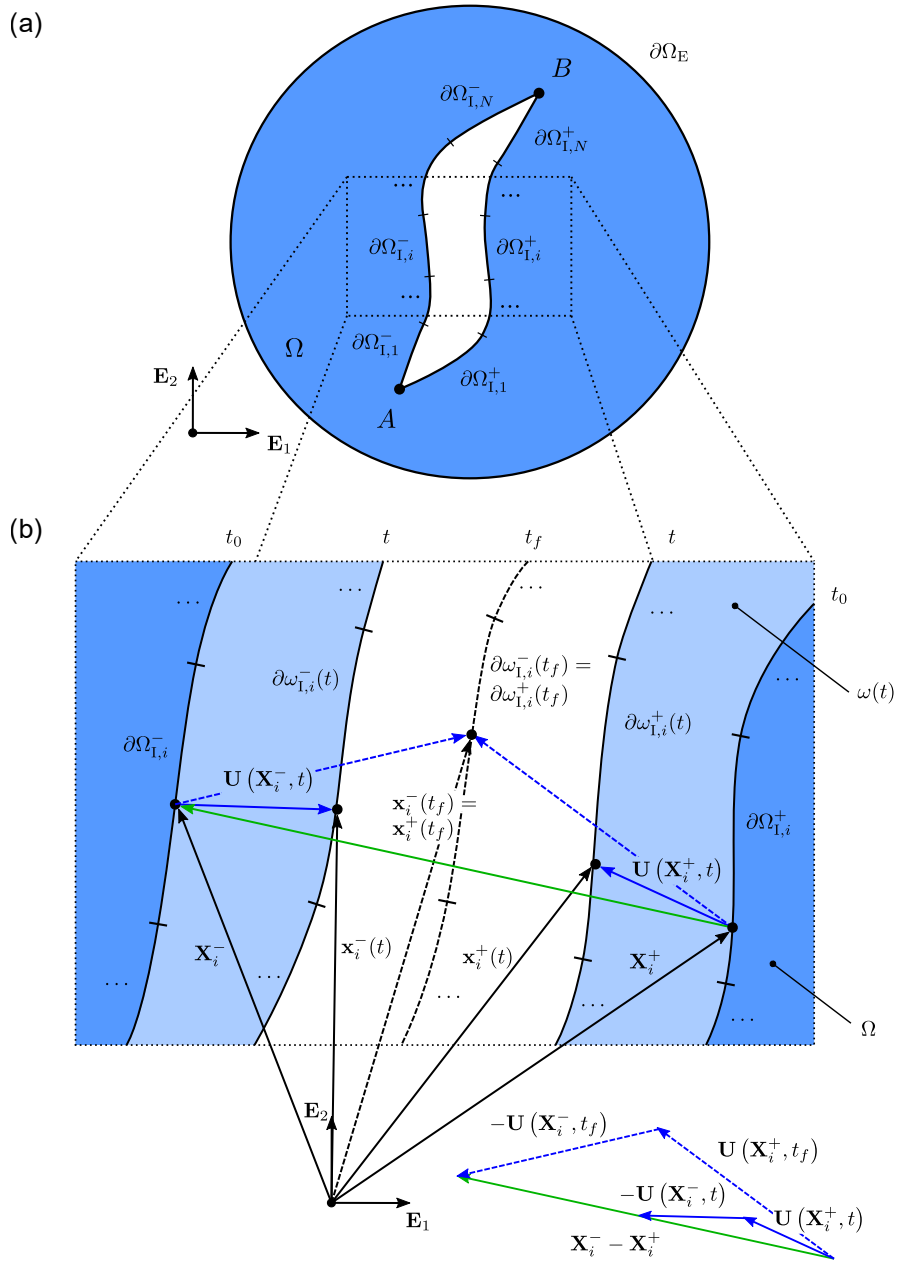

(Caption on next page)

Figure 6.1: Schematics of joining dislocations kinematic constraint applied to paired subsets $\partial\Omega^{+}_{\mathrm{I},i}$ and $\partial\Omega^{-}_{\mathrm{I},i}$ of the internal boundary $\partial\Omega_{\mathrm{I}}$: (a) domain Ω in the reference configuration at time t_0 delimited by the external boundary $\partial\Omega_{\mathrm{E}}$ and the internal boundary $\partial\Omega_{\mathrm{I}}$ partitioned in paired subsections $\partial\Omega^{-}_{\mathrm{I},i}$ and $\partial\Omega^{+}_{\mathrm{I},i}$; (b) schematics of the joining dislocation kinematic constraint applied to the paired points $\mathbf{X}^{+}_{i} \in \partial\Omega^{+}_{\mathrm{I},i}$ and $\mathbf{X}^{-}_{i} \in \partial\Omega^{-}_{\mathrm{I},i}$. Dashed vectors are referred to the final unknown configuration $\omega(t_f)$. The magnified domain shown in (b) is referred to the dotted region in (a). The graphical vector summation of initial positions and displacements referred to Equation (6.1) is reported in the bottom-right corner.

6.2 FE Model Geometry of Skin Surgeries

In this section the theory behind the algorithm developed for automatic generation of bidimensional FE models geometry of skin surgeries is addressed. The algorithm incorporates the automeshing tool DistMesh [232], which is capable to discretize topologically complex domains offering simple tools for managing the element refinement close to arbitrary points within the domain Ω. This feature is pivotal for automating the generation process of the FE model geometry, as it allows us to fully control the discretization using few geometrical parameters, regardless the complexity of the surgery.

The first step of the algorithm consists in defining the internal and external boundary through a counterclockwise sequence of points, denoted $\mathcal{V}_{\mathrm{I}}$, representing the vertices of the internal polygonal boundary $\partial\Omega_{\mathrm{I}}$ of the specific surgical technique. Likewise, it is defined the sequence of points $\mathcal{V}_{\mathrm{E}}$ relative to the external boundary. Then, the set of paired nodes on $\partial\Omega_{\mathrm{I}}$, denoted $\mathcal{N}_{\mathrm{I}}$, is generated according to the prescribed element size function and the mapping function Γ between paired internal boundary subsets. This step is essential to correctly apply the kinematic constraint function (6.1) in the FE analysis. Finally, the domain Ω is automatically discretized with DistMesh.

6.2.1 Boundaries Topology

For fairly general applications, the shape of the external boundary can be assumed circular and approximated by a regular M polygon, whose sequence of evenly spaced vertices $\mathbf{V}_{\mathrm{E},j} \in \partial\Omega_{\mathrm{E}}$, $j = 1,\dots,M$ are collected in the set $\mathcal{V}_{\mathrm{E}}$. Accordingly, each segment $\partial\Omega_{\mathrm{E},j}$ is expressed by the linear Bézier curve

$$\mathbf{X}_j(\xi) = (1-\xi)\mathbf{V}_{\mathrm{E},j} + \xi\mathbf{V}_{\mathrm{E},j+1}\,, \tag{6.4}$$

with $\xi \in [0,1]$, and $\mathbf{V}_{\mathrm{E},M+1} = \mathbf{V}_{\mathrm{E},1}$.

Concerning the internal boundary $\partial\Omega_{\mathrm{I}}$, its subsets are approximated as linear segments whose vertices $\mathbf{V}_{\mathrm{I},k} \in \partial\Omega_{\mathrm{I}}$, $k = 1,\dots,2N$ are collected in the set $\mathcal{V}_{\mathrm{I}}$. Therefore, each segment $\partial\Omega_{\mathrm{I},k}$ is parametrically expressed by the Bézier curve as in Equation (6.4), i.e.

$$\mathbf{X}_k(\xi) = (1-\xi)\mathbf{V}_{\mathrm{I},k} + \xi\mathbf{V}_{\mathrm{I},k+1}\,, \tag{6.5}$$

with $\xi \in [0,1]$. Note that $\partial\Omega_{\mathrm{I},k}$ represents a generic subset $\partial\Omega^{+}_{\mathrm{I},i}$ or $\partial\Omega^{-}_{\mathrm{I},i}$. Accordingly, since all the subsets are assumed to be paired (Figure 6.1(a)), the set $\mathcal{V}_{\mathrm{I}}$ contains $2N$ vertices.

In case $\partial\Omega_{\mathrm{I}}$ represents a cut in the membrane, the various subsets coincide and are positioned along the interface of the cut. While this alignment does not pose a challenge from a geometric standpoint, it can lead to complications during the automatic mesh generation process, as elements might end up being created across the cut. To address this issue, the original boundary $\partial\Omega_{\mathrm{I}}$ is modified by shifting it outwards by a small distance of $s/2$. This adjustment ensures that the two opposing subsets on either side of the cut are separated by a gap of s. We refer to this adjusted boundary as $\partial\overline{\Omega}_{\mathrm{I}}$. The magnitude of this gap is determined based on the average size of the elements in the mesh. Hence, the new set $\overline{\mathcal{V}}_{\mathrm{I}}$ includes the offset vertices $\overline{\mathbf{V}}_{\mathrm{I},k} \in \partial\overline{\Omega}_{\mathrm{I}}$, as shown in Figure 6.2(a), given by

$$\overline{\mathbf{V}}_{\mathrm{I},k} = \mathbf{V}_{\mathrm{I},k} + \mathbf{s}^{-}_{k} + \mathbf{s}^{+}_{k}\,, \tag{6.6}$$

where

$$\mathbf{s}^{-}_{k} = \bar{s}\frac{\mathbf{V}_{\mathrm{I},k} - \mathbf{V}_{\mathrm{I},k-1}}{\left|\mathbf{V}_{\mathrm{I},k} - \mathbf{V}_{\mathrm{I},k-1}\right|} \times \mathbf{E}_3 \quad , \quad \mathbf{s}^{+}_{k} = \bar{s}\frac{\mathbf{V}_{\mathrm{I},k+1} - \mathbf{V}_{\mathrm{I},k}}{\left|\mathbf{V}_{\mathrm{I},k+1} - \mathbf{V}_{\mathrm{I},k}\right|} \times \mathbf{E}_3\,, \tag{6.7}$$

and

$$\bar{s} = \frac{s}{2(1+\cos\Delta\vartheta)}\,, \tag{6.8}$$

where $\Delta\vartheta$ is the angle between the segments converging in $\mathbf{V}_{\mathrm{I},k}$ as shown in Figure 6.2(a). Segments between two offset vertices are still defined by the linear curve in Equation (6.5), using $\overline{\mathbf{V}}_{\mathrm{I},k}$ in place of $\mathbf{V}_{\mathrm{I},k}$.

When $\mathbf{V}_{\mathrm{I},k}$ represents a cut tip, the segments before and after it are parallel, marked by an angle change $\Delta\vartheta = \pi$. This scenario, according to Equation (6.8), would position $\overline{\mathbf{V}}_{\mathrm{I},k}$ infinitely far away, as $\bar{s}$ becomes infinite when $\Delta\vartheta$ approaches π. To maintain the position of the tip while still enabling the offsetting of the internal boundary, the segments preceding and following the tip must be altered from straight lines to curved ones. These curves should run parallel at a distance from the tip but converge at $\overline{\mathbf{V}}_{\mathrm{I},k} = \mathbf{V}_{\mathrm{I},k}$ near the tip. To achieve this, the segments

can be represented parametrically using quadratic Bézier curves, as illustrated in Figure 6.2(b). These curves are used for the subsets immediately before and after the tip $\bar{\mathbf{V}}_{\mathrm{I},k}$, and are defined as

$$\begin{aligned} \bar{\mathbf{X}}_{k-1}(\xi) &= (1-\xi)^2\bar{\mathbf{V}}_{\mathrm{I},k-1} + 2(1-\xi)\xi\bar{\mathbf{V}}^{-}_{\mathrm{I},k} + \xi^2\bar{\mathbf{V}}_{\mathrm{I},k}\,, \\ \bar{\mathbf{X}}_{k}(\xi) &= (1-\xi)^2\bar{\mathbf{V}}_{\mathrm{I},k} + 2(1-\xi)\xi\bar{\mathbf{V}}^{+}_{\mathrm{I},k} + \xi^2\bar{\mathbf{V}}_{\mathrm{I},k+1}\,, \end{aligned} \tag{6.9}$$

with $\bar{\mathbf{X}}_{k-1} \in \partial\bar{\Omega}_{\mathrm{I},k-1}$ and $\bar{\mathbf{X}}_{k} \in \partial\bar{\Omega}_{\mathrm{I},k}$. The two auxiliary vertices $\bar{\mathbf{V}}^{-}_{\mathrm{I},k}$ and $\bar{\mathbf{V}}^{+}_{\mathrm{I},k}$ are computed as

$$\begin{cases} \bar{\mathbf{V}}^{-}_{\mathrm{I},k} = \mathbf{V}_{\mathrm{I},k} + \mathbf{s}'_k + \mathbf{s}^{-}_k\,, \\ \bar{\mathbf{V}}^{+}_{\mathrm{I},k} = \mathbf{V}_{\mathrm{I},k} + \mathbf{s}'_k + \mathbf{s}^{+}_k\,, \end{cases} \tag{6.10}$$

where

$$\mathbf{s}'_k = \frac{3s}{2}\frac{(\mathbf{V}_{\mathrm{I},k+1} - \mathbf{V}_{\mathrm{I},k})}{\left|\mathbf{V}_{\mathrm{I},k+1} - \mathbf{V}_{\mathrm{I},k}\right|}\,, \tag{6.11}$$

and $\mathbf{s}^{-}_j$, $\mathbf{s}^{+}_j$ are calculated by means of Equation (6.7), with $s/2$ in place of $\bar{s}$.

For the properties of the Bézier curves, the boundaries $\partial\bar{\Omega}_{\mathrm{I},k-1}$ and $\partial\bar{\Omega}_{\mathrm{I},k}$ described by Equation (6.9) are tangent to the polygons with vertices $\{\bar{\mathbf{V}}_{\mathrm{I},k-1}, \bar{\mathbf{V}}^{-}_{\mathrm{I},k}, \bar{\mathbf{V}}_{\mathrm{I},k}\}$, and $\{\bar{\mathbf{V}}_{\mathrm{I},k}, \bar{\mathbf{V}}^{+}_{\mathrm{I},k}, \bar{\mathbf{V}}_{\mathrm{I},k+1}\}$, as depicted in Figure 6.2(b). Accordingly the auxiliary vertices do not belong to the internal boundary $\partial\Omega_{\mathrm{I}}$, but are still included in the set $\bar{\mathcal{V}}_{\mathrm{I}}$, since they are required for the description of the boundary offset. This design ensures that the opening angle at the tip matches the angle created by the polygon of vertices $\{\bar{\mathbf{V}}^{-}_{\mathrm{I},k}, \bar{\mathbf{V}}_{\mathrm{I},k}, \bar{\mathbf{V}}^{+}_{\mathrm{I},k}\}$. As a result, the placement of the auxiliary vertices can be modified to create a specific opening angle at the tip. To control this opening angle, the magnitude of $\mathbf{s}'_k$ is set to be $3s/2$, which is selected to form an acute angle $\sim 36°$ at the tip.

6.2.2 Meshing

The size of elements throughout the domain is determined by a function $h(\mathbf{X})$, which specifies the average element size at each point $\mathbf{X}$ within the domain Ω. Points of geometrical discontinuity require finer meshing for accuracy. In our case, these discontinuities are represented by the vertices of the internal boundary $\partial\bar{\Omega}_{\mathrm{I}}$, i.e. the elements contained in the set $\bar{\mathcal{V}}_{\mathrm{I}}$. Accordingly, the overall mesh refinement function $h(\mathbf{X})$ is defined as

$$h(\mathbf{X}) = \arg\min_k \left[h_k(\mathbf{X}, \bar{\mathbf{V}}_{\mathrm{I},k})\right]\,, \tag{6.12}$$

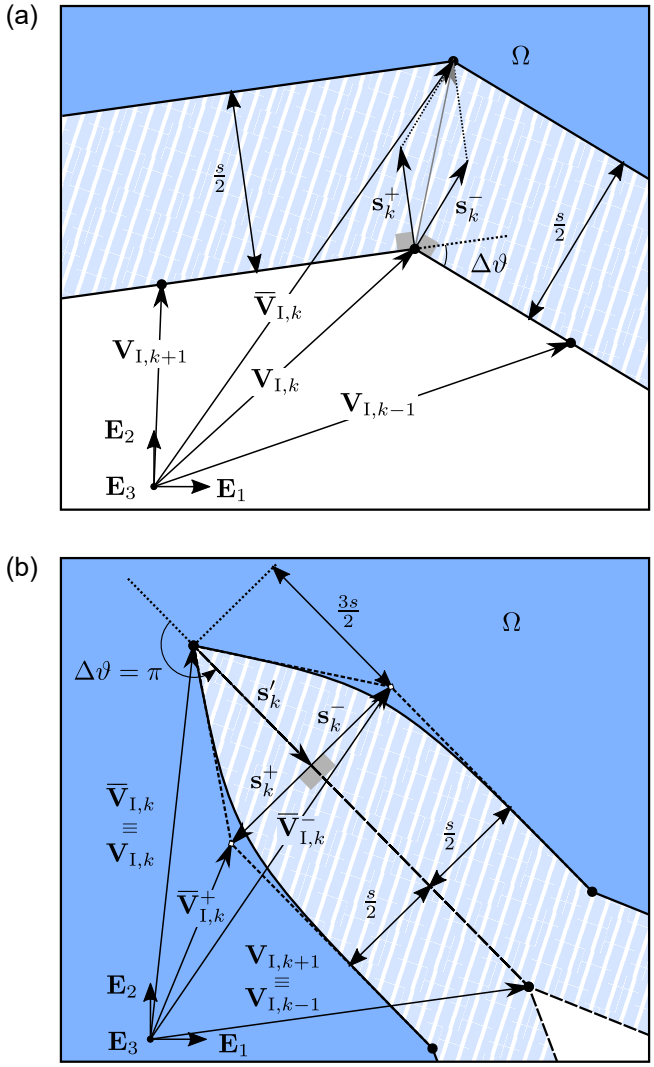

Figure 6.2: Offset scheme of the internal boundary vertices $\mathbf{V}_{\mathrm{I},k}$. (a) Offset for a standard vertex $\mathbf{V}_{\mathrm{I},k}$, (b) offset for vertex $\mathbf{V}_{\mathrm{I},k}$ corresponding to a cut tip.

with h_k being defined as

$$h_k(\mathbf{X}, \bar{\mathbf{V}}_{\mathrm{I},k}) = h_{\max} - \frac{h_{\max} - h_{\min}}{\left(c^{-2}\left|\mathbf{X} - \bar{\mathbf{V}}_{\mathrm{I},k}\right|^2 + 1\right)^a}\,. \tag{6.13}$$

In this equation, a is an exponent that controls the grading of the mesh, and c is a parameter that determines the extent of mesh refinement. The function $h_k(\mathbf{X}, \bar{\mathbf{V}}_{\mathrm{I},k})$ is conceived such that it equals $h_{\min}$ when $\left|\mathbf{X} - \bar{\mathbf{V}}_{\mathrm{I},k}\right| = 0$, and equals $h_{\max}$ as $\left|\mathbf{X} - \bar{\mathbf{V}}_{\mathrm{I},k}\right|$ approaches infinity. Here, $h_{\min}$ and $h_{\max}$ represent the minimum and maximum element sizes, respectively.

6.2.3 Disposition of Internal Boundary Nodes

The arrangement of element nodes along the internal offset boundary $\partial\bar{\Omega}_{\mathrm{I}}$ needs to comply with both the refinement function $h(\mathbf{X})$ and the linear mapping function $\Gamma : \partial\bar{\Omega}^{+}_{\mathrm{I},i} \to \partial\bar{\Omega}^{-}_{\mathrm{I},i}$. To fulfill these requirements simultaneously, nodes are first generated on the boundary segment that demands the larger number of nodes. These nodes are then mirrored onto the opposing segment using the mapping function Γ.

To calculate the average element size along a particular boundary segment $\partial\bar{\Omega}_{\mathrm{I},k}$, the mean value theorem is employed

$$h_{m,k} = \int_0^1 h(\bar{\mathbf{X}}_{\mathrm{I},k}(\xi)) \left|\frac{\partial \bar{\mathbf{X}}_{\mathrm{I},k}}{\partial \xi}\right| \mathrm{d}\xi\,, \tag{6.14}$$

The estimated number of elements along the boundary is then determined by dividing the length of the boundary segment $\partial\bar{\Omega}_{\mathrm{I},k}$ by this average element size $h_{m,k}$:

$$N_k = \frac{1}{h_{m,k}} \int_0^1 \left|\frac{\partial \bar{\mathbf{X}}_{\mathrm{I},k}}{\partial \xi}\right| d\xi\,. \tag{6.15}$$

For instance we assume $\partial\bar{\Omega}^{+}_{\mathrm{I},i}$ as the dominant subset. Starting from $\xi = 0$, each node $\mathbf{N}^{+}_{i,n} = \bar{\mathbf{X}}^{+}_{i}(\xi_n) \in \partial\bar{\Omega}^{+}_{\mathrm{I},i}$ is placed along the subset using Equations (6.5) and (6.9) increasing progressively ξ_n by an arbitrary increment $\Delta\xi$, until the length $|\mathbf{N}^{+}_{i,n} - \mathbf{N}^{+}_{i,n-1}|$ attains the prescribed size computed at the centroid of the element, which is approximately $h(\bar{\mathbf{X}}^{+}_{i}(\frac{\xi_n + \xi_{n-1}}{2}))$, so that each element size perfectly matches the dimension defined by the function $h(\mathbf{X})$. After this procedure, the nodes $\mathbf{N}^{+}_{i,n}$, $n = 1, \ldots, N_i$ are duplicated on the paired subset $\partial\bar{\Omega}^{-}_{\mathrm{I},i}$ with the

mapping function, $\mathbf{N}^-_{i,n} = \Gamma(\mathbf{N}^+_{i,n})$. On the other hand, if $\partial\overline{\Omega}^-_{\mathrm{I},i}$ is the dominant subset, the procedure is analogous and crated nodes $\mathbf{N}^-_{i,n}$ are finally duplicated with the inverse mapping function, $\mathbf{N}^+_{i,n} = \Gamma^{-1}(\mathbf{N}^-_{i,n})$. The nodal distribution such created is suitable for applying the dislocation constraint, Equation (6.1), in a discretized way to each couple of nodes $(\mathbf{N}^-_{i,n}, \mathbf{N}^+_{i,n})$, $n = 1, \ldots, N_i$, for each pair of subsets $(\partial\overline{\Omega}^-_{\mathrm{I},i}, \partial\overline{\Omega}^+_{\mathrm{I},i})$, $i = 1, ..., N$.

An example of nodes disposition on the internal boundary $\partial\overline{\Omega}_{\mathrm{I}}$ is illustrated in Figure 6.3 for the Z-plasty. The external boundary $\partial\overline{\Omega}_{\mathrm{E}}$ has a radius of $R = 100$ mm, and the cuts defining the internal boundary have a length of $l = 50$ mm. The domain is discretized using triangular elements, with size ranging between $h_{\max} = l/5$, $h_{\min} = l/150$ and refinement parameters $a = 8$, $c = l$. The cut offset is assumed to be equal to $s = h_{max}/20$.

6.3 Representative Examples

To test the capabilities of the algorithm, representative FE model geometries are generated for some of the skin surgical techniques presented in Section 2.5. Then, the generated models are simulated in the FE software ABAQUS to verify the kinematic constraint for joining dislocations on the internal boundary $\partial\overline{\Omega}_{\mathrm{I}}$ were correctly applied. Techniques considered are the single Z-plasty, the triple Z-plasty, the four-flaps plasty, the square flap method, and the W-V plasty. All the models are generated with a circular external boundary with radius $R = 200$ mm and a spacing between facing edges of $s = l/20$, where l is the length of the cuts equal to $l = 50$ mm, except for the square flap method which is $l = 30$ mm. Mesh refinement parameters are $a = 8$, $h_{\min} = l/150$, $h_{\max} = l/5$. The simulations are performed using fixed constraints on the external boundary $\partial\overline{\Omega}_{\mathrm{E}}$. For the sake of simplicity the Ogden wrinkling constitutive model in Equation (3.77) is employed, using the mechanical parameters $\mu_1 = 110$ Pa from ref. [72], derived from an *in vivo* test on human skin. As reported in Figure 6.4, the algorithm generated FE models with an element mesh properly refined in all the vertices $\overline{\mathbf{V}}_{\mathrm{I},k}$ of the internal boundary $\partial\overline{\Omega}_{\mathrm{I}}$, and correctly distributed the nodes $\mathbf{N}^-_{i,n}$ and $\mathbf{N}^+_{i,n}$, allowing to achieve a perfect closure in the final configuration $\omega(t_f)$.

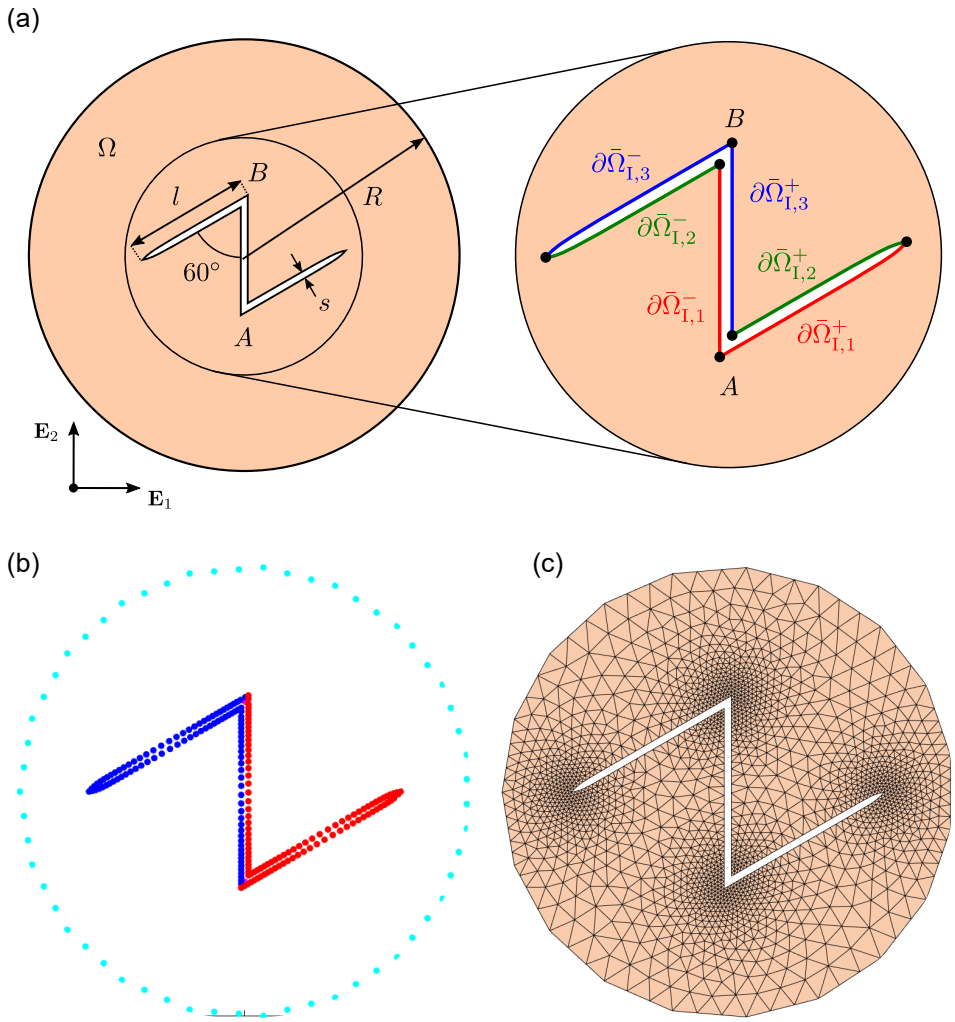

Figure 6.3: Application of the algorithm to a Z-plasty model. (a) Geometrical description of the problem, with the offset on the cut already applied. Paired subsets have been highlighted with same colors. (b) Disposition of the nodes on the two sides of the cut are highlighted in red for the subsets $\partial\bar{\Omega}^{+}_{\mathrm{I},i}$, and in blue for the subsets $\partial\bar{\Omega}^{-}_{\mathrm{I},i}$. Nodes on the external boundary are highlighted in cyan. (c) Discretized FE model in the reference configuration.

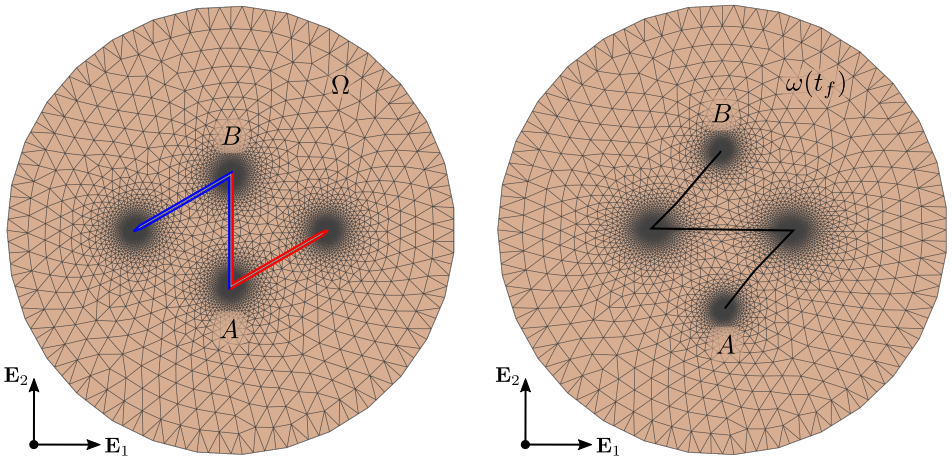

(a) Single Z-plasty

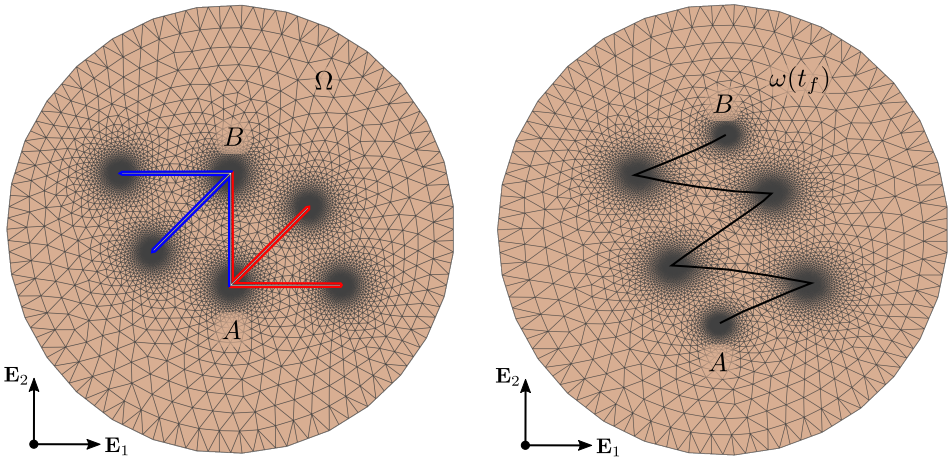

(b) Four-flaps plasty

Figure 6.4: Representative FE model geometries generated with the developed algorithm in the reference configuration Ω (left figures) and in the final configuration $\omega(t_f)$. Paired internal boundaries $\partial\overline{\Omega}^{-}_{\mathrm{I},i}$, and $\partial\overline{\Omega}^{+}_{\mathrm{I},i}$ are highlighted in blue and red, respectively.

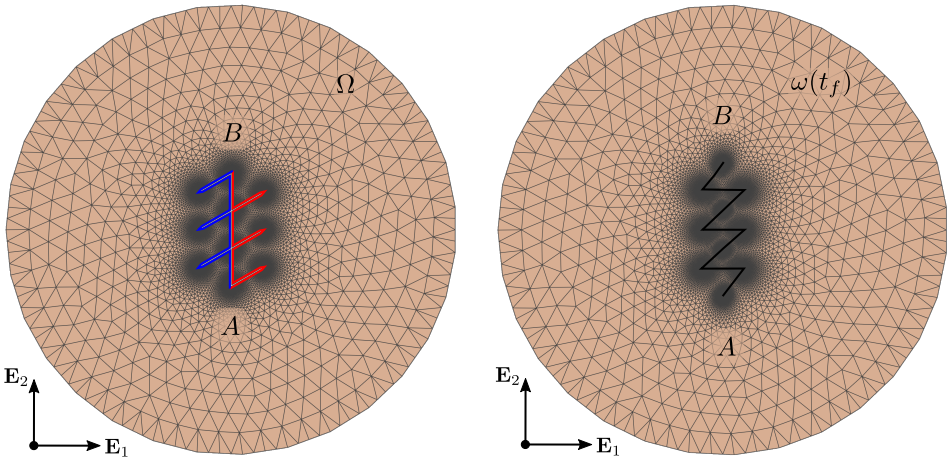

(c) Triple Z-plasty

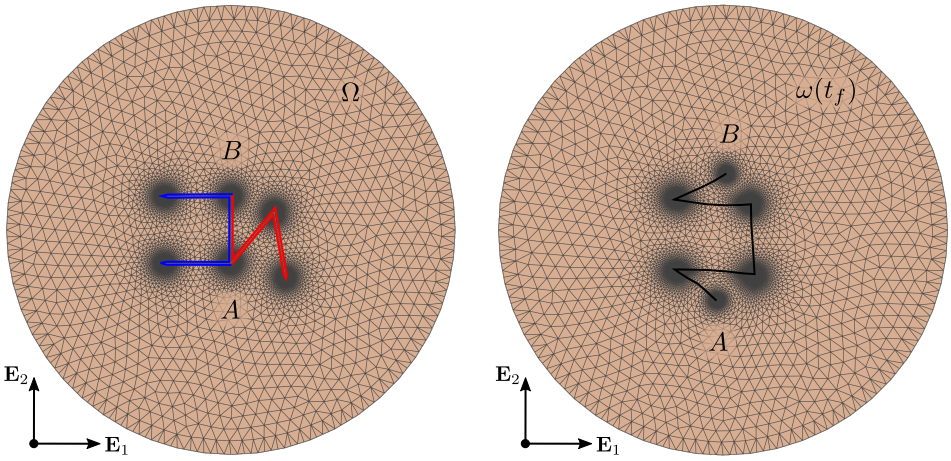

(d) Square flap method

Figure 6.4: Representative FE model geometries generated with the developed algorithm in the reference configuration Ω (left figures) and in the final configuration $\omega(t_f)$. Paired internal boundaries $\partial\overline{\Omega}^{-}_{\mathrm{I},i}$, and $\partial\overline{\Omega}^{+}_{\mathrm{I},i}$ are highlighted in blue and red, respectively. Continued.

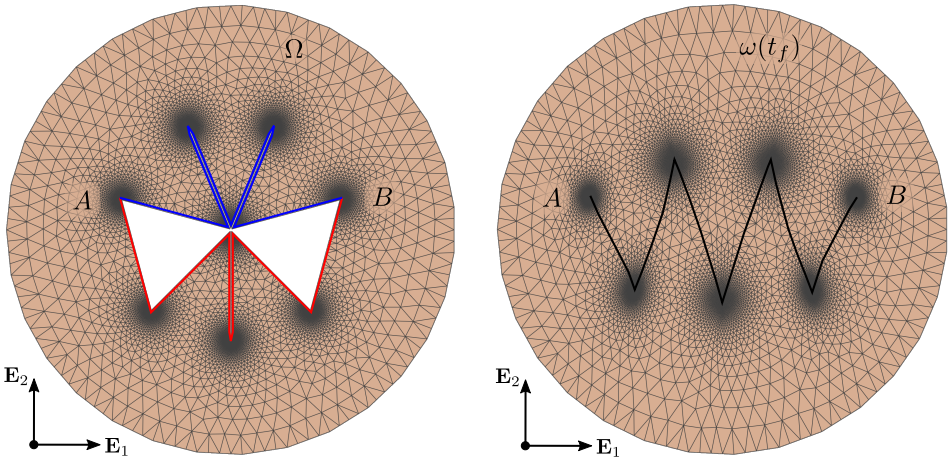

(e) W-V plasty

Figure 6.4: Representative FE model geometries generated with the developed algorithm in the reference configuration Ω (left figures) and in the final configuration $\omega(t_f)$. Paired internal boundaries $\partial\overline{\Omega}^{-}_{\mathrm{I},i}$, and $\partial\overline{\Omega}^{+}_{\mathrm{I},i}$ are highlighted in blue and red, respectively. Continued.

Chapter 7

Numerical Simulations of Skin Corrective Surgeries

Skin surgeries typically employ basic geometric configurations that are adaptable to the local topology of the body and the size of the defect being treated. These surgeries usually involve cuts of equal length, which aids in aligning and suturing distant edges. The length of these cuts is generally determined by the size of the defect to treat and it has minimal scope for adaptation. For scar relaxation surgeries this length is related to the length of the contracted scar, while for defect closure surgeries it depends on the size of the defect. The angles between these incisions, instead, can be adjusted based on specific requirements. In Z-plasty, for instance, larger angles tend to provide greater relief to the scar [2, 36], while in rhombic flap transposition, modifying angles allows the design of flaps that reduce the tension across the final wound. Therefore, these angles can be modified to achieve a specific outcomes while also aiming to minimize negative effects like excessive stress or the formation of dog-ears.

To provide quantitative mechanical insights and evaluate the performances of these surgeries, possibly identifying optimal configurations, a series of FEM simulations have been conducted. Surgeries herein analyzed are the single and triple Z-plasty with constant scar length and varying lateral limbs angle ϑ (see Figures 7.1 and 7.2), and the rhombic flap transposition with consistent rhombic excisions and different combinations of flap angles ϑ_1, ϑ_2 (see Figure 7.16).

The selected mechanical metrics used to assess the performances of the surgeries are the average peak stress σ_{p} across the sutured wound, directly related to hypertrophic scar formation [19, 20, 129], the total strain energy W_{tot}, used to quantify the overall state of deformation, and the total slack area A_{s} of the

biaxially compressed regions, used to evaluate the extension of the dog-ear formations [43, 45, 151]. The average peak stress σ_{p} is herein computed averaging the stresses normal to the suture within a 7 mm interval around the point of maximum stress. This interval represents the average space between stitches [234, 235]. Thus, σ_{p} reflects the average tension exerted by the most stressed stitch. These metrics collectively provide a comprehensive assessment of the mechanical effects resulting from the surgical procedures. In addition, the performances of scar relaxation surgeries are assessed by means of the vertical elongation strain ε_{v} parallel to the $\mathbf{E}_2$ direction, defined as

$$\varepsilon_{\mathrm{v}} = \frac{(\Delta\mathbf{x}_{\mathrm{v}} - \Delta\mathbf{X}_{\mathrm{v}}) \cdot \mathbf{E}_2}{|\Delta\mathbf{X}_{\mathrm{v}}|}\,, \tag{7.1}$$

with $\Delta\mathbf{X}_{\mathrm{v}} = \mathbf{X}_B - \mathbf{X}_A$ and $\Delta\mathbf{x}_{\mathrm{v}} = \mathbf{x}_B - \mathbf{x}_A$ the distance vectors between the two ends points A and B of the scar in the reference and current configurations (see e.g. Figure 7.1 where points A and B are shown). The horizontal shortening strain ε_{h} is also considered, defined as

$$\varepsilon_{\mathrm{h}} = \frac{(\Delta\mathbf{X}_{\mathrm{h}} - \Delta\mathbf{x}_{\mathrm{h}}) \cdot \mathbf{E}_1}{|\Delta\mathbf{X}_{\mathrm{v}}|}\,, \tag{7.2}$$

where $\Delta\mathbf{X}_{\mathrm{h}} = \mathbf{X}_D - \mathbf{X}_C$ and $\Delta\mathbf{x}_{\mathrm{h}} = \mathbf{x}_D - \mathbf{x}_C$ are the distance vectors between the two side points C and D of the surgery in the reference and current configurations (see e.g. Figure 7.1 where points C and D are shown). Note that ε_{h} is normalized with respect to $|\Delta\mathbf{X}_{\mathrm{v}}|$, and not $|\Delta\mathbf{X}_{\mathrm{h}}|$ as one would assume intuitively. The motivation behind this choice is that the initial positions $\mathbf{X}_C$ and $\mathbf{X}_D$ can vary significantly between different surgeries, and normalizing with respect to $|\Delta\mathbf{X}_{\mathrm{h}}| = |\mathbf{X}_D - \mathbf{X}_C|$ would reduce the objectivity of ε_{h}. Instead, $|\Delta\mathbf{X}_{\mathrm{v}}|$ represents the initial scar length, which is assumed to be constant for all the surgeries analyzed, hence enabling a fair comparison between different types of surgeries.

The FE modes have been generated using the algorithm described in Chapter 6 [233], and the analyses have been performed using the commercial FEM software ABAQUS, employing the constitutive models introduced in Chapter 3. The isotropic Ogden wrinkling model has been used as a pragmatic approximation of the nonlinear mechanical behavior of the skin to obtain the plausible insights about the scar relaxation performances [236]. The DFD model, instead, is used as a more precise tool to determine the influence of the fiber orientation.

7.1 Isotropic Analysis of the Z-plasty and the Triple Z-plasty

For the single and triple Z-plasty simulations, a round domain of $R = 100$ mm is considered, with a central vertical cut of $l = 50$ mm coinciding with the scar to be lengthened. Accordingly, the lateral cuts forming the triangular flaps have a length l for the singe Z-plasty and $l/3$ for the triple Z-plasty (see Figures 7.1(a) and 7.2(a)). A small gap of $s = 0.5$ mm between the facing edges of cuts is left for numerical purposes. In order to analyze the influence of the angle ϑ defining the amplitude of the triangular flaps, 15 models for each surgery are considered, with $20° \leq \vartheta \leq 90°$ at steps of 5°. These limits represent an extended range in which Z-plasties are usually performed in clinical procedures.

Each domain in the study is discretized using three-node plane stress isoparametric elements (CPS3 in ABAQUS), with a maximum size $h_{\max} = l/5$ in peripheral regions from the triangular flaps, progressively reducing to $h_{\min} = l/150$ near areas of geometrical discontinuities, such as the cut tips. An example of discretized single and triple Z-plasty models for $\vartheta = 60°$ is reported Figures 7.1(b) and 7.2(b), respectively.

Simulations have been performed employing the isotropic Ogden wrinkling model (Equation (3.77)) using the set of material parameters $\mu_1 = 110$ Pa and $\alpha_1 = 26$, based on data from an *in-vivo* experiment conducted on the volar side of the forearm [237]. A membrane thickness of $t = 1.5$ mm is used, representing the average skin thickness in that particular body region [238].

To replicate the natural skin tension on the human body, a uniform initial stress field $\boldsymbol{\sigma}_0$ is applied to the model in the reference configuration Ω. This state is induced by an equibiaxial deformation $\mathbf{F}_0$, with $\lambda_{1,0} = \lambda_{2,0} = 1.1$ and $\lambda_{3,0} = (\lambda_{1,0}\lambda_{2,0})^{-1}$ [167]. The tensor $\boldsymbol{\sigma}_0$, calculated analytically from $\mathbf{F}_0$ using the constitutive model (3.77) and Equation (3.47), is defined in the ABAQUS input files as a predefined stress field. The initial deformation gradient $\mathbf{F}_0$ is then communicated to the subroutine UMAT of ABAQUS through an external file, enabling the correct computation of the tangent stiffness tensor in Equation (3.65) using the total deformation gradient $\mathbf{F} = \mathbf{F}_n\mathbf{F}_0$, where $\mathbf{F}_n$ represents the deformation gradient provided as input in UMAT at the nth increment.

The analysis proceeds in two steps. Initially, the model is relaxed under the uniform stress field $\boldsymbol{\sigma}_0$, representing the configuration of skin post-cutting and delamination. Subsequently, suturing is applied, and the skin flaps are transposed into their final arrangement by imposing the kinematic constraint in Equation (6.1) on the internal boundary. The final configuration of the single and triple Z-plasty

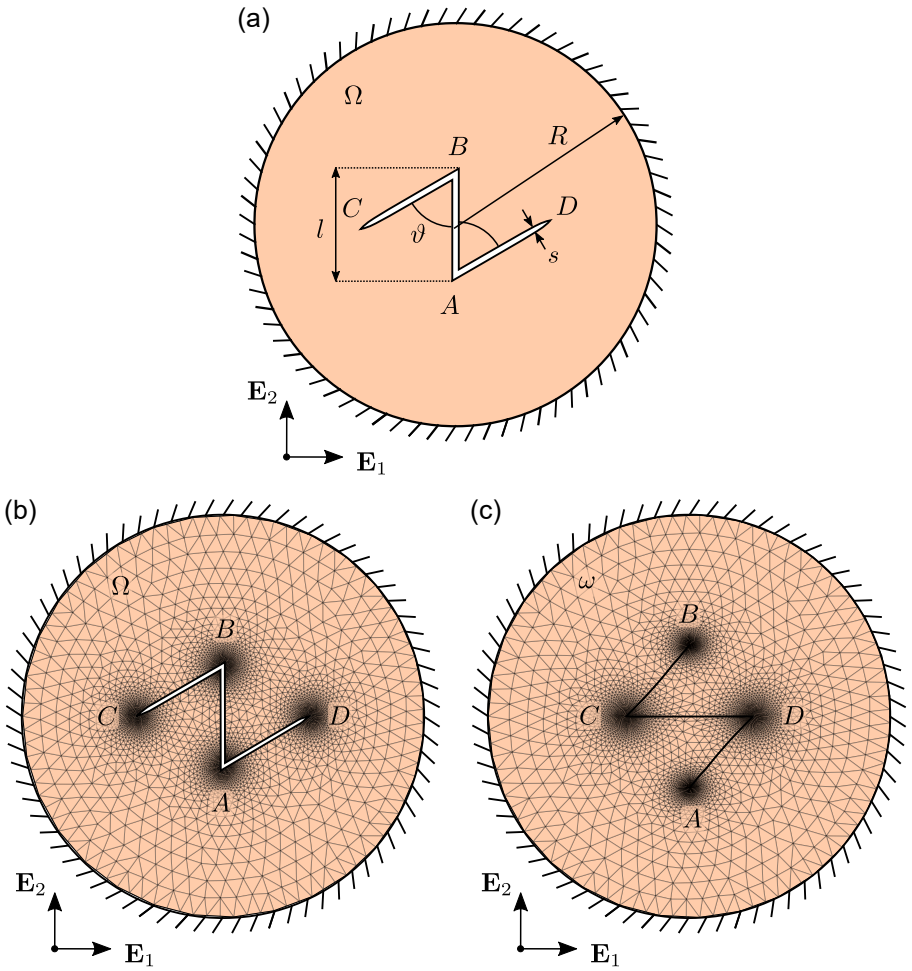

Figure 7.1: General scheme of the single Z-plasty. (a) Geometrical parameters, (b) discretized FE model for $\vartheta = 60°$ in the reference configuration, and (c) in the final configuration.

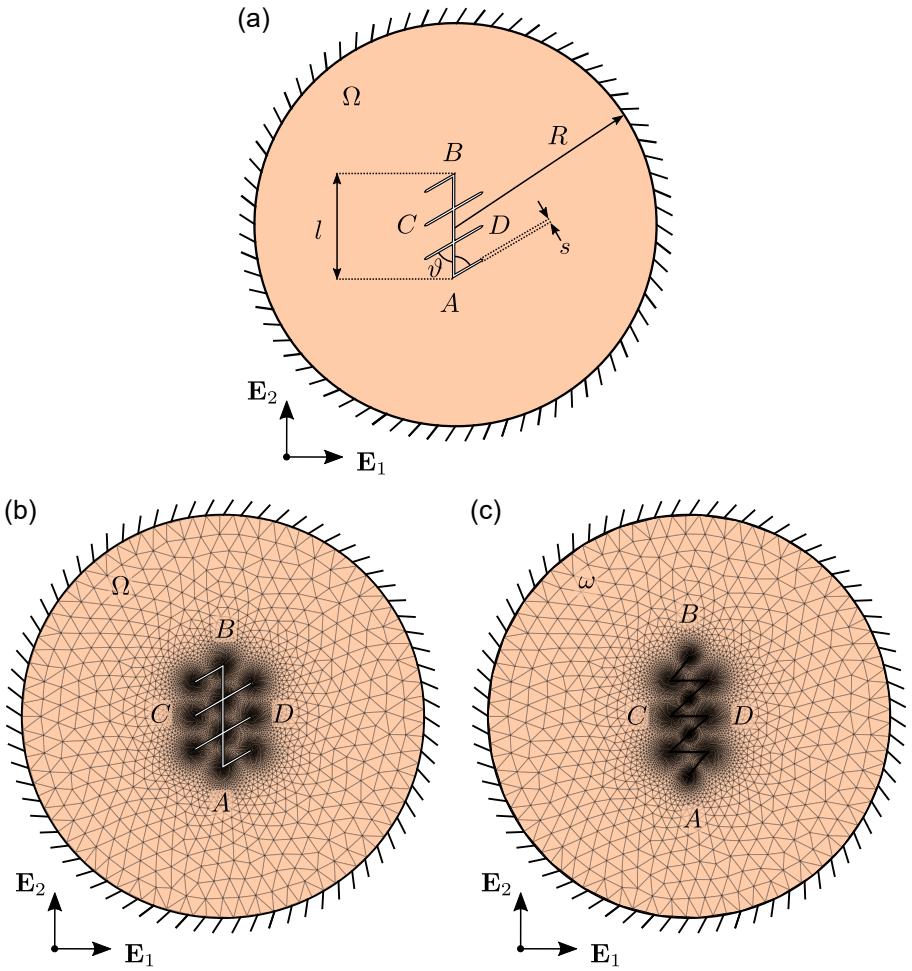

Figure 7.2: General scheme of the triple Z-plasty. (a) Geometrical parameters, (b) discretized FE model for $\vartheta = 60°$ in the reference configuration, and (c) in the final configuration.

models for $\vartheta = 60°$ is reported Figures 7.1(c) and 7.2(c), respectively. During the entire analysis the external boundary is fixed.

Figure 7.3 illustrates the relationship between the angle ϑ and the vertical elongation and horizontal shortening strains, ε_{v} and ε_{h}, respectively. The elongation strain ε_{v}, shown in Figure 7.3(a), is always greater than zero regardless of the angle ϑ. This indicates that both surgical procedures consistently produce a lengthening effect. The increase in ε_{v} is almost linear with ϑ, reaching a maximum of 0.73 for the Z-plasty and 0.29 for the triple Z-plasty at $\vartheta = 90°$. Conversely, the horizontal contraction ε_{h}, as depicted in Figure 7.3(b), shows an increasing trend for both types of surgeries, with maximum values of 0.69 for the single Z-plasty and 0.32 for the triple Z-plasty, both occurring at $\vartheta = 90°$. These findings align with the experiments conducted by Furnas and Fischer [50], despite potential uncertainties regarding boundary conditions and the variability in skin properties among individuals. Clinically, such increased shortening is not ideal due to the potential for induced stress along the horizontal direction. This issue predominantly arises at higher angles, where the initial distance between points C and D in the reference configuration significantly exceeds the scar length l (see geometrical scheme in Figure 7.1(a)). Following the transposition, points C and D align along the central limb, corresponding to the joined sides of the two triangular flaps initially sized l, meaning that $|\Delta\mathbf{x}_{\mathrm{h}}| \approx l$. Consequently, ε_{h}, being proportional to $(\Delta\mathbf{X}_{\mathrm{h}} - \Delta\mathbf{x}_{\mathrm{h}}) \cdot \mathbf{E}_1 \approx |\Delta\mathbf{X}_{\mathrm{h}}| - |\Delta\mathbf{x}_{\mathrm{h}}| \approx |\Delta\mathbf{X}_{\mathrm{h}}| - l$, attains high values when the initial distance $|\Delta\mathbf{X}_{\mathrm{h}}|$ between points C and D is much larger than l.

The profile of the Cauchy stress normal to the suture line, indicative of the tension necessary for defect closure, is depicted in Figure 7.4 for the Z-plasty and in Figure 7.5 for the triple Z-plasty. In the Z-plasty, the stress curves are mostly symmetrical, exhibiting zero stress at the suture ends, corresponding to the points A and B, and peaking at the geometrical singularities located at points C and D. Between these points, the stress decreases rapidly, reaching zero for $\vartheta \geq 55°$. This pattern is further illustrated in the strain domain distribution shown in Figure 7.6, where the ends of the suture are consistently slack, and a narrow wrinkling region emerges in the central limb for $\theta \geq 55°$. In contrast, the stress curves for the triple Z-plasty, shown in Figure 7.5, feature multiple peaks corresponding to each geometrical singularity. However, these peaks are of significantly lower magnitude compared to those in the single Z-plasty. Unloaded, or slack, regions are also present between these peaks, resulting in the formation of more but smaller wrinkling/slack regions along the suture, as observed in Figure 7.7. Nevertheless, in both cases slack domains are always localized close to the discontinuities in the suture line and surrounded by wrinkling regions.

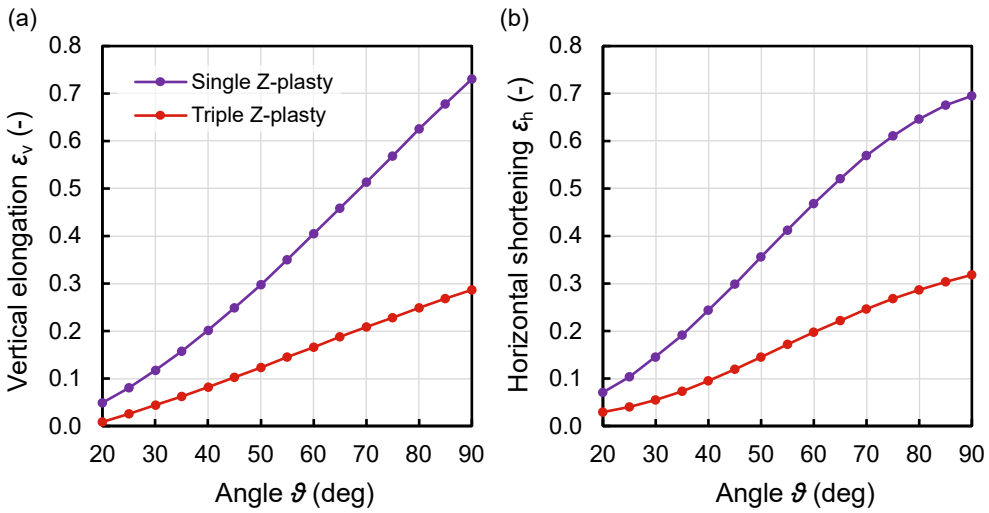

Figure 7.3: Vertical elongation and horizontal shortening strains in relation to the angle ϑ for the single and triple Z-plasty models. (a) Vertical elongation strain ε_v, (b) horizontal shortening strain ε_h.

Diagrams of the average peak stress σ_p, the total strain energy W_tot, and the total slack area A_s are reported in Figure 7.8. In both the single Z-plasty and the triple Z-plasty, the mechanical metrics exhibit an increasing pattern with ϑ, but they tend to be significantly lower in the triple Z-plasty. Conversely, the single Z-plasty achieves considerably higher vertical elongation strains ε_v, a primary objective in skin surgery. To assess the performance of these surgeries and enable a comparison between the two techniques, three elongation efficiency coefficients are introduced: η_σ, η_W, and η_A. These coefficients are designed to evaluate the cost-benefit ratio of each model's elongation capabilities concerning the quantities σ_p, W_tot, and A_s, respectively. These coefficients are defined as

$$\eta_\sigma = \eta \cdot p_\sigma, \qquad \eta_W = \eta \cdot p_W, \qquad \eta_A = \eta \cdot p_A, \tag{7.3}$$

with

$$\eta = \frac{\varepsilon_\mathrm{v}}{\varepsilon_\mathrm{v,ref}} \cdot p_\vartheta \cdot p_\mathrm{h}, \tag{7.4}$$

where η represents the base efficiency coefficient, and the subscript *ref* refers to the value of the model chosen as reference. Here, we used the single Z-plasty with $\vartheta = 60°$, representing the standard configuration adopted in the surgical practice. The factor p_ϑ accounts for the relative size of the triangular flaps. For very small

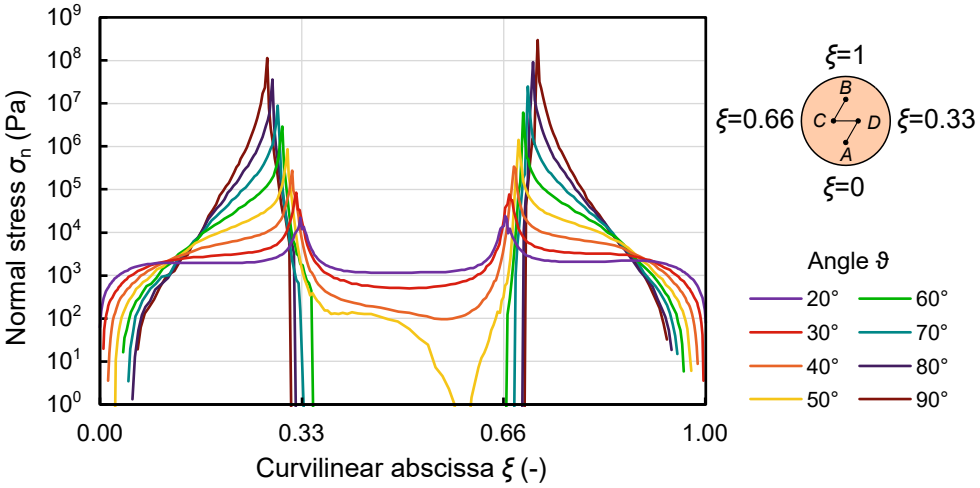

Figure 7.4: Normal Cauchy stress along the suture of the single Z-plasty. The curvilinear abscissa $\xi = L/L_s$, $\xi \in (0,1)$ represents the distance L from the point A at the lower end of the suture normalized with respect to the global length of the suture L_s in the final configuration.

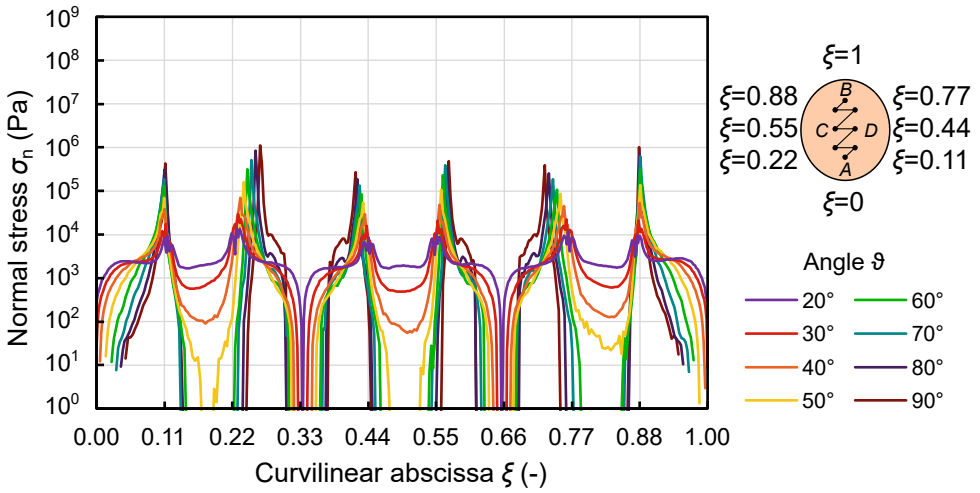

Figure 7.5: Normal Cauchy stress along the suture of the triple Z-plasty. The curvilinear abscissa $\xi = L/L_s$, $\xi \in (0,1)$ represents the distance L from the point A at the lower end of the suture normalized with respect to the global length of the suture L_s in the final configuration.

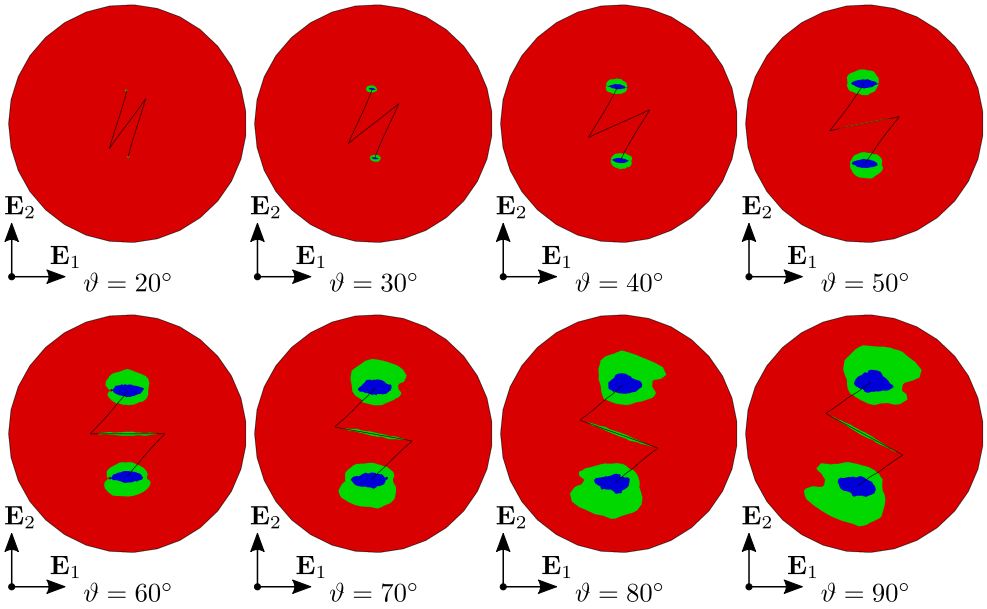

Figure 7.6: Taut (red), wrinkling (green) and slack (blue) domains for the single Z-plasty.

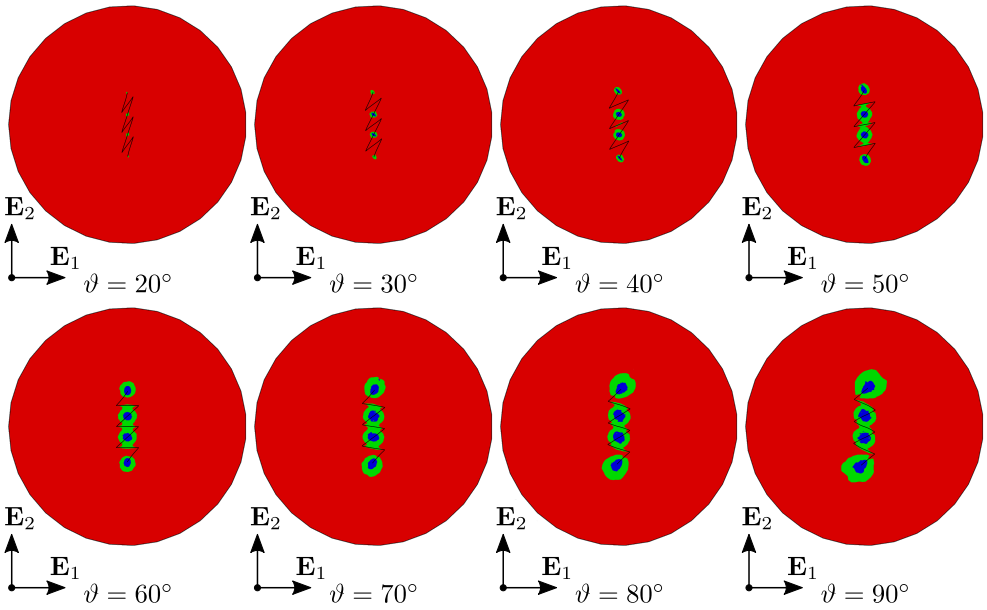

Figure 7.7: Taut (red), wrinkling (green) and slack (blue) domains for the triple Z-plasty.

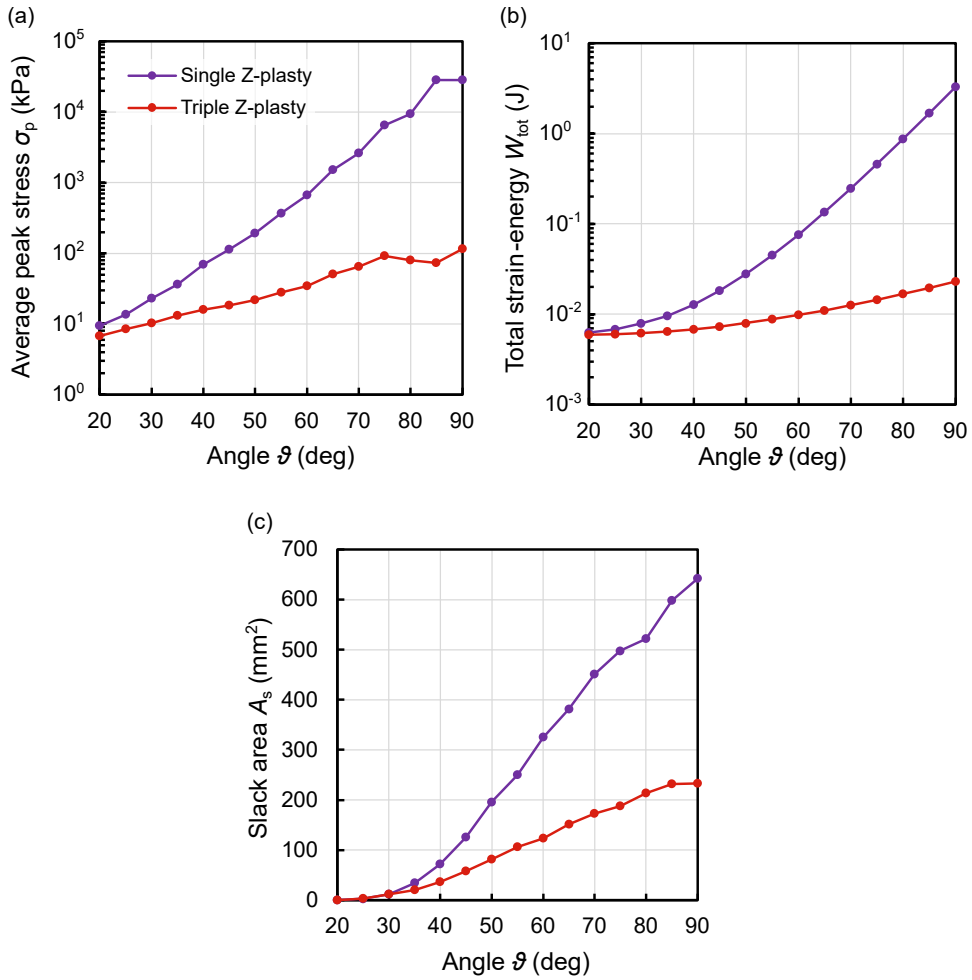

Figure 7.8: Diagrams of the mechanical metrics for the single and triple Z-plasty. (a) Average peak stress σ_p, computed by averaging the peak Cauchy stress normal to the wound in a 7 mm interval; (b) total strain energy W_{tot}; (c) total slack area A_s.

angles ϑ, the section at the base of the the flap might be insufficiently sized to maintain adequate blood flow within the flap, increasing the risk of distal necrosis [18, 128]. This aspect is quantified using the ratio $r(\vartheta)$ between the base and the side of the flap. Given that skin flaps are isosceles triangles, this ratio is given by $r(\vartheta) = \sqrt{2(1-\cos\vartheta)}$. Consequently, p_ϑ is calculated as $p_\vartheta = r(\vartheta)/r(\vartheta)_{\text{ref}}$, thereby penalizing configurations with angles smaller than that of the reference model. The factor p_{h} is introduced to address excessive shortening in the horizontal direction. It is defined as $p_{\text{h}} = \varepsilon_{\text{h,ref}}/\varepsilon_{\text{h}}$, being set to 1 for the reference model, approaching 0 as $\varepsilon_{\text{h}} \to \infty$, and tending towards infinity as $\varepsilon_{\text{h}} \to 0$. Similarly, factors p_σ, p_W, and p_A are defined as ratios between the values of the mechanical metrics with respect to those of the reference model.

All efficiency coefficients mentioned in Equation (7.3) are dimensionless and serve not as direct physical representations but as tools for a reliable and straightforward comparison of different surgical configurations. In this context, the higher the efficiency and the better is the cost-benefit ratio for a given surgical configuration. The outcomes of the simulations under consideration are presented in Figure 7.9 as a function of the elongation ratio ε_{v}. This visualization of the results clarifies which technique is preferable for a specific ε_{v} value. It also allows for the comparison of diverse elongation surgeries that depend on different geometrical parameters.

Figure 7.9(a)-(b) clearly demonstrates that the triple Z-plasty consistently exhibits higher efficiencies η_σ and η_W for the same value of ε_{v} compared to the single Z-plasty. This suggests a preference for the triple Z-plasty to minimize deformation and peak stresses along the suture line, potentially improving healing times and reducing the risk of flap failure. Indeed the triple Z-plasties, for given a scar of length l, spreads the shortening effects across three transverse axes, with a maximum value $\varepsilon_{\text{h}} = 0.32$ for $\vartheta = 90°$, thereby diminishing the peak stresses, as depicted in Figure 7.5. As demonstrated in Figure 7.8, this approach also positively impacts the analyzed mechanical metrics, with an average reduction of 81% in total strain energy, 66% in mean peak stress at the wound, and 46% in total slack area, compared to the single Z-plasty. However, the elongation ratio is also decreased by an average of 62%, yet the overall efficiencies η_σ and η_W remains relatively favorable, even surpassing that of the single Z-plasty in terms of stress and strain-energy reduction.

However, in terms of η_A, as seen in Figure 7.9(c), the triple Z-plasty seems to be less effective, except within a narrow range of $0.25 \leq \varepsilon_{\text{v}} \leq 0.29$. This indicates that while the triple Z-plasty reduces slack area, it may not provide adequate lengthening to justify its use for aesthetic purposes. Nonetheless, it is important

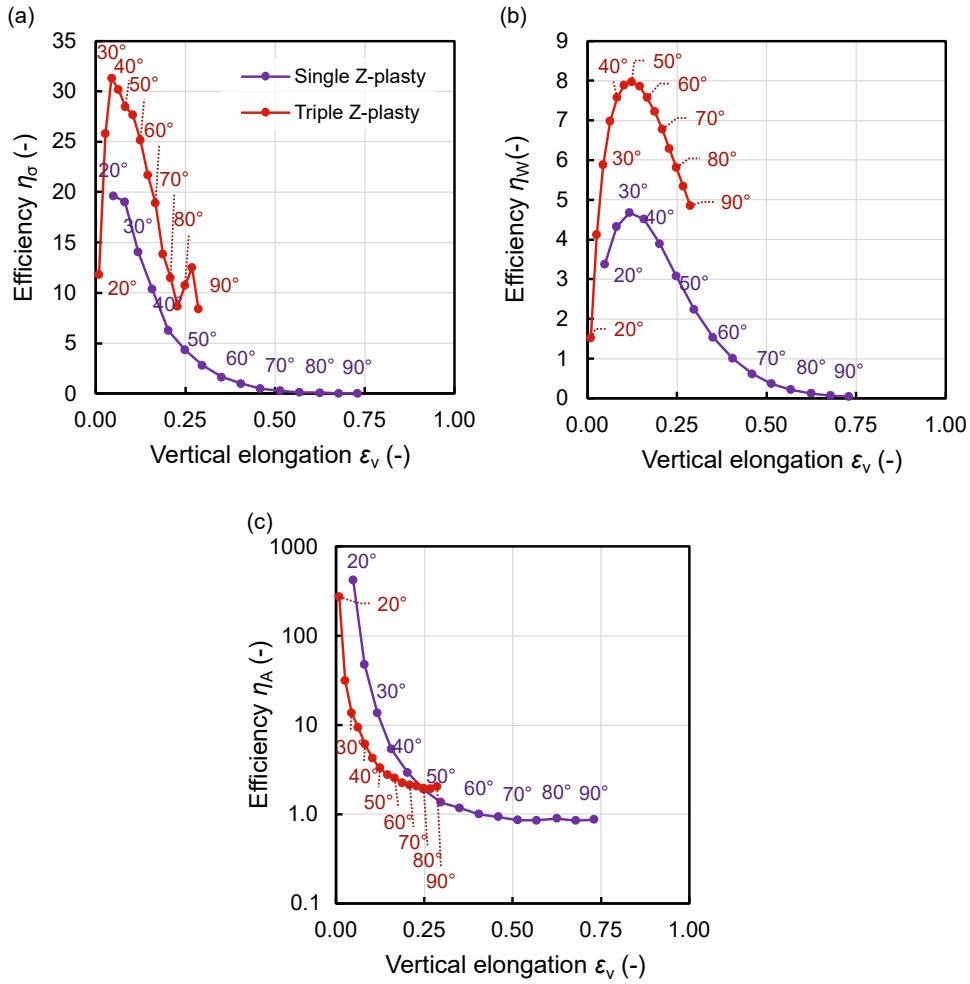

Figure 7.9: Elongation efficiency coefficients of the single and triple Z-plasty. (a) Efficiency η_σ relative to the average peak stress; (b) efficiency η_W relative to the total strain energy; (c) efficiency η_A relative to the total slack area. Efficiencies are plotted as a function of the elongation ratio ε_v. Data labels on the plots indicate the angle ϑ

.

to remember that these procedures are often employed to achieve elongations around body joints. In such cases, the presence of slack areas may not necessarily be a cosmetic concern but rather a beneficial feature that accommodates body movements. A specific study focusing on the impact of externally applied stretch on the post-suture elongation properties of these surgeries would be insightful.

Examining the overall trends of the three coefficients, it is evident that efficiencies generally improve with a reduction in the elongation ratio, i.e. by reducing ϑ. However, there is a critical lower limit for ε_{v} below which the values of η_σ and η_W peak and then decline. Notably, Figure 7.9(b) shows that both techniques reach their maximum efficiency at approximately $\varepsilon_{\mathrm{v}} = 0.12$, though at different angles ϑ: 30° for the Z-plasty and 50° for the triple Z-plasty. A similar pattern is observed in Figure 7.9(a), with the local maximum occurring at $\varepsilon_{\mathrm{v}} = 0.04$. This suggests that models displaying elongations lower than $\varepsilon_{\mathrm{v}} = 0.12$, based on the more restrictive coefficient η_W, are less desirable as they offer reduced elongation and efficiency. Consequently, this implies that the range of suitable angles ϑ may have a lower boundary of 30° for the Z-plasty and 50° for the triple Z-plasty.

Synthesizing all the observations, it appears that an optimal range of configurations can be identified. Specifically, when the goal of a surgical procedure is to minimize deformations and stresses in favor of wound healing, the triple Z-plasty emerges as a more suitable choice than the Z-plasty for equivalent vertical elongation strains ε_{v}. Therefore, for desired elongations within the range of $\varepsilon_{\mathrm{v}} = 0.12$ to $\varepsilon_{\mathrm{v}} = 0.29$, the triple Z-plasty is recommended, selecting an angle between 50° and 90°. For elongations exceeding $\varepsilon_{\mathrm{v}} = 0.29$, the Z-plasty becomes the only viable option, with angles greater than 50°. However, data on the triple Z-plasty are currently limited to angles up to 90°. It is likely that angles beyond 90° might enable even greater elongations while maintaining higher efficiency compared to the Z-plasty, potentially extending the elongation limit beyond $\varepsilon_{\mathrm{v}} = 0.29$. Nonetheless, such angles are not typically employed in corrective surgery [36]. It is plausible that an intermediate approach, such as the double Z-plasty, could yield higher elongations more efficiently than the Z-plasty.

7.2 Anisotropic Analysis of the Z-plasty

The single Z-plasty is herein reanalyzed using the anisotropic DFD model to examine the effects of varying anisotropy direction on the elongation performances. For these simulations a round domain of $R = 300$ mm is considered. The length of the central vertical cut is kept $l = 50$ mm, leaving a gap of $s = 0.5$ mm between the facing edges of cuts for numerical purposes. As previously done in Sec-

tion 7.1, 15 models with $20° \leq \vartheta \leq 90°$ at steps of 5° are analyzed (see scheme in Figure 7.1(a) for reference). Each domain in the study is discretized using three-node plane stress isoparametric elements (CPS3 in ABAQUS), with a maximum size $h_{\max} = l/5$ in regions far from the surgery, and a minimum size $h_{\min} = l/150$ close to the cut tips. Membrane thickness $t = 2.92$ mm is taken from the average value reported in Table 5.3.

Simulations are performed using the average mechanical parameters from Table 5.3, $\mu = 1.142$ kPa, $c_1 = 1.907$ kPa, $c_2 = 43.59$, employing a single fiber family with in-plane and out-of-plane concentrations $a = 2.060$ and $b = 12.363$, averaged from the parameters of the Family 1 in Table 5.2. The fiber distribution is assumed to lie in the mean membrane plane, with out of-plane angle $\beta = 0°$ and rolling angle $\gamma = 0°$. Concerning the mean in-plane fiber orientation, different angles are considered, i.e. $\alpha = 0°$, 30°, 60°, 90°, 120°, 150°.

The natural skin tension is again induced by an equibiaxial deformation field $\mathbf{F}_0$, with $\lambda_{1,0} = \lambda_{2,0} = 1.1$ and $\lambda_{3,0} = (\lambda_{1,0}\lambda_{2,0})^{-1}$ [167]. As a consequence of the material anisotropy, the initial stress field $\boldsymbol{\sigma}_0$ computed from Equation (3.56) using the constitutive model in Equation (3.98) is anisotropic, with the maximum principal stress occurring in the direction of the in-plane fiber orientation α. This state represents a condition in which the direction of the Langer's lines and the RSTL coincide. As described in Section 7.1, the tangent stiffness tensor in Equation (3.68) is computed in the subroutine UMAT of ABAQUS employing the effective deformation gradient $\mathbf{F} = \mathbf{F}_n\mathbf{F}_0$, where $\mathbf{F}_n$ represents the deformation gradient provided as input in UMAT at the nth increment.

The analysis is performed in a unique closure step by imposing the kinematic constraint in Equation (6.1) on the internal boundary, while keeping the external boundary fixed.

In Figure 7.10 are reported the relationships between the flap amplitude ϑ and the strains ε_{v} and ε_{h} for all the fiber orientations α. Similarly to the isotropic analyses, the vertical elongation strain ε_{v} in Figure 7.10(a) increases almost linearly with ϑ. Values are also similar to those observed in Figure 7.3(a) ranging from $0.032 \div 0.041$ at $\vartheta = 20°$ to $0.67 \div 0.72$ at $\vartheta = 90°$. Interestingly, ε_{v} is almost insensitive to the mean fiber orientation α, with only 7% difference between the maximum and minimum values at $\vartheta = 90°$. Concerning the horizontal shortening strain ε_{h}, shown in Figure 7.10(b), the trends are analogous to the isotropic case in Figure 7.3(b), showing a linear increasing progression in the initial stage, which deflects downward beyond $\vartheta = 60°$. Analogously to the vertical elongation strain ε_{v}, the horizontal shortening strain ε_{h} does not appear to be significantly influenced by the average fiber orientations α. However, while ε_{h} at lower angles

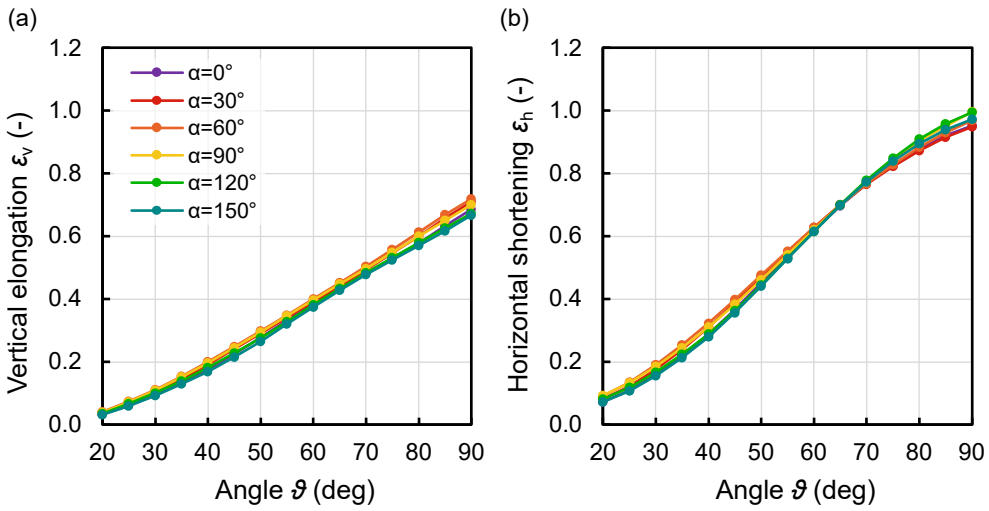

Figure 7.10: Vertical elongation and horizontal shortening strains in relation to the angle ϑ and the mean in-plane fiber orientation α for the single and Z-plasty models. (a) Vertical elongation strain ε_v, (b) horizontal shortening strain ε_h.

is modest and comparable in both analyses, being approximately 0.07 at $\vartheta = 20°$, a notable rise is observed in the anisotropic analysis for higher angles. Indeed, at $\vartheta = 90°$, ε_h reaches 0.99 in the anisotropic case, surpassing the peak of the isotropic analysis by 43%.

The influence of the anisotropy can be clearly appreciated from the distribution of stresses and strains in the final configuration. Figures 7.11 and 7.12 illustrate the distribution of the von Mises stress field and the strain domains maps of the standard Z-plasty ($\vartheta = 60°$) for the different mean in-plane fiber orientations α considered. Due to the anisotropy, the zones of compression surrounding the endpoints A and B of the suture (blue shades in Figure 7.11) tend to align with the mean direction of the fibers. This becomes even more noticeable from the strain domains maps in Figure 7.12, where the major axis of the elliptic slack regions around the endpoints A and B, representing the extension of the so-called dog-ear, roughly follow the mean fiber direction $\mathbf{M}(\alpha)$.

Differently from the isotropic analysis, the wrinkling domain, shown in green in Figure 7.12, is more extended around the slack regions and wider along the central limb for all the angles α. This phenomenon is also reflected in the profiles of the stresses normal to the wound. Representative plots for $\alpha = 90°$ (mean in-plane fiber orientation parallel to the scar) are shown in Figure 7.13. Therein,

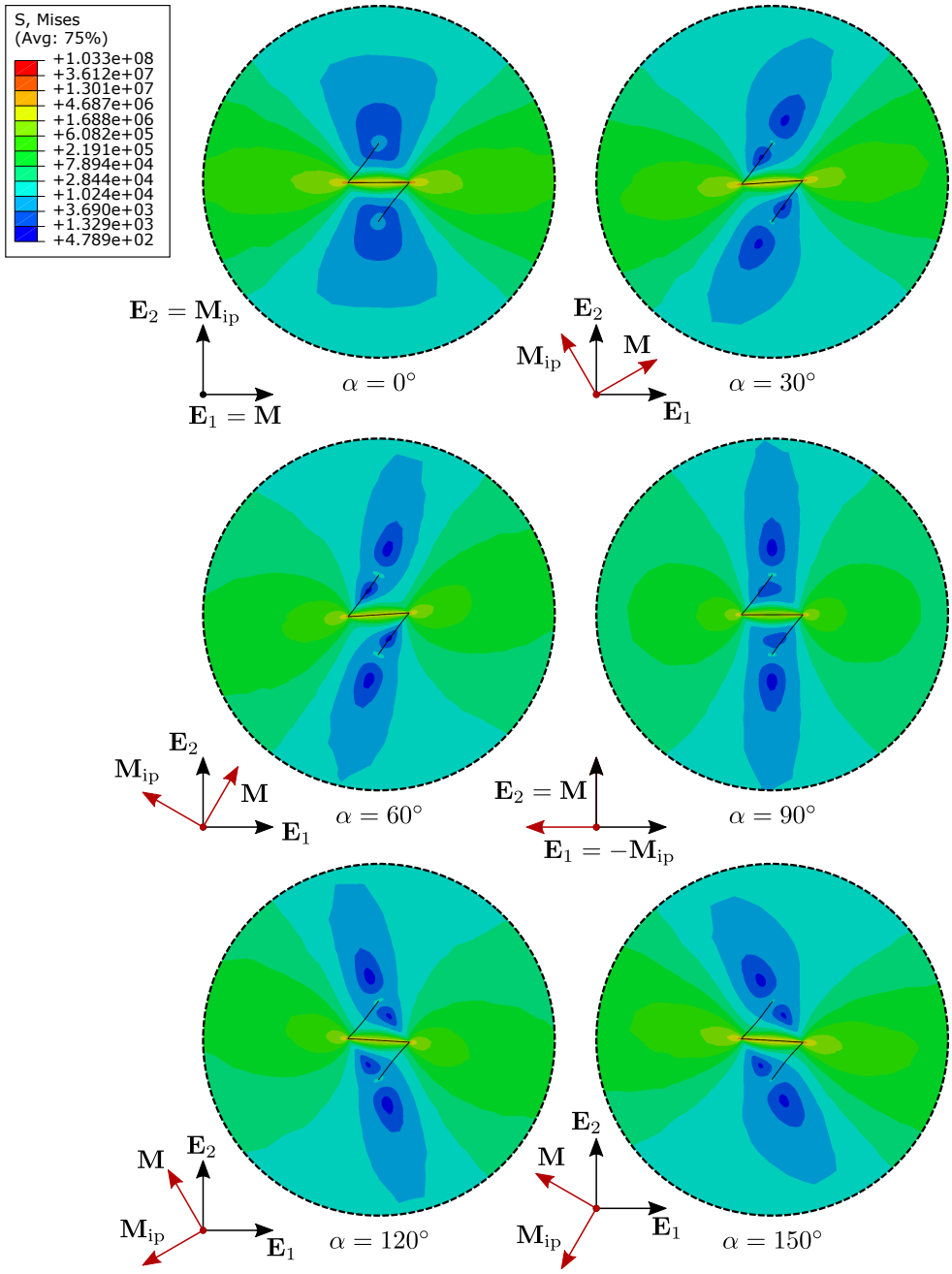

Figure 7.11: Maps of the von Mises stress field of the single Z-plasty with $\vartheta = 60°$ for different mean in-plane fiber orientations α. Note that shown maps are cropped from the full circular domain.

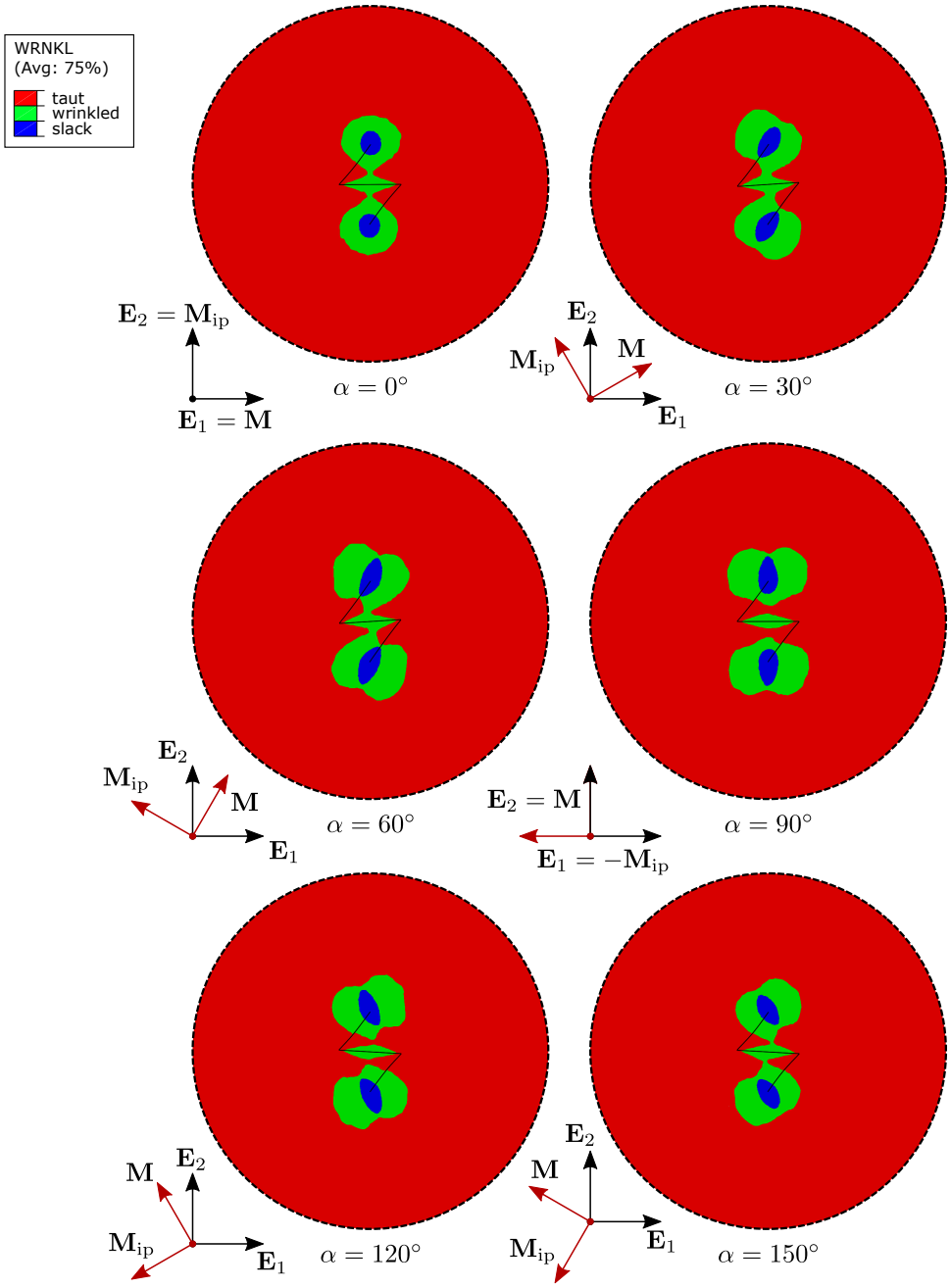

Figure 7.12: Strain domains maps of the single Z-plasty with $\vartheta = 60°$ for different mean in-plane fiber orientations α. Note that shown maps are cropped from the full circular domain.

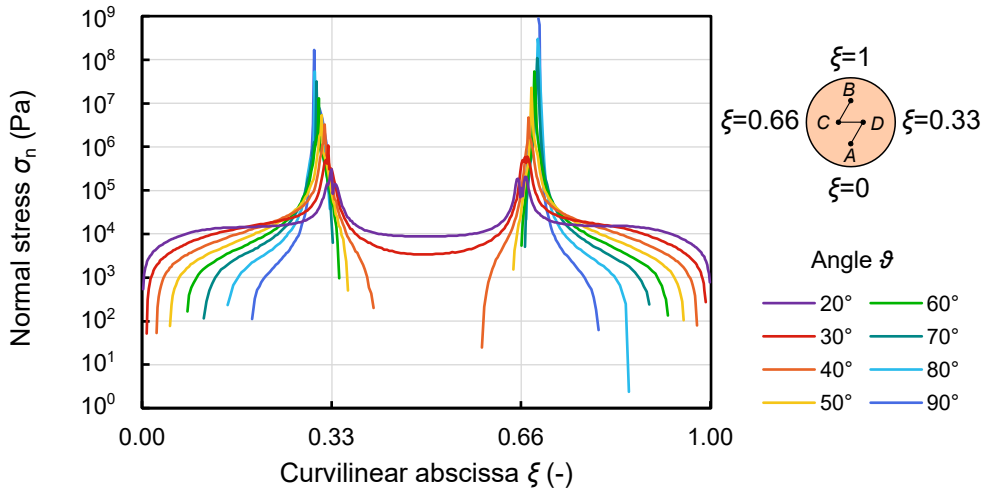

Figure 7.13: Normal Cauchy stress along the suture of the single Z-plasty for the mean in-plane fiber orientation $\alpha = 90°$. The curvilinear abscissa $\xi = L/L_s$, $\xi \in (0,1)$ represents the distance L from the point A at the lower end of the suture normalized with respect to the global length of the suture L_s in the final configuration.

the ranges of positive stresses are narrower and more concentrated around the geometrical discontinuities in the points D ($\xi = 0.33$) and C ($\xi = 0.66$), although magnitudes of the stress peaks are comparable to those of the isotropic analysis reported in Figure 7.4. This stress redistribution in favor of compressive stresses might be due to the strain-energy component of the ground matrix, which still contributes in compression even when the fiber strain-energy component vanishes (see Equation (3.98)).

The selected mechanical metrics σ_p, W_{tot}, and A_s are reported in Figure 7.14. From Figure 7.14(a) it is possible to notice that the average peak stress increases exponentially with ϑ. Trends are almost identical for all the considered in-plane fiber orientations α. In general, σ_p reduces as the fiber become aligned in the direction of the axis A-B, reaching the minimum for $\alpha = 60° \div 90°$, but only for $\vartheta \geq 60°$. For the extreme flap amplitude $\vartheta = 90°$ the reduction of the stress is considerable, being 5.77×10^4 kPa for $\alpha = 60°$ against a peak of 1.90×10^5 kPa for $\alpha = 150°$. For lower ϑ, instead, the stress σ_p is slightly higher, but values are of 1 to 2 orders of magnitude lower than the extreme case $\vartheta = 90°$.

The total strain energy W_{tot} (Figure 7.14(b)) is relatively small for low flap amplitudes ϑ and displays a rapid growth as ϑ approaches 90°. However, it is

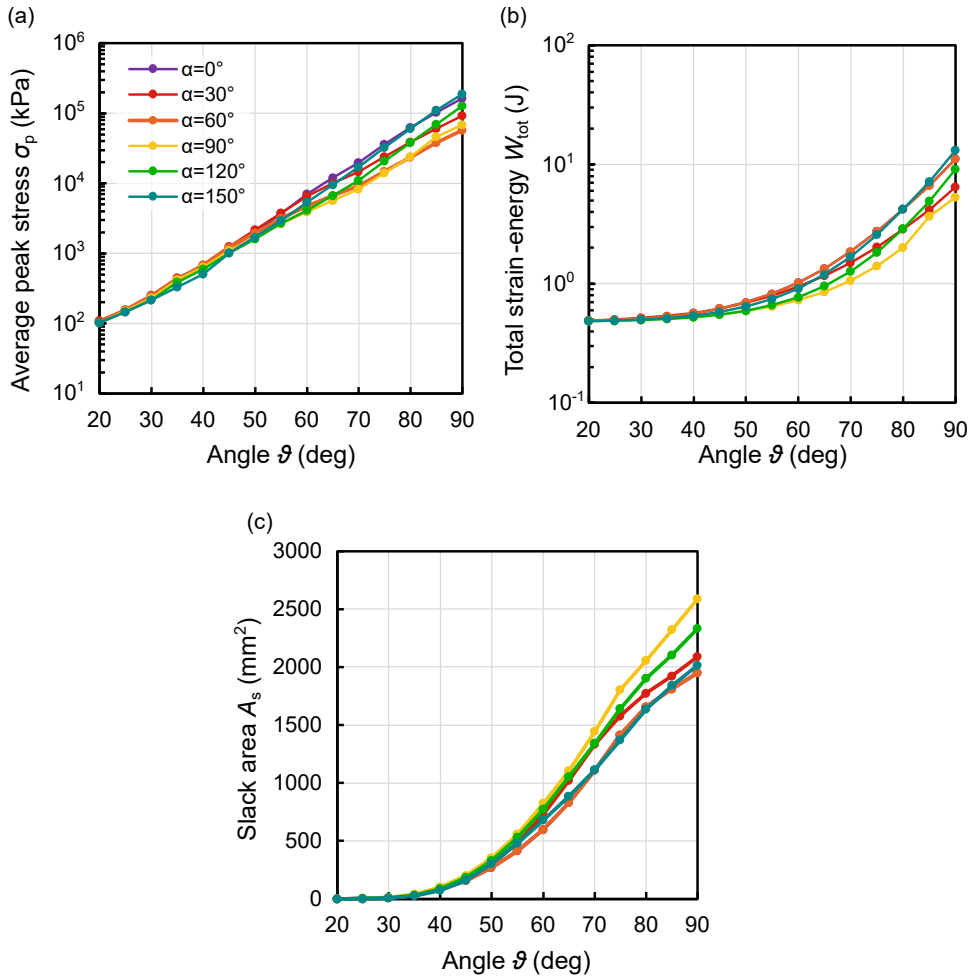

Figure 7.14: Diagrams of the mechanical metrics for the single and triple Z-plasty for all the in-plane fiber orientation α. (a) Average peak stress σ_p, computed by averaging the peak Cauchy stress normal to the wound in a 7 mm interval; (b) total strain energy W_{tot}; (c) total slack area A_s.

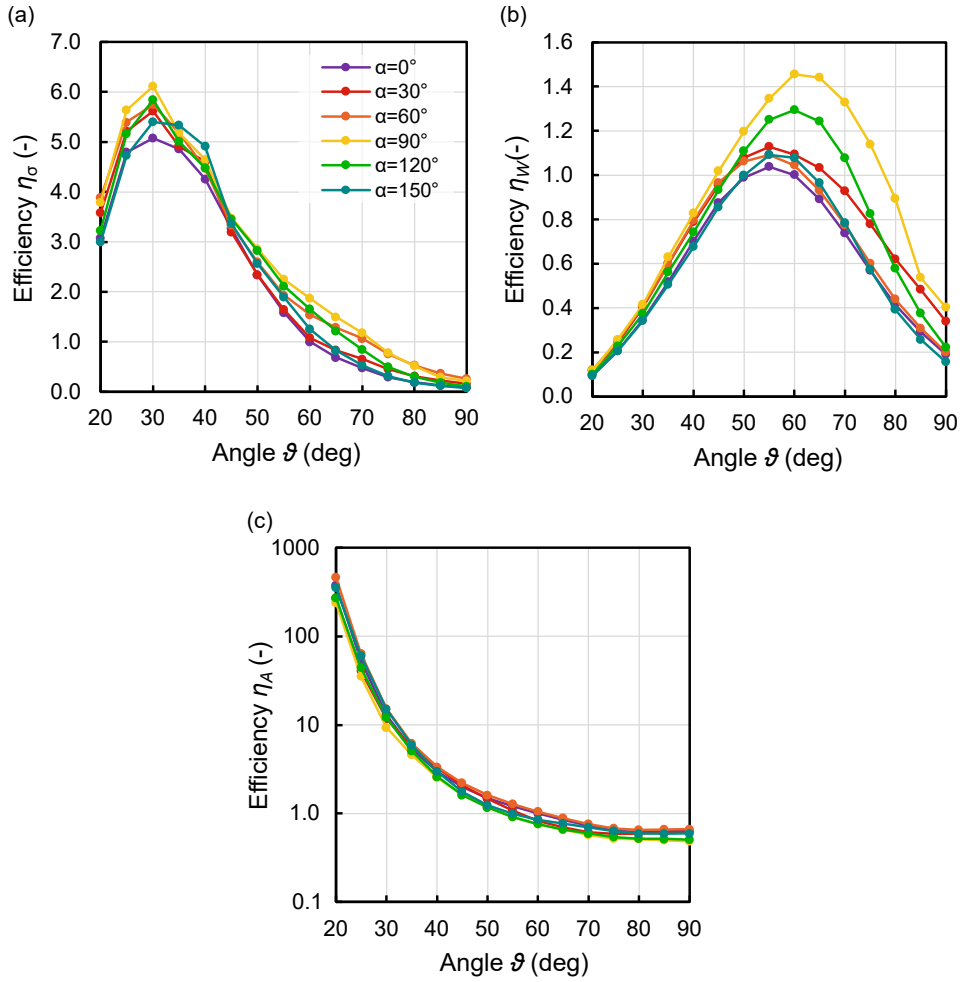

Figure 7.15: Elongation efficiency coefficients of the single Z-plasty for different mean in-plane fiber orientations α. (a) Efficiency η_σ relative to the average peak stress; (b) efficiency η_W relative to the total strain energy; (c) efficiency η_A relative to the total slack area. Efficiencies are plotted as a function of the angle ϑ.

consistently lower for $\alpha = 90°$. As a consequence, the slack area A_s for such fiber angle, as shown in Figure 7.14(c), is higher for all the flap amplitudes ϑ. All the trends for A_s exhibit an exponential growth with ϑ, then reaching an inflection point at about $\vartheta = 75°$.

Then, to analyze the influence of the mean fiber orientation α on elongation performances of the Z-plasty, the elongation efficiency coefficients as defined in Equation (7.3) are computed based on the mechanical data from Figures 7.10 and 7.14, using the model with $\vartheta = 60°$ and $\alpha = 0°$ as reference. Since the vertical elongation strain ε_v mainly depends on ϑ, the efficiencies in Figure 7.15 are plotted with respect to ϑ (instead of ε_v) to facilitate the comparison between the curves of different orientations α.

The efficiencies η_σ relative to the average peak stress σ_p in Figure 7.15(a) all exhibit the same trend. Notably, the local maximum for all the curves occurs at $\vartheta = 30°$. This value, as also pointed out in the isotropic analysis, set a lower limit for the range of suitable flaps amplitudes, below which the Z-plasty produces scarce strains ε_v with low stress efficiency η_σ regardless the orientation α of the fibers. Considering the efficiencies η_W relative to the total strain-energy W_{tot} in Figure 7.15(b), this lower limit is shifted toward higher amplitudes ϑ depending on α. In fact, the local maximum η_W occurs at $\vartheta = 60°$ for fiber orientations in the range $90° \leq \alpha \leq 120°$, and at $\vartheta = 55°$ for the other fiber orientations. In general, both the efficiencies η_σ and η_W are maximized for $\alpha = 90°$, save for a small interval $35° \leq \vartheta \leq 40°$ in which η_σ is better for $\alpha = 150°$. The efficiency η_A relative to the slack area A_s exhibits no local maximum, and it is practically independent of the fiber orientation α. The efficiency always decreases by increasing the flap amplitude ϑ, seemingly reaching an horizontal asymptote of about $\eta_A = 0.5$.

7.3 Isotropic Analysis of the Rhombic Flap Transposition

To analyze the rhombic flap transposition, 48 configurations of the rhombic flap with $0° \leq \vartheta_1 \leq 70°$ and $30° \leq \theta_2 \leq 70°$, at steps of 10°, have been considered. The rhombic excision, equal for all models and characterized by a minor angle of $\varphi = 60°$, and sides of $l = 30$ mm, is centered in a circular domain with radius $R = 100$ mm (Figure 7.16). The two cuts forming the donor flap have the same length of the rhombic sides, in which a spacing of $s = 0.5$ mm is left for numerical purposes. Each domain in the study is discretized using three-node plane stress isoparametric elements (CPS3 in ABAQUS), with a maximum size $h_{max} = l/5$ in peripheral regions from the triangular flaps, progressively reducing to $h_{min} = l/150$ near areas of geometrical discontinuities, such as the cut

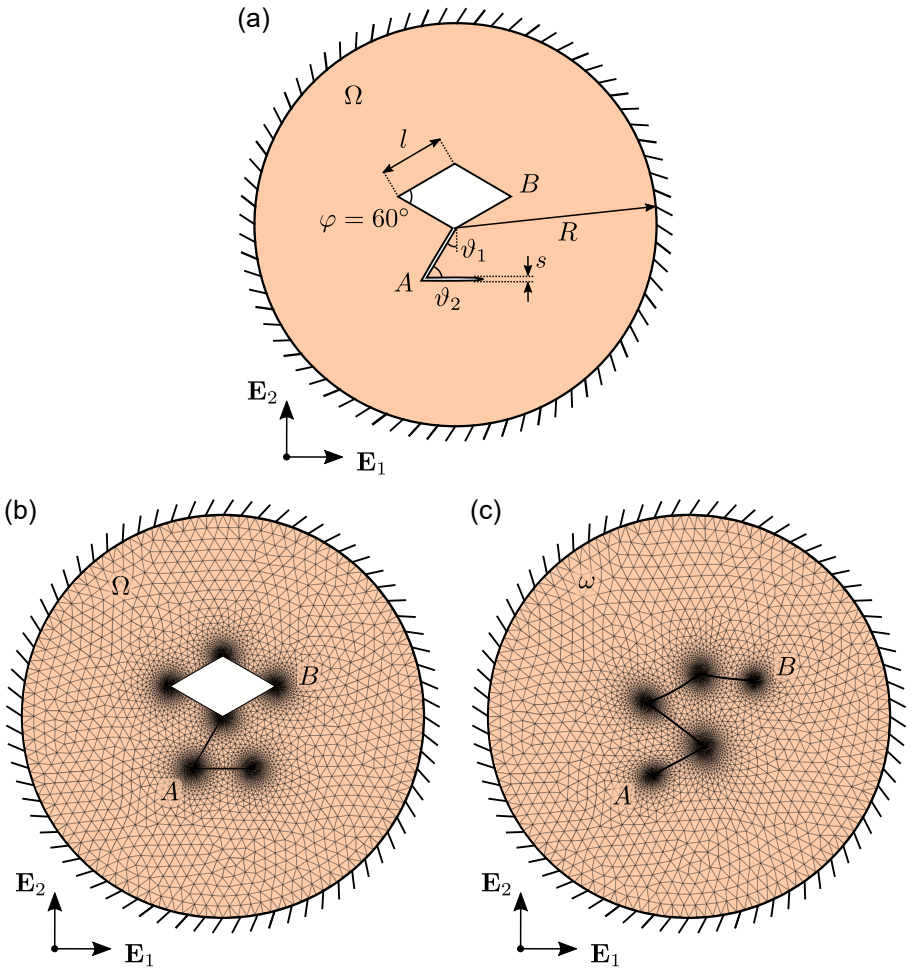

Figure 7.16: General scheme of the rhombic flap transposition. (a) Geometrical parameters, (b) discretized FE model for $\vartheta_1 = 30°$ and $\vartheta_2 = 60°$ in the initial configuration, and (c) the same model in its final configuration.

tips. An example of discretized model with $\vartheta_1 = 30°$, $\vartheta_2 = 60°$ is reported in Figure 7.16(b)-(c), showing it before and after the suturing, respectively. Simulations have been performed employing the isotropic Ogden wrinkling model (Equation (3.77)) adopting the same material parameters and membrane thickness used in Section 7.1. The initial stress field $\boldsymbol{\sigma}_0$ is the same as well.

The closure is achieved in two steps, first allowing the model to relax under the initial stress field, and then applying the kinematic constraint in Equation (6.1) on the internal boundary to close the suture, while keeping fixed the external boundary.

Since the only purpose of the rhombic flap transposition is to close large sized defects, relative performances are analyzed only in terms of average peak stress σ_p, total strain energy W_tot, and total slack area A_s. No vertical and horizontal strains has been evaluated, since these two parameters have no meaning for defect closure operations. Hence, the primary goal is to identify an optimized configuration for rhombic flap that minimizes all the three metrics at the same time.

Similar to the Z-plasty, slack areas in the rhombic flap transposition are primarily concentrated at the suture line ends (Figure 7.17). The diagrams of the mechanical metrics in Figure 7.18(c) show that, regardless of ϑ_1, all curves have a qualitatively similar shape, with an increasing trend observed as both ϑ_1 and ϑ_2 angles increase. Notably, above $\vartheta_1 = 30°$, the curves tend to overlap, indicating a diminishing dependence on ϑ_1. The total strain energy, depicted in 7.18(b), consistently grows with ϑ_2 for a constant ϑ_1. However, for a constant ϑ_2, two contrasting trends are noted: the energy increases with ϑ_1 for $\vartheta_2 < 60°$, but this trend reverses for $\vartheta_2 \geq 60°$. A similar pattern is observed for the wound mean peak stress in Figure 7.18(a), although the values are more varied.

The most effective configuration discovered corresponds to angles $\vartheta_1 = 0°$ and $\vartheta_2 = 30°$, aligning with the findings of Topp *et al.* [56]. This specific angle combination benefits from requiring only a small rhombic flap to close the defect and distributes the wrinkling/slack strain domains over three drop-shaped areas, unlike other configurations which tend to concentrate them around the suture ends A and B, as shown in Figure 7.17. This results in a more uniform distribution of strains along the suture line, smoothing peak stresses, thereby reducing σ_p. Nonetheless, as it can be seen from Figure 7.16(a), for $\vartheta_1 = 0°$ the rhombic flap is placed perpendicularly to the defect, making this choice not viable in some circumstances. For facial landmarks, for instance, there are a lot webs and clefts which constrain the design of the flap. In these situations a different configuration is required to achieve the closure. The manipulation of the ϑ_1 angle can be useful for accommodating the flap to the available space, rotating it nearby or faraway

the lozenge depending on the needs, while ϑ_2 can be hold constant to simplify the design of the surgery. The challenge then becomes finding a suitable ϑ_2 that still minimizes W_{tot}, σ_{p}, and A_{s}. Analysis of the mechanical metrics in Figure 7.18 indicates that these quantities generally increase with ϑ_2. Therefore, maintaining $\vartheta_2 = 30°$ allows for a range of ϑ_1 angles from 0° to 70° to be used, ensuring minimal impact on mechanical features and offering flexibility in flap design.

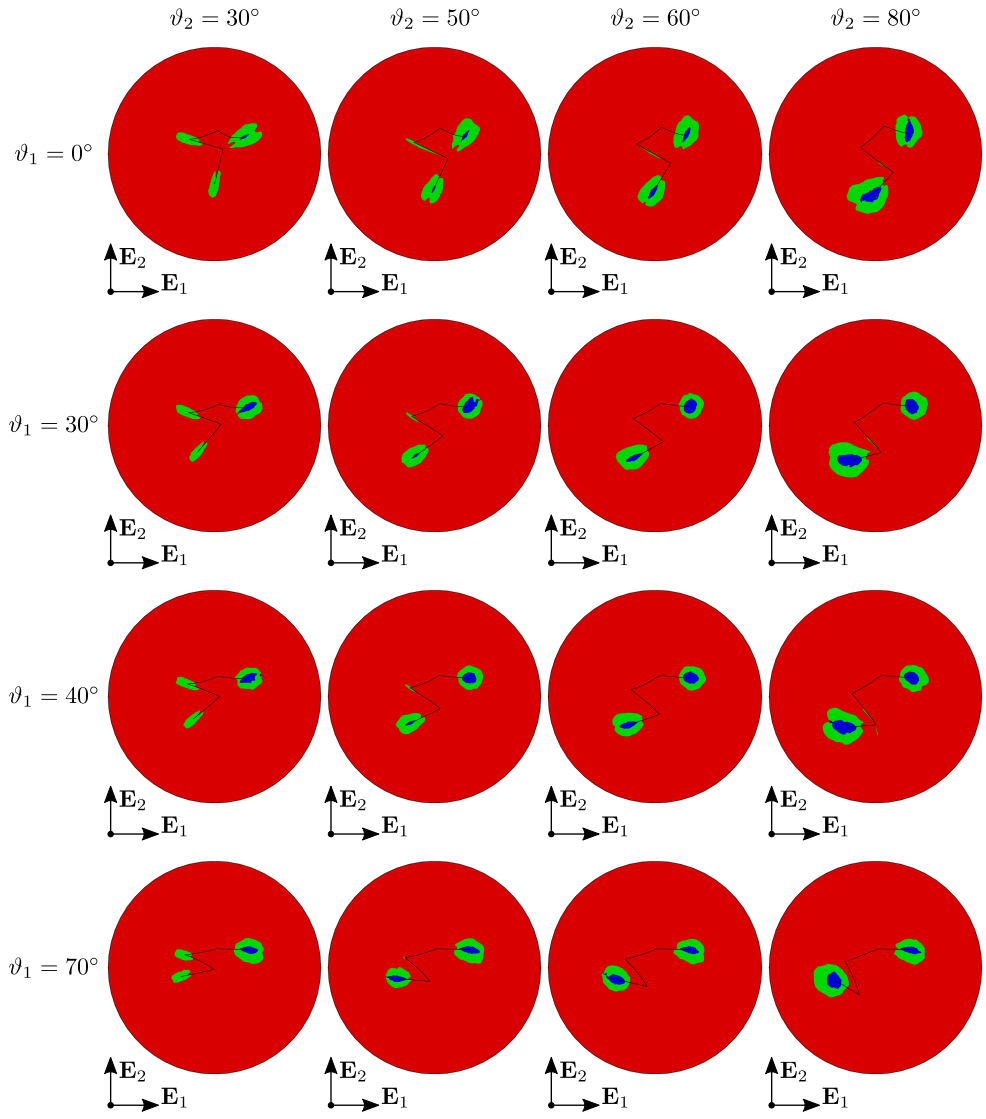

Figure 7.17: Taut (red), wrinkling (green) and slack (blue) domains for the rhombic flap transposition.

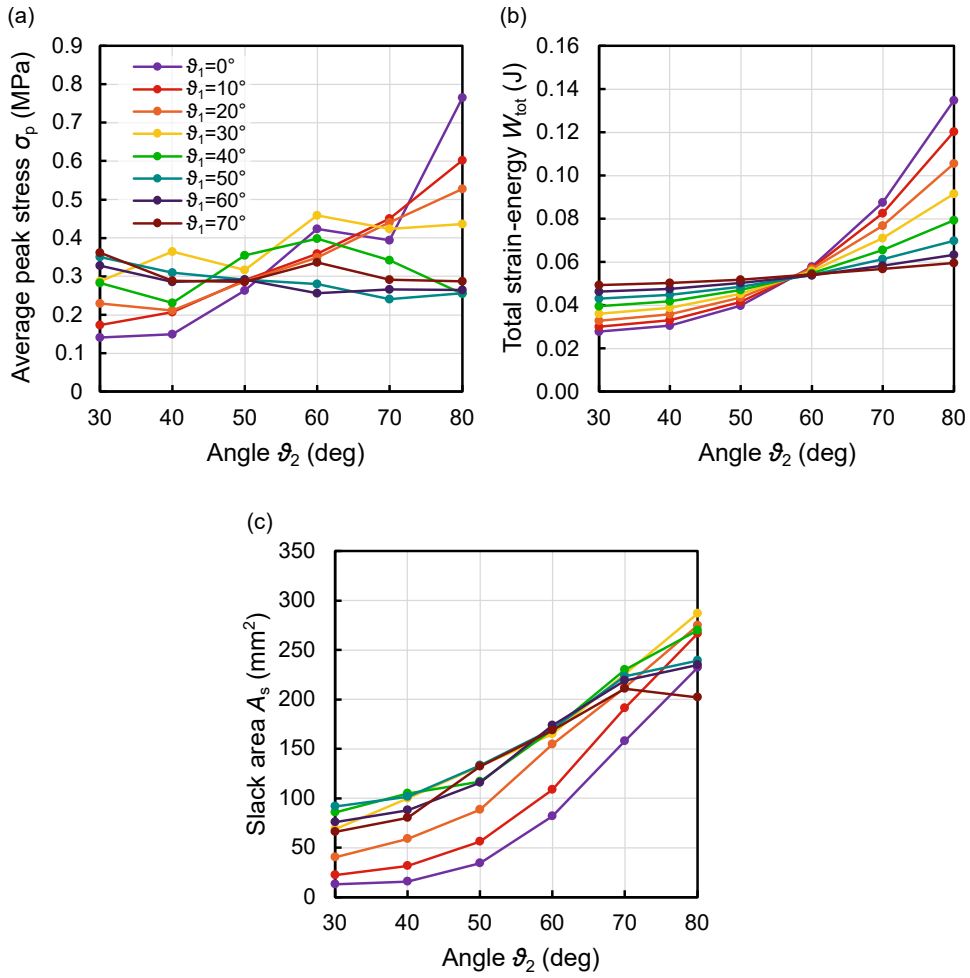

Figure 7.18: Diagrams of the mechanical metrics for the rhombic flap transposition. (a) Average peak stress σ_p, computed by averaging the peak Cauchy stress normal to the wound in a 7 mm interval; (b) total strain energy W_{tot}; (c) total slack area A_s.

Chapter 8

Conclusions

Skin is an extraordinary material featuring a complex mechanical behavior optimized through millennia of evolution to protect organs from external hazards while accommodating large deformations required for the body movement. Understanding its mechanical properties is not only fundamental for dermatological research but also pivotal for clinical applications, ranging from surgery to cosmetic procedures.

In this thesis, the mechanical modeling of the human skin was addressed covering both the theoretical and experimental aspects, with the final objective of performing precise FE simulations of skin corrective surgeries. The theoretical background of the continuum mechanics for finite strain was first introduced as the foundation for the mechanical modeling of soft fiber-reinforced biological materials. In particular, stress and stiffness tensors were derived for the plane stress formulation, allowing to analyze the skin as a bi-dimensional structure. Then, three different constitutive models for the skin were presented.

First, an isotropic constitutive model based on the Ogden model was developed. To account for the wrinkling of thin membranes under compressive forces, such as skin, the model was modified by reducing the stiffness in compression. This so-called Ogden wrinkling model was implemented in the commercial FE software ABAQUS, and validated with elementary tests on unit elements, and benchmark test from the literature. In all the examples provided, there was a noticeable redistribution of stress and strain fields upon analysis with the wrinkling function compared to the results obtained with the standard Ogden model. This led to a significant enhancement in the qualitative prediction of the taut, wrinkling, and slack regions within the tested membranes. Such improvements demonstrated that the approach is highly suitable for advanced FE analyses.

In addition to the isotropic model, two anisotropic models specifically conceived to describe the mechanics of soft fiber-reinforced biological tissues were described and implemented in a custom MATLAB script. The first one is the GST model for non-symmetrical fiber dispersion developed by Holzapfel *et al.* [80], while the second is the DFD model proposed by Li *et al.* [87]. Since the two models have comparable predictive power, as pointed out in [79], only the DFD model was additionally implemented in user subroutines of ABAQUS, as it allows to efficiently exclude the mechanical contribution of the compressed fibers. However, differently to the original formulation, the DFD model was implemented using the Lebedev quadrature rule [175] which allowed to precisely integrate the strain-energy function with a reduced number of representative fiber directions, thus increasing the computational efficiency. Indeed, benchmark tests revealed that 194 integrand evaluations are sufficient to provide an accurate result, in contrast to the 2571 to 4000 required in the originally proposed formulation.

To obtain the fundamental mechanical and microstructural parameters for the GST and DFD models, a campaign of experimental test on 14 *ex vivo* human skin samples from the abdominal region was conducted. Microstructural parameters were computed from SHG tomographies of the collagen fibers, while the mechanical parameters were determined by fitting the models onto the measured stress versus strain responses of biaxial tests. Further uniaxial test were performed to investigate the volumetric behavior of the skin. The out-of-plane stretch deduced from the in-plane stretches using incompressibility constraint revealed an unexpected expansion at high levels of uniaxial deformation, questioning the incompressibility hypothesis commonly assumed to simplify the mechanical modeling of the skin. These results indeed, although not confirmed by out-of-plane measurements, are in contrast to the common behavior of biological tissues, and corroborate the findings of Wahlsten *et al.* [227].

To compute the microstructural parameters from SHG topographies of the collagen fibers a new algorithm based on the 3D discrete Fourier transform was developed. The algorithm represents an extension of the Fourier transform methods already available in the literature for the 2D case. The algorithm provides precise quantitative characterizations of the spatial distribution of complex fiber dispersions. Unlike 2D methods that struggle to detect fibers significantly inclined from the plane of the tissue membrane due to their minimal cross-section, this technique is capable of detecting fibers of any orientation in 3D space. Differently from existing 3D methods, which provide separate distributions along θ and ϕ, the proposed algorithm provides a complete description of the spatial fiber distribution over the whole 3D angular domain. As a result, it facilitates the iden-

tification of various fiber families within the volume, enabling the calculation of the specific microstructural parameters set for each family without ambiguities. Moreover, since the algorithm computes fiber distributions from 3D grayscale images, any technique for acquiring the tomographies can be used, thus extending its applications to the analysis of other fiber-reinforced materials.

Finally, skin corrective surgeries were analyzed. Due to the geometrical complexity of these operations, as well as the difficult application of the boundary conditions required to simulate the suturing, a parametric algorithm was developed and implemented in a MATLAB script. The algorithm incorporates the DistMesh automeshing code developed by Persson and Strang [232], and it is capable of generating topologically complex FE models geometries using few and simple geometrical input parameters. This approach not only generates models with high quality mesh, but also reduces the time for model generation compared to user-guider tools.

Two scar relaxation surgeries were simulated and analyzed, employing the wrinkling and the DFD constitutive models implemented in ABAQUS, namely the single Z-plasty, the triple Z-plasty. Results from the wrinkling constitutive model revealed that the scar elongation of both the surgical techniques increase linearly with the angle ϑ between the vertical and the lateral cuts, but the triple Z-plasty attains less than half the vertical elongation strain of the Z-plasty. On the other hand, the triple Z-plasty minimizes adverse mechanical features, related to the risk of flap failure or distal necrosis and connected to the stresses and the global strain-energy, and the aesthetic defects represented by the extension of slack regions. Therefore, by analyzing the elongation efficiency ratios of the two techniques it was found that the triple Z-plasty generally provide higher elongation efficiency ratios. In particular, for desired elongations within the range of $\varepsilon_{\mathrm{v}} = 0.12$ to $\varepsilon_{\mathrm{v}} = 0.29$, the triple Z-plasty is recommended, selecting an angle between 50° and 90°. Then, to achieve higher vertical elongation $\varepsilon_{\mathrm{v}} = 0.12$ the Z-plasty becomes the only viable option, with angles greater than 50°. From the anisotropic analysis of the Z-plasty a further perspective emerged. In fact, while the vertical elongation was almost the same as that found by the wrinkling model, the efficiency with respect to the global strain energy pointed out that the best performance of the Z-plasty is achieved for angles between 55° and 60°, showing low sensitivity to the direction of the anisotropy.

The rhombic flap transposition was also analyzed using the wrinkling model. For this case, the objective was to minimize the adverse mechanical features. Results showed that a flap opening angle of $\vartheta_2 = 30°$ provide the best results, while the angle ϑ_1, defining the orientation of the flap, can be selected in a range from

0° to 70°, depending on the specific surgical needs. This ensures minimal impact on mechanical features, offering high versatility in flap design.

These findings might seem useful for restricted and limited clinical applications. Nonetheless, they demonstrated the great potential of the FEM analyses for understanding the mechanics behind complex skin surgical operation. Moreover, all the steps done to arrive at the results herein presented have led to the development of new algorithms, implemented in dedicated in-house codes, and to new insights about the mechanical behavior of human skin, which might be useful, hopefully, for applications beyond those presented in this thesis.

Bibliography

[1] F. Martini and J. Nath, *Anatomy & Physiology*. Benjamin Cummings, 2010, ISBN: 9780321597137.

[2] T. Burns and A. Rook, *Rook's textbook of dermatology*, 7th ed., J. Wiley, Ed. Blackwell Publishing, 2008, ISBN: 1-4051-2974-3.

[3] M. J. Blair, J. D. Jones, A. E. Woessner, and K. P. Quinn, "Skin Structure–Function Relationships and the Wound Healing Response to Intrinsic Aging," *Advances in Wound Care*, vol. 9, no. 3, pp. 127–143, 2020, ISSN: 2162-1918. DOI: 10.1089/wound.2019.1021.

[4] H. Linares, "From wound to scar," *Burns*, vol. 22, no. 5, pp. 339–352, 1996, ISSN: 03054179. DOI: 10.1016/0305-4179(95)00164-6.

[5] A. Kawasumi, N. Sagawa, S. Hayashi, H. Yokoyama, and K. Tamura, "Wound Healing in Mammals and Amphibians: Toward Limb Regeneration in Mammals," in *Current Topics in Microbiology and Immunology*, 1, vol. 367, 2012, pp. 33–49. DOI: 10.1007/82_2012_305.

[6] C. C. Yates, P. Hebda, and A. Wells, "Skin Wound Healing and Scarring: Fetal Wounds and Regenerative Restitution," *Birth Defects Research Part C: Embryo Today: Reviews*, vol. 96, no. 4, pp. 325–333, 2012, ISSN: 1542-975X. DOI: 10.1002/bdrc.21024.

[7] R. Sgonc and J. Gruber, "Age-Related Aspects of Cutaneous Wound Healing: A Mini-Review," *Gerontology*, vol. 59, no. 2, pp. 159–164, 2013, ISSN: 0304-324X. DOI: 10.1159/000342344.

[8] A. F. Borges, "Scar prognosis of wounds," *British Journal of Plastic Surgery*, vol. 13, pp. 47–54, 1960, ISSN: 00071226. DOI: 10.1016/S0007-1226(60)80009-4.

[9] F. Addor, "Beyond photoaging: additional factors involved in the process of skin aging," *Clinical, Cosmetic and Investigational Dermatology*, vol. Volume 11, pp. 437–443, 2018, ISSN: 1178-7015. DOI: 10.2147/CCID.S177448.

[10] S. W. Liu, M. H. Lien, and N. A. Fenske, "The effects of alcohol and drug abuse on the skin," *Clinics in Dermatology*, vol. 28, no. 4, pp. 391–399, 2010, ISSN: 0738081X. DOI: 10.1016/j.clindermatol.2010.03.024.

[11] H. Korting, C. Schöllmann, and R. White, "Management of minor acute cutaneous wounds: importance of wound healing in a moist environment," *Journal of the European Academy of Dermatology and Venereology*, vol. 25, no. 2, pp. 130–137, 2011, ISSN: 0926-9959. DOI: 10.1111/j.1468-3083.2010.03775.x.

[12] S. Chadwick, R. Heath, and M. Shah, "Abnormal pigmentation within cutaneous scars: A complication of wound healing," *Indian Journal of Plastic Surgery*, vol. 45, no. 02, pp. 403–411, 2012, ISSN: 0970-0358. DOI: 10.4103/0970-0358.101328.

[13] M. F. Jonkman, E. A. Hoeksma, and P. Nieuwenhuis, "Accelerated Epithelization Under a Highly Vapor-Permeable Wound Dressing Is Associated with Increased Precipitation of Fibrin(ogen) and Fibronectin," *Journal of Investigative Dermatology*, vol. 94, no. 4, pp. 477–484, 1990, ISSN: 0022202X. DOI: 10.1111/1523-1747.ep12874624.

[14] G. L. Brown, L. B. Nanney, J. Griffen, A. B. Cramer, J. M. Yancey, L. J. Curtsinger, L. Holtzin, G. S. Schultz, M. J. Jurkiewicz, and J. B. Lynch, "Enhancement of Wound Healing by Topical Treatment with Epidermal Growth Factor," *New England Journal of Medicine*, vol. 321, no. 2, pp. 76–79, 1989, ISSN: 0028-4793. DOI: 10.1056/NEJM198907133210203.

[15] I. H. Leigh and G Bennett, "Pressure ulcers: Prevalence, etiology, and treatment modalities," *The American Journal of Surgery*, vol. 167, no. 1, S25–S30, 1994, ISSN: 00029610. DOI: 10.1016/0002-9610(94)90007-8.

[16] S. R. Baker, *Local Flaps in Facial Reconstruction*, Second. Elsevier Inc., 2007, ISBN: 978-0-323-03684-9.

[17] K. W. Cox and W. Larrabee, "A Study of Skin Flap Advancement as a Function of Undermining," *Archives of Otolaryngology - Head and Neck Surgery*, vol. 108, no. 3, pp. 151–155, 1982, ISSN: 0886-4470. DOI: 10.1001/archotol.1982.00790510023005.

[18] W. F. Larrabee, G. A. Holloway, and D. Sutton, "Wound Tension and Blood Flow in Skin Flaps," *Annals of Otology, Rhinology & Laryngology*, vol. 93, no. 2, pp. 112–115, 1984, ISSN: 0003-4894. DOI: 10.1177/00034894840 9300202.

[19] C. Cacou, J. M. Anderson, and I. F. K. Muir, "Measurements of closing force of surgical wounds and relation to the appearance of resultant scars," *Medical & Biological Engineering & Computing*, vol. 32, no. 6, pp. 638–642, 1994, ISSN: 0140-0118. DOI: 10.1007/BF02524239.

[20] T. Gibson and R. Kenedi, "Biomechanical Properties of Skin," *Surgical Clinics of North America*, vol. 47, no. 2, pp. 279–294, 1967, ISSN: 00396109. DOI: 10.1016/S0039-6109(16)38180-4.

[21] Y. Akasaka, K. Fujita, Y. Ishikawa, N. Asuwa, K. Inuzuka, M. Ishihara, M. Ito, T. Masuda, Y. Akishima, L. Zhang, K. Ito, and T. Ishii, "Detection of apoptosis in keloids and a comparative study on apoptosis between keloids, hypertrophic scars, normal healed flat scars, and dermatofibroma," *Wound Repair and Regeneration*, vol. 9, no. 6, pp. 501–506, 2001, ISSN: 1067-1927. DOI: 10.1046/j.1524-475x.2001.00501.x.

[22] B. Brown, S. McKenna, K. Siddhi, D. McGrouther, and A. Bayat, "The hidden cost of skin scars: quality of life after skin scarring," *Journal of Plastic, Reconstructive & Aesthetic Surgery*, vol. 61, no. 9, pp. 1049–1058, 2008, ISSN: 17486815. DOI: 10.1016/j.bjps.2008.03.020.

[23] N. E. E. Van Loey and M. J. M. Van Son, "Psychopathology and Psychological Problems in Patients with Burn Scars," *American Journal of Clinical Dermatology*, vol. 4, no. 4, pp. 245–272, 2003, ISSN: 1175-0561. DOI: 10 .2165/00128071-200304040-00004.

[24] C. K. Sen, G. M. Gordillo, S. Roy, R. Kirsner, L. Lambert, T. K. Hunt, F. Gottrup, G. C. Gurtner, and M. T. Longaker, "Human skin wounds: A major and snowballing threat to public health and the economy," *Wound Repair and Regeneration*, vol. 17, no. 6, pp. 763–771, 2009, ISSN: 10671927. DOI: 10.1111/j.1524-475X.2009.00543.x.

[25] R. G. Wheeland, "Reconstruction of the Lower Lip and Chin Using Local and Random-Pattern Flaps," *The Journal of Dermatologic Surgery and Oncology*, vol. 17, no. 7, pp. 605–615, 1991, ISSN: 01480812. DOI: 10.1111 /j.1524-4725.1991.tb03660.x.

[26] J. D. Turissini, T. Elmarsafi, K. K. Evans, and P. J. Kim, "Major Risk Factors Contributing to Split Thickness Skin Graft Failure," *Georgetown Medical Review*, vol. 3, no. 1, pp. 1–11, 2019, ISSN: 2689-095X. DOI: 10.52504/001c.7755.

[27] J. Rustemeyer, L. Günther, and A. Bremerich, "Complications after nasal skin repair with local flaps and full-thickness skin grafts and implications of patients' contentment," *Oral and Maxillofacial Surgery*, vol. 13, no. 1, pp. 15–19, 2009, ISSN: 1865-1550. DOI: 10.1007/s10006-008-0139-z.

[28] J. P. Stone, C. Webb, J. G. McKinnon, J. C. Dawes, C. D. McKenzie, and C. F. Temple-Oberle, "Avoiding Skin Grafts," *Plastic and Reconstructive Surgery*, vol. 136, no. 2, pp. 404–408, 2015, ISSN: 0032-1052. DOI: 10.1097/PRS.0000000000001449.

[29] A. F. Borges and J. E. Alexander, "Relaxed skin tension lines, z-plasties on scars, and fusiform excision of lesions," *British Journal of Plastic Surgery*, vol. 15, no. C, pp. 242–254, 1962, ISSN: 00071226. DOI: 10.1016/S0007-1226(62)80038-1.

[30] W. E. Horner, "Art. V. Clinical Report on the Surgical Department of the Philadelphia Hospital, Blockley, for the months of May, June, and July, 1837.," *The American Journal of the Medical Sciences*, vol. 20, no. 41, pp. 99–112, 1837, ISSN: 0002-9629. DOI: 10.1097/00000441-183720410-00005.

[31] A. F. Borges and T. Gibson, "The original Z-plasty," *British Journal of Plastic Surgery*, vol. 26, no. 3, pp. 237–246, 1973, ISSN: 00071226. DOI: 10.1016/0007-1226(73)90008-8.

[32] S. L. McCurdy, "Z-plastic surgery: plastic operation to elongate cicatricial contraction of the neck, lips, and eyelids and across joints," *Surgery, Gynecology and Obstetrics*, vol. 16, pp. 209–212, 1913.

[33] A. A. Limberg, *Skin Plastic with Shifting Triangle Flaps*. Leningrad: Traumatological Institute, 1929, p. 862.

[34] J. S. Davis, "The Relaxation of Scar Contractures by Means of the Z-, or Reversed Z-type Incision," *Annals of Surgery*, vol. 94, no. 5, pp. 871–884, 1931, ISSN: 0003-4932. DOI: 10.1097/00000658-193111000-00006.

[35] A. A. Limberg, *Planimetrie Und Stereometrie Der Hautplastik*. Gustav Fischer Verlag, Jena, 1967, vol. 43.

[36] C. R. Hove, E. F. Williams, III, and B. J. Rodgers, "Z-Plasty: A Concise Review," *Facial Plastic Surgery*, vol. 17, no. 04, pp. 289–294, 2001, ISSN: 07366825. DOI: 10.1055/s-2001-18828.

[37] H. Koyama and R. Fujimori, "V-W Plasty," *Annals of Plastic Surgery*, vol. 9, no. 3, pp. 216–220, 1982, ISSN: 0148-7043. DOI: 10.1097/00000637-198209000-00004.

[38] N. Karacaoglan and A. Uysal, "The seven flap-plasty," *British Journal of Plastic Surgery*, vol. 47, no. 5, pp. 372–374, 1994, ISSN: 00071226. DOI: 10.1016/0007-1226(94)90098-1.

[39] R. C. Webster, T. M. Davidson, and R. C. Smith, "The Thirty Degree Transposition Flap," *The Laryngoscope*, vol. 88, no. 1, pp. 85–94, 1978, ISSN: 0023852X. DOI: 10.1002/lary.1978.88.1.85.

[40] J. L. Cook, "Reconstructive Utility of the Bilobed Flap," *Dermatologic Surgery*, vol. 31, no. s2, pp. 1024–1033, 2005, ISSN: 1076-0512. DOI: 10.1111/j.1524-4725.2005.31827.

[41] E. G. Zook, A. L. Van Beek, R. C. Russell, and J. B. Moore, "V-Y Advancement Flap for Facial Defects," *Plastic and Reconstructive Surgery*, vol. 65, no. 6, pp. 786–797, 1980, ISSN: 0032-1052. DOI: 10.1097/00006534-198006000-00011.

[42] R. J. Rohrich and I. Ross Zbar, "A Simplified Algorithm for the Use of Z-plasty," *Plastic and Reconstructive Surgery*, vol. 103, no. 5, pp. 1513–1517, 1999.

[43] T. Humphreys, "Cutaneous Flaps," in *Skin Cancer Management*, New York, NY: Springer New York, 2009, pp. 153–178. DOI: 10.1007/978-0-387-88495-0_12.

[44] G. Hundeshagen, R. Zapata-Sirvent, J. Goverman, and L. K. Branski, "Tissue Rearrangements," *Clinics in Plastic Surgery*, vol. 44, no. 4, pp. 805–812, 2017, ISSN: 00941298. DOI: 10.1016/j.cps.2017.05.011.

[45] J. E. Leedy, J. E. Janis, and R. J. Rohrich, "Reconstruction of Acquired Scalp Defects: An Algorithmic Approach," *Plastic and Reconstructive Surgery*, vol. 116, no. 4, 54e–72e, 2005, ISSN: 0032-1052. DOI: 10.1097/01.prs.0000179188.25019.6c.

[46] V. M. Grishkevich, "The post-burn elbow medial flexion scar contracture treatment with trapeze-flap plasty," *Burns*, vol. 35, no. 2, pp. 280–287, 2009, ISSN: 03054179. DOI: 10.1016/j.burns.2008.06.001.

[47] J. S. Davis and E. A. Kitlowski, "The Theory and Practical Use of the Z-Incision for the Relief of Scar Contractures," *Annals of Surgery*, vol. 109, no. 6, pp. 1001–1015, 1939, ISSN: 0003-4932. DOI: 10.1097/00000658-193906000-00012.

[48] I. A. McGregor, "The theoretical basis of the z-plasty," *British Journal of Plastic Surgery*, vol. 9, pp. 256–259, 1956, ISSN: 00071226. DOI: 10.1016/S0007-1226(56)80048-9.

[49] D. W. Furnas, "The Tetrahedral Z-Plasty," *Plastic and Reconstructive Surgery*, vol. 35, no. 3, pp. 291–302, 1965.

[50] D. W. Furnas and G. W. Fischer, "The Z-plasty: Biomechanics and mathematics," *British Journal of Plastic Surgery*, vol. 24, no. C, pp. 144–160, 1971, ISSN: 00071226. DOI: 10.1016/S0007-1226(71)80034-6.

[51] D. Danielson and S. Natarajan, "Tension field theory and the stress in stretched skin," *Journal of Biomechanics*, vol. 8, no. 2, pp. 135–142, 1975, ISSN: 00219290. DOI: 10.1016/0021-9290(75)90094-9.

[52] O. Zienkiewicz, R. Taylor, and D. Fox, *The Finite Element Method for Solid and Structural Mechanics*, E. Ltd, Ed. Elsevier, 2014, p. 624, ISBN: 978-1-856-17634-7. DOI: 10.1016/C2009-0-26332-X.

[53] P. H. DeHoff and J. E. Key, "Application of the finite element analysis to determine forces and stresses in wound closing," *Journal of Biomechanics*, vol. 14, no. 8, pp. 549–554, 1981, ISSN: 00219290. DOI: 10.1016/0021-9290(81)90004-X.

[54] D. Lott-Crumpler and H. Chaudhry, "Optimal patterns for suturing wounds of complex shapes to foster healing," *Journal of Biomechanics*, vol. 34, no. 1, pp. 51–58, 2001, ISSN: 00219290. DOI: 10.1016/S0021-9290(00)00160-3.

[55] H. Kawabata, H. Kawai, K. Masada, and K. Ono, "Computer-Aided Analysis of Z-Plasties," *Plastic and Reconstructive Surgery*, vol. 83, no. 2, pp. 319–325, 1989, ISSN: 0032-1052. DOI: 10.1097/00006534-198902000-00022.

[56] S. G. Topp, S. Lovald, T. Khraishi, and C. W. Gaball, "Biomechanics of the Rhombic Transposition Flap," *Otolaryngology–Head and Neck Surgery*, vol. 151, no. 6, pp. 952–959, 2014, ISSN: 0194-5998. DOI: 10.1177/0194599814551128.

[57] A. Rajabi, A. T. Dolovich, and J. Johnston, "From the rhombic transposition flap toward Z-plasty: An optimized design using the finite element method," *Journal of Biomechanics*, vol. 48, no. 13, pp. 3672–3678, 2015, ISSN: 00219290. DOI: 10.1016/j.jbiomech.2015.08.021.

[58] C. Stowers, T. Lee, I. Bilionis, A. K. Gosain, and A. B. Tepole, "Improving reconstructive surgery design using Gaussian process surrogates to capture material behavior uncertainty," *Journal of the Mechanical Behavior of Biomedical Materials*, vol. 118, p. 104 340, 2021, ISSN: 17516161. DOI: 10.1016/j.jmbbm.2021.104340. arXiv: 2010.02800.

[59] T. Lee, A. K. Gosain, I. Bilionis, and A. B. Tepole, "Predicting the effect of aging and defect size on the stress profiles of skin from advancement, rotation and transposition flap surgeries," *Journal of the Mechanics and Physics of Solids*, vol. 125, pp. 572–590, 2019, ISSN: 00225096. DOI: 10.1016/j.jmps.2019.01.012.

[60] Y. Lanir and Y. Fung, "Two-dimensional mechanical properties of rabbit skin—II. Experimental results," *Journal of Biomechanics*, vol. 7, no. 2, pp. 171–182, 1974, ISSN: 00219290. DOI: 10.1016/0021-9290(74)90058-X.

[61] R. Minns, P. Soden, and D. Jackson, "The role of the fibrous components and ground substance in the mechanical properties of biological tissues: A preliminary investigation," *Journal of Biomechanics*, vol. 6, no. 2, pp. 153–165, 1973, ISSN: 00219290. DOI: 10.1016/0021-9290(73)90084-5.

[62] V. R. Sherman, W. Yang, and M. A. Meyers, "The materials science of collagen," *Journal of the Mechanical Behavior of Biomedical Materials*, vol. 52, pp. 22–50, 2015, ISSN: 17516161. DOI: 10.1016/j.jmbbm.2015.05.023.

[63] R. B. Groves, S. A. Coulman, J. C. Birchall, and S. L. Evans, "An anisotropic, hyperelastic model for skin: Experimental measurements, finite element modelling and identification of parameters for human and murine skin," *Journal of the Mechanical Behavior of Biomedical Materials*, vol. 18, pp. 167–180, 2013, ISSN: 17516161. DOI: 10.1016/j.jmbbm.2012.10.021.

[64] W. Yang, V. R. Sherman, B. Gludovatz, E. Schaible, P. Stewart, R. O. Ritchie, and M. A. Meyers, "On the tear resistance of skin," *Nature Communications*, vol. 6, no. 1, p. 6649, 2015, ISSN: 2041-1723. DOI: 10.1038/ncomms7649.

[65] I. A. Brown, "A scanning electron microscope study of the effects of uniaxial tension on human skin," *British Journal of Dermatology*, vol. 89, no. 4, pp. 383–393, 1973, ISSN: 00070963. DOI: 10.1111/j.1365-2133.1973.tb02993.x.

[66] S. Bancelin, B. Lynch, C. Bonod-Bidaud, G. Ducourthial, S. Psilodimitrakopoulos, P. Dokládal, J.-M. Allain, M.-C. Schanne-Klein, and F. Ruggiero, "Ex vivo multiscale quantitation of skin biomechanics in wild-type and genetically-modified mice using multiphoton microscopy," *Scientific Reports*, vol. 5, no. 1, p. 17 635, 2015, ISSN: 2045-2322. DOI: 10.1038/srep17635.

[67] M. L. Crichton, B. C. Donose, X. Chen, A. P. Raphael, H. Huang, and M. A. Kendall, "The viscoelastic, hyperelastic and scale dependent behaviour of freshly excised individual skin layers," *Biomaterials*, vol. 32, no. 20, pp. 4670–4681, 2011, ISSN: 01429612. DOI: 10.1016/j.biomaterials.2011.03.012.

[68] R. Massabò and L. Gambarotta, "Wrinkling of Plane Isotropic Biological Membranes," *Journal of Applied Mechanics*, vol. 74, no. 3, pp. 550–559, 2007, ISSN: 0021-8936. DOI: 10.1115/1.2424240.

[69] M. Mooney, "A Theory of Large Elastic Deformation," *Journal of Applied Physics*, vol. 11, no. 9, pp. 582–592, 1940, ISSN: 0021-8979. DOI: 10.1063/1.1712836.

[70] O. H. Yeoh, "Characterization of Elastic Properties of Carbon-Black-Filled Rubber Vulcanizates," *Rubber Chemistry and Technology*, vol. 63, no. 5, pp. 792–805, 1990, ISSN: 1943-4804. DOI: 10.5254/1.3538289.

[71] R. W. Ogden, "Large deformation isotropic elasticity – on the correlation of theory and experiment for incompressible rubberlike solids," *Proceedings of the Royal Society of London. A. Mathematical and Physical Sciences*, vol. 326, no. 1567, pp. 565–584, 1972, ISSN: 0080-4630. DOI: 10.1098/rspa.1972.0026.

[72] S. L. Evans and C. A. Holt, "Measuring the mechanical properties of human skin in vivo using digital image correlation and finite element modelling," *The Journal of Strain Analysis for Engineering Design*, vol. 44, no. 5, pp. 337–345, 2009, ISSN: 0309-3247. DOI: 10.1243/03093247JSA488.

[73] M. F. Leyva-Mendivil, A. Page, N. W. Bressloff, and G. Limbert, "A mechanistic insight into the mechanical role of the stratum corneum during stretching and compression of the skin," *Journal of the Mechanical Behavior of Biomedical Materials*, vol. 49, pp. 197–219, 2015, ISSN: 17516161. DOI: 10.1016/j.jmbbm.2015.05.010.

[74] Z. Kwan, N. N. Khairu Najhan, Y. H. Yau, Y. Luximon, and F. M Nor, "Anticipating local flaps closed-form solution on 3D face models using finite element method," *International Journal for Numerical Methods in Biomedical Engineering*, vol. 36, no. 11, pp. 1–16, 2020, ISSN: 20407947. DOI: 10.1002/cnm.3390.

[75] Y. Fung, "Elasticity of soft tissues in simple elongation," *American Journal of Physiology-Legacy Content*, vol. 213, no. 6, pp. 1532–1544, 1967, ISSN: 0002-9513. DOI: 10.1152/ajplegacy.1967.213.6.1532.

[76] P. Tong and Y.-C. Fung, "The stress-strain relationship for the skin," *Journal of Biomechanics*, vol. 9, no. 10, pp. 649–657, 1976, ISSN: 00219290. DOI: 10.1016/0021-9290(76)90107-X.

[77] Y. Lanir, "Constitutive equations for fibrous connective tissues," *Journal of Biomechanics*, vol. 16, no. 1, pp. 1–12, 1983, ISSN: 00219290. DOI: 10.1016/0021-9290(83)90041-6.

[78] T. C. Gasser, R. W. Ogden, and G. A. Holzapfel, "Hyperelastic modelling of arterial layers with distributed collagen fibre orientations," *Journal of The Royal Society Interface*, vol. 3, no. 6, pp. 15–35, 2006, ISSN: 1742-5689. DOI: 10.1098/rsif.2005.0073.

[79] G. A. Holzapfel and R. W. Ogden, "On Fiber Dispersion Models: Exclusion of Compressed Fibers and Spurious Model Comparisons," *Journal of Elasticity*, vol. 129, no. 1-2, pp. 49–68, 2017, ISSN: 0374-3535. DOI: 10.1007/s10659-016-9605-2.

[80] G. A. Holzapfel, J. A. Niestrawska, R. W. Ogden, A. J. Reinisch, and A. J. Schriefl, "Modelling non-symmetric collagen fibre dispersion in arterial walls," *Journal of The Royal Society Interface*, vol. 12, no. 106, p. 20 150 188, 2015, ISSN: 1742-5689. DOI: 10.1098/rsif.2015.0188.

[81] SIMULIA, *Abaqus 6.14 Online Documentation*, 2016.

[82] D. G. Roddeman, J. Drukker, C. W. J. Oomens, and J. D. Janssen, "The Wrinkling of Thin Membranes: Part I—Theory," *Journal of Applied Mechanics*, vol. 54, no. 4, pp. 884–887, 1987, ISSN: 0021-8936. DOI: 10.1115/1.3173133.

[83] A. Jarasjarungkiat, R. Wüchner, and K.-U. Bletzinger, "A wrinkling model based on material modification for isotropic and orthotropic membranes," *Computer Methods in Applied Mechanics and Engineering*, vol. 197, no. 6-8, pp. 773–788, 2008, ISSN: 00457825. DOI: 10.1016/j.cma.2007.09.005.

[84] K. Li, R. W. Ogden, and G. A. Holzapfel, "Modeling fibrous biological tissues with a general invariant that excludes compressed fibers," *Journal of the Mechanics and Physics of Solids*, vol. 110, pp. 38–53, 2018, ISSN: 00225096. DOI: 10.1016/j.jmps.2017.09.005.

[85] A. V. Melnik, H. Borja Da Rocha, and A. Goriely, "On the modeling of fiber dispersion in fiber-reinforced elastic materials," *International Journal of Non-Linear Mechanics*, vol. 75, pp. 92–106, 2015, ISSN: 00207462. DOI: 10.1016/j.ijnonlinmec.2014.10.006.

[86] M. Latorre and F. J. Montáns, "On the tension-compression switch of the Gasser–Ogden–Holzapfel model: Analysis and a new pre-integrated proposal," *Journal of the Mechanical Behavior of Biomedical Materials*, vol. 57, pp. 175–189, 2016, ISSN: 1751-6161. DOI: 10.1016/J.JMBBM.2015.11.018.

[87] K. Li, R. W. Ogden, and G. A. Holzapfel, "A discrete fibre dispersion method for excluding fibres under compression in the modelling of fibrous tissues," *Journal of The Royal Society Interface*, vol. 15, no. 138, p. 20 170 766, 2018, ISSN: 1742-5689. DOI: 10.1098/rsif.2017.0766.

[88] M. Rolf-Pissarczyk, M. P. Wollner, D. R. Q. Pacheco, and G. A. Holzapfel, "Efficient computational modelling of smooth muscle orientation and function in the aorta," *Proceedings of the Royal Society A: Mathematical, Physical and Engineering Sciences*, vol. 477, no. 2255, 2021, ISSN: 1364-5021. DOI: 10.1098/rspa.2021.0592.

[89] R. B. Groves, S. A. Coulman, J. C. Birchall, and S. L. Evans, "Quantifying the mechanical properties of human skin to optimise future microneedle device design," *Computer Methods in Biomechanics and Biomedical Engineering*, vol. 15, no. 1, pp. 73–82, 2012, ISSN: 1025-5842. DOI: 10.1080/10255842.2011.596481.

[90] H. Wei, X. Liu, L. Li, C. Li, W. Chen, S. Wang, Z. Wang, and J. Ma, "Visual indentation apparatus and finite element modelling as a method to characterize 3D mechanical properties of facial skin in vivo," *Mechanics of Materials*, vol. 157, p. 103 852, 2021, ISSN: 01676636. DOI: 10.1016/j.mechmat.2021.103852.

[91] S. Luebberding, N. Krueger, and M. Kerscher, "Mechanical properties of human skin in vivo : a comparative evaluation in 300 men and women," *Skin Research and Technology*, vol. 20, no. 2, pp. 127–135, 2014, ISSN: 0909-752X. DOI: 10.1111/srt.12094.

[92] J. Weickenmeier, M. Jabareen, and E. Mazza, "Suction based mechanical characterization of superficial facial soft tissues," *Journal of Biomechanics*, vol. 48, no. 16, pp. 4279–4286, 2015, ISSN: 00219290. DOI: 10.1016/j.jbiomech.2015.10.039.

[93] M. A. Kirby, P. Tang, H.-C. Liou, M. Kuriakose, J. J. Pitre, T. N. Pham, R. E. Ettinger, R. K. Wang, M. O'Donnell, and I. Pelivanov, "Probing elastic anisotropy of human skin in vivo with light using non-contact acoustic micro-tapping OCE and polarization sensitive OCT," *Scientific Reports*, vol. 12, no. 1, p. 3963, 2022, ISSN: 2045-2322. DOI: 10.1038/s41598-022-07775-3.

[94] M. Nagle, S. Price, A. Trotta, M. Destrade, M. Fop, and A. Ní Annaidh, "Analysis of In Vivo Skin Anisotropy Using Elastic Wave Measurements and Bayesian Modelling," *Annals of Biomedical Engineering*, vol. 51, no. 8, pp. 1781–1794, 2023, ISSN: 0090-6964. DOI: 10.1007/s10439-023-03185-2.

[95] Y. A. Kvistedal and P. M. F. Nielsen, "Estimating material parameters of human skin in vivo," *Biomechanics and Modeling in Mechanobiology*, vol. 8, no. 1, pp. 1–8, 2009, ISSN: 1617-7959. DOI: 10.1007/s10237-007-0112-z.

[96] C. Flynn, A. Taberner, and P. Nielsen, "Mechanical characterisation of in vivo human skin using a 3D force-sensitive micro-robot and finite element analysis," *Biomechanics and Modeling in Mechanobiology*, vol. 10, no. 1, pp. 27–38, 2011, ISSN: 1617-7959. DOI: 10.1007/s10237-010-0216-8.

[97] J. W. Jor, M. D. Parker, A. J. Taberner, M. P. Nash, and P. M. Nielsen, "Computational and experimental characterization of skin mechanics: identifying current challenges and future directions," *Wiley Interdisciplinary Reviews: Systems Biology and Medicine*, vol. 5, no. 5, pp. 539–556, 2013, ISSN: 19395094. DOI: 10.1002/wsbm.1228.

[98] H. Joodaki and M. B. Panzer, "Skin mechanical properties and modeling: A review," *Proceedings of the Institution of Mechanical Engineers, Part H: Journal of Engineering in Medicine*, vol. 232, no. 4, pp. 323–343, 2018, ISSN: 0954-4119. DOI: 10.1177/0954411918759801.

[99] N. Kumaraswamy, H. Khatam, G. P. Reece, M. C. Fingeret, M. K. Markey, and K. Ravi-Chandar, "Mechanical response of human female breast skin under uniaxial stretching," *Journal of the Mechanical Behavior of Biomedical Materials*, vol. 74, pp. 164–175, 2017, ISSN: 17516161. DOI: 10.1016/j.jmbbm.2017.05.027.

[100] S. J. Mostafavi Yazdi and J. Baqersad, "Mechanical modeling and characterization of human skin: A review," *Journal of Biomechanics*, vol. 130, p. 110 864, 2022, ISSN: 00219290. DOI: 10.1016/j.jbiomech.2021.110864.

[101] G. A. Holzapfel and R. W. Ogden, "On planar biaxial tests for anisotropic nonlinearly elastic solids. A continuum mechanical framework," *Mathematics and Mechanics of Solids*, vol. 14, no. 5, pp. 474–489, 2009, ISSN: 1081-2865. DOI: 10.1177/1081286507084411.

[102] H. Fehervary, M. Smoljkić, J. Vander Sloten, and N. Famaey, "Planar biaxial testing of soft biological tissue using rakes: A critical analysis of protocol and fitting process," *Journal of the Mechanical Behavior of Biomedical Materials*, vol. 61, pp. 135–151, 2016, ISSN: 17516161. DOI: 10.1016/j.jmbbm.2016.01.011.

[103] J. A. Niestrawska, C. Viertler, P. Regitnig, T. U. Cohnert, G. Sommer, and G. A. Holzapfel, "Microstructure and mechanics of healthy and aneurysmatic abdominal aortas: experimental analysis and modelling," *Journal of The Royal Society Interface*, vol. 13, no. 124, p. 20 160 620, 2016, ISSN: 1742-5689. DOI: 10.1098/rsif.2016.0620.

[104] C. Laville, C. Pradille, and Y. Tillier, "Mechanical characterization and identification of material parameters of porcine aortic valve leaflets," *Journal of the Mechanical Behavior of Biomedical Materials*, vol. 112, p. 104 036, 2020, ISSN: 17516161. DOI: 10.1016/j.jmbbm.2020.104036.

[105] M. J. Sadeghinia, B. Skallerud, G. A. Holzapfel, and V. Prot, "Biomechanics of mitral valve leaflets: Second harmonic generation microscopy, biaxial mechanical tests and tissue modeling," *Acta Biomaterialia*, vol. 141, pp. 244–254, 2022, ISSN: 17427061. DOI: 10.1016/j.actbio.2022.01.003.

[106] W. D. Meador, G. P. Sugerman, H. M. Story, A. W. Seifert, M. R. Bersi, A. B. Tepole, and M. K. Rausch, "The regional-dependent biaxial behavior of young and aged mouse skin: A detailed histomechanical characterization, residual strain analysis, and constitutive model," *Acta Biomaterialia*,

vol. 101, pp. 403–413, 2020, ISSN: 17427061. DOI: 10.1016/j.actbio.2019.10.020.

[107] B. L. Wen, M. A. Brewer, O. Nadiarnykh, J. Hocker, V. Singh, T. R. Mackie, and P. J. Campagnola, "Texture analysis applied to second harmonic generation image data for ovarian cancer classification," *Journal of Biomedical Optics*, vol. 19, no. 9, p. 096 007, 2014, ISSN: 1083-3668. DOI: 10.1117/1.JBO.19.9.096007.

[108] Z. Püspöki, M. Storath, D. Sage, and M. Unser, "Transforms and Operators for Directional Bioimage Analysis: A Survey," in *Focus on Bio-Image Informatics*, vol. 219, Springer International Publishing, 2016, pp. 69–93, ISBN: 9783319285498. DOI: 10.1007/978-3-319-28549-8_3.

[109] K. P. Quinn and I. Georgakoudi, "Rapid quantification of pixel-wise fiber orientation data in micrographs," *Journal of Biomedical Optics*, vol. 18, no. 4, p. 046 003, 2013, ISSN: 1083-3668. DOI: 10.1117/1.JBO.18.4.046003.

[110] O. S. Osman, J. L. Selway, P. E. Harikumar, C. J. Stocker, E. T. Wargent, M. A. Cawthorne, S. Jassim, and K. Langlands, "A novel method to assess collagen architecture in skin," *BMC Bioinformatics*, vol. 14, no. 1, pp. 1–10, 2013, ISSN: 14712105. DOI: 10.1186/1471-2105-14-260/TABLES/2.

[111] Y. Mega, M. Robitaille, R. Zareian, J. McLean, J. Ruberti, and C. DiMarzio, "Quantification of lamellar orientation in corneal collagen using second harmonic generation images," *Optics Letters*, vol. 37, no. 16, p. 3312, 2012, ISSN: 0146-9592. DOI: 10.1364/OL.37.003312.

[112] M. Witte, S. Jaspers, H. Wenck, M. Rübhausen, and F. Fischer, "Noise reduction and quantification of fiber orientations in greyscale images," *PLOS ONE*, vol. 15, no. 1, W. Speier, Ed., e0227534, 2020, ISSN: 1932-6203. DOI: 10.1371/journal.pone.0227534.

[113] J. P. McLean, Y. Gan, T. H. Lye, D. Qu, H. H. Lu, and C. P. Hendon, "High-speed collagen fiber modeling and orientation quantification for optical coherence tomography imaging," *Optics Express*, vol. 27, no. 10, pp. 14 457–14 471, 2019, ISSN: 1094-4087. DOI: 10.1364/OE.27.014457.

[114] Z. Liu, D. Pouli, D. Sood, A. Sundarakrishnan, C. K. Hui Mingalone, L. M. Arendt, C. Alonzo, K. P. Quinn, C. Kuperwasser, L. Zeng, T. Schnelldorfer, D. L. Kaplan, and I. Georgakoudi, "Automated quantification of three-dimensional organization of fiber-like structures in biological tissues,"

Biomaterials, vol. 116, pp. 34–47, 2017, ISSN: 01429612. DOI: 10.1016/j.biomaterials.2016.11.041.

[115] T. Y. Lau, R. Ambekar, and K. C. Toussaint, "Quantification of collagen fiber organization using three-dimensional Fourier transform-second-harmonic generation imaging," *Optics Express*, vol. 20, no. 19, p. 21 821, 2012, ISSN: 1094-4087. DOI: 10.1364/OE.20.021821.

[116] Z. Nejim, L. Navarro, C. Morin, and P. Badel, "Quantitative analysis of second harmonic generated images of collagen fibers: a review," *Research on Biomedical Engineering*, vol. 39, no. 1, pp. 273–295, 2022, ISSN: 2446-4740. DOI: 10.1007/s42600-022-00250-y.

[117] J. E. Lai-Cheong and J. A. McGrath, "Structure and function of skin, hair and nails," *Medicine*, vol. 41, no. 6, pp. 317–320, 2013, ISSN: 13573039. DOI: 10.1016/j.mpmed.2013.04.017.

[118] E. N. Marieb and K. Hoehn, *Human Anatomy & Physiology*, 11th ed. Upper Saddle River, NJ: Pearson, 2018, ISBN: 9780134580999.

[119] J. G. Betts, P. Desaix, and E. Johnson, *Layers Of Epidermis*, https://en.m.wikipedia.org/wiki/File:502_Layers_of_epidermis.jpg, 2013.

[120] O. Castaño, S. Pérez-Amodio, C. Navarro-Requena, M. Á. Mateos-Timoneda, and E. Engel, "Instructive microenvironments in skin wound healing: Biomaterials as signal releasing platforms," *Advanced Drug Delivery Reviews*, vol. 129, pp. 95–117, 2018, ISSN: 0169409X. DOI: 10.1016/j.addr.2018.03.012.

[121] M. W. King, *Extracellular Matrix (ECM)*, https://themedicalbiochemistrypage.org/extracellular-matrix-ecm/, 2023.

[122] L. E. Tracy, R. A. Minasian, and E. Caterson, "Extracellular Matrix and Dermal Fibroblast Function in the Healing Wound," *Advances in Wound Care*, vol. 5, no. 3, pp. 119–136, 2016, ISSN: 2162-1918. DOI: 10.1089/wound.2014.0561.

[123] J. M. Benítez and F. J. Montáns, "The mechanical behavior of skin: Structures and models for the finite element analysis," *Computers & Structures*, vol. 190, pp. 75–107, 2017, ISSN: 00457949. DOI: 10.1016/j.compstruc.2017.05.003.

[124] J. Uitto, D. R. Olsen, and M. J. Fazio, "Extracellular Matrix of the Skin: 50 Years of Progress," *Journal of Investigative Dermatology*, vol. 92, no. 4, S61–S77, 1989, ISSN: 0022202X. DOI: 10.1038/jid.1989.34.

[125] V. R. Sherman, Y. Tang, S. Zhao, W. Yang, and M. A. Meyers, "Structural characterization and viscoelastic constitutive modeling of skin.," *Acta biomaterialia*, vol. 53, pp. 460–469, 2017, ISSN: 1878-7568. DOI: 10.1016/j.actbio.2017.02.011.

[126] D. T. Corr and D. A. Hart, "Biomechanics of Scar Tissue and Uninjured Skin," *Advances in Wound Care*, vol. 2, no. 2, pp. 37–43, 2013, ISSN: 2162-1918. DOI: 10.1089/wound.2011.0321.

[127] H. Sorg, D. J. Tilkorn, S. Hager, J. Hauser, and U. Mirastschijski, "Skin Wound Healing: An Update on the Current Knowledge and Concepts," *European Surgical Research*, vol. 58, no. 1-2, pp. 81–94, 2017, ISSN: 0014-312X. DOI: 10.1159/000454919.

[128] P. Stell, "The effects of varying degrees of tension on the viability of skin flaps in pigs," *British Journal of Plastic Surgery*, vol. 33, no. 3, pp. 371–376, 1980, ISSN: 00071226. DOI: 10.1016/S0007-1226(80)90085-5.

[129] G. C. Gurtner, R. H. Dauskardt, V. W. Wong, K. A. Bhatt, K. Wu, I. N. Vial, K. Padois, J. M. Korman, and M. T. Longaker, "Improving Cutaneous Scar Formation by Controlling the Mechanical Environment," *Annals of Surgery*, vol. 254, no. 2, pp. 217–225, 2011, ISSN: 0003-4932. DOI: 10.1097/SLA.0b013e318220b159.

[130] S. W. Carmichael, "The tangled web of Langer's lines," *Clinical Anatomy*, vol. 27, no. 2, pp. 162–168, 2014, ISSN: 0897-3806. DOI: 10.1002/ca.22278.

[131] T. Goran, *Langer's lines female-male*, https://upload.wikimedia.org/wikipedia/commons/a/a2/Langer%27s_lines_female-male_front-back_3d-shaded.svg, Dec. 2021.

[132] K. Langer, "On the anatomy and physiology of the skin. I. The cleavability of the cutis. (Translated from Langer, K. (1861). Zur Anatomie und Physiologie der Haut. I. Uber die Spaltbarkeit der Cutis. Sitzungsbericht der Mathematisch-naturwissenschaftlichen Classe der Kaiserlichen Academie der Wissenschaften, 44, 19.)," *British journal of plastic surgery*, vol. 31, no. 1, pp. 3–8, 1978, ISSN: 0007-1226.

[133] S. P Paul, "Biodynamic Excisional Skin Tension (BEST) Lines: Revisiting Langer's Lines, Skin Biomechanics, Current Concepts in Cutaneous Surgery, and the (lack of) Science behind Skin Lines used for Surgical Excisions," *Journal of Dermatological Research*, vol. 2, no. 1, pp. 77–87, 2017, ISSN: 2413-8223. DOI: 10.17554/j.issn.2413-8223.2017.02.19.

[134] A. F. Borges, "Relaxed Skin Tension Lines (RSTL) versus Other Skin Lines," *Plastic and Reconstructive Surgery*, vol. 73, no. 1, pp. 144–150, 1984, ISSN: 0032-1052. DOI: 10.1097/00006534-198401000-00036.

[135] D. Veronda and R. Westmann, "Mechanical characterization of skin—Finite deformations," *Journal of Biomechanics*, vol. 3, no. 1, pp. 111–124, 1970, ISSN: 00219290. DOI: 10.1016/0021-9290(70)90055-2.

[136] C. H. Daly, "Biomechanical Properties of Dermis," *Journal of Investigative Dermatology*, vol. 79, no. 1, pp. 17–20, 1982, ISSN: 0022202X. DOI: 10.1038/jid.1982.4.

[137] H. Oxlund, J. Manschot, and A. Viidik, "The role of elastin in the mechanical properties of skin," *Journal of Biomechanics*, vol. 21, no. 3, pp. 213–218, 1988, ISSN: 00219290. DOI: 10.1016/0021-9290(88)90172-8.

[138] H. Eshel and Y. Lanir, "Effects of strain level and proteoglycan depletion on preconditioning and viscoelastic responses of rat dorsal skin," *Annals of Biomedical Engineering*, vol. 29, no. 2, pp. 164–172, 2001, ISSN: 00906964. DOI: 10.1114/1.1349697.

[139] Z Liu, K Yeung, and Z. Liu, "The Preconditioning and Stress Relaxation of Skin Tissue," *Journal of Biomedical & Pharmaceutical Engineering*, vol. 2, pp. 22–28, 2008, ISSN: 1793-4532.

[140] O. A. Shergold, N. A. Fleck, and D. Radford, "The uniaxial stress versus strain response of pig skin and silicone rubber at low and high strain rates," *International Journal of Impact Engineering*, vol. 32, no. 9, pp. 1384–1402, 2006, ISSN: 0734743X. DOI: 10.1016/j.ijimpeng.2004.11.010.

[141] B. Zhou, F. Xu, C. Q. Chen, and T. J. Lu, "Strain rate sensitivity of skin tissue under thermomechanical loading," *Philosophical Transactions of the Royal Society A: Mathematical, Physical and Engineering Sciences*, vol. 368, no. 1912, pp. 679–690, 2010, ISSN: 1364-503X. DOI: 10.1098/rsta.2009.0238.

[142] B. Lynch, C. Bonod-Bidaud, G. Ducourthial, J.-S. Affagard, S. Bancelin, S. Psilodimitrakopoulos, F. Ruggiero, J.-M. Allain, and M.-C. Schanne-Klein, "How aging impacts skin biomechanics: a multiscale study in mice," *Scientific Reports*, vol. 7, no. 1, p. 13 750, 2017, ISSN: 2045-2322. DOI: 10.1038/s41598-017-13150-4.

[143] A. Wahlsten, A. Stracuzzi, I. Lüchtefeld, G. Restivo, N. Lindenblatt, C. Giampietro, A. E. Ehret, and E. Mazza, "Multiscale mechanical analysis of the elastic modulus of skin," *Acta Biomaterialia*, vol. 170, pp. 155–168, 2023, ISSN: 17427061. DOI: 10.1016/j.actbio.2023.08.030.

[144] A. Pissarenko, W. Yang, H. Quan, K. A. Brown, A. Williams, W. G. Proud, and M. A. Meyers, "Tensile behavior and structural characterization of pig dermis," *Acta Biomaterialia*, vol. 86, pp. 77–95, 2019, ISSN: 17427061. DOI: 10.1016/j.actbio.2019.01.023.

[145] A. Ní Annaidh, K. Bruyère, M. Destrade, M. D. Gilchrist, and M. Otténio, "Characterization of the anisotropic mechanical properties of excised human skin," *Journal of the Mechanical Behavior of Biomedical Materials*, vol. 5, no. 1, pp. 139–148, 2012, ISSN: 17516161. DOI: 10.1016/j.jmbbm.2011.08.016.

[146] A. Ní Annaidh, K. Bruyère, M. Destrade, M. D. Gilchrist, C. Maurini, M. Otténio, and G. Saccomandi, "Automated Estimation of Collagen Fibre Dispersion in the Dermis and its Contribution to the Anisotropic Behaviour of Skin," *Annals of Biomedical Engineering*, vol. 40, no. 8, pp. 1666–1678, 2012, ISSN: 0090-6964. DOI: 10.1007/s10439-012-0542-3. arXiv: 1203.4733.

[147] P. Berger, "Autoplastie par dèdoublement de la palmure et echange de lambeaux," *Chirurgie de l'Orthopédique*, vol. 16, pp. 180–185, 1904.

[148] J. S. Davis, "Present Evaluation of the Merits of the Z-plastic Operation," *Plastic and Reconstructive Surgery*, vol. 1, no. 1, pp. 26–38, 1946, ISSN: 0032-1052. DOI: 10.1097/00006534-194607000-00003.

[149] A. A. Limberg, "Mathematical principles of local plastic procedures on the surface of the human body," *Leningrad: Medgis*, 1946.

[150] H. Hyakusoku and M. Fumiiri, "The square flap method," *British Journal of Plastic Surgery*, vol. 40, no. 1, pp. 40–46, 1987, ISSN: 00071226. DOI: 10.1016/0007-1226(87)90009-9.

[151] D. A. Hudson, "Some Thoughts on Choosing a Z-Plasty: The Z Made Simple," *Plastic and Reconstructive Surgery*, vol. 106, no. 3, pp. 665–671, 2000, ISSN: 0032-1052. DOI: 10.1097/00006534-200009030-00024.

[152] E. Roggendorf, "The Planimetric Z-Plasty," *Plastic and Reconstructive Surgery*, vol. 71, no. 6, pp. 834–842, 1983, ISSN: 0032-1052. DOI: 10.1097/00006534-198306000-00018.

[153] S. Suzuki, K. Matsuda, and Y. Nishimura, "Proposal for a New Comprehensive Classification of V-Y Plasty and Its Analogues: The Pros and Cons of Inverted versus Ordinary Burow's Triangle Excision," *Plastic and Reconstructive Surgery*, vol. 98, no. 6, pp. 1016–1022, 1996, ISSN: 0032-1052. DOI: 10.1097/00006534-199611000-00014.

[154] G. Lister and T. Gibson, "Closure of rhomboid skin defects: The flaps of Limberg and Dufourmentel," *British Journal of Plastic Surgery*, vol. 25, no. C, pp. 300–314, 1972, ISSN: 00071226. DOI: 10.1016/S0007-1226(72)80067-5.

[155] C Dufourmentel, "An L-shaped flap for lozenge shaped defects. Principle-Technique-Application," *Trans. Third Internat. Cong. Plast. Surg.*, pp. 772–773, 1964.

[156] G. Holzapfel, *Nonlinear Solid Mechanics: A Continuum Approach for Engineering Science*. John Wiley & Sons, 2000, vol. 37, pp. 489–490, ISBN: 047182304X. DOI: https://doi.org/10.1023/A:1020843529530.

[157] J. Marsden and T. Hughes, *Mathematical Foundations of Elasticity* (Dover Civil and Mechanical Engineering Series). Dover, 1994, ISBN: 978-0-486-67865-8.

[158] D. Balzani, P. Neff, J. Schröder, and G. Holzapfel, "A polyconvex framework for soft biological tissues. Adjustment to experimental data," *International Journal of Solids and Structures*, vol. 43, no. 20, pp. 6052–6070, 2006, ISSN: 00207683. DOI: 10.1016/j.ijsolstr.2005.07.048.

[159] C. Truesdell and W. Noll, *The Non-Linear Field Theories of Mechanics / Die Nicht-Linearen Feldtheorien der Mechanik* (Encyclopedia of Physics / Handbuch der Physik 3). Berlin, Heidelberg: Springer Berlin Heidelberg, 1965, vol. 2 / 3 / 3, pp. 638–640, ISBN: 978-3-642-46017-3. DOI: 10.1007/978-3-642-46015-9.

[160] S. J. Connolly, D. Mackenzie, and Y. Gorash, "Isotropic hyperelasticity in principal stretches: explicit elasticity tensors and numerical implementation," *Computational Mechanics*, vol. 64, no. 5, pp. 1273–1288, 2019, ISSN: 0178-7675. DOI: 10.1007/s00466-019-01707-1.

[161] G. A. Holzapfel, T. C. Gasser, and R. W. Ogden, "A New Constitutive Framework for Arterial Wall Mechanics and a Comparative Study of Material Models," *Journal of elasticity and the physical science of solids 2000 61:1*, vol. 61, no. 1, pp. 1–48, 2000, ISSN: 1573-2681. DOI: 10.1023/a:1010835316564.

[162] J. Kiendl, M.-C. Hsu, M. C. Wu, and A. Reali, "Isogeometric Kirchhoff–Love shell formulations for general hyperelastic materials," *Computer Methods in Applied Mechanics and Engineering*, vol. 291, pp. 280–303, 2015, ISSN: 00457825. DOI: 10.1016/j.cma.2015.03.010.

[163] X. F. Wang, Q. S. Yang, and S.-s. Law, "Wrinkled membrane element based on the wrinkling potential," *International Journal of Solids and Structures*, vol. 51, no. 21-22, pp. 3532–3548, 2014, ISSN: 00207683. DOI: 10.1016/j.ijsolstr.2014.06.004.

[164] T. Iwasa, M. C. Natori, and K. Higuchi, "Evaluation of Tension Field Theory for Wrinkling Analysis With Respect to the Post-Buckling Study," *Journal of Applied Mechanics*, vol. 71, no. 4, pp. 532–540, 2004, ISSN: 0021-8936. DOI: 10.1115/1.1767171.

[165] V. Nayyar, K. Ravi-Chandar, and R. Huang, "Stretch-induced stress patterns and wrinkles in hyperelastic thin sheets," *International Journal of Solids and Structures*, vol. 48, no. 25-26, pp. 3471–3483, 2011, ISSN: 00207683. DOI: 10.1016/j.ijsolstr.2011.09.004.

[166] C. Fu, T. Wang, F. Xu, Y. Huo, and M. Potier-Ferry, "A modeling and resolution framework for wrinkling in hyperelastic sheets at finite membrane strain," *Journal of the Mechanics and Physics of Solids*, vol. 124, pp. 446–470, 2019, ISSN: 00225096. DOI: 10.1016/j.jmps.2018.11.005.

[167] L. Gambarotta, R. Massabò, R. Morbiducci, E. Raposio, and P. Santi, "In vivo experimental testing and model identification of human scalp skin," *Journal of Biomechanics*, vol. 38, no. 11, pp. 2237–2247, 2005, ISSN: 00219290. DOI: 10.1016/j.jbiomech.2004.09.034.

[168] S. Evans, "On the implementation of a wrinkling, hyperelastic membrane model for skin and other materials," *Computer Methods in Biomechanics and Biomedical Engineering*, vol. 12, no. 3, pp. 319–332, 2009, ISSN: 1025-5842. DOI: 10.1080/10255840802546762.

[169] A. Patil, A. Nordmark, and A. Eriksson, "Instabilities of wrinkled membranes with pressure loadings," *Journal of the Mechanics and Physics of Solids*, vol. 94, pp. 298–315, 2016, ISSN: 0022-5096. DOI: 10.1016/J.JMPS.2016.05.014.

[170] A. C. Pipkin, "Relaxed energy densities for large deformations of membranes," *IMA Journal of Applied Mathematics*, vol. 52, no. 3, pp. 297–308, 1994, ISSN: 0272-4960. DOI: 10.1093/imamat/52.3.297.

[171] R. Barsotti, S. S. Ligarò, and G. F. Royer-Carfagni, "The web bridge," *International Journal of Solids and Structures*, vol. 38, no. 48-49, pp. 8831–8850, 2001, ISSN: 00207683. DOI: 10.1016/S0020-7683(01)00115-9.

[172] A. Spagnoli, M. Terzano, R. Brighenti, F. Artoni, and A. Carpinteri, "How Soft Polymers Cope with Cracks and Notches," *Applied Sciences*, vol. 9, no. 6, p. 1086, 2019, ISSN: 2076-3417. DOI: 10.3390/app9061086.

[173] A. J. Schriefl, H. Wolinski, P. Regitnig, S. D. Kohlwein, and G. A. Holzapfel, "An automated approach for three-dimensional quantification of fibrillar structures in optically cleared soft biological tissues," *Journal of The Royal Society Interface*, vol. 10, no. 80, p. 20 120 760, 2013, ISSN: 1742-5689. DOI: 10.1098/rsif.2012.0760.

[174] K. Li, R. W. Ogden, and G. A. Holzapfel, "Computational method for excluding fibers under compression in modeling soft fibrous solids," *European Journal of Mechanics - A/Solids*, vol. 57, pp. 178–193, 2016, ISSN: 09977538. DOI: 10.1016/j.euromechsol.2015.11.003.

[175] V. I. Lebedev and D. N. Laikov, "A quadrature formula for the sphere of the 131st algebraic order of accuracy," in *Doklady Mathematics*, Pleiades Publishing, Ltd., vol. 59, 1999, pp. 477–481.

[176] K. Li, R. W. Ogden, and G. A. Holzapfel, "An exponential constitutive model excluding fibres under compression: Application to extension–inflation of a residually stressed carotid artery," *Mathematics and Mechanics of Solids*, vol. 23, no. 8, pp. 1206–1224, 2018, ISSN: 1081-2865. DOI: 10.1177/1081286517712077.

[177] A. E. Ehret, M. Itskov, and H. Schmid, "Numerical integration on the sphere and its effect on the material symmetry of constitutive equations-A comparative study," *International Journal for Numerical Methods in Engineering*, vol. 81, no. 2, pp. 189–206, 2010, ISSN: 00295981. DOI: 10.1002/nme.2688.

[178] P. Skacel and J. Bursa, "Numerical implementation of constitutive model for arterial layers with distributed collagen fibre orientations," *Computer Methods in Biomechanics and Biomedical Engineering*, vol. 18, no. 8, pp. 816–828, 2015, ISSN: 1025-5842. DOI: 10.1080/10255842.2013.847928.

[179] M. Sivaguru, S. Durgam, R. Ambekar, D. Luedtke, G. Fried, A. Stewart, and K. C. Toussaint, "Quantitative analysis of collagen fiber organization in injured tendons using Fourier transform-second harmonic generation

imaging," *Optics Express*, vol. 18, no. 24, pp. 24 983–24 993, 2010, ISSN: 1094-4087. DOI: 10.1364/OE.18.024983.

[180] A. J. Schriefl, G. Zeindlinger, D. M. Pierce, P. Regitnig, and G. A. Holzapfel, "Determination of the layer-specific distributed collagen fibre orientations in human thoracic and abdominal aortas and common iliac arteries," *Journal of The Royal Society Interface*, vol. 9, no. 71, pp. 1275–1286, 2012, ISSN: 1742-5689. DOI: 10.1098/rsif.2011.0727.

[181] C. P. Fleming, C. M. Ripplinger, B. Webb, I. R. Efimov, and A. M. Rollins, "Quantification of cardiac fiber orientation using optical coherence tomography," *Journal of Biomedical Optics*, vol. 13, no. 3, p. 030 505, 2008, ISSN: 10833668. DOI: 10.1117/1.2937470.

[182] V. Ayyalasomayajula, B. Pierrat, and P. Badel, "A computational model for understanding the micro-mechanics of collagen fiber network in the tunica adventitia," *Biomechanics and Modeling in Mechanobiology*, vol. 18, no. 5, pp. 1507–1528, 2019, ISSN: 1617-7959. DOI: 10.1007/s10237-019-01161-1.

[183] W. Hu, H. Li, C. Wang, S. Gou, and L. Fu, "Characterization of collagen fibers by means of texture analysis of second harmonic generation images using orientation-dependent gray level co-occurrence matrix method," *Journal of Biomedical Optics*, vol. 17, no. 2, p. 026 007, 2012, ISSN: 1083-3668. DOI: 10.1117/1.JBO.17.2.026007.

[184] A. M. Stein, D. A. Vader, L. M. Jawerth, D. A. Weitz, and L. M. Sander, "An algorithm for extracting the network geometry of three-dimensional collagen gels," *Journal of Microscopy*, vol. 232, no. 3, pp. 463–475, 2008, ISSN: 00222720. DOI: 10.1111/j.1365-2818.2008.02141.x.

[185] J. S. Bredfeldt, Y. Liu, C. A. Pehlke, M. W. Conklin, J. M. Szulczewski, D. R. Inman, P. J. Keely, R. D. Nowak, T. R. Mackie, and K. W. Eliceiri, "Computational segmentation of collagen fibers from second-harmonic generation images of breast cancer," *Journal of Biomedical Optics*, vol. 19, no. 1, p. 016 007, 2014, ISSN: 1083-3668. DOI: 10.1117/1.JBO.19.1.016007.

[186] R. Rezakhaniha, A. Agianniotis, J. T. C. Schrauwen, A. Griffa, D. Sage, C. V. C. Bouten, F. N. van de Vosse, M. Unser, and N. Stergiopulos, "Experimental investigation of collagen waviness and orientation in the arterial adventitia using confocal laser scanning microscopy," *Biomechanics and*

Modeling in Mechanobiology, vol. 11, no. 3-4, pp. 461–473, 2012, ISSN: 1617-7959. DOI: 10.1007/s10237-011-0325-z.

[187] Z. Liu, K. P. Quinn, L. Speroni, L. Arendt, C. Kuperwasser, C. Sonnenschein, A. M. Soto, and I. Georgakoudi, "Rapid three-dimensional quantification of voxel-wise collagen fiber orientation," *Biomedical Optics Express*, vol. 6, no. 7, pp. 2294–2310, 2015, ISSN: 2156-7085. DOI: 10.1364/boe.6.002294.

[188] S. Polzer, T. C. Gasser, C. Forsell, H. Druckmüllerova, M. Tichy, R. Staffa, R. Vlachovsky, and J. Bursa, "Automatic Identification and Validation of Planar Collagen Organization in the Aorta Wall with Application to Abdominal Aortic Aneurysm," *Microscopy and Microanalysis*, vol. 19, no. 6, pp. 1395–1404, 2013, ISSN: 1431-9276. DOI: 10.1017/S1431927613013251.

[189] A. Rauff, L. H. Timmins, R. T. Whitaker, and J. A. Weiss, "A Nonparametric Approach for Estimating Three-Dimensional Fiber Orientation Distribution Functions (ODFs) in Fibrous Materials," *IEEE Transactions on Medical Imaging*, vol. 41, no. 2, pp. 446–455, 2022, ISSN: 0278-0062. DOI: 10.1109/TMI.2021.3115716.

[190] R. Alberini, A. Spagnoli, M. J. Sadeghinia, B. Skallerud, M. Terzano, and G. A. Holzapfel, "Fourier transform-based method for quantifying the three-dimensional orientation distribution of fibrous units," *Scientific Reports*, vol. 14, no. 1, p. 1999, 2024, ISSN: 2045-2322. DOI: 10.1038/s41598-024-51550-5.

[191] J. P. Marquez, "Fourier analysis and automated measurement of cell and fiber angular orientation distributions," *International Journal of Solids and Structures*, vol. 43, no. 21, pp. 6413–6423, 2006, ISSN: 00207683. DOI: 10.1016/j.ijsolstr.2005.11.003.

[192] E. E. Morrill, A. N. Tulepbergenov, C. J. Stender, R. Lamichhane, R. J. Brown, and T. J. Lujan, "A validated software application to measure fiber organization in soft tissue," *Biomechanics and Modeling in Mechanobiology*, vol. 15, no. 6, pp. 1467–1478, 2016, ISSN: 1617-7959. DOI: 10.1007/s10237-016-0776-3.

[193] D. Sage, L. Donati, F. Soulez, D. Fortun, G. Schmit, A. Seitz, R. Guiet, C. Vonesch, and M. Unser, "DeconvolutionLab2: An open-source software for deconvolution microscopy," *Methods*, vol. 115, no. 2017, pp. 28–41, 2017, ISSN: 10462023. DOI: 10.1016/j.ymeth.2016.12.015.

[194] C. Zaiontz, *Real Statistics Using Excel*, https://real-statistics.com/, 2023.

[195] M.-T. Ke, S. Fujimoto, and T. Imai, "SeeDB: a simple and morphology-preserving optical clearing agent for neuronal circuit reconstruction," *Nature Neuroscience*, vol. 16, no. 8, pp. 1154–1161, 2013, ISSN: 1097-6256. DOI: 10.1038/nn.3447.

[196] M. J. Sadeghinia, H. M. Aguilera, S. Urheim, R. M. Persson, V. S. Ellensen, R. Haaverstad, G. A. Holzapfel, B. Skallerud, and V. Prot, "Mechanical behavior and collagen structure of degenerative mitral valve leaflets and a finite element model of primary mitral regurgitation," *Acta Biomaterialia*, vol. 164, pp. 269–281, 2023, ISSN: 17427061. DOI: 10.1016/j.actbio.2023.03.029.

[197] J. Schindelin, I. Arganda-Carreras, E. Frise, V. Kaynig, M. Longair, T. Pietzsch, S. Preibisch, C. Rueden, S. Saalfeld, B. Schmid, J.-Y. Tinevez, D. J. White, V. Hartenstein, K. Eliceiri, P. Tomancak, and A. Cardona, "Fiji: an open-source platform for biological-image analysis," *Nature Methods*, vol. 9, no. 7, pp. 676–682, 2012, ISSN: 1548-7091. DOI: 10.1038/nmeth.2019.

[198] S. F. Gibson and F. Lanni, "Experimental test of an analytical model of aberration in an oil-immersion objective lens used in three-dimensional light microscopy," *Journal of the Optical Society of America A*, vol. 8, no. 10, pp. 1601–1613, 1991, ISSN: 1084-7529. DOI: 10.1364/JOSAA.8.001601.

[199] H. Kirshner, D. Sage, and M. Unser, "3D PSF Models for Fluorescence Microscopy in ImageJ," in *Proceedings of the Twelfth International Conference on Methods and Applications of Fluorescence Spectroscopy, Imaging and Probes (MAF11)*, vol. 1, Strasbourg, French Republic, 2011, p. 154.

[200] A. E. Woessner, J. D. Jones, N. J. Witt, E. A. Sander, and K. P. Quinn, "Three-Dimensional Quantification of Collagen Microstructure During Tensile Mechanical Loading of Skin," *Frontiers in Bioengineering and Biotechnology*, vol. 9, p. 153, 2021, ISSN: 2296-4185. DOI: 10.3389/fbioe.2021.642866.

[201] M. Witte, S. Jaspers, H. Wenck, M. Rübhausen, and F. Fischer, "General method for classification of fiber families in fiber-reinforced materials: application to in-vivo human skin images," *Scientific Reports*, vol. 10, no. 1, p. 10 888, 2020, ISSN: 2045-2322. DOI: 10.1038/s41598-020-67632-z.

[202] A. J. Schriefl, A. J. Reinisch, S. Sankaran, D. M. Pierce, and G. A. Holzapfel, "Quantitative assessment of collagen fibre orientations from two-dimensional images of soft biological tissues," *Journal of The Royal Society Interface*, vol. 9, no. 76, pp. 3081–3093, 2012, ISSN: 1742-5689. DOI: 10.1098/rsif.2012.0339.

[203] K. Yanny, K. Monakhova, R. W. Shuai, and L. Waller, "Deep learning for fast spatially varying deconvolution," *Optica*, vol. 9, no. 1, p. 96, 2022, ISSN: 2334-2536. DOI: 10.1364/OPTICA.442438.

[204] J. Lehtinen, J. Munkberg, J. Hasselgren, S. Laine, T. Karras, M. Aittala, and T. Aila, "Noise2Noise: Learning Image Restoration without Clean Data," *35th International Conference on Machine Learning, ICML 2018*, vol. 7, no. 3, pp. 4620–4631, 2018. arXiv: 1803.04189.

[205] L. Bailly, T. Cochereau, L. Orgéas, N. Henrich Bernardoni, S. Rolland du Roscoat, A. McLeer-Florin, Y. Robert, X. Laval, T. Laurencin, P. Chaffanjon, B. Fayard, and E. Boller, "3D multiscale imaging of human vocal folds using synchrotron X-ray microtomography in phase retrieval mode," *Scientific Reports*, vol. 8, no. 1, p. 14 003, 2018, ISSN: 2045-2322. DOI: 10.1038/s41598-018-31849-w.

[206] O. Babalola, A. Mamalis, H. Lev-Tov, and J. Jagdeo, "Optical coherence tomography (OCT) of collagen in normal skin and skin fibrosis," *Archives of Dermatological Research*, vol. 306, no. 1, pp. 1–9, 2014, ISSN: 0340-3696. DOI: 10.1007/s00403-013-1417-7.

[207] B. H. Oh, K. H. Kim, and K. Y. Chung, "Skin Imaging Using Ultrasound Imaging, Optical Coherence Tomography, Confocal Microscopy, and Two-Photon Microscopy in Cutaneous Oncology," *Frontiers in Medicine*, vol. 6, no. November, pp. 1–11, 2019, ISSN: 2296-858X. DOI: 10.3389/fmed.2019.00274.

[208] C. H. Daly and G. F. Odland, "Age-related Changes in the Mechanical Properties of Human Skin," *Journal of Investigative Dermatology*, vol. 73, no. 1, pp. 84–87, 1979, ISSN: 0022202X. DOI: 10.1111/1523-1747.ep12532770.

[209] A. B. Cua, K. P. Wilhelm, and H. I. Maibach, "Elastic properties of human skin: relation to age, sex, and anatomical region," *Archives of Dermatological Research*, vol. 282, no. 5, pp. 283–288, 1990, ISSN: 0340-3696. DOI: 10.1007/BF00375720.

[210] C.-Y. Lin, G. P. Sugerman, S. Kakaletsis, W. D. Meador, A. T. Buganza, and M. K. Rausch, "Sex- and age-dependent skin mechanics—A detailed look in mice," *Acta Biomaterialia*, vol. 175, pp. 106–113, 2024, ISSN: 17427061. DOI: 10.1016/j.actbio.2023.11.032.

[211] D. W. Laurence, S. Wang, R. Xiao, J. Qian, A. Mir, H. M. Burkhart, G. A. Holzapfel, and C.-H. Lee, "An investigation of how specimen dimensions affect biaxial mechanical characterizations with CellScale BioTester and constitutive modeling of porcine tricuspid valve leaflets," *Journal of Biomechanics*, vol. 160, no. October, p. 111 829, 2023, ISSN: 00219290. DOI: 10.1016/j.jbiomech.2023.111829.

[212] T. K. Tonge, L. M. Voo, and T. D. Nguyen, "Full-field bulge test for planar anisotropic tissues: Part II – A thin shell method for determining material parameters and comparison of two distributed fiber modeling approaches," *Acta Biomaterialia*, vol. 9, no. 4, pp. 5926–5942, 2013, ISSN: 17427061. DOI: 10.1016/j.actbio.2012.11.034.

[213] M. Diab, N. Kumaraswamy, G. P. Reece, S. E. Hanson, M. C. Fingeret, M. K. Markey, and K. Ravi-Chandar, "Characterization of human female breast and abdominal skin elasticity using a bulge test.," *Journal of the Mechanical Behavior of Biomedical Materials*, vol. 103, p. 103 604, Mar. 2020, ISSN: 17516161. DOI: 10.1016/j.jmbbm.2019.103604.

[214] E. Fagerholt, T. Børvik, and O. Hopperstad, "Measuring discontinuous displacement fields in cracked specimens using digital image correlation with mesh adaptation and crack-path optimization," *Optics and Lasers in Engineering*, vol. 51, no. 3, pp. 299–310, 2013, ISSN: 01438166. DOI: 10.1016/j.optlaseng.2012.09.010.

[215] S. Zhuo, X. Zhu, J. Chen, and S. Xie, "Quantitative biomarkers of human skin photoaging based on intrinsic second harmonic generation signal," *Scanning*, vol. 35, no. 4, pp. 273–276, 2013, ISSN: 0161-0457. DOI: 10.1002/sca.21062.

[216] D. S. Richardson and J. W. Lichtman, "Clarifying Tissue Clearing," *Cell*, vol. 162, no. 2, pp. 246–257, 2015, ISSN: 00928674. DOI: 10.1016/j.cell.2015.06.067.

[217] J. M. Bueno, R. M. Martinez-Ojeda, L. M. Mugnier, and P. Artal, "Deconvolution Method for Multiphoton Microscopy: An Application to Thick Ocular Tissues," in *2019 21st International Conference on Transparent Op-*

tical Networks (ICTON), Angers, France: IEEE, Jul. 2019, pp. 1–4, ISBN: 978-1-72812-779-8. DOI: 10.1109/ICTON.2019.8840328.

[218] A. Feuchtinger, A. Walch, and M. Dobosz, "Deep tissue imaging: a review from a preclinical cancer research perspective," *Histochemistry and Cell Biology*, vol. 146, no. 6, pp. 781–806, 2016, ISSN: 0948-6143. DOI: 10.1007/s00418-016-1495-7.

[219] M. S. Sacks, "Biaxial Mechanical Evaluation of Planar Biological Materials," *Journal ofElasticity*, vol. 61, pp. 199–246, 2000. DOI: 10.1023/A:1010917028671.

[220] J. Murphy, W. Goodhall, and A. Patterson, "Langer's Lines – What are they and do they matter?" *British Journal of Oral and Maxillofacial Surgery*, vol. 55, no. 10, e86–e87, 2017, ISSN: 02664356. DOI: 10.1016/j.bjoms.2017.08.012.

[221] S. Calve, A. Ready, C. Huppenbauer, R. Main, and C. P. Neu, "Optical Clearing in Dense Connective Tissues to Visualize Cellular Connectivity In Situ," *PLOS ONE*, vol. 10, no. 1, P. McNeil, Ed., e0116662, 2015, ISSN: 1932-6203. DOI: 10.1371/journal.pone.0116662.

[222] M. Muntifering, D. Castranova, G. A. Gibson, E. Meyer, M. Kofron, and A. M. Watson, "Clearing for Deep Tissue Imaging," *Current Protocols in Cytometry*, vol. 86, no. 1, pp. 1–21, 2018, ISSN: 1934-9297. DOI: 10.1002/cpcy.38.

[223] S. Abadie, C. Jardet, J. Colombelli, B. Chaput, A. David, J. Grolleau, P. Bedos, V. Lobjois, P. Descargues, and J. Rouquette, "3D imaging of cleared human skin biopsies using light-sheet microscopy: A new way to visualize in-depth skin structure," *Skin Research and Technology*, vol. 24, no. 2, pp. 294–303, 2018, ISSN: 0909-752X. DOI: 10.1111/srt.12429.

[224] Y. Tan, C. P. L. Chiam, Y. Zhang, H. L. Tey, and L. G. Ng, "Research Techniques Made Simple: Optical Clearing and Three-Dimensional Volumetric Imaging of Skin Biopsies," *Journal of Investigative Dermatology*, vol. 140, no. 7, 1305–1314.e1, 2020, ISSN: 0022202X. DOI: 10.1016/j.jid.2020.04.014.

[225] S. Budday, G. Sommer, C. Birkl, C. Langkammer, J. Haybaeck, J. Kohnert, M. Bauer, F. Paulsen, P. Steinmann, E. Kuhl, and G. Holzapfel, "Mechanical characterization of human brain tissue," *Acta Biomaterialia*, vol. 48, pp. 319–340, 2017, ISSN: 17427061. DOI: 10.1016/j.actbio.2016.10.036.

[226] A. E. Ehret, K. Bircher, A. Stracuzzi, V. Marina, M. Zündel, and E. Mazza, "Inverse poroelasticity as a fundamental mechanism in biomechanics and mechanobiology," *Nature Communications*, vol. 8, no. 1, p. 1002, 2017, ISSN: 2041-1723. DOI: 10.1038/s41467-017-00801-3.

[227] A. Wahlsten, M. Pensalfini, A. Stracuzzi, G. Restivo, R. Hopf, and E. Mazza, "On the compressibility and poroelasticity of human and murine skin," *Biomechanics and Modeling in Mechanobiology*, vol. 18, no. 4, pp. 1079–1093, 2019, ISSN: 1617-7959. DOI: 10.1007/s10237-019-01129-1.

[228] P. D. H. M. Verhaegen, P. P. M. Van Zuijlen, N. M. Pennings, J. Van Marle, F. B. Niessen, C. M. A. M. Van Der Horst, and E. Middelkoop, "Differences in collagen architecture between keloid, hypertrophic scar, normotrophic scar, and normal skin: An objective histopathological analysis," *Wound Repair and Regeneration*, vol. 17, no. 5, pp. 649–656, 2009, ISSN: 1067-1927. DOI: 10.1111/j.1524-475X.2009.00533.x.

[229] L. Mostaço-Guidolin, N. Rosin, and T.-L. Hackett, "Imaging Collagen in Scar Tissue: Developments in Second Harmonic Generation Microscopy for Biomedical Applications," *International Journal of Molecular Sciences*, vol. 18, no. 8, p. 1772, 2017, ISSN: 1422-0067. DOI: 10.3390/ijms18081772.

[230] L. Baumann, E. F. Bernstein, A. S. Weiss, D. Bates, S. Humphrey, M. Silberberg, and R. Daniels, "Clinical Relevance of Elastin in the Structure and Function of Skin," *Aesthetic Surgery Journal Open Forum*, vol. 3, no. 3, pp. 1–8, 2021, ISSN: 2631-4797. DOI: 10.1093/asjof/ojab019.

[231] M. Zhou, P. J. González, L. Van Haasterecht, A. Soylu, M. Mihailovski, P. Van Zuijlen, and M. L. Groot, "Uniaxial mechanical stretch properties correlated with three-dimensional microstructure of human dermal skin," *Biomechanics and Modeling in Mechanobiology*, Feb. 2024, ISSN: 1617-7959, 1617-7940. DOI: 10.1007/s10237-023-01813-3.

[232] P.-o. Persson and G. Strang, "A Simple Mesh Generator in MATLAB," *SIAM Review*, vol. 46, no. 2, pp. 329–345, 2004, ISSN: 0036-1445. DOI: 10.1137/S0036144503429121.

[233] R. Alberini, A. Spagnoli, and M. Terzano, "Numerical modelling of wrinkled hyperelastic membranes with topologically complex internal boundary conditions," *International Journal of Mechanical Sciences*, vol. 212, no. July, p. 106 816, 2021, ISSN: 00207403. DOI: 10.1016/j.ijmecsci.2021.106816.

[234] T. J. Zuber, "The Mattress Sutures: Vertical, Horizontal, and Corner Stitch," *American Family Physician*, vol. 66, no. 12, p. 2231, 2002, ISSN: 0002-838X.

[235] A. L. Krunic, S. Weitzul, and R. S. Taylor, "Running Combined Simple and Vertical Mattress Suture: A Rapid Skin-Everting Stitch," *Dermatologic Surgery*, vol. 31, no. 10, pp. 1325–1329, 2006, ISSN: 10760512. DOI: 10.1111/j.1524-4725.2005.31212.

[236] A. Spagnoli, R. Alberini, E. Raposio, and M. Terzano, "Simulation and optimization of reconstructive surgery procedures on human skin," *Journal of the Mechanical Behavior of Biomedical Materials*, vol. 131, p. 105 215, 2022, ISSN: 17516161. DOI: 10.1016/j.jmbbm.2022.105215.

[237] L. Mahmud, N. F. Adull Manan, M. H. Ismail, and J. Mahmud, "Characterisation of soft tissues biomechanical properties using 3D Numerical Approach," in *2013 IEEE Business Engineering and Industrial Applications Colloquium (BEIAC)*, vol. 3, IEEE, 2013, pp. 801–806, ISBN: 978-1-4673-5968-9. DOI: 10.1109/BEIAC.2013.6560246.

[238] E. Berardesca, J. de Rigal, J. Leveque, and H. Maibach, "In vivo Biophysical Characterization of Skin Physiological Differences in Races," *Dermatology*, vol. 182, no. 2, pp. 89–93, 1991, ISSN: 1018-8665. DOI: 10.1159/000247752.